Development of heterogeneous chemoenzymatic catalysts based on Metal-Organic Framework for the selective and eco-friendly amination of alcohols

Yifan Zan

Sorbonne Université

Ecole doctorale 397 Physique et Chimie des Matériaux

Laboratoire de Réactivité de Surface

Development of heterogeneous chemoenzymatic catalysts based on Metal-Organic Framework for the selective and eco-friendly amination of alcohols

Par Yifan Zan

Thèse de doctorat de Chimie

Dirigée par Prof. Claude Jolivalt et Dr. Julien Reboul

Présentée et soutenue publiquement le 7 Novembre 2023

Devant un jury composé de :

Laurence HECQUET	Professeure	Rapporteure
Mickael CAPRON	Maître de conférences	Rapporteur
Clémence SICARD	Maîtresse de conférences	Examinatrice
Jean-François LAMBERT	Professeur	Examinateur, president de jury
Claude JOLIVALT	Professeure	Directrice de thèse
Julien REBOUL	Chargé de recherche	Co-encadrant de thèse

Acknowledgments

After completing this Ph.D. thesis at Laboratoire de Réactivité de Surface (LRS), CNRS, Sorbonne Université, I would like to express my deep gratitude to all those who have supported me during this academic journey.

Firstly, I would like to extend my sincere appreciation to my supervisors, Prof. Claude Jolivalt and Dr. Julien Reboul. I am grateful for the opportunity to learn from and collaborate with you. Over the past three years, I have not only learnt a lot from your profound knowledge in chemistry, material sciences, and catalysis, along with a rigorous scientific attitude, but also benefited from your patience, generosity, and kindness, making my international academic experience exceptionally enriching.

Secondly, my gratitude goes to the members of my thesis committee: Prof. Jean-Francois Lambert, Prof. Laurence Hecquet, Dr. Mickael Capron, and Dr. Clémence Sicard. Thank you for dedicating your valuable time to reviewing my thesis and providing professional and constructive feedback. I also acknowledge the contribution of Prof. Uwe T. Bornscheuer from the University of Greifswald, who generously donated the transaminase crucial for completing my thesis. Special thanks to ED 397 Physique et Chimie des Materiaux for the financial support of this project.

My academic journey in France began four years ago in the summer, after completing my master's degree in China. I was fully sponsored by the French Embassy in China to attend the France Excellence Summer School at Lille, delving into the knowledge of sustainable catalysis. It was during this program that I first set foot in France and discovered the prospect of pursuing a doctoral degree here. I extend my thanks to the French Embassy in China for this opportunity, without which I may not have visited and finally chosen France. During the summer school at Lille University, I had the chance to meet outstanding master's students from around the world and gained a preliminary understanding of French culture. Special gratitude to Prof. Andrei Khodakov from Lille University, who helped me significantly during the Ph.D. position search.

In late October 2020, I arrived in France to commence my doctoral studies. It was a challenging moment, and I vividly recall the warm welcome from my supervisors, Prof. Claude Jolivalt and Dr. Julien Reboul, on my first day at the laboratory. Subsequently, I returned home to undergo a month-long quarantine. Starting from scratch in a foreign land was not easy, but with the assistance of my laboratory colleagues, I quickly adapted to the new environment. Especially my first office mate, Josefine Schnee, who is not only an outstanding colleague in research but also a good friend who has consistently provided me with encouragement. The permanent staffs of LRS were genuinely helpful. I am grateful for the support extended by individuals such as Antoine Miche, Christophe Méthivier, Clément Guibert, Ferdaous Ben Romdhane, Franck Launay, Frederic Averseng, Laetitia Valentin, Laurent Delannoy, Jean-Marc Krafft, Juliettte

Blanchard, Mireille Turmine, Sandra Casale, Saremblé Koné-Guira, Hélène Pernot, Vincent LosIinho, Mohamed Selmane, for both their help in experiments and daily life. I also express gratitude to the administrative staff of the laboratory, namely Annie Mettendorff, Aurélien Chervalier, and Sonia M'barek, for their assistance with administrative procedures.

During the initial year, I was a newcomer to the lab and unfamiliar with French life. Fortunately, several senior Ph.D. students, including Louis Ter-ovanessian and Silvia Leccese, along with my dear friend Sunyoung Hur, provided valuable advice, helping me integrate rapidly into lab life. Special thanks to my office mates in Office 302, namely Nawres Hmili, Yacoub Smati, Andrea Calcinoni, Ravit Abecassis, and Marwa Dahabi. Over these three years, we shared most of our time together, and I will always cherish the laughter and camaraderie in our office. Deep gratitude extends to my dear friends, Alert Issa, Ali Djellali, Ana Carolina Schuh Frantz, Bakytzhan Yeskendir, Cyrine Lamloum, Manon Miran, Mathieu Delom, Youssef Kharchouf, Walid Ait Mammar. Honestly, I have already started missing the jokes we shared during our daily lunches at CROUS; your sense of humor is truly impressive. You are not just brilliant scientists but also the best colleagues! I would also like to express my thanks to other LRS colleagues, including Brittany Foley, Corentin Reynaud, Ekaterina Kurchavova, Fanny Duhalde, Jihye Lee, Joanne Le-chesnais, Rita Raachini, and Valentin Saliba. LRS, we are the best!

Gratitude extends to my friends from the Chinese community: Zhaoxin Wang, Daoming Sun, Gaoyu Li, Haozheng Yu, Hefei Sun, Yang Yu, Huanjun Kong, Yaojun Hou, Yu Fan, Yuelin Xie, Yuxin Deng, Zhihang Zhang, and Zhihao Yu. In our pursuit of Ph.D. in France, we supported each other, overcoming every challenge together due to our shared cultural background. Special thanks to Moktar Sound sysTem at Sorbonne Université, a warm brass band (fanfare) that felt more like a home. The joyful year spent with you was memorable, and I appreciate the opportunities you provided for me to showcase my art talents on the streets of Paris, as well as your patience with my imperfect French.

Lastly, I express deep gratitude to my family in China, especially my parents. Due to the epidemic, I have not been able to reunite with you over the past three years. It was very hard for me, especially since my grandmother left us during this time and I was not able to see her one last time. But your unwavering support was crucial to me.

In the limited space available, I cannot thank everyone who has helped and supported me during my doctoral thesis. Without your help, I could not have achieved what I have today. Once again, I convey my sincere appreciation.

Yifan Zan

Abbreviations

ACN	Acetonitrile
2-AHP	2-Amino-2-(hydroxymethyl)propane-1,3-diol
3-ATZ	3-Amino-1,2,4-triazole
AP	Acetophenone
BA	Benzyl alcohol
DAP	1,2-Diaminopropane
DMAP	4-Dimethylaminopyridine
GDH	Glucose dehydrogenase
IPA	Isopropylamine
ImC	Imidazole-2-carboxaldehyde
LDH	Lactic dehydrogenase
MBA	α-Methylbenzylamine
2-MeIM	2-Methylimidazole
MOFs	Metal-Organic Frameworks
NPs	Nanoparticles
NAD^+	β-Nicotinamide adenine dinucleotide, oxidized form
NADH	β-nicotinamide adenine dinucleotide, reduced form
PE	1-phenylethanol
PLP	pyridoxal 5'-phosphate hydrate
PVP	Polyvinylpyrrolidone
TEMPO	2,2,6,6-Tetramethylpiperidine 1-oxyl
TA	Transaminase
TFA	Trifluoroacetic acid
ZIF-8	Zeolitic imidazolate framework-8

Table of content

General introduction

In the pursuit of sustainable and eco-friendly processes, green chemistry has emerged as a promising discipline. The concept of green chemistry revolves around the development of innovative methodologies and catalytic systems aimed at minimizing the environmental impact of chemical processes. It shows a particular focus on chemical processes related to the sustainable conversion of biomass-derived chemicals.[1,2] With the global crises of climate change and the depletion of fossil resources, the conversion of renewable biomass into valuable chemicals has drew significant attention of the academic community.[3,4] In this context, cascade reactions are of great interest due to their potential to streamline synthetic pathways and enhance overall efficiency.[5] Among them, the chemoenzymatic cascade reaction becomes interesting due to the inclusion of a biocatalytic step, as it has the potential to synthesize complex chiral molecules in a sustainable manner.[6,7] The aim of this doctoral thesis is to realize a challenging cascade reaction: the creation of an efficient one-pot system comprising two catalytic steps—chemical catalytic oxidation of alcohols and biocatalytic amination of aldehydes and ketones. This system will utilize Metal-Organic Frameworks (MOFs) as heterogeneous supports, incorporating chemical catalytic sites and ω-transaminases (ω-TAs) enzymes to construct a heterogeneous chemoenzymatic catalyst. This chemoenzymatic catalyst will facilitate the one-pot cascade reaction for the synthesis of chiral amines. My research explores the convergence of MOF-based heterogeneous catalysis, enzyme immobilization, and amination of alcohol in green chemistry.

Biomass-based chemicals and green chemistry

The use of biomass as feedstocks for chemical synthesis is a central theme of modern green chemistry. Derived from renewable resources such as plants, agricultural waste and forestry waste, biomass is a sustainable alternative to fossil fuels and petrochemical feedstocks.[2,8,9] Under the challenges of climate change and the energy crisis, the Paris Agreement, signed by

195 countries including the European Union, sets a goal of realizing carbon neutral by 2050.[10] In order to achieve this goal, the conversion of biomass into valuable chemicals is an indispensable strategy for moving towards a more sustainable and environmentally friendly chemical industry. The concept of green chemistry is crucial in achieving sustainable conversion of biomass resources.[1] In contrast to conventional chemical processes with their harsh reaction conditions, use of hazardous reagents, and consequent high energy consumption and severe environmental pollution, green chemistry overcomes these limitations by designing processes that are atomically economical, environmentally friendly, and highly efficient. The environmentally friendly conversion of biomass-derived alcohols into high-value chiral amines is in line with the goals of green chemistry, which is this framework that forms the background of this work.

Oxidation and amination of alcohols: key transformations

In order to guide the high value of biomass-based resources, the U.S. Department of Energy (DOE) screened 12 of the most representative platform compounds, including alcohols, from more than 300 compounds derived from biomass.[11] Alcohols are a class of organic molecules containing hydroxyl (-OH) groups, which have a wide range of applications in organic synthesis as they can be oxidized to a wide range of organic functional groups such as aldehydes, ketones and carboxylic acids, which can be used to prepare a variety of high value-added compounds.[12,13] The amination of alcohols is a strategically important transformation in organic synthesis, which allows the conversion of readily available and diverse alcohol substrates into valuable chiral amines.[14] Chiral amines are essential building blocks for the synthesis of pharmaceuticals, pesticides and fine chemicals.[15] The stereoselective synthesis of chiral amines is particularly challenging and has traditionally relied on transition metal-catalyzed approaches. However, these methods are usually limited by a limited range of substrates, harsh reaction conditions, high energy intensity, and the need for expensive ligands and catalysts.[16] Therefore, how to synthesize chiral amines in a more sustainable and environmentally friendly way attracts interests.

Chemoenzymatic cascade reactions: an advanced strategy in green synthesis of chiral amine

One-pot cascades allow multi-step reactions to occur sequentially in a single reactor, reducing the number of discrete synthetic steps, reducing the need for purification and isolation of intermediates, and minimizing waste generation.[6,7] Ultimately, the cascade reaction significantly reduces the overall carbon footprint relative to traditional processes. In cascade reactions, chemoenzymatic cascade catalysis has attracted much attention. The introduction of biocatalysis as part of a cascade reaction can take advantage of the high specificity, stereoselectivity, and regioselectivity of enzymes.[17] Chemoenzymatic cascade reactions provide more sustainable methods of assembling complex molecules, including modelling complex life processes such as photosynthesis.[18] In this study, we develop chemical catalysts based on MOFs for alcohol oxidation and immobilize on the same MOFs with ω-TAs, enzymes which have shown to be able to efficiently and sustainably asymmetric synthesize chiral amines.[19–21] We aim to achieve the one-pot synthesis of chiral amines from alcohols in the presence of chemical catalysts and ω-TAs.

Scientific questions: compatibility of the two catalytic steps

In order to achieve the above objectives, our core scientific challenge is to develop a heterogeneous one-pot catalytic system comprising two catalytic steps: chemocatalytic oxidation over MOF-based chemocatalysts and biocatalytic amination catalyzed by ω-TAs. Achieving compatibility between these two catalytic steps is critical. Specifically, it is essential that the operating conditions of the developed chemical catalysts have a window of compatibility with those of the ω-TAs. In addition, the chemical catalysts will also serve as carriers for the immobilization of ω-TAs, giving them recyclability while ensuring their stability. Metal-organic frameworks (MOFs) are ideal supports to be developed to meet these requirements. MOFs are indeed known for their ultra-large specific surface area, 3D-pore structure, and high structural tunability.[22] It has been developed rapidly in the last two decades, and a large number of MOFs-based materials for catalysis have been investigated.[23–25] In

addition, its unique bioaffinity gives it great potential in life science fields such as drug delivery, gene delivery and enzyme immobilization.[26–28]

In conclusion, in order to address the above scientific issues, we developed MOFs-based chemoenzymatic catalysts compatible with the reaction conditions of ω-TAs and optimized the conditions for the oxidation and amination reactions of alcohols, confirming the feasibility of the one-pot method for the cascade reaction. Various methods of immobilization of ω-TAs on MOFs-based catalysts were investigated, and finally, we preliminarily explored the above chemoenzymatic heterogeneous catalysts for the catalytic one-pot/two-steps amination reaction of alcohols. The study of this integrated catalytic system provides a theoretical basis for the development of chemical catalysts for the oxidation of MOFs-based alcohols, the immobilization of ω-TAs transaminases on MOFs, and new possibilities for the environmentally friendly synthesis of chiral amines.

References

(1) Sheldon, R. A. Green Chemistry, Catalysis and Valorization of Waste Biomass. *Journal of Molecular Catalysis A: Chemical* **2016**, *422*, 3–12. https://doi.org/10.1016/j.molcata.2016.01.013.

(2) Dusselier, M.; Mascal, M.; Sels, B. F. Top Chemical Opportunities from Carbohydrate Biomass: A Chemist's View of the Biorefinery. In *Selective Catalysis for Renewable Feedstocks and Chemicals*; Nicholas, K. M., Ed.; Springer International Publishing: Cham, 2014; 1–40. https://doi.org/10.1007/128_2014_544.

(3) Martin Alonso, D.; Q. Bond, J.; A. Dumesic, J. Catalytic Conversion of Biomass to Biofuels. *Green Chemistry* **2010**, *12* (9), 1493–1513. https://doi.org/10.1039/C004654J.

(4) Luterbacher, J. S.; Alonso, D. M.; Dumesic, J. A. Targeted Chemical Upgrading of Lignocellulosic Biomass to Platform Molecules. *Green Chem.* **2014**, *16* (12), 4816–4838. https://doi.org/10.1039/C4GC01160K.

(5) F. Mayer, S.; Kroutil, W.; Faber, K. Enzyme-Initiated Domino (Cascade) Reactions. *Chemical Society Reviews* **2001**, *30* (6), 332–339. https://doi.org/10.1039/B105493G.

(6) van Dongen, S. F. M.; Nallani, M.; Cornelissen, J. J. L. M.; Nolte, R. J. M.; van Hest, J. C. M. A Three-Enzyme Cascade Reaction through Positional Assembly of Enzymes in a

Polymersome Nanoreactor. *Chemistry – A European Journal* **2009**, *15* (5), 1107–1114. https://doi.org/10.1002/chem.200802114.

(7) Ricca, E.; Brucher, B.; Schrittwieser, J. H. Multi-Enzymatic Cascade Reactions: Overview and Perspectives. *Advanced Synthesis & Catalysis* **2011**, *353* (13), 2239–2262. https://doi.org/10.1002/adsc.201100256.

(8) Vassilev, S. V.; Baxter, D.; Andersen, L. K.; Vassileva, C. G. An Overview of the Chemical Composition of Biomass. *Fuel* **2010**, *89* (5), 913–933. https://doi.org/10.1016/j.fuel.2009.10.022.

(9) Román-Leshkov, Y.; Barrett, C. J.; Liu, Z. Y.; Dumesic, J. A. Production of Dimethylfuran for Liquid Fuels from Biomass-Derived Carbohydrates. *Nature* **2007**, *447* (7147), 982–985. https://doi.org/10.1038/nature05923.

(10) Paris Agreement. *Int'l Legal Materials* **2016**, *55*, 743.

(11) Werpy, T.; Petersen, G. *Top Value Added Chemicals from Biomass: Volume I -- Results of Screening for Potential Candidates from Sugars and Synthesis Gas*; DOE/GO-102004-1992; National Renewable Energy Lab. (NREL), Golden, CO (United States), 2004. https://doi.org/10.2172/15008859.

(12) Chan-Thaw, C. E.; Savara, A.; Villa, A. Selective Benzyl Alcohol Oxidation over Pd Catalysts. *Catalysts* **2018**, *8* (10), 431. https://doi.org/10.3390/catal8100431.

(13) Sheldon, R. A. Recent Advances in Green Catalytic Oxidations of Alcohols in Aqueous Media. *Catalysis Today* **2015**, *247*, 4–13. https://doi.org/10.1016/j.cattod.2014.08.024.

(14) Hameury, S.; Bensalem, H.; De Oliveira Vigier, K. Sustainable Amination of Bio-Based Alcohols by Hydrogen Borrowing Catalysis. *Catalysts* **2022**, *12* (11), 1306. https://doi.org/10.3390/catal12111306.

(15) *Stereoselective Formation of Amines*; Li, W., Zhang, X., Eds.; Topics in Current Chemistry; Springer: Berlin, Heidelberg, 2014; Vol. 343. https://doi.org/10.1007/978-3-642-53929-9.

(16) Cabré, A.; Verdaguer, X.; Riera, A. Recent Advances in the Enantioselective Synthesis of Chiral Amines via Transition Metal-Catalyzed Asymmetric Hydrogenation. *Chem. Rev.* **2022**, *122* (1), 269–339. https://doi.org/10.1021/acs.chemrev.1c00496.

(17) Faisca Phillips, A. M.; Pombeiro, A. J. L.; Kopylovich, M. N. Recent Advances in Cascade Reactions Initiated by Alcohol Oxidation. *ChemCatChem* **2017**, *9* (2), 217–246. https://doi.org/10.1002/cctc.201601176.

(18) Cai, T.; Sun, H.; Qiao, J.; Zhu, L.; Zhang, F.; Zhang, J.; Tang, Z.; Wei, X.; Yang, J.; Yuan, Q.; Wang, W.; Yang, X.; Chu, H.; Wang, Q.; You, C.; Ma, H.; Sun, Y.; Li, Y.; Li, C.; Jiang, H.; Wang, Q.; Ma, Y. Cell-Free Chemoenzymatic Starch Synthesis from Carbon Dioxide. *Science* **2021**, *373* (6562), 1523–1527. https://doi.org/10.1126/science.abh4049.

(19) Guo, F.; Berglund, P. Transaminase Biocatalysis: Optimization and Application. *Green Chemistry* **2017**, *19* (2), 333–360. https://doi.org/10.1039/C6GC02328B.

(20) Mathew, S.; Renn, D.; Rueping, M. Advances in One-Pot Chiral Amine Synthesis Enabled by Amine Transaminase Cascades: Pushing the Boundaries of Complexity. *ACS Catal.* **2023**, *13* (8), 5584–5598. https://doi.org/10.1021/acscatal.3c00555.

(21) Savile, C. K.; Janey, J. M.; Mundorff, E. C.; Moore, J. C.; Tam, S.; Jarvis, W. R.; Colbeck, J. C.; Krebber, A.; Fleitz, F. J.; Brands, J.; Devine, P. N.; Huisman, G. W.; Hughes, G. J.

Biocatalytic Asymmetric Synthesis of Chiral Amines from Ketones Applied to Sitagliptin Manufacture. *Science* **2010**, *329* (5989), 305–309. https://doi.org/10.1126/science.1188934.

(22) Zhu, Q.-L.; Xu, Q. Metal–Organic Framework Composites. *Chem. Soc. Rev.* **2014**, *43* (16), 5468–5512. https://doi.org/10.1039/C3CS60472A.

(23) Chen, L.; Zhan, W.; Fang, H.; Cao, Z.; Yuan, C.; Xie, Z.; Kuang, Q.; Zheng, L. Selective Catalytic Performances of Noble Metal Nanoparticle@MOF Composites: The Concomitant Effect of Aperture Size and Structural Flexibility of MOF Matrices. *Chemistry – A European Journal* **2017**, *23* (47), 11397–11403. https://doi.org/10.1002/chem.201702103.

(24) Wang, W.; Chen, S.; Cal, E. G.; Moro, M. M.; Moya, S.; Coy, E.; Wang, C.; Hamon, J.-R.; Astruc, D. ZIF-8-Based vs. ZIF-8-Derived Au and Pd Nanoparticles as Efficient Catalysts for the Ullmann Homocoupling Reaction. *Inorg. Chem. Front.* **2020**, *7* (20), 3945–3952. https://doi.org/10.1039/D0QI00831A.

(25) Tang, J.; Zhao, J.; Wang, S.; Zhang, L.; Zhao, M.; Huang, Z.; Hu, Y. Pre-Modification Strategy to Prepare a Novel Zr-Based MOF for Selective Adsorption of Palladium(II) from Solution. *Chemical Engineering Journal* **2021**, *407*, 127223. https://doi.org/10.1016/j.cej.2020.127223.

(26) Zhuang, J.; Young, A. P.; Tsung, C.-K. Integration of Biomolecules with Metal–Organic Frameworks. *Small* **2017**, *13* (32), 1700880. https://doi.org/10.1002/smll.201700880.

(27) Liu, J.; Li, Y.; Lou, Z. Recent Advancements in MOF/Biomass and Bio-MOF Multifunctional Materials: A Review. *Sustainability* **2022**, *14* (10), 5768. https://doi.org/10.3390/su14105768.

(28) Lian, X.; Fang, Y.; Joseph, E.; Wang, Q.; Li, J.; Banerjee, S.; Lollar, C.; Wang, X.; Zhou, H.-C. Enzyme–MOF (Metal–Organic Framework) Composites. *Chem. Soc. Rev.* **2017**, *46* (11), 3386–3401. https://doi.org/10.1039/C7CS00058H.

Chapter 1.

Bibliography

1.1. Metal-Organic Framework (MOFs) for catalysis and enzymes immobilization

1.1.1. Definition and classification of MOFs

Metal-organic frameworks (MOFs), also known as porous coordination polymers (PCP), are inorganic-organic hybrid porous materials formed by the self-assembly of metal cations or clusters (secondary building units, SBUs) and organic ligands via coordination bonds.

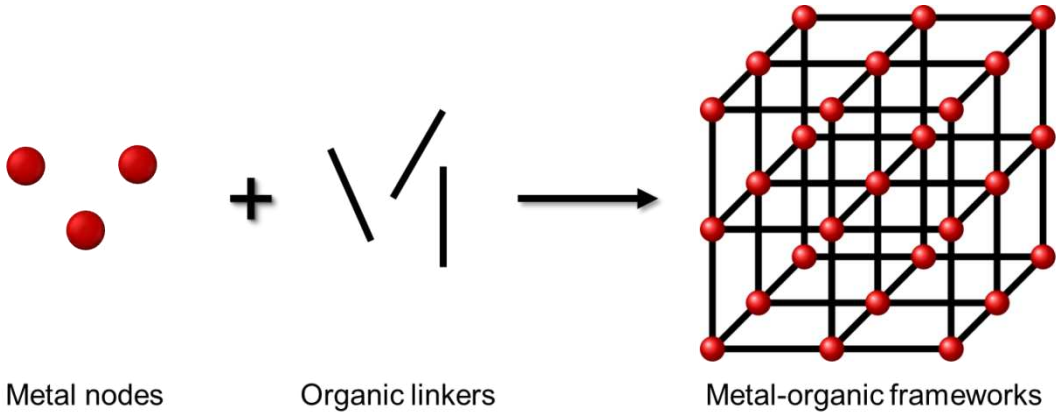

Figure 1.1. Conceptual scheme of MOFs

MOFs have emerged as an interdisciplinary field combining coordination chemistry and crystalline materials over the past two decades. [1–3] Before the concept of MOFs was introduced, similar structures had already been identified in natural and in synthetic compounds.[4] Among them, early-stage coordination polymers such as Hofmann clathrates ($Ni(CN)_4 \cdot Ni(NH_3)_2$) and Prussian Blue ($Fe_7(CN)_{18} \cdot 14H_2O$) are considered to be the forerunners of MOFs.[5,6] In 1990, R. Robson and B. Hoskins introduced the concept of topology to coordination chemistry through the synthesis of $Cu^I[C(C_6H_4.CN)_4]BF_4$ and $[N(CH_3)_4]$ $[CuZn(CN)_4]$ laying the foundation for the development of MOFs.[7] The term of Metal-organic Frameworks was first introduced by O. M. Yaghi's group in 1995.[8] In 1997, S. Kitagawa's group discovered the porosity of MOF($\{[M_2(4,4'\text{-bpy})_3(NO_3)_4](H_2O)_x\}_n$ (M = Co, x = 4; M = Ni, x = 4; M = Zn, x = 2)) by gas adsorption experiment.[9] In 1999, two important MOFs were reported in the same year. MOF-5

($Zn_4O(BDC)_3$, BDC^{2-}=1,4-benzodicarboxylate) consisting of Zn(II) and terephthalate linker (or 1,4-benzodicarboxylate) was reported by the group of O. M. Yaghi (See Figure 1.2 left).[10] MOF-5 has a relatively high-temperature stability after removing the guest molecule. The second MOF, HKUST-1 ($Cu_3(BTC)_2$, BTC= benzene-1,3,5-tricarboxylate), who exhibits an octahedral cage structure was reported by I. D. Williams.[11] The thermal treatment of this MOFs composed of Cu (II) and trimesate linker (or benzene-1,3,5-tricarboxylate) frees coordinatively unsaturated copper sites (CUS) (Lewis acid sites) in its structure which can be exploited as catalytic active centers accessed by substrates. (See Figure 1.2 middle) The discovery of MOF-5 and HKUST-1 has laid the foundation for the design, modification, and functionalization of MOFs. In 2005, Gérard Férey's group reported MIL family such as MIL-53, MIL-100, MIL-101 with high-valent metals (Fe^{3+}, Al^{3+}, Cr^{3+}, Ti^{4+}) as nodes and terephthalic acid or trimesic acid as linker.[12–14] MIL-101 (See Figure 1.2 right) with 4 nm pore diameter and 4000 m^2/g specific surface area pioneered mesoporous MOFs.[15] In fact MIL-101 is one of the representatives of high specific surface area properties of MOFs.

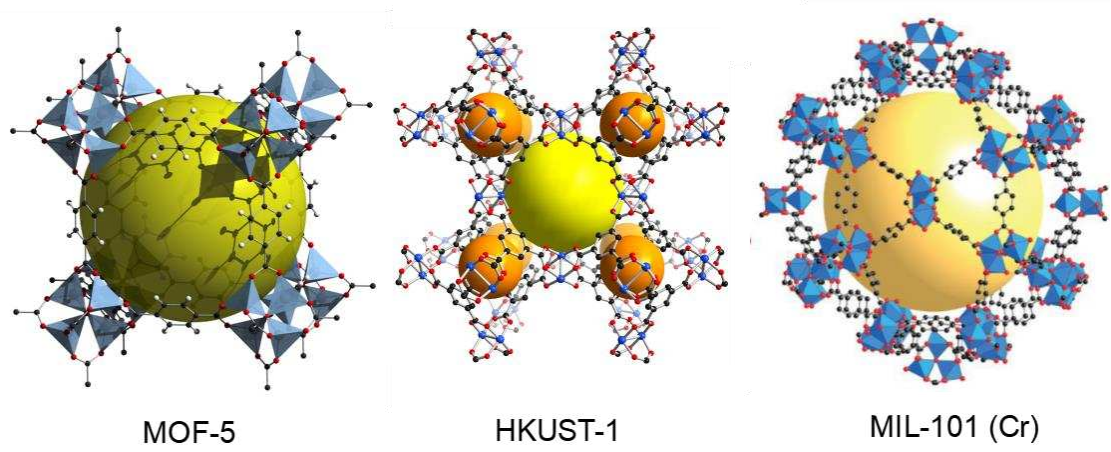

Figure 1.2. Three representative MOFs: MOF-5, HKUST-1, MIL-101[16]

MOFs have attracted a wide range of interest due to their large specific surface area, 3-dimensional structural and pore-size tunability, since they were discovered.[17] As hybrid materials with molecular-level design of the structure and simple synthesis, MOFs have rich prospects for physical, chemical and biological applications.[18–21] For example, the large specific

surface area of MOFs is promising for the adsorption, storage of H_2, CO_2, and other gases.[22,23] Some properties such as substrates size selectivity for catalytic reactions and selective molecular separation of gas or liquid can be achieved by tuning the 3-dimensional structure of MOFs, such as pore size and pore volume. Moreover, the large versatility of their chemical composition and of their synthesis conditions facilitate their combination with a variety of materials, such as organic polymers (monoliths, membranes…) metal and metal oxides (nanoparticles, surfaces…), as well as biological compounds (proteins, bacteria…) to form multifunctional stable composites of great interest for applications such as molecular separation, heterogeneous catalysis, drug delivery, and biosensors. [24,25]

In the past 2 decades, research related to MOFs has expanded rapidly. The Cambridge Crystal Database reported more than 90,000 documented MOFs structures.[26] Besides MOFs materials, MOFs hybrid materials, 2D-MOFs, flexible MOFs, etc. Covalent organic frameworks (COFs) and hydrogen-bonded organic frameworks (HOFs) derived from the concept of MOFs have also been developed significantly.[27,28]

The zeolitic imidazolate frameworks (ZIF) family was first reported in 2006 (See Figure 1.3).[29] ZIF family is named from their topological resemblance to zeolites. Indeed, the coordination of divalent cations (typically Zn^{2+} and Co^{2+}) and imidazole-derived linkers (typically 2-methylimidazole (2-MeIM)) features a metal-linker-metal angle of 120°, which is equivalent to the 120° Si-O-Si angle in zeolites. As a representative ZIFs, ZIF-8 ($Zn(2\text{-}MeIM)_2$) is known for its tolerance to high temperature over 500 °C and several solvents including water, particularly under basic conditions. This good thermal and chemical stability is due to the coordination of a soft acid center (typically Zn^{2+}) and a soft base center (like then nitrogen in 2-MeIM). The tolerance to harsh conditions gives it a wider range of application scenery, especially for heterogeneous catalysis. More, ZIF-8 could be synthesized in under particularly mild and green conditions, even at room temperature and in water.[30–32]

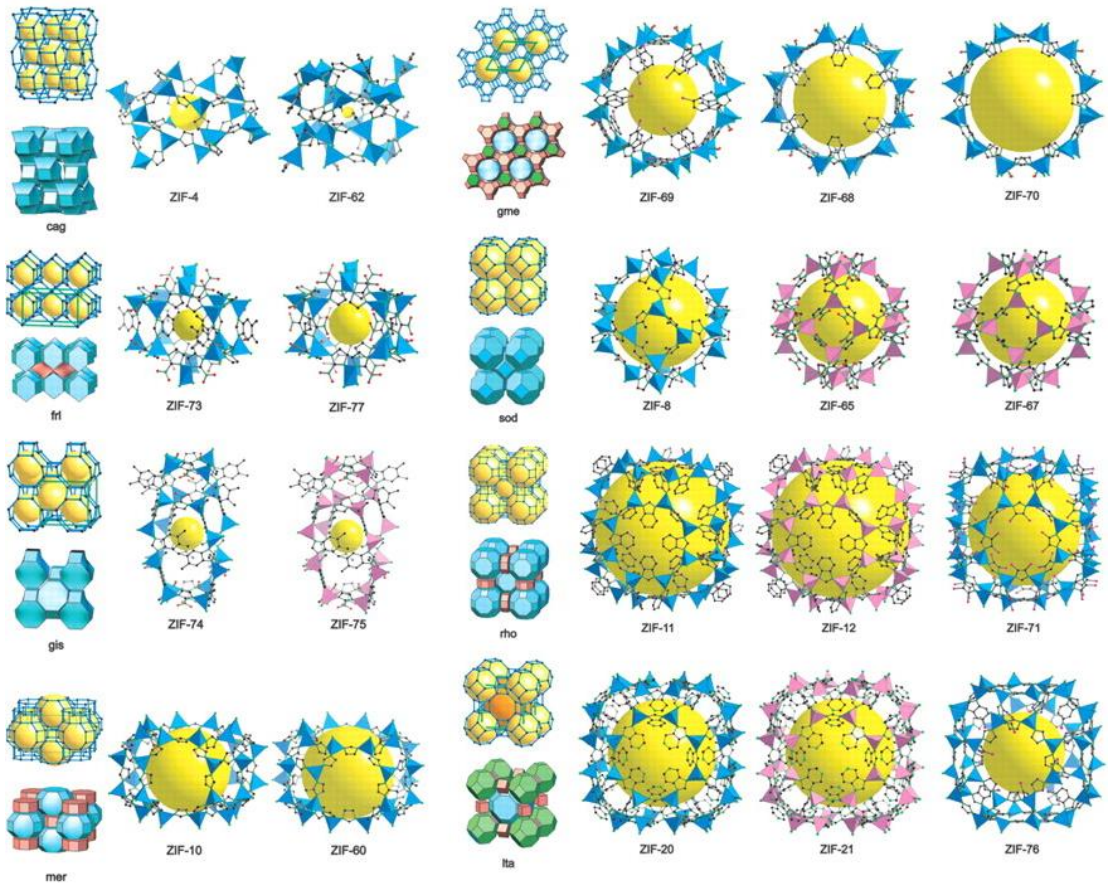

Figure 1.3. Some representatives of the ZIFs family (the yellow sphere is to indicate space in the cage.) [22]

1.1.2. Metal-Organic Frameworks as heterogeneous catalysts

In 1994, K. Ogura's group reported $[Cd(4,4'\text{-bpy})_2](NO_3)_2$ and its application as a catalyst for the cyanation reaction of aldehydes.[33] This study contributed to the early development of MOFs catalysis. Generally, MOFs are used as heterogeneous catalysts taking advantage of two different properties (Figure 1.4). Firstly, MOFs may participate in catalytic reactions through one of their hybrid framework attributes, such as coordinatively unsaturated metal sites (CUS) generated by the post-synthesis removal of coordinated solvent molecules or due to structural defects, or functional groups on their organic linkers. Second, MOFs can also serve as the support to anchor additional guest catalytic active sites, by exploiting their porosity. The following paragraphs will present three different options for using MOFs as heterogeneous catalysts.

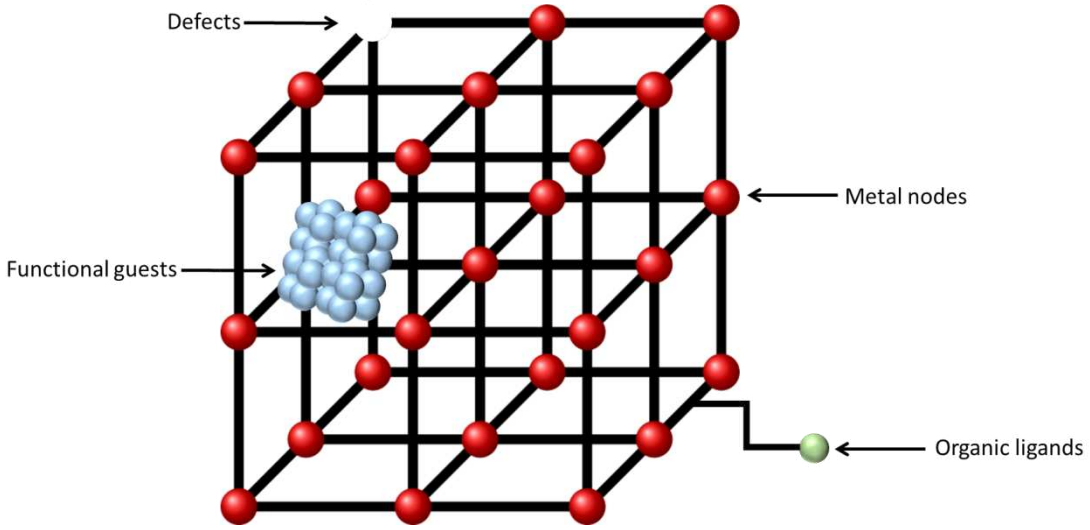

Figure 1.4. Potential catalytic active sites on MOFs

1.1.2.1. Metal nodes as catalytic sites

The metal nodes of MOFs themselves can serve as catalytic active sites, generally as Lewis acid sites, when they are partially uncoordinated.

On some MOF structures, coordinatively unsaturated metal sites (CUS) can be post-synthetically generated by removing coordinated solvent molecules that are not involved in the construction of the framework (so that they can be eliminated without fragilizing the structure). This is the case of the HKUST-1, where water molecules coordinated to the paddlewheel nodes formed between copper cations and carboxylate groups of trimesate linkers in the as-synthesized material are removed after a thermal treatment. The Lewis acid site hence formed were efficiently exploited to catalyze reactions such as the oxidation of trans-ferulic acid to vanillin.[34] The same strategy was applied by the group of Pr. G. Férey to generate Lewis acid sites at the oxo-centered chromium trimers of MIL-101, that could be then used as a catalyst for the selective sulfoxidation of aryl sulfides with H_2O_2 to corresponding sulfoxides.[35] Partially uncoordinated metal nodes are also existing within MOFs at structural defects. It is now well-accepted that MOFs do not possess perfect structures, but rather intrinsically display a variable number of defects due to missing linkers. These linker defects sites are located at both crystal

surface and within the bulk. This type of CUS was exploited with ZIF-8, for which the Zn(II) nodes were reported as catalyst for many reactions such as Friedel-Kraft acylation,[36] Knoevenagel reaction,[37] transesterification,[38] cycloaddition reaction,[39] photocatalytic degradation etc.[40]

A strategy was then developed to generate on-purpose reactive CUS within MOFs that are, without it not always reactive.[41–43] Indeed the active metal nodes are saturatetedly coordinated, the substrate could hardly access to the active sites.[44]

1.1.2.1.1. Crystal defects formation

Some MOFs crystallize as compact and without any defects crystallites, so that only metallic nodes localized at the external edge of the crystal are in contact with the substrate, resulting in inertness toward binding and activation of the substrate.[45] One idea is thus to intentionally create defects in MOFs. A typical example of defect engineering in MOFs is UiO-66 ($(Zr_6O_4(OH)_4(BDC))$, a framework with a cuboctahedral crystal structure composed of oxo-hydroxo metal nodes composed of 6 zirconium cations and ideally connected by 12 terephtalate ligands.[46] This high connectivity number (12) provides to this structure a particularly high stability and allows it to tolerate a minimum number of linker defects being detrimental to its stability. [47] As expected, these missing ligands create coordinately unsaturated zirconium sites at the metal nodes, that are exploited as Lewis acid sites for catalysis. [47] The most studied method to modulate the number of missing linkers is to replace a portion of the multifunctional linker used in the MOF synthesis (i.e. the terephthalis acid) by monofunctional linkers, so-called modulators, such as formic acid, acetic acid benzoic acid or trifluoroacetic acid. These modulators replace the multifunctional linkers within the MOF framework without affecting the integrity of the structure. Their low boiling temperature relative to their multifunctional counterparts allows their easy removal from the framework by a simple thermal treatment, leading to the generation of partially uncoordinated metal nodes. As an example, in the work of Dr. Priyanka Gairola, who worked on the same topic with this thesis, she synthesized

defective UiO-66. The UiO-66 with defects is a highly active catalyst for the Lewis acid-catalyzed alcohol dehydrogenation.[48,49]

1.1.2.1.2 Formation of bimetallic MOF

A second active metal node could be introduced to entirely or partially replace the original metal. The introduction of a second metal is often based on the following aims: to generate additional defect sites,[50] to provide redox centers,[51] photocatalytically active centres,[52] or heterogeneity of metal centers known to be active for specific reactions.[53]

In order to introduce a second metal node, we can use two general approaches: Bottom-up method, where the MOF is synthesized in the presence of the doping metal cations (also called "*in-situ*" introduction of the doping metal), and Top-down method, where the doping metal cations are introduced post-synthetically by cation exchange. In both cases, the introduced metal needs to have similarities with the original metal cation of the MOF: e.g. ionic radius and similar valence states, similar soft/hard acidity (hard (Ti, Zr, Al ...) VS soft (Zn, Cu, Co ...)). Otherwise, the doped metal cations will not be introduced into the framework and may even lead to affecting the stability of the original MOF structure.

i. Bottom-up method.

The advantages of the in-situ introduction of metal nodes are obvious, as they provide a more uniform distribution of doped-metal nodes. N. Iqbal's group reported the in-situ synthesis of Cu-doped ZIF-8 using a solvothermal method for the electrocatalytic reduction of CO_2.[53] (See Figure 1.5) Cu^{2+} centers being known to be efficient active sites to catalyze electrochemical CO_2 reduction. Cu-doped ZIF-8 catalysts exhibited good selectivity toward methane and CO formation.

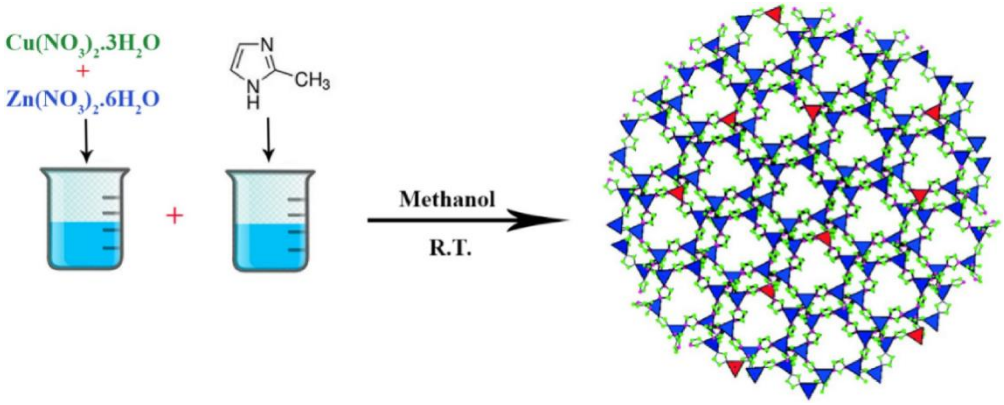

Figure 1.5. Illustration of Cu-doped ZIF-8 crystals synthesis. [53]

Z. Yang's group reported the one-step synthesis of bifunctional Co-doped UiO-66 nanoparticles as a catalyst for the photodegradation of tetracycline under natural light.[54] Co-doping modification broadens the light absorption and promotes charge separation of UiO-66, which improved the photocatalytic performance. C. Chen's group synthesized a Ni-MOF-5 materials to catalyze the ethylene dimerization into butadiene using a facile one-pot co-precipitation method at room temperature.[55] The partial replacement of Zn^{2+} by Ni^{2+} in the feedstock resulted in the coordination of Ni^{2+} with extra solvent molecules. Ni-MOF-5 catalyst showed excellent activity with butadiene productivity of 9040 g/g(catalyst)/h, at 35 °C and 50 bar.

However, the in-situ introduction of metal nodes may face some challenges, such as the disruption of the MOF constituent self-assembly.[56] For example, the introduction of some metallic precursors can change the topology of MOFs, thereby causing the lost their porosity or more crystal defects.[57,58]

ii. Top-down method by cation exchange.

The cation exchange method refers to the post-synthetic partial replacement of metal nodes of the presynthesized MOFs framework with active metal nodes. By controlling the reaction conditions of metal exchange, the proportion and even the spatial distribution of metal node replacement can be controlled.[59,60] W. Fan's group modified TiO_2-ZIF-8 by exchanging the Zn^{2+} of ZIF-8 with Ni^{2+} (See Figure 1.6).[59] The presence of Ni^{2+} ions stabilize the Zn-N bond, which improved the aqueous phase stability of modified TiO_2-ZnNi ZIF-8 in the presence of light.

The introduction of Ni^{2+} also further affected the electronic structure of Zn^{2+} and optimized the electron transport channels, which is conducive to the improvement of PEC performance.

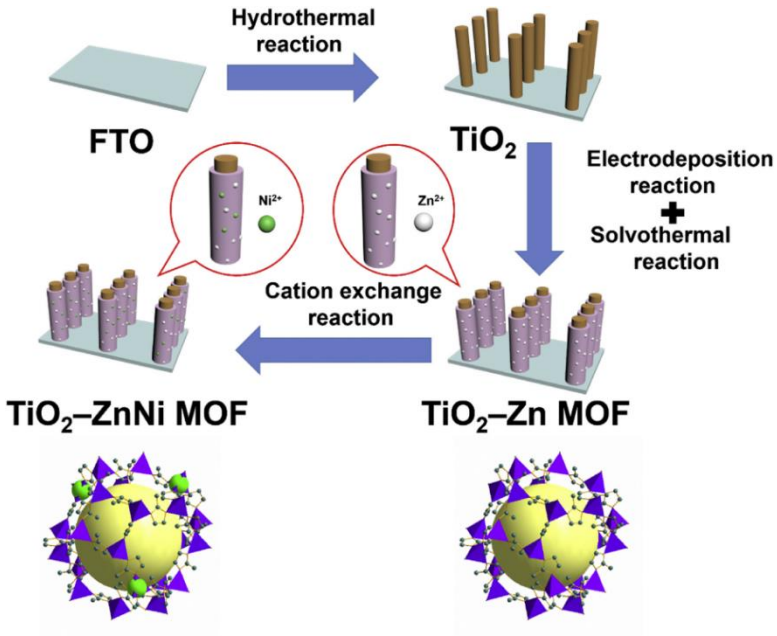

Figure 1.6. Synthesis process of TiO_2–ZnNi ZIF-8 [59]

1.1.2.2. Organic ligands engineering

In addition to the metal nodes of MOFs, organic ligands can also serve as active catalytic sites or as anchoring points for catalytic sites. A variety of organic functional groups, such as alcohols,[61] amines,[62] sulfonyl,[63] and pyridines,[64] can be used as active acidic or basic sites. Such functionalized MOFs are mainly synthesized by bottom-up (use of a functional ligand to synthesize the MOF) and top-down (ligand modification after the synthesis of MOFs).

i. Bottom-up method.

In this method, a part of the organic linkers of the targeted MOF is replaced by (often commercial) functional derivatives. This method is based on the isoreticular chemistry concept, for which identical MOF structures can be obtained whatever is the organic linker as soon as it possesses the same geometry and the same connectivity number (the same number of

coordinating functions). Hence, O. M. Yaghi's group firstly reported on IRMOF series based on the MOF-5, a MOF with a cubic structure composed of zinc tetramers connected by the linear bifunctional terephthalic acid as linker. To do so, terephthalic acid ligand was replaced by -Br, $-NH_2$, $-OC_3H_7$, and $-OC_5H_{11}$ terephthalic acid derivatives.[65] The functionalized IRMOF series have the same topology but different pore chemistry and pore size than the original MOF-5. For instance, the MOF synthesized with $-OC_3H_7$ and $-OC_5H_{11}$ derivatives are expected to possess highly hydrophobic and congested pore environment compared to MOF-5. The amine-functionalized IRMOF-3 (obtained with the amine derivative of terephthalic acid) exhibited excellent adsorption property toward CO_2. The same idea was subsequently applied to the modification of other MOFs systems.[66–68] S. Wang`s group reported a Zr-based AHPP- MOF for the adsorption of Pd (II).[69] (See Figure 1.7).

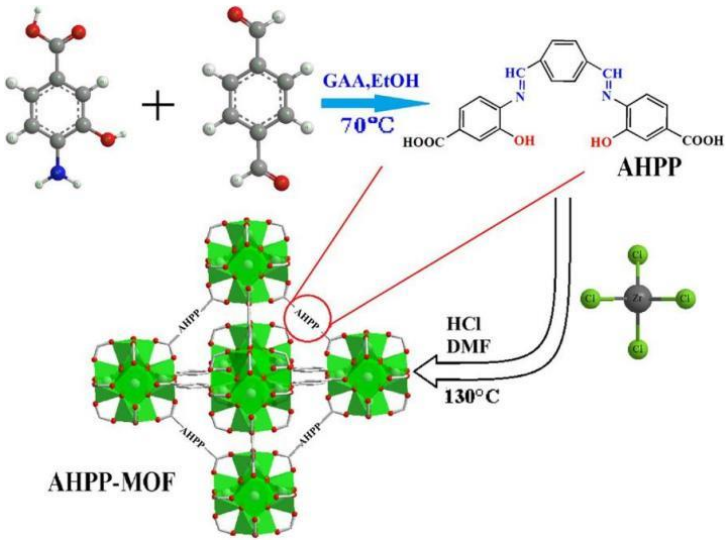

Figure 1.7. Zr based AHPP- MOF consists of prefunctionalized ligands AHPP [69]

One of the most significant limitations of prefunctionalization of MOFs is that many organic ligands with functional groups (such as alcohol (phenol) hydroxyl group, aldehyde group, carboxyl group, amino group, etc) are not compatible with the conditions required for solvothermal synthesis of MOFs.[70] Instead, these functionalized ligands tend to form complexes

with metal nodes rather than forming MOFs. Therefore, the top-down is more widely used than prefunctionalization.

ii Top-down method.

The top-down method refers to modify the linkers of the MOFs after they have been synthesized. The common top-down method is aimed at introducing acidic or basic functional groups by ligand-exchange.[71–73] C. Wang's group utilized 3-amino-1,2,4-triazole (ATR) to partially replace 2-methyl imidazole (2-MeIM) linker in the ZIF-8 framework, thereby introducing -NH_2 group[74]. This amino-functionalized MOF, called ZIF-A24 (ATR exchange rate of 48%), exhibited a significant decrease in the dehydrogenation reaction temperature of the adsorbed ammonia borane (See Figure 1.8).

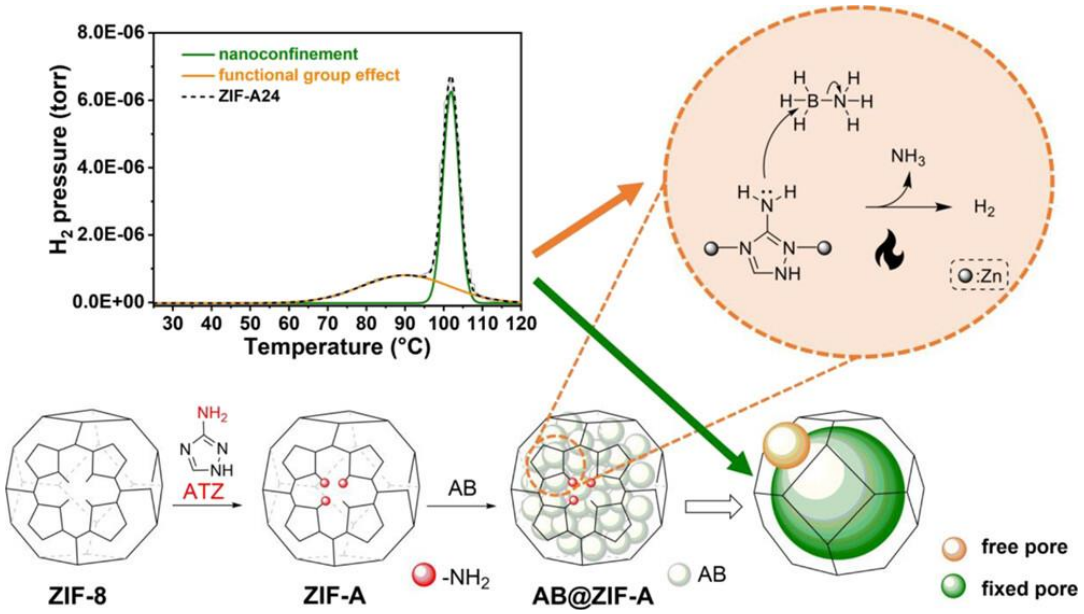

Figure 1.8. The ATZ functionalized ZIF-8 attracts AB molecules near the free pore to lower the dehydrogenation temperature.[74]

K.Baek's group performed a two steps post-synthetic modification of ZIF-8. First the ZIF-8 imidazole linker, 2-methyl imidazole (2-Mim on Figure 1.9) was partly exchanged with 3-amino-1,2,4-triazole to form ZIF-8-A61 (because it contained 61 % of amine functionalized linker) followed by the sulfonic acid functionalization by the ring-opening reaction of 1,3-

propanesultone with the incorporated amino groups in ZIF8-A61. (See Figure 1.9).[75] The resulting ZIF8-A61-SO_3H materials showed good catalytic performance toward the one pot two steps deacetylation-Knoevenagel condensation reaction with 100% conversion of benzaldehyde dimethyl acetal and 98% selectivity of the final Knoevenagel product. This enhanced catalytic activity compared to ZIF-8 (58% conversion) and ZIF-8-A61 (76 % conversion) can be attributed to the co-existence of site-isolated acid-base pairs on the ZIF8-A61-SO_3H catalyst in proximity.

.

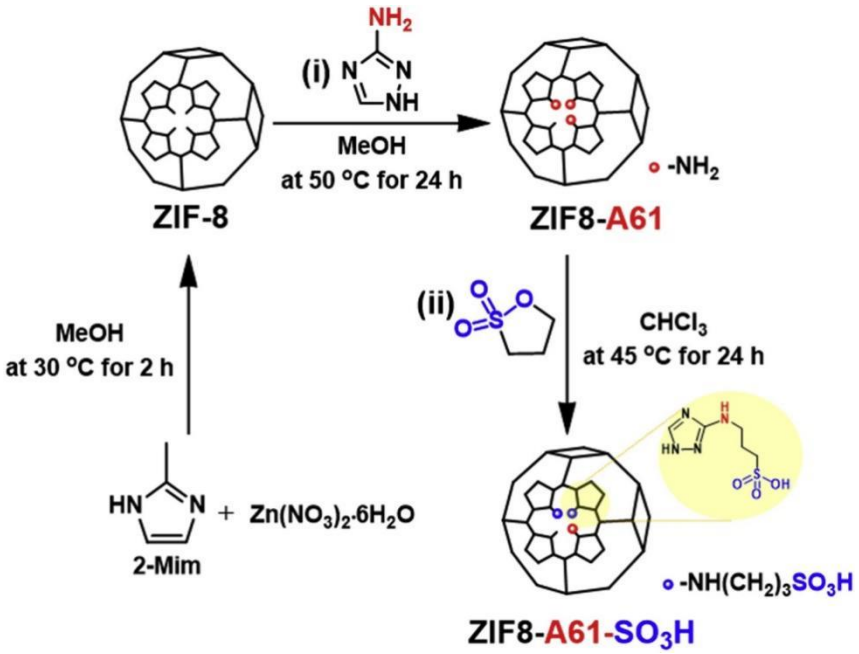

Figure 1.9. Synthesis of (i) amine-functionalized ZIF-8 with 61% 3-amino-1,2,4-triazole (Atz) conversion (ZIF8-A61) and (ii) acid/amine-bifunctionalized ZIF8-A61-SO_3H by ring-opening reaction of 1,3-propanesulfonolactone on ZIF8-A61.[75]

1.1.2.3. Metal-Organic Frameworks as host for metal nanoparticles

Thanks to their large specific surface area, tunable 3D pore channels and versatile pore chemistry, MOFs can serve as supports for various guest catalytic active sites. These sites include metal nanoparticles, metal oxides, transition metal cations, quantum dots, enzymes, etc.[76–81] The guest catalysts can be immobilized on the external surface of MOFs or encapsulated within the pore of MOFs. They benefit from the highly customizable chemical

environment of MOFs, where factors such as charge density, rigidity/flexibility variation of the frameworks, nano confinement effect of the pore size, hydrophobicity, acidity and basicity, etc can be tuned. Metal nanoparticles (NPs) are one of the representative guest catalysts, which is the focus of this section. The approaches to introduce metal NPs include post-synthesis infiltration and encapsulation. (See Figure 1.10)

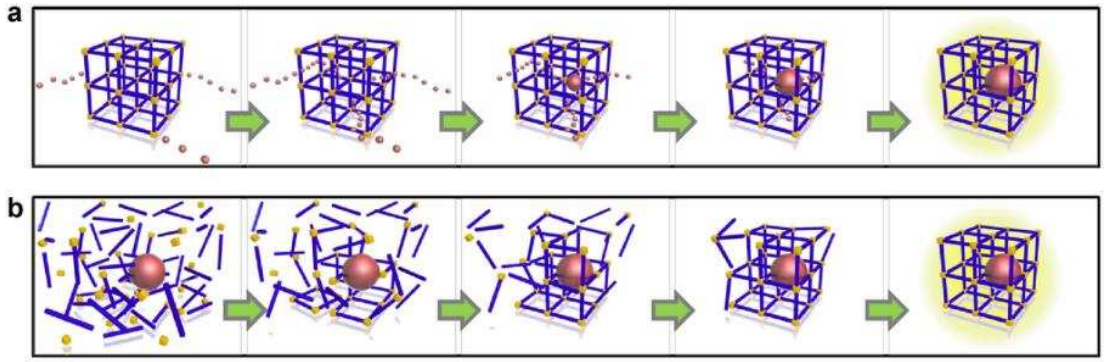

Figure 1.10. Approaches for the preparation of NPs@MOF composites: a) post-synthesis infiltration, b) encapsulation.[82]

Post-synthesis infiltration method is a common method for introducing metal NPs into MOFs, ie the introduction of NPs to a prepared MOF. This approach offers the flexibility to introduce metal precursors through various methods such as liquid-phase impregnation, double-solvent impregnation, chemical vapor deposition, or solid mechanical grinding. Subsequently, the nanoparticles can be grown in situ through reduction.[77,83–85] In this case, the nano-cage structure of MOFs inhibits (or limits) the growth or agglomeration of metal NPs, eliminating the need for stabilizers such as PVP. It is also possible to introduce NPs directly when the size of NPs is smaller than the window of MOFs.

Zhao's group reported a novel Zr-MOF ([Zr_6] cluster in {[$Ni_3Zr_6(\mu_3\text{-}O)_4(\mu_3\text{-}OH)_4(IN)_{12})(H_2O)_6$] · Cl_6 · 4DMF · $18H_2O$}$_n$) assembled from [Zr_{48} Ni_6] cubic nanocages using isonicotinic acid as a linker (See Figure 1.11).[86] After soaking the MOF in a $AuCl_4^-$ solution, the adsorbed $AuCl_4^-$ is further reduced at 200°C under H_2/Ar mixed atmosphere to form Au NPs, which exhibit excellent CO_2 electrocatalytic reduction activity. Due to the pore-

limiting effect of the MOFs, only a small amount of NPs agglomeration was observed after the reaction.

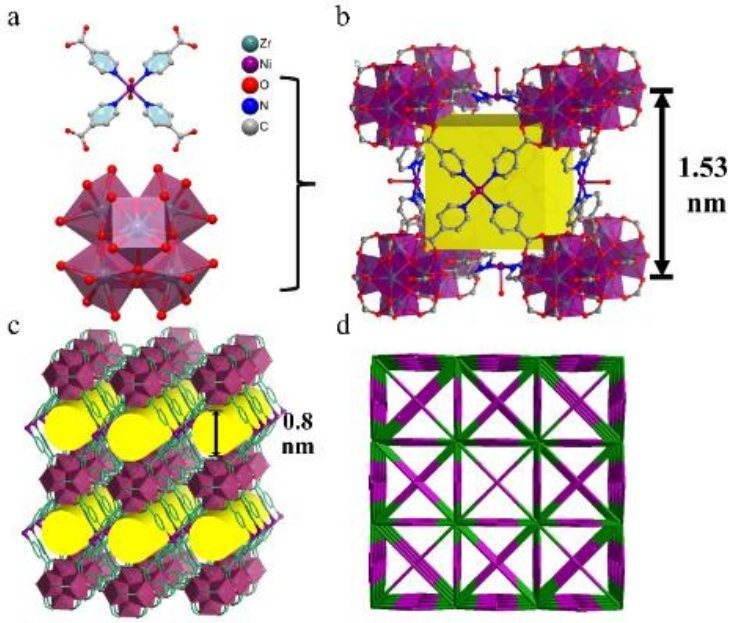

Figure 1.11. a) Tetracarboxylate linker and [Zr_6] cluster in Zr-MOF. b) Cubic cage in Zr-MOF. c) 3D framework of Zr-MOF along the {1 1 0} plane. d) (4,12) connected *ftw*-type net of Zr-MOF [86]

D. Astruc's group reported ZIF-8-derived Au and Pd Nanoparticles as catalysts for Ullmann homocoupling reaction.[87] The NPs@ZIF-8 were prepared by impregnation of ZIF-8 with Au and pd precursors followed by their reduction within ZIF-8. According to the TEM image, the synthesized metal NPs display excellent dispersion within the MOF crystals. Pd@ZIF-8 and Au@ZIF-8 exhibit excellent catalytic activity for the Ullmann homocoupling reaction of aromatic iodides. In some cases, the size of the pores alone cannot inhibit the growth or agglomeration of nanoparticles. Low dispersion and inhomogeneous sizes of the NPs can still occur during the formation of the NPs. At this point, the presence of functional groups can promote the stabilization of the precursor during their reduction into metal NPs. As a result, metal NPs can form, which are homogeneous in size even in the absence of a surfactant as a capping agent.[88] M. Jia's group developed UiO-66-NH_2 supported Au-Pd bimetallic nanoparticles for formic acid dehydrogenation using a double solvent-solvent impregnation

method. Ultrasmall and well-dispersed PdAu bimetallic nanoparticles (~1.4 nm) are uniformly distributed in the cavity of UiO-66-NH_2. (See Figure 1.12) The high turnover frequency (TOF) value of 722 h^{-1} of formic acid dehydrogenation is realized at 298K. The -NH_2 group allows the impregnated Pd^{2+} and Au^{3+} to be uniformly distributed throughout the cage of the UiO-66-NH_2 due to its strong coordination ability. After the reduction by $NaBH_4$, the stronger electron density of -NH_2 combined with the cage of UiO-66 inhibited the agglomeration of Pd/Au NPs. Therefore, -NH_2 plays a decisive role in the formation of ultra-small PdAu particles during catalyst preparation and in improving the catalytic performance of formic acid dehydrogenation.

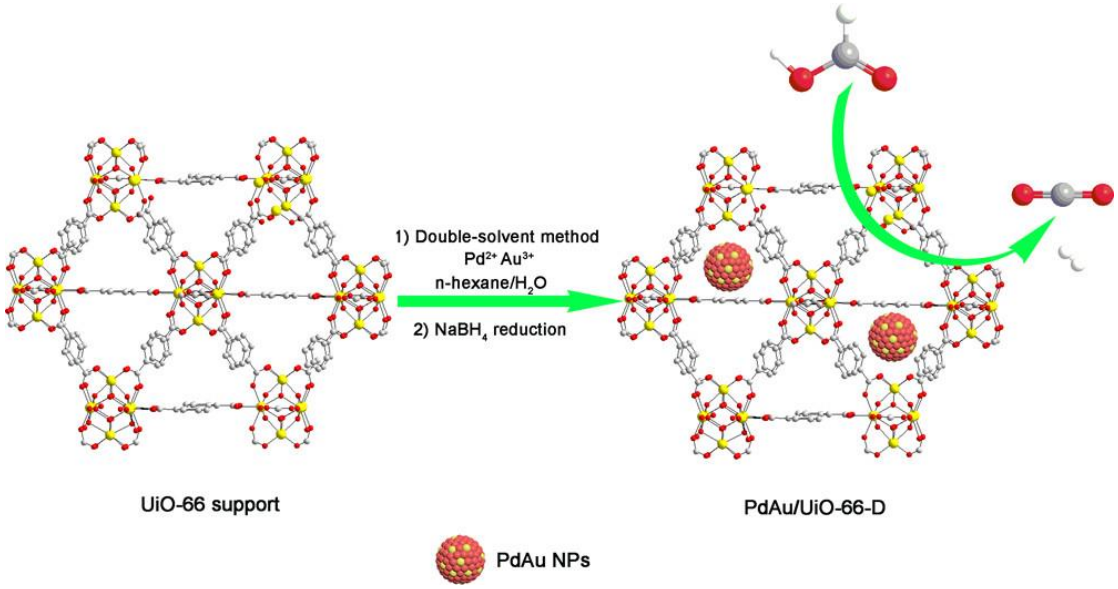

Figure 1.12. The synthesis of PdAu NPs within a UiO-66-NH_2 matrix using a double-solvent approach [88]

As an alternative, the growth of MOFs around the metal NPs, ie an encapsulation procedure, results in the excellent dispersion of metal NPs whose size can be controlled during their synthesis. Huo's group employed polyvinylpyrrolidone (PVP) to functionalize the surface of gold NPs and encapsulated them into ZIF-8 to obtain a series of well-dispersed Au@ZIF-8.[76] PVP-modified gold NPs were immersed in a methanol solution containing ZIF-8 precursors, and then ZIF-8 crystals were grown around the NPs. By controlling the order of addition of gold nanoparticles (i.e., added at the beginning (T_0) or after a specific time (T) during ZIF-8 synthesis), the authors obtained Au@ZIF-8 with different spatial distributions (See Figure 1.13).

The same authors extended this encapsulation method to other metals such as silver, platinum and achieved similar ZIF-8 encapsulated nanoparticles. Among them, Pt@ZIF-8 has excellent activity in catalyzing the gas-phase hydrogenation of CO. However, in catalyzing the liquid-phase hydrogenation of hexene, the smaller pore size of ZIF-8 limited the diffusion of reactants, resulting in a low conversion of hexene. Also, by comparing the hydrogenation reactions of several isomers of hexene, Pt@ZIF-8 showed absolute regioselectivity and hydrogenation of terminal olefins only, which is quite different from the results obtained with unsupported Pt NPs. In summary, the encapsulation method allows more precise control of NPs distribution. It is worth noting that although some substrate molecules are small enough to enter the pores of MOFs, the problem of substrate diffusion inhibition is still possible.

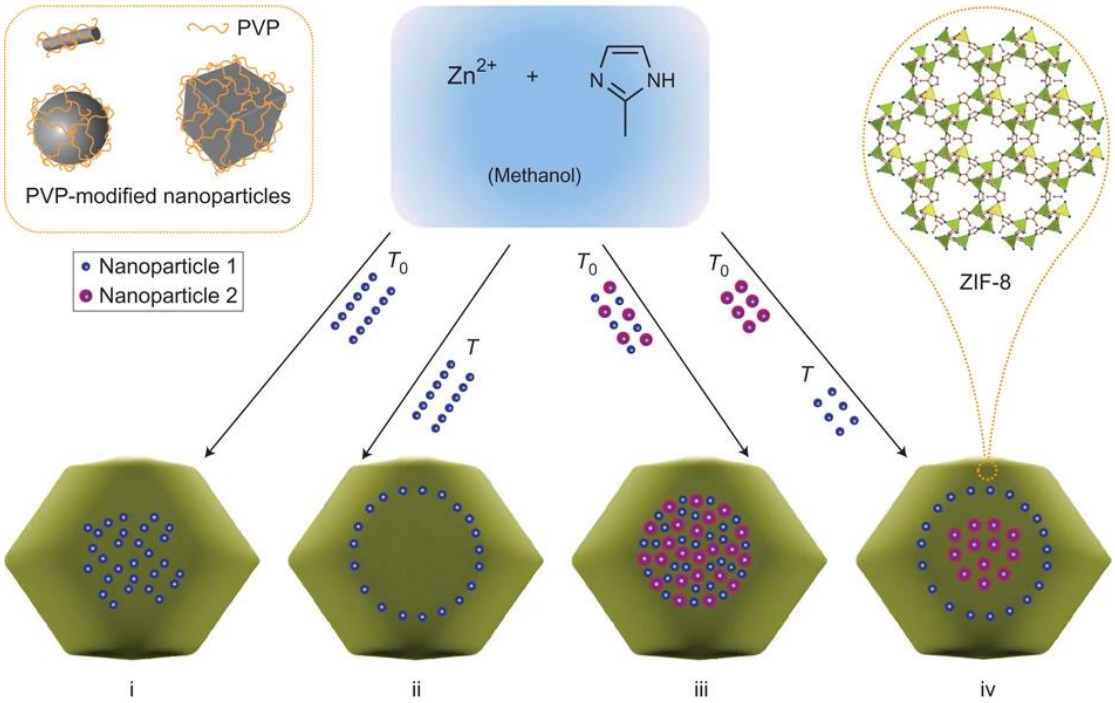

Figure 1.13. Encapsulation of PVP-modified NPs into ZIF-8 with various NPs dispersion [76]

In summary, post-synthesis infiltration and in situ encapsulation are the two main methods for synthesizing NPs in MOFs. Post-synthetic infiltration can make full use of the pore structure of MOFs to limit the growth of NPs so that avoiding the use of capping agents. The drawback of it is the difficulty of controlling the distribution of NPs. In-situ encapsulation allows more

precise control of the size of NPs and their distribution in the crystal. However, the application of capping agents causes the NPs to lose part of their accessibility, and the removal of the capping agents adds additional steps.

1.1.3. Metal-Organic Frameworks as support materials for enzyme immobilization

In addition to their high potential as heterogeneous catalysts, notably to stabilize metal nanoparticles, MOFs were also more recently shown to serve as heterogeneous platforms for loaded biomacromolecules such as proteins.[89,90] It has broad application prospects in sensing, drug delivery, gene delivery, targeted therapy, and biocatalysis fields. In particular, MOFs have been extensively studied as enzyme supports.[91,92] Immobilization of enzymes has proven particularly effective at increasing the stability of these otherwise fragile molecules. The hybrid nature, the three-dimensional pore structure as well as the structural and chemical adjustability of MOF have natural advantages in immobilizing enzymes. Therefore, this section will focus on the methods of immobilizing enzymes on MOFs and the progress of ZIF family immobilized enzymes and specially to synthesize multi-enzymatic or chemoenzymatic catalytic systems.

1.1.3.1. Enzymes as catalysts

Enzyme is a general term for biocatalysts, mostly proteins and to a lesser extent RNA, that catalyze various chemical reactions in living cells. Most of the metabolic reactions in living organisms are catalyzed by enzymes. Just like other catalysts, enzymes can greatly accelerate the reaction rate. The advantage of enzymes is their specificity, selectivity and efficiency, as compared to artificial chemical catalysts. The specificity of an enzyme is demonstrated by the fact that an enzyme can use a very limited number of substrates. The selectivity includes not only chemoselectivity, but also regioselectivity and stereoselectivity. Enzymatic reactions are considered environment-friendly or "green process" due to their mild operation conditions, such as near-ambient temperature, atmospheric pressure, aqueous solvent.[93,94]

Enzymes activity is determined by their tertiary structure. whose stability mostly relies on weak interactions (hydrogen bonds, electrostatic interactions, van des Waals interactions), so that there are relatively unstable. Therefore, enzymatic reactions require specific reaction conditions in terms of temperature and pH ranges, which vary depending on the type of enzyme. The choice of solvent for enzymatic reactions is often restricted to water,[95] although some enzymes can tolerate a certain proportion of organic solvents.[96] As a result, wild type enzymes often do not meet the needs of practical application. An important driving force for the development of biocatalysis application for chemical synthesis since the last two decades has been the discovery of new enzyme variants thanks to the combination of computer modelling supported enzyme engineering and rational design or directed evolution, high-throughput screening tools, resulting in enzymes with enhanced stability and activity.[97] Currently, the majority of enzymes used in industrial applications are produced through bioengineering processes, which can incur higher production costs. In general, the inherent fragility, high cost, and inability to be recycled together limit the prospects of enzyme applications.

One strategy to address these challenges is the immobilization of enzymes, a technique in which the enzyme is heterogenized on solid support materials by a physical or chemical process.[98] Compared to free enzymes, immobilized enzymes offer advantages such as separability, recyclability, enhanced activity, solvent tolerance, and thermal stability. These attributes are significant for reducing the overall cost of enzyme applications. At present, immobilization of enzyme is the mainstream solution for its industrial application.

The choice of support materials is a critical factor in enzyme immobilization. Similar to heterogeneous catalysts, support materials for the immobilization of enzymes need to have a large specific surface area, water-solvent stability. Many inorganic, organic and inorganic-organic hybrid materials have been used for enzyme immobilization, such as SiO_2 [99], metal oxides[100], activated carbon[101], hydroxyapatite [102], porous glass[103], chitosan[104], cellulose[105], ion exchange resins[106], SiO_2-chitosan[107], etc (See Figure 1.14). Metal-Organic Frameworks (MOFs), as emerging organic-inorganic hybrid materials, offer a combination of favorable properties including the rich functional groups, large surface area, and the tunability of shape

and size. These characteristics make MOFs quite suitable for enzyme immobilization.[108] Therefore, here we will further introduce the enzyme immobilization technology using MOFs as support materials.

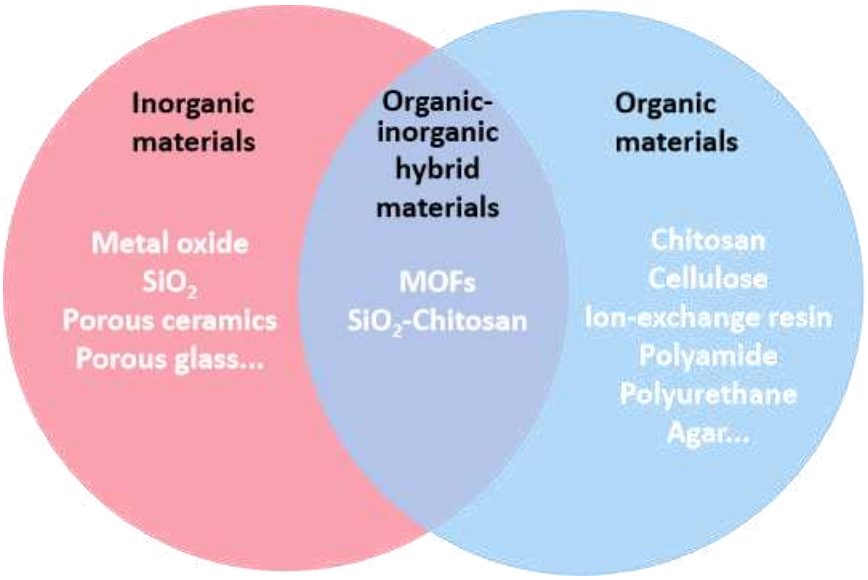

Figure 1.14. Classification of commonly used enzyme immobilization support materials

1.1.3.2. Metal-Organic Frameworks as enzyme immobilization support

The first biocomposite of enzyme-MOFs was reported in 2006. Microperoxidase-11 was immobilized on MOFs and mesoporous organosilicon hybrid materials.[109] Since then, MOFs have been widely investigated as support materials for enzyme immobilization. Due to the properties of their organic-inorganic hybrid materials, MOFs are compatible with many conventional strategies for enzyme immobilization. According to the type of targeted interaction between enzymes and MOFs, enzyme immobilization methods can be classified into physical and chemical methods. Physical methods, such as encapsulation and adsorption, involve relatively weak interactions between MOFs and enzymes, such as Van der Waals, hydrogen or hydrophobic interactions. On the other hand, chemical methods achieve enzyme immobilization by forming stable covalent bonds between MOFs and enzymes. (See Figure 1.15).

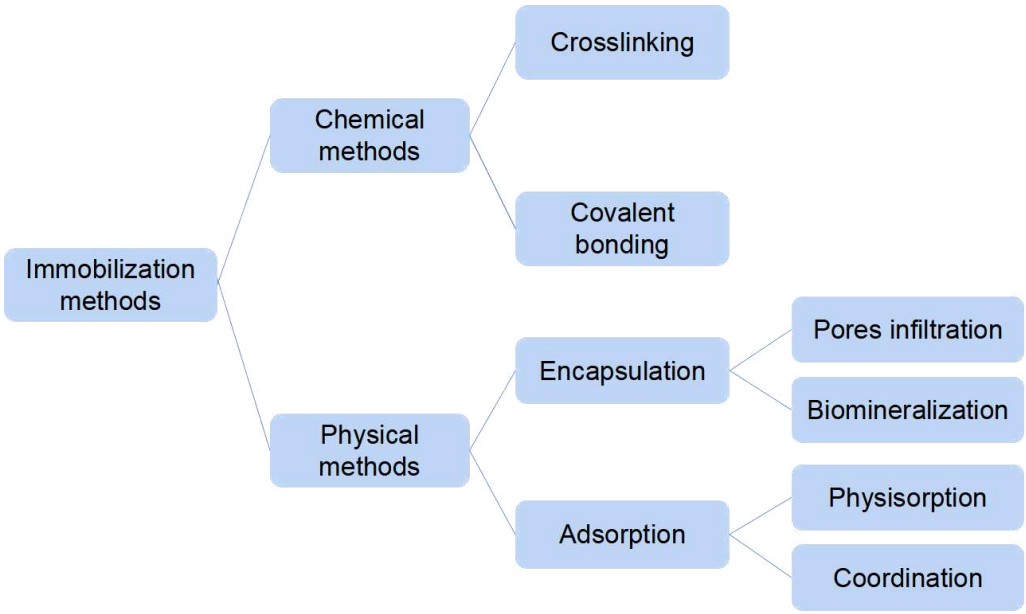

Figure 1.15. MOFs as support materials for enzyme immobilization

i. Non-covalent immobilization methods

Adsorption is the simplest and most straightforward method for enzyme immobilization. Enzymes bind to the surface of MOFs through various interactions, including hydrogen bonds, van der Waals forces, electrostatic interactions, hydrophobic interactions or coordination. The physical adsorption of enzymes to MOFs is a dynamic equilibrium process and its stability is highly dependent on the surrounding environmental factors. As an example, electrostatic interactions are likely to occur between the enzyme's electrostatic charges, positive or negative depending on the protonation state of its amino-acid residues such as glutamic, aspartic or lysine, and the charged groups on MOFs such as $-NH_3^+$, $-COO^-$ existing on the organic linkers pending on the crystal surface. It is generally believed that the enzyme loading is maximized when the immobilization takes place at a pH between the isoelectric points of MOF and that of the enzyme.[110,111] A similar situation applies to hydrophobic interactions.[112] Additionally, surface modifications can be applied to the targeted MOF to adjust its surface charge,[113] hydrophilicity,[114] and other parameters.[115]

Apart from the charged functional groups of the organic ligands of MOFs, coordinately unsaturated metal sites (CUS) inherently existing at the surface of the MOF crystals can also

interact with amino acid residues on the enzyme surface through coordination bonds. A common example is the interaction between histidine residues on some tagged recombinant proteins, known as oligohistidine affinity tags (his-tag) and some metal nodes of MOFs such as Zn(II), Ni(II), Cu(II), and Co(II) (see Figure 1.16).[116] Such his-tag are usually included at the end of the recombinant protein sequence genetic engineering tools in order to facilitate the protein purification process using affinity chromatography tools. As an example, Y. Chen's group synthesized polyphosphate kinase (PPK2)-MIL-101(Fe)-NH_2@Fe_3O_4-COOH biocomposites through a self-assembly process, utilizing the interaction between the imidazole group of histidine and the coordinatively unsaturated iron sites on the MOFs' surface.[117] The authors successfully expressed recombinant ArPPK2 with his-tag in *E. coli Rosetta* (DE3). ArPPK2 was subsequently immobilized on three Fe-base MIL-101 derivatives (MIL-101, MIL-101-NH_2 and MIL-101-NH_2@Fe_3O_4-COOH) by self-assembly. After 30 minutes of immobilization under the optimal conditions, the loading of ArPPK2 on MIL-101-NH_2@Fe_3O_4-COOH was approximately 0.122 g/g of support materials. The ArPPK2-MIL-101(Fe)-NH_2@Fe_3O_4-COOH composite exhibited the highest catalytic efficiency of Adenosine-5-triphosphate (ATP) regeneration compared to the immobilized ArPPK2 on the other two MIL-101 supports, retaining 70.1% of its activity after 13 cycles. Fe_3O_4-COOH particles were used to promote the recycling of the solid thanks to their magnetic properties.

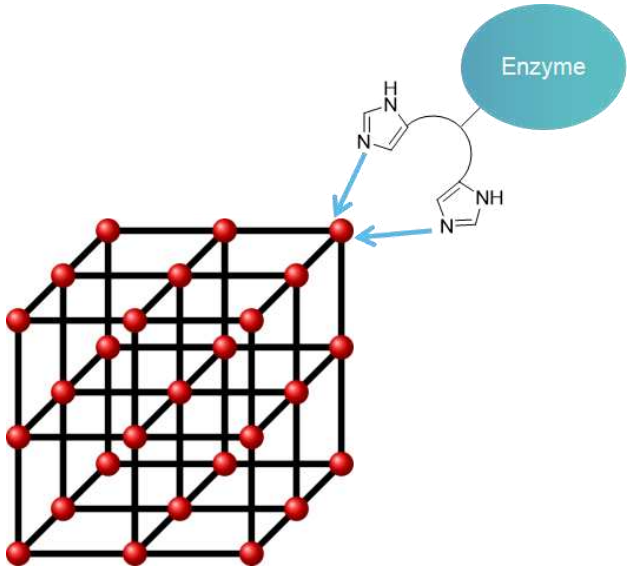

Figure 1.16. Illustration of coordinative self-assembly of His-tagged enzyme with MOF crystal

ii. Covalent grafting of proteins on MOF

The dynamic equilibrium of physical adsorption poses challenges in preventing enzyme leaching under practical conditions. Therefore, covalent grafting or crosslinking of the protein on the materials provides a more solid bonding between enzymes and MOFs. More, the formation of multiple covalent bonds between MOF and enzyme surfaces is likely to reduce their structural flexibility, thereby preventing enzyme leaching, unfolding, collapse, or denaturation.[118] Common covalent bonding sites in enzyme molecules include amino, carboxyl, imidazole, indole thiol and phenol groups. For instance, amide bonds are formed between the amino or carboxyl groups on the enzyme's residues and the organic linkers present on the surface of the MOFs. The activation of carboxylic groups involved in this reaction is often required to successfully perform the reaction in water.

The first reported immobilization of enzymes on MOFs using covalent bonds was in 2011. S. Park's group immobilized *Candida antartica* lipase B (CAL-B) on 3D-MOF with the help of 1-ethyl-3-(3-dimethylaminopropyl) carbodiimide (EDC) or dicyclohexyl carbodiimide (DCC) to activate the carbon of the carboxylate groups of the organic linker (1,4-phenylenediacetic acid) of the MOFs in order to make the carbonyl group more nucleophilic.[119] The activated carboxylate group can be readily conjugated to the pendant amino groups of CAL-B. There are other common crosslinkers such as glutaraldehyde (GA), N-hydroxysuccinimide (NHS), and dibenzylcyclooctyne (DBCO).

However, the covalent bonding method has certain limitations. For instance, while multi-point covalent bonding is effective in creating strong anchor points for the enzyme, it also carries the potential risk of altering the protein structure. Strong multi-point anchoring may twist the tertiary structure of the protein and cause loss of enzyme activity, in particular if some of the covalent bonding sites are located in the active center of the enzyme.[120]

iii. Encapsulation of enzyme inside MOFs

The above methods immobilize the enzymes on the surface of MOFs, which insures a high accessibility of the enzymes. However, washing and immobilization procedures pose challenges in preventing enzyme loss or denaturation, leading to decreased activity.[121] Taking advantages of the 3D porous structure and large specific surface area of MOFs, encapsulation of enzymes within MOFs can significantly enhance enzyme resilience against harsh conditions (such as temperature, solvent, pH), while ensuring efficient substrate accessibility to the enzymes.

The smaller enzymes can be effectively encapsulated within the nano- or meso- porous structure of MOFs through infiltration. The 3-dimensional porous can be likened to “cages”, providing protection for the enzymes and preventing enzyme unfolding and their aggregation. C. Sicard’s group encapsulated microperoxidase-8 (MP8) (3.3 x 1.1 x 1.7 nm) into mesoporous MIL-101(Cr) (cage size 2.9 nm and 3.4 nm) by post-synthesis infiltration.[122] MIL-101 was simply mixed with MP8 solution at a pH (pH = 5) for which the surface of MIL-101(Cr) is positively charged and MP8 bears a negative charge. After 48 hours of permeation, the loosely adsorbed enzymes on the surface were washed away with water. The encapsulation extent of the enzyme can reach 5 wt. % on MP8@MIL-101. More, the enzyme remained active and resistant to acidic conditions. Furthermore, the immobilized enzyme exhibited recyclability and improved long-term stability. Omar K. Farha’s group reported a series of Zr-based hierarchical mesoporous NU-100x (x = 3, 4, 5, 6, 7) with pore sizes from 3.3 to 6.7 nm for encapsulation of enzymes and their co-enzymes.[123] NU-100x has an isoreticular structure (See Figure 1.17) and shows a good water stability. The hierarchical porous structure enables the encapsulation of lactate dehydrogenase in larger pores and coenzymes NAD^+ and NADH in smaller pores. Co-enzymes and substrates can diffuse through small channels and bridging windows to the enzyme to complete the reaction.

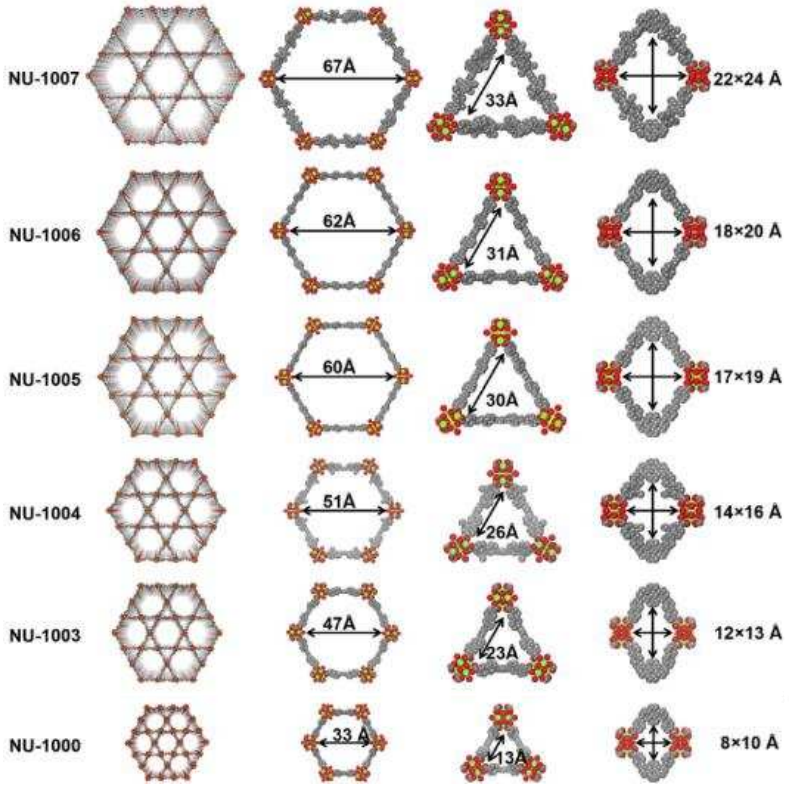

Figure 1.17. Packing Diagram, Hexagonal Pores, Triangular Pores, and Windows between Hexagonal and Triangular Pores in NU-100x [123]

Infiltration encapsulation of enzymes by MOFs has been shown to provide a high level of protection for enzymes. However, one of the major limitations of the infiltration encapsulation is that the size of the enzyme must be smaller than the window of the MOFs to allow its diffusion into the pores of the MOFs, with the exception of a few reported cases where enzymes larger than the MOF windows were observed to enter the pores through possible conformational changes.[124] The vast majority of applied permeation assays are combinations of small size enzymes such as horseradish peroxidase (HRP),[125] catalase(CAT),[126] etc. and and mesoporous MOFs, such as Tb- mesoMOF, MIL-101, NU-100x, PCN-888, PCN-160, etc. To overcome the size limitation imposed by the enzyme and MOF windows, an in-situ encapsulation method was developed.

The in-situ encapsulation method refers to the addition of enzyme solutions prior to or during the self-assembly of MOFs to enable the growth of MOFs around the enzyme, a process also called “biomimetic encapsulation or biomineralization”.(See Figure 1.18)[127] In comparison to

infiltration encapsulation, in-situ encapsulation involves fewer steps and simpler strategies. Due to the embedding of in-situ encapsulated enzymes within the frameworks or pores of MOFs, the size of the enzyme is no longer restricted by the size of the MOF windows.

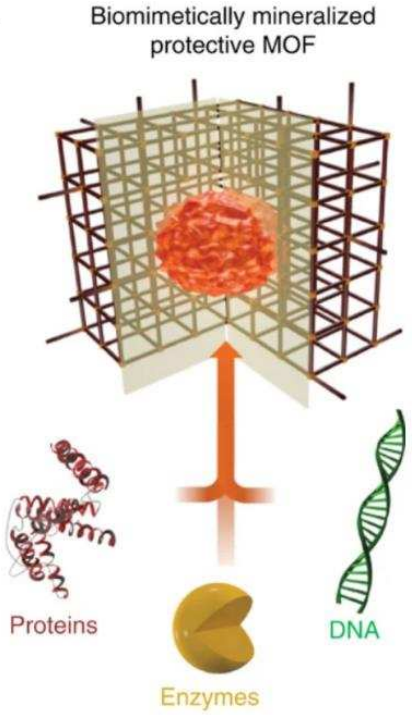

Figure 1.18 MOF biocomposite with encapsulated biomacromolecules (protein, enzyme or DNA)[128]

The application of in-situ encapsulation is currently limited to a specific subset of MOFs, such as the ZIF family, which can be synthesized in neat water at ambient temperature, synthesis conditions that preserve the integrity of the encapsulated enzymes.

In addition to the direct encapsulation of the enzyme, some additives such as polyvinylpyrrolidone (PVP) have been adsorbed on the enzyme prior to its encapsulation, enhancing its stability. It is also worth mentioning the work of Y. Wang's group who performed in-situ encapsulation of β-glucosidase (β-G) into Cu (PABA), which consists of Cu(II) p-aminobenzoic acid (PABA), in the presence of PVP, resulting in immobilized β-G with 200% activity compared to free β-G.[129] Immobilized β-G also exhibit excellent long-term stability, maintaining 90% activity even after 10 cycles.

1.1.3.3. Advances in ZIF material as enzymes supports

ZIF-8 is a particularly appealing MOF as support to stabilize biomolecules. This MOF was found to grow around some biomolecules such as amino acid, nucleic acid[128,130] before the first experiments showing its ability to encapsulate also enzymes. Compared to other MOFs, ZIF-8 can be synthesized in a milder and greener way, even at room temperature and in water, which gives it a greater potential for biological applications.[23–25] Since the working solvent of enzymes is usually water, the aqueous phase stability of ZIF-8 is also very attractive. ZIF-8 is hence at the origin of the approach for the biocomposites synthesis described in the previous section (Figure 1.18) based on the in-situ encapsulation of biomolecules in MOF.

As an example, C. Tsung's group embedded catalase (CAT) into ZIF-90 and ZIF-8 in a work published in 2014.[131] The immobilized enzymes were exposed to denaturants (urea) and high temperature (80 °C) but retained their biological activity, whereas the free enzymes were completely inactivated. However, different results have also been reported. Doonan's group in-situ encapsulated fluorescein isothiocyanate (FITC)-labeled catalase (FCAT) in ZIF-8, ZIF-90, and MAF-7.[132] Unlike in the hydrophilic ZIF-90 and MAF-7, FCAT encapsulated in hydrophobic ZIF-8 showed no catalytic activity, which is in contradiction to the results of the Tsung group mentioned above. The authors of this article concluded that the strong hydrophobicity of ZIF-8 not only induced conformational changes in the enzyme but also hindered the diffusion of the substrate.[132] Therefore, there is still controversy about the factors that influence the activity of CAT encapsulated in ZIF-8. It reveals that encapsulation of enzymes in MOFs is a complex process with multiple influences.

In addition to hydrophobicity, the smaller pores of ZIF-8 can lead to substrate diffusion limitations. J. Ge's group reported the in-situ encapsulation of glucose oxidase (GOx) in an amorphous version of ZIF-8 (aZIF).[30] The aZIF was prepared with the same precursors to ZIF-8 but with reduced amount of 2-MeIM in water. GOx@aZIF exhibited almost the same relative activity as free GOx, which is 20 times of GOx@ZIF-8. The authors believe that GOx encapsulated in aZIF are partially exposed, resulting in better substrate accessibility than ZIF-

8 encapsulated in a perfect ZIF-8 crystal. It can therefore be concluded that the main reason for the unactivity of the immobilized GOx is the substrat diffusion limitation rather than a denaturation of the enzyme due to unfavorable interactions with the hydrophobic ZIF-8. Similar results were obtained for the encapsulation of Candida Antartica lipase B (CALB) and catalase (CAT) within ZIF-8 and aZIF by the same authors thus illustrating this substrate diffusion limitation when the enzyme is embedded in ZIF-8.

In addition to their encapsulation, enzymes were also immobilized on the external surface of ZIF-8 crystals. To this end, some methods were elaborated to moderate the surface hydrophobicity of ZIF-8. Ma's group modified the surface of ZIF-8 by soaking the solid in a Ni^{2+} solution to modulate surface charge and hydrophobicity of ZIF-8 without affecting the crystal structure.[113] Ni^{2+}-modified ZIF-8 has lower surface positive charge and weaker hydrophobicity. Whereas pepsine (PEP) immobilization on unmodified ZIF-8 (ZIF-8@PEP) significantly altered the protein conformation, leading to the loss of its activity, Ni^{2+}-modified ZIF-8 @PEP-Ni exhibited excellent OER reactivity, the model reaction used to test the protein reactivity. The reason for this change may be that Ni^{2+} improves the surface hydrophobicity of ZIF-8 and changed the charge properties of the ZIF-8 surface, which reduces the risk of enzyme inactivation due to hydrophobic interactions.

Thanks to the ligand adjustability of ZIF-8, ligand exchange (See Section 1.1.2.2 (ii)) has also been used to improve the enzyme immobilization on ZIF-8 crystal external surface and adapt this MOF to the working conditions of enzymatic reactions. W. Du’s group performed Ligand exchange of ZIF-8 with phthalic acid and used it for immobilization of lipase.[133] Immobilized enzymes are used in methanolysis of soybean oil. Compared with unmodified ZIF-8, phthalate ligand-exchanged ZIF-8 has better stability under reaction conditions. In addition, lipase immobilized on phthalic acid-modified ZIF-8 also showed stronger specific activity. In five catalytic reactions and the remaining specific activity was about 20% higher than that immobilized in unmodified ZIF-8.

In summary, MOFs have been widely demonstrated as suitable support materials for enzyme immobilization. The enzymes can be immobilized on the surface or encapsulated in the solid

by a variety of physical and chemical interactions whose panel is expected to be enlarged in the next future. As water-phase stable MOFs, the ZIF family has simple and mild synthesis conditions (water-phase compatible) and is a highly potential enzyme immobilization support also an ideal platform for chemoenzymatic cascade catalytic system. However, the use of ZIF-8 for enzyme immobilization still needs to overcome many limitations, such as substrate diffusion, hydrophobicity and so on. immobilization of enzymes on the surface of ZIF was still scarcely studied and ligand exchange to favor the formation of a strong enzyme/ZIF interface was still not too much reported.

1.2. Stereoselective two-step synthesis of amines from alcohols

In this PhD thesis, our target reaction is the synthesis of amines from alcohols via a two-step cascade reaction of oxidation and amination. (As shown in Scheme 1.1). The idea is to heterogenize both chemical oxidation catalysts and ω-transaminases using MOFs as heterogeneous supports. They will be used to catalyze the oxidation of alcohols and the amination of aldehydes and ketones, respectively. Consequently, the following section will present the background of the two sub-reactions in the cascade reaction, namely the oxidation of alcohols and the transamination of aldehydes and ketones.

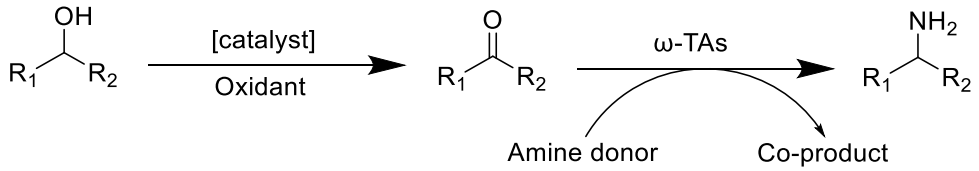

Scheme 1.1. One-pot amine production of alcohols

Since the oxidation of alcohols is a broad subject, in the next section we will focus on advances in catalytic oxidation that can be compatible with the working conditions of ω-transaminases. The coupling of these two different catalytic systems can indeed be regarded as the main challenge of this project, as illustrated in Figure 1.19.

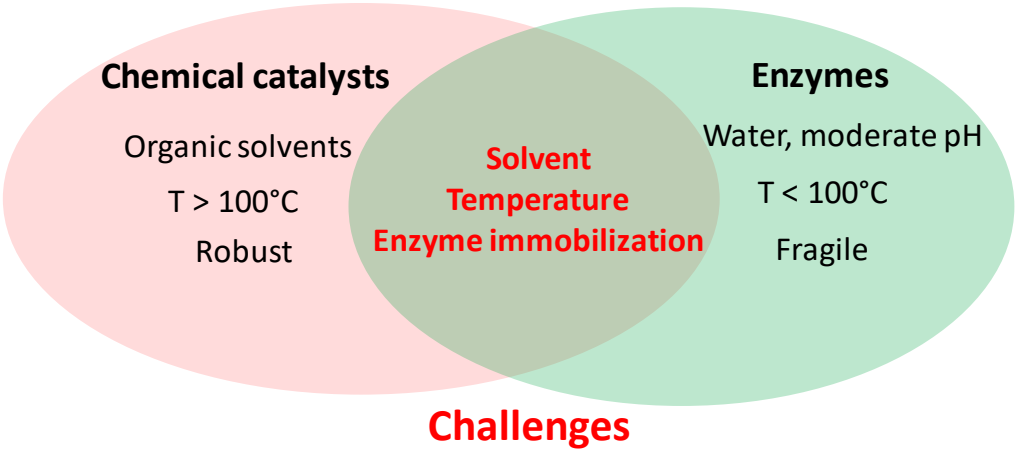

Figure 1.19. Challenges to the chemoenzymatic cascade oxidation and amination of alcohols

1.2.1. Alcohol oxidation reactions: a brief state of art

As an important part of the conversion of oxygen-containing functional groups from biomass resources, alcohols can be selectively oxidized to platform chemicals such as aldehydes, ketones or carboxylic acids, which are highly valuable in the fields of fine synthesis, pharmaceuticals, food, coatings, energy, etc. Conventional alcohol oxidation processes use stoichiometric high valence metal oxidizers such as permanganates, dichromates, etc. This process generates large amounts of toxic heavy metal contaminants and generates high equipment maintenance costs, which is contrary to the concept of green chemistry. In addition, the application of strong oxidants leads to uncontrollable reaction products. Therefore, the development of a green and sustainable selective alcohol oxidation process has always been a direction of effort for the scientific community.

Oxygen, air, and hydrogen peroxide are named green oxidants because of their low cost and sustainability, and the oxidation co-products are only water. Therefore, it becomes critical to make these ideal oxidants more efficient in the oxidation of alcohols under mild conditions by designing reasonable catalysts. Up to now, the selective oxidation of alcohols has been well studied.[134–136] Many homogeneous and heterogeneous catalytic systems have been available for the thermocatalytic oxidation, photocatalytic oxidation and electrocatalytic oxidation of

alcohols. Here, since the topic of the PhD project lies in the creation of a chemoenzymatic cascade catalytic one-pot oxidation and amination of alcohols, we will focus on the two oxidation catalytic systems whose working conditions are the closest to those of transaminases: under mild temperature and pH conditions, with O_2 as oxidant and in water or water/organic mixtures.

1.2.1.1. Copper/TEMPO system as a catalyst for the aerobic oxidation of alcohol

Copper, a non-precious metal with abundant reserves, is a widely used element for catalysis. The combination of homogeneous Cu(I/II) complexes with free radical, especially 2,2,6,6-tetramethylpiperidine 1-oxyl (TEMPO), is well established as classic catalytic system of alcohol aerobic oxidation under mild temperature conditions. The first reports on copper/radical-catalyzed alcohol oxidation was published by W. Beckman in the 1960s.[137] More recently, the catalytic triad of Cu(I) bipyridines(bpy) with TEMPO, DMAP (4-dimethylaminopyridine) or NMI (N-methylimdazole) attracted much attention,[138,139] so that the catalytic mechanism of this system is fairly well understood.[140,141] (As shown in Scheme 1.2) The oxidation state of copper interacting with the nitrogen-containing ligand varies between (I) and (II), with the radical acting as an electron-carrying agent between the oxidant and copper. Nitrogen-containing organic compounds such as DMAP and NMI not only act as organic bases, but their coordination to bpy Cu(I) centers is thought to promote the oxidation of Cu(I) to Cu(II) and also activate oxygen molecules.[142,143] A significant feature of this catalytic system is its high aldehyde selectivity for primary alcohols.

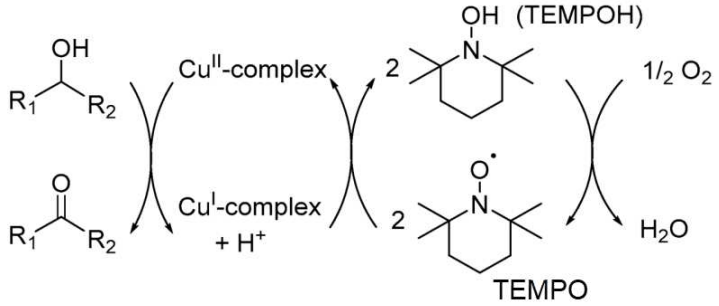

Scheme 1.2. Mechanism of aerobic oxidation of alcohols over Cu/TEMPO system[144]

The catalytic system described above is mainly used as a homogeneous catalysis system. Recently there have also been several attempts to heterogenize the system using MOF containing copper at their metal nodes, such as HKUST-1.[145]

H. Garcia's group used HKUST-1 as a catalyst for the oxidation of benzyl alcohol to benzaldehyde using molecular oxygen as the oxidant in the presence of TEMPO in acetonitrile.[145] The yield of benzaldehyde is good (yield up to 91%) and the catalyst can be reused. However, catalyst deactivation occurred during the cycling process, and since the specific surface area of HKUST-1 decreased from 1019 to 14.1 m^2/g before and after the reaction, the authors attributed the deactivation to the blocking of the micropores of HKUST-1 due to the amorphization of the structure during the test. The small pore size of HKUST-1 likewise limits the diffusion of large size substrates. In addition to HKUST-1, other copper-based MOFs, such as Cu-MOF-74, Cu-MOF-1 and Cu-MOF-2, etc, have also been used for the catalytic oxidation of benzyl alcohol.[146–148] The number of Cu-based MOFs is rather limited, but Cu(I/II) or TEMPO can be introduced in non-Cu-based MOFs as guest catalytic sites by post-synthetic modifications or in situ synthesis.[53] Besides copper, other transition metals can also be involved in TEMPO-assisted alcohol-catalyzed oxidation, such as Zr[149], Fe[150], Co[151], etc.

1.2.1.2. Noble metal nanoparticles as a catalyst for the aerobic oxidation of alcohol

Nanoparticles of some noble metals such as gold, palladium and platinum have been shown to catalyze the oxidation of alcohols efficiently even in water.[152–156] The noble metal NPs, whether free or supported, have excellent activity towards primary alcohols, especially aromatic primary alcohols. It is generally believed that noble metal-catalyzed liquid-phase oxidation of primary alcohols follows the adsorption-dehydrogenation pathway.(As shown in Scheme 1.3)[157,158] Taking Pd as an example, deprotonated alcohols are firstly adsorbed on the surface of Pd NPs to form alkoxides.[159] Then the β-H on the alkoxide is transferred to the surface of Pd NPs to form Pd-H species and aldehydes. Finally, Pd-H is reactivated by oxygen. Pd(0) is considered to be the active site in this pathway, and basic conditions is required to dissociate alcohols. In

addition, some mechanisms supporting that oxidation states of Pd such as Pd(II) are also involved have also been proposed.[160,161] Therefore, the aerobic oxidation of alcohols over Pd NPs is a complex process whose mechanism is not elucidated yet. An alternative mechanism is proposed via the Pd(II)/Pd(0) redox reaction.[161]

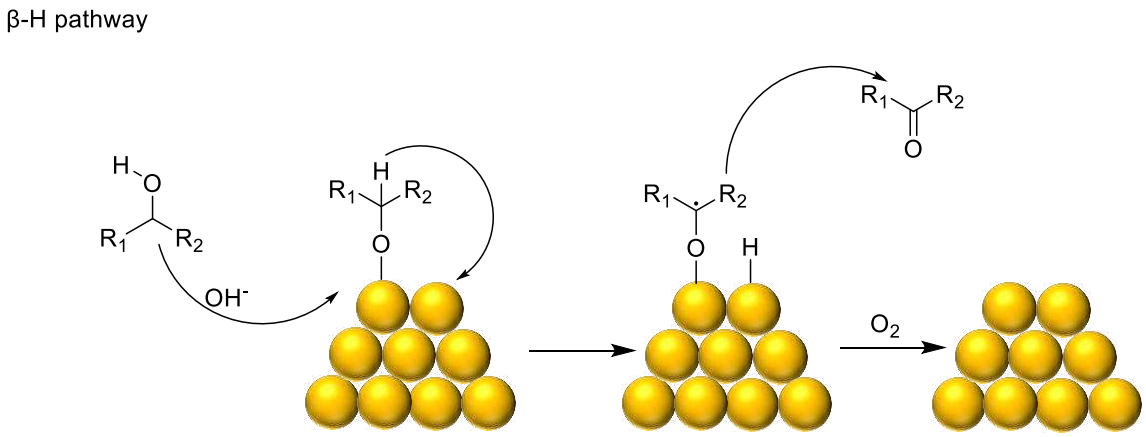

Scheme 1.3. Mechanism of aerobic oxidation of alcohols over Pd NPs

A significant drawback with noble metal NPs is selectivity. Taking benzyl alcohol as an example, due to the high catalytic activity observed, many overoxidation products and other side-products are also produced, including benzoic acid, benzene, toluene (a benzyl alcohol dispropornation product), benzyl benzoate and anisole.[162] Therefore, many modifications have been proposed to improve Pd NPs selectivity. For example, introducing an additional metal or metal oxide to form multi-metal nanoparticles or the selective passivation of a specific crystal face of metal nanoparticles, thereby inhibiting the occurrence of side reactions has been proposed. G. J. Hutchings group suggested a reaction mechanism in which 2 molecules of benzyl alcohol undergo disproportionation to obtain equal amounts of benzaldehyde and toluene.[163] R. Chen group grew MnO_x onto Pd NPs by atomic layer deposition to form a Pd-MnO_X reversed catalytic structure. MnO_x selectively passivates the Pd {111} facets, which inhibits the decarbonylation of benzaldehyde as well as the formation of toluene.[164] Taking into account the high cost of Pd, the supported noble metal NPs have higher economic potential due to their recyclability. NPs supported on support materials like MOFs could also benefit from

the above positive effects, such as acido-basic properties, electron transfer effects, substrate size selectivity, etc.[165–167]

Bimetallic nanoparticles have gained attention due to synergistic effects, including electronic effects, lattice strain, and bifunctional effects that greatly enhance their catalytic properties.[163,168] The alcohol oxidation reaction catalyzed by bimetallic nanoparticles, such as PdAu nanoparticles, exhibits higher activity, selectivity, stability, and leaching resistance relative to monometallic NPs.

1.2.2. Amine synthesis: a brief state of the art

Organoamines are important chemical platforms and are key components and intermediates of pharmaceuticals, pesticides, fine chemicals, and bioactive substances. An important process in the chemical industry for obtaining organic amines is the reductive amination of aldehydes and ketones.[169] The process often requires transition metal catalysis and hydrogen as a reducing agent under harsh reaction conditions. In particular, the preparation of chiral amines, which are biologically active in many drugs, is more complex. It requires asymmetric synthesis over transition metal organic compounds catalyst, or chiral resolution after the synthesis.[170] These costly and unsustainable processes remain the norm today.

An interesting alternative pathway is biocatalysis. As already mentioned in the previous section, one of the major advantages of enzymes is their stereoselectivity. Moreover, enzymes are obtained sustainably, the catalytic conditions of enzymes are environmentally friendly and mild. Thus, enzyme catalysis is more in line with the concept of green chemistry than the transition metal-catalyzed chemical pathway.

The synthesis of optically active alcohols using lipases or alcohol dehydrogenases can be considered an established technology, the biocatalytic asymmetric synthesis of enantiomerically enriched amines is more recent. Transaminases (TAs) and amino acid dehydrogenases (AADHs) are traditionally employed for the synthesis of amines. Amino acid dehydrogenases (AADHs) are cofactor- nicotinamide adenine dinucleotide phosphate ($NAD(P)^+$) dependent enzymes which produce amino acids through coupling of keto acids and

ammonia, followed by imino acid (intermediate) reduction via hydride transferred by the cofactor.[171] Early studies employing, for instance, phenylalanine dehydrogenase were limited by the narrow substrate specificity of the enzyme and substrate inhibition effects.[172] The regeneration of the cofactor is also a drawback because it requires an additional biocatalytic reaction. The biocatalytic reductive amination of keto acids represents a promising approach for the synthesis of D-amino acids as well. However, unlike their L selective counterparts, D-AADHs are not ubiquitous in nature, but are only found in some bacterial strains. Moreover, these enzymes are usually membrane-bound flavoproteins coupled to the respiratory chain and therefore rarely soluble in their biological active form.

1.2.2.1. Principles and examples of amination biocatalyzed by ω-transaminases

The development of transaminases (TAs) routes has proven to be efficient for the synthesis of chiral amines, many of which are crucial for the pharmaceutical industry.

TAs are enzymes that are widespread in nature and act in a variety of processes such as metabolism and signaling. TAs catalyze the transfer of amino groups from amine donors to carbonyl compound acceptors (Scheme 1.4). The mechanism of this reaction has been thoroughly investigated. TAs are pyridoxal 5'-phosphate (PLP)-dependent enzymes.[173] PLP is a cofactor od transaminase (one PLP complexed to each TA peptidic chain.

According to the type of amine acceptor, TAs can be divided into α-TA, which acts only with α-amino acids and α-keto acids, and ω-TA, which does not require any the carboxyl group at the α-position. ω-TAs thus can aminate keto-acids, aldehydes and ketones. TAs are classified into five subgroups depending on protein structures and multiple sequence alignments.[174] ω-amino acid aminotransferase, fall in the subgroup III of ATAs, show broad substrate specificity and quite useful in the synthesis of enantiopure chiral amines by asymmetric amination of prochiral ketones. Covering broad range of amino donor and acceptors for amination, has facilitated the quick entry of ω-TA to the industrial application. Till date, more than sixty microbial TAs have been reported,[175] about twenty have been identified in just last couple of years. In terms of substrate scope, bifunctional transaminases, that accept simple and cheap

mono or diamine donors as well as a wide range of ketone acceptors as substrates, have been recently discovered, for instance, enzymes from *P putida, P. chlororaphis*, and *P. aureofaciens,* are resulted to be very efficient in the stereoselective transamination of various ketones in the presence of natural diamines as amino donors, thus providing a convenient biocatalytic access to different pharmaceutically relevant chiral amines.[176]

Irrespective of microbial world representing an extraordinary source of new enzymes, natural biocatalysts that show all the desirable features required for industrial applications are not too many. To overcome this problem, different protein engineering approaches have been used to optimize available ATAs. A milestone was set in 2010 with the remarkable work by Merck Sharp & Dohme (MSD) and Codexis in the development of anti-diabatic drug sitagliptin by a biocatalytic route.[177]

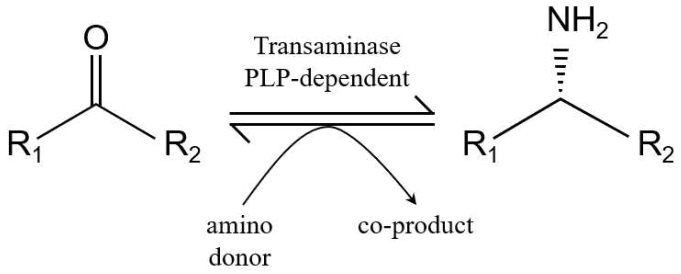

Scheme 1.4. Conversion of ketone into optically pure enantiomeric amine catalyzed by ω-TA. Reprinted from [178]

Sitagliptin structure has a unique amine-based chiral active center that can be introduced by asymmetric hydrogenation catalyzed by organorhodium catalysts.[179] However, rhodium is an unsustainable, rare, and expensive precious metal, which increases the total cost of production. Therefore, researchers at MSD and Codexis employed transaminases (TAs), allowing the new process route to avoid the hydrogenation step and directly convert ketones to target chiral amines with an excellent selectivity (99.95% ee) at 92 % yield using isopropylamaine as an amine donor. without any side-product formation (See Figure 1.20).[177] The new process avoids high-pressure of hydrogenation and recovery of unsustainable organorhodium catalysts, reducing the total footprint and waste generation with a 53% higher productivity. Starting from

a transaminase with very low activity (0.2 % conversion of 2 g/L substrate using 10 g/L enzyme, the most efficient variant obtained by several rounds of directed evolution was able to convert 200 g/L ketone into Sitagliptin.[177]

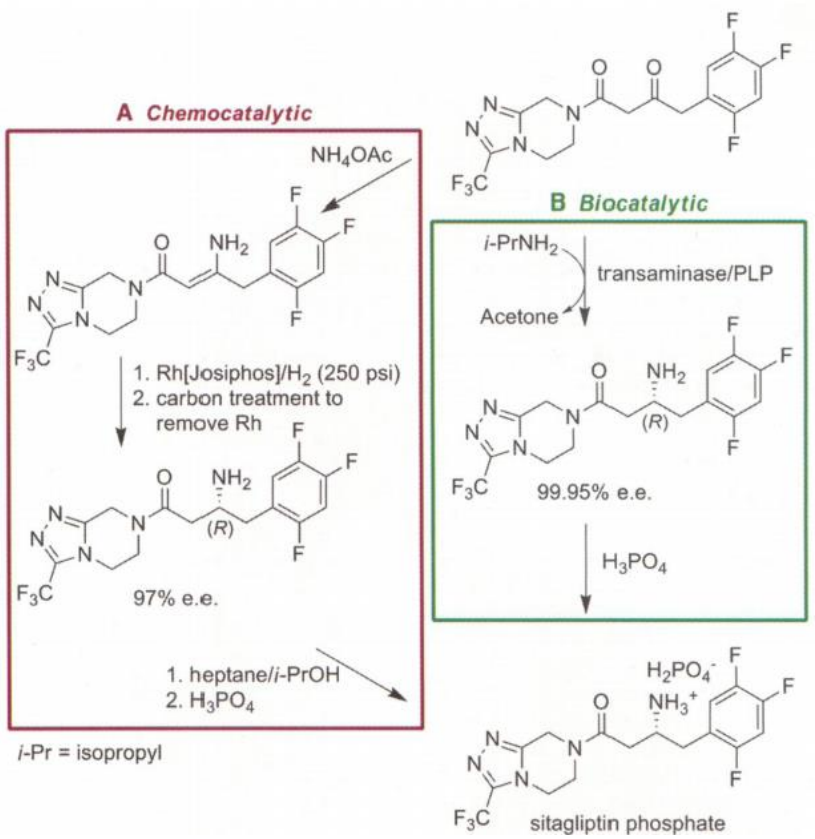

Figure 1.20. A comparison of the chemocatalytic and biocatalytic pathways: production of sitagliptin.[177]

1.2.2.2. Thermodynamic limitations of amination biocatalyzed with ω-TAs

One major bottleneck for the exploitation of ω-TAs is associated with the unfavorable thermodynamic equilibrium of the asymmetric synthesis. For example, the equilibrium constant $K_{eq} = 10^{-3}$ M for the synthesis of α-methylbenzylamine (MBA) from acetophenone (AP) and L-alanine.[180] Due to this unfavorable thermodynamic equilibrium, it is necessary to shift equilibrium in the direction of product formation. There has been plenty of research focused on developing new methods for shifting the equilibrium of substitution reactions.

Currently, there are two dominant strategies used to drive the chemical reaction equilibrium in a direction that favors the generation of the target chiral amine. One is the use of an excess of amine donors, and this approach is applicable to all amine donors. The second strategy is to physically or chemically remove the transamination reaction co-products away. For example, when Isopropylamine (IPA) is used as an amine donor, low boiling point co-product acetophenone is removed by heating or nitrogen purging.(As shown in Scheme 1.5 a)[181] Another physical approach is the utilization of bi-solvent systems, where the partition coefficient of co-products in different solvent phases is leveraged.[182] Additionally, selective filtration of co-products can be achieved by employing supported liquid membrane (SLM).[183] C. Grey group reported developed SLM consisting of hollow fiber membrane contactors, in which the pores contained undecane. The SLM was sufficient for the continuous extraction of amine products and successfully changed the thermodynamic equilibrium in the asymmetric synthesis of (S)-α-methylbenzylamine (S-MBA).

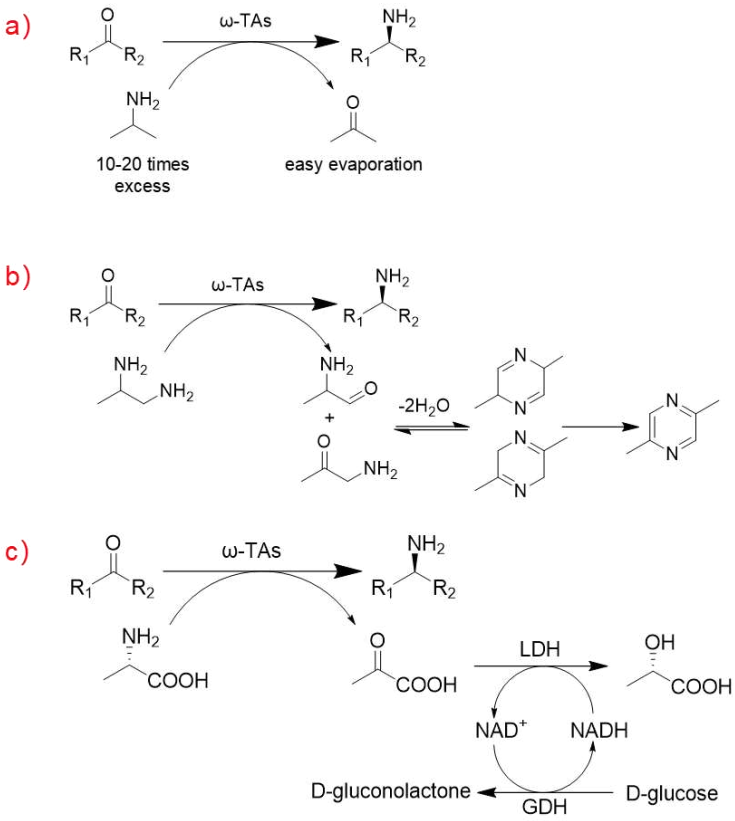

Scheme 1.5. Commonly used methods to shift the equilibrium of transamination reaction of ketones or aldehydes over TAs [181,184,185]

The chemical approach for equilibrium shifting is to further convert the by-product of the targeted amine reaction, the carbonyl compound resulting from the amine donor deamination.[184,186,187] In some cases, some smart amine donors have been used such as 1,2-diaminopropane, whose transformation products spontaneously dimerize and undergo oxidation, leading to the formation of pyrazine (As shown in Scheme 1.5b).[184] However, one major drawback of this method is due to the substrate selectivity of ω-TAs, which do not recognize this amine as a substrate.[188] The high cost of certain smart amine donors as sacrificial substrates also restricts their practical utility in industrial applications.[186]

When alanine is used as an amine donor, there are several well established, yet costly, enzymatic methods based on irreversible conversion of pyruvate (See Scheme 1.5c).[189–191] An ingenious design involves the conversion of pyruvate to lactate catalyzed by lactate dehydrogenase (LDH). In order to reduce the formed cofactor NAD^+, glucose and glucose dehydrogenase (GDH) are added to convert NAD^+ to NADH. This multi-enzyme cascade system is known as the LDH/GDH method.[185]

Robustness, recyclability and long-term stability are necessary to utilize transaminases in industrial applications. Therefore, transaminases are often immobilized on or within natural support materials to ensure their stability. The most common support materials are chitosan,[120,192] agarose,[193,194] resin,[195–197] etc. The common feature of these materials is their good bioaffinity. Although MOFs are widely used as inorganic-organic hybrid porous supporting materials with bioaffinity, there are only few reports on MOFs-based immobilization of TA. Q. Jiao group immobilized several ω-TAs on amino-functionalized UiO-66-NH_2 by physisorption.[198] ω-TA@UiO-66-NH_2 exhibited excellent activity against aromatic aldehyde substrates, with conversions from 60.4% to 96.6% for 18 substrates. Immobilized ω-TA@UiO-66-NH_2 showed good recovered activity (95.8%) and enhanced reusability, long-term stability, and tolerance to organic solvents and extreme pH.

1.2.3. One-pot chemoenzymatic cascade oxidation and amination of alcohols

Chemoenzymatic cascade reaction is that chemical catalysts and enzyme catalysts act on different steps in the sequential reaction, and the product of the previous reaction will serve as the substrate for the subsequent reaction.[199] It is an attractive emerging concept which takes advantage of the comprehensive superiority of chemical catalysts and enzymes to realize chemical processes that are difficult to achieve with a single catalytic system. A recent encouraging example is the synthesis of starch from CO_2, a similar process in nature known as photosynthesis. Photosynthesis is a complex biochemical process that is completed by the green cells of plants or algae and requires the participation of chlorophyll. Y. Ma group designed an artificial starch anabolic pathway (ASAP) consisting of 11 core reactions.[200] ASAP started from rational design and underwent multiple modular spatio-temporally separated chemoenzymatic catalytic systems to successfully achieve starch synthesis from CO_2 driven by hydrogen. This process showed a higher efficiency than the photosynthesis in corn. The realization of this technology is a concentrated expression of the advantages of chemoenzymatic catalysis, i.e., through a modular design that makes full use of the high activity of the chemical catalysis and the stereoselectivity of the enzyme, overcoming the unwelcome mutual obstruction between the different steps. In addition to this, cascade reactions avoid the isolation and purification of intermediates, thus saving time and cost and increasing overall yields.[199,201]

Since the conditions of each step of the cascade reaction are often very different, a huge challenge is how to find a condition compatibility window between each reaction, so that the catalysts of each step can play a role with acceptable activity.[202] The existence of this compatible gap makes chemical enzyme cascade catalysis unable to pursue mainly yield and selectivity like the traditional catalytic industry, but rather a compromised process. Therefore, there are various forms of chemical enzyme cascade catalysis, including one-pot/one-step, two-pot/one-step reactions that are consistent in time and space, and one-pot/multi-step reactions that are time-sequential.[203] (See Figure 1.21)

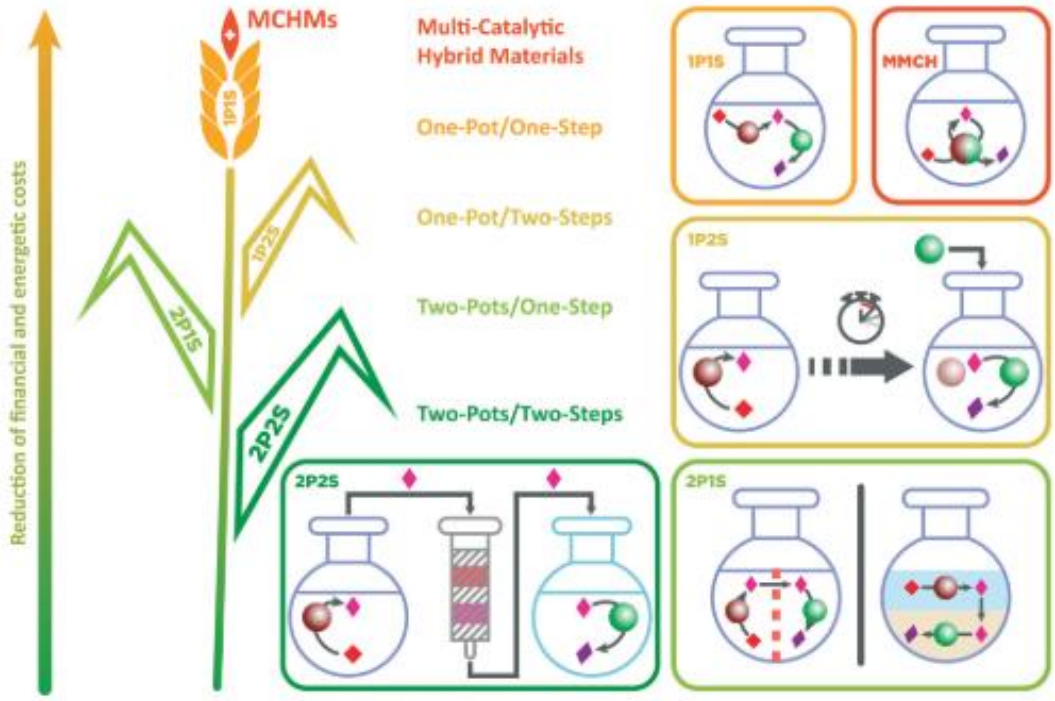

Figure 1.21. Different sequence forms of chemoenzymatic cascade catalysis[203]

In recent years, cascade catalytic systems involving ω-TAs have been continuously reported.[204–208] These cascade reactions have fully expanded the substrates for the preparation of chiral amines, especially some cascade oxidation-amination reactions using alcohol as substrate.[209–211] As one of the bio-based platform compounds, alcohols are easily and sustainably available. Therefore, this section will focus on the latest progress in the cascade catalytic oxidation-amination process of ω-TAs starting from alcohol.

Cascade catalytic oxidative amination involving ω-TAs of alcohols provides excellent regioselectivity and stereoselectivity.[212] In addition, the reaction conditions are milder relative to chemocatalytic processes. Some early attempts were made to catalyze the oxidation-amination of alcohols through multi-enzyme cascade reactions. W. Kroutil ‘s group reported cascade oxidation-amination reaction of primary alcohols catalyzed by alcohol dehydrogenase (ADH) and ω-TAs in 2012 (See Scheme 1.6).[212] The multi-enzyme system utilizes ADH from *Rhodococcus ruber* DSM 4454 to oxidize primary alcohols to aldehydes with the conversion of NAD^+ to NADH. In the second step, the amination reaction catalyzed by w-TA uses L-alanine as the amine donor, producing primary amines and pyruvate. The authors employ a

third enzyme, alanine dehydrogenase (AlaDH), to convert pyruvate acid back to L-alanine while converting the cofactor NADH to NAD^+, thereby achieving catalytic cycling. The advantages of this system are its redox neutrality and the low-cost NH_3 as a nitrogen source. The amine donor L-alanine involved in the reaction is recyclable. However, chiral amines cannot be prepared from primary alcohols.

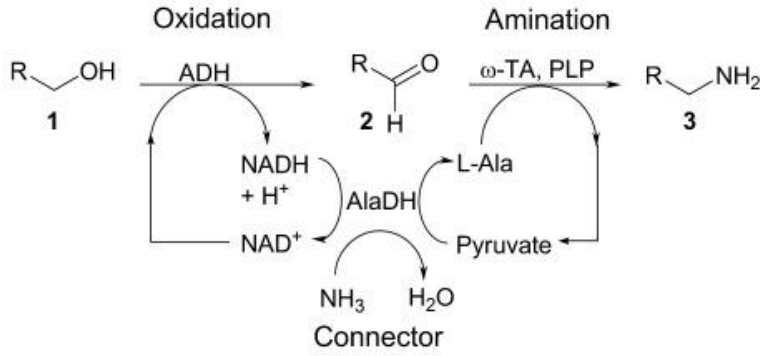

Scheme 1.6. Redox-neutral multi-enzyme network for the bioamination of primary alcohols[212]

In 2020, Z. Li's group reported a multi-enzyme cascade catalytic system for the synthesis of chiral amines.[213] The authors designed an ambidextrous ADH (CpSADH-W286A) to oxidize racemic secondary alcohols. Isopropylamine was used as the amine donor for the ketone amination reaction catalysed by BmTA. This cascade catalytic system not only produces a wide range of amines with high conversion (up to 99%) and high ee (>99%). It also uses isopropylamine as the sole co-substrate to regenerate two cofactors, PMP (pyridoxamine 5'-phosphate) and NAD^+, via a reverse cascade reaction (See Scheme 1.7).

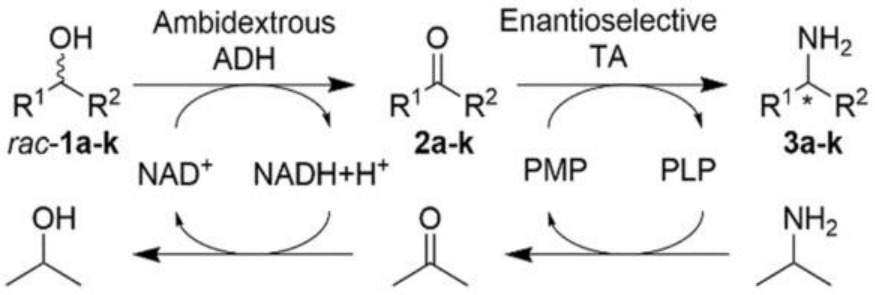

Scheme 1.7. The cascade conversion of racemic alcohols to enantiomerically pure amines by using ADH and TA, and the reversal of the cascade reaction with isopropylamine as the sole "coupling substrate" to regenerate PMP and NAD^+. [213]

In addition to multi-enzyme cascades, chemoenzymatic cascade catalysis for the preparation of chiral amines has also been developed. M. Anderson designed a chemoenzymatic cascade catalytic system with a heterogeneous palladium (0) catalyst or a homogeneous copper (I) catalyst & TA for the one-pot/two-step conversion of alcohols to amines.[206] This enzyme system can be operated in an aqueous/organic solvent two-phase system. High amine yield was achieved for a range of benzyl alcohols and similar compounds. Unfortunately, high conversions could not be obtained with fatty alcohols, and the method refers to primary alcohols, which do not give chiral amines.

J. González-Sabín group reported a chemoenzymatic cascade catalyzed preparation of chiral amines based on organocatalytic reactions. The organocatalyst 2-azaadamantane N-yloxy (AZADO)/NaOCl system was used for the oxidation of alcohols.[214] In combination with TA, this chemoenzymatic cascade catalysis achieved high yields and high stereoselectivity (> 90% yield, > 99% ee). The advantage of this cascade system is the wide range of substrates including conventional secondary alcohols and site-hindered β-substituted cycloalkanols.

1.3. Motivation and objective of the study

Although a few multi-enzyme cascade catalysis and homogeneous chemoenzymatic cascade catalysis systems have been designed for the amination of alcohols, fewer heterogeneous chemoenzymatic cascade catalysis systems are currently used for the above reactions.

In this PhD thesis, we will investigate the scientific problem of synthesis of chiral amines from alcohols by the one-pot method. We aim to create a chemoenzymatic heterogeneous catalyst that integrates the chemical oxidation catalyst with transaminase on the same solid support materials. The constructed chemoenzymatic catalyst will be able to catalyze the cascade oxidation and amination reaction of alcohol to amine under eco-friendly conditions. As mentioned earlier, MOFs, as novel porous organic-inorganic hybrid materials, have been widely studied in heterogeneous catalysis and enzyme immobilization. Therefore, we will base

on aqueous-phase stable MOFs by introducing chemical oxidation catalytic sites and transaminases, respectively, to achieve the goals (As shown in Scheme 1.8).

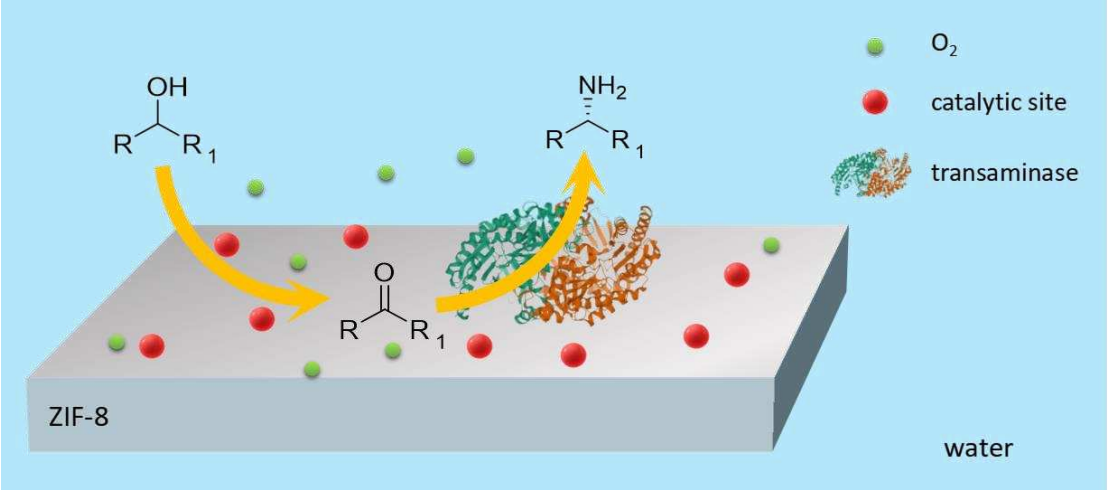

Scheme 1.8. Chemoenzymatic heterogeneous catalyst for one pot amination of alcohols

A PhD student has already worked on the subject. Dr. Priyanka successfully developed defect-engineered UiO-66 based catalysts for aerobic oxidation of alcohols.[215] This UiO-66 catalyst has a strong Lewis acid site and can catalyze the oxidation of benzyl alcohol to benzaldehyde under mild conditions.[49] However, due to its Lewis acidity it can likewise induce hydrolysis of the enzyme. Therefore, it cannot be used as a support for transaminases.

Therefore, we propose an alternative strategy, i.e., one-pot chemoenzymatic synthesis of chiral amines from alcohols, but in which MOF is only used as a heterogeneous support, while the chemo and biocatalysts are immobilized on the same MOF support, respectively. In order to achieve the above objectives, the selected MOF must be aqueous phase stable, especially in the weakly basic aqueous phase. Another major challenge in this topic is the compatibility of the working conditions of the two catalysts involved in the chemoenzymatic cascade catalysis. Therefore, the designed chemical catalysts for alcohol oxidation must have a window of compatibility with ω-TA in terms of working conditions, i.e., aqueous phase, low temperature, and weak alkalinity. Finally, the alcohol oxidation catalyst and ω-TA must be immobilized on the same MOF support.

After this first chapter of literature review focusing on the background of the research, the chapter 2 lists the chemical reagents and material characterization methods applied during the thesis research. Chapter 3 then describes the synthesis of Cu/ZIF-8 catalyst and its use in the aerobic oxidation reaction of benzyl alcohol. Chapter 4 presents the synthesis of the PdAu@ZIF-8 catalyst and explores its potential for the catalysis of the aerobic oxidation reaction of benzyl alcohol and 1-phenylethanol. Chapter 5 deals with the biocatalytic amination of acetophenone and a preliminary investigation of the one-pot, two-step amination of 1-phenylethanol based on the combination of PdAu@ZIF-8 and 3HMU. Chapter 6 investigates different methods for the immobilization of 3HMU on PdAu@ZIF-8 towards the synthesis of the targeted fully heterogenized chemoenzymatic catalyst.

References

(1) Zhu, Q.-L.; Xu, Q. Metal–Organic Framework Composites. *Chem. Soc. Rev.* **2014**, *43* (16), 5468–5512. https://doi.org/10.1039/C3CS60472A.

(2) Li, C.; Zhang, H.; Liu, M.; Lang, F.-F.; Pang, J.; Bu, X.-H. Recent Progress in Metal–Organic Frameworks (MOFs) for Electrocatalysis. *Industrial Chemistry & Materials* **2023**, *1* (1), 9–38. https://doi.org/10.1039/D2IM00063F.

(3) Gomollón-Bel, F. Ten Chemical Innovations That Will Change Our World: IUPAC identifies emerging technologies in Chemistry with potential to make our planet more sustainable. *Chemistry International* **2019**, *41* (2), 12–17. https://doi.org/10.1515/ci-2019-0203.

(4) Huskić, I.; Pekov, I. V.; Krivovichev, S. V.; Friščić, T. Minerals with Metal-Organic Framework Structures. *Science Advances* **2016**, *2* (8), e1600621. https://doi.org/10.1126/sciadv.1600621.

(5) Piñeiro-López, L.; Seredyuk, M.; Muñoz, M. C.; Real, J. A. Two- and One-Step Cooperative Spin Transitions in Hofmann-like Clathrates with Enhanced Loading Capacity. *Chem. Commun.* **2014**, *50* (15), 1833–1835. https://doi.org/10.1039/C3CC48595A.

(6) Estelrich, J.; Busquets, M. A. Prussian Blue: A Nanozyme with Versatile Catalytic Properties. *International Journal of Molecular Sciences* **2021**, *22* (11), 5993. https://doi.org/10.3390/ijms22115993.

(7) Hoskins, B. F.; Robson, R. Design and Construction of a New Class of Scaffolding-like Materials Comprising Infinite Polymeric Frameworks of 3D-Linked Molecular Rods. A Reappraisal of the Zinc Cyanide and Cadmium Cyanide Structures and the Synthesis and

Structure of the Diamond-Related Frameworks $[N(CH_3)_4][CuIZnII(CN)_4]$ and CuI[4,4',4'',4'''-Tetracyanotetraphenylmethane]BF4.XC6H5NO2. *J. Am. Chem. Soc.* **1990**, *112* (4), 1546–1554. https://doi.org/10.1021/ja00160a038.

(8) Yaghi, O. M.; Li, G.; Li, H. Selective Binding and Removal of Guests in a Microporous Metal–Organic Framework. *Nature* **1995**, *378* (6558), 703–706. https://doi.org/10.1038/378703a0.

(9) Kondo, M.; Yoshitomi, T.; Matsuzaka, H.; Kitagawa, S.; Seki, K. Three-Dimensional Framework with Channeling Cavities for Small Molecules: $[M_2(4, 4'\text{-}Bpy)_3(NO_3)_4]\cdot xH_2On$ (M = Co, Ni, Zn). *Angewandte Chemie International Edition in English* **1997**, *36* (16), 1725–1727. https://doi.org/10.1002/anie.199717251.

(10) Li, H.; Eddaoudi, M.; O'Keeffe, M.; Yaghi, O. M. Design and Synthesis of an Exceptionally Stable and Highly Porous Metal-Organic Framework. *Nature* **1999**, *402* (6759), 276–279. https://doi.org/10.1038/46248.

(11) Chui, S. S.-Y.; Lo, S. M.-F.; Charmant, J. P. H.; Orpen, A. G.; Williams, I. D. A Chemically Functionalizable Nanoporous Material $[Cu_3(TMA)_2(H_2O)_3]_n$. *Science* **1999**, *283* (5405), 1148–1150. https://doi.org/10.1126/science.283.5405.1148.

(12) Loiseau, T.; Serre, C.; Huguenard, C.; Fink, G.; Taulelle, F.; Henry, M.; Bataille, T.; Férey, G. A Rationale for the Large Breathing of the Porous Aluminum Terephthalate (MIL-53) Upon Hydration. *Chemistry – A European Journal* **2004**, *10* (6), 1373–1382. https://doi.org/10.1002/chem.200305413.

(13) Latroche, M.; Surblé, S.; Serre, C.; Mellot-Draznieks, C.; Llewellyn, P. L.; Lee, J.-H.; Chang, J.-S.; Jhung, S. H.; Férey, G. Hydrogen Storage in the Giant-Pore Metal–Organic Frameworks MIL-100 and MIL-101. *Angewandte Chemie* **2006**, *118* (48), 8407–8411. https://doi.org/10.1002/ange.200600105.

(14) Horcajada, P.; Surblé, S.; Serre, C.; Hong, D.-Y.; Seo, Y.-K.; Chang, J.-S.; Grenèche, J.-M.; Margiolaki, I.; Férey, G. Synthesis and Catalytic Properties of MIL-100(Fe), an Iron(III) Carboxylate with Large Pores. *Chemical Communications* **2007**, *0* (27), 2820–2822. https://doi.org/10.1039/B704325B.

(15) Férey, G.; Mellot-Draznieks, C.; Serre, C.; Millange, F.; Dutour, J.; Surblé, S.; Margiolaki, I. A Chromium Terephthalate-Based Solid with Unusually Large Pore Volumes and Surface Area. *Science* **2005**, *309* (5743), 2040–2042. https://doi.org/10.1126/science.1116275.

(16) Alshammari, A.; Jiang, Z.; Cordova, K. E.; Alshammari, A.; Jiang, Z.; Cordova, K. E. Metal Organic Frameworks as Emerging Photocatalysts. In *Semiconductor Photocatalysis - Materials, Mechanisms and Applications*; IntechOpen, 2016. https://doi.org/10.5772/63489.

(17) Zhou, H.-C. "Joe"; Kitagawa, S. Metal–Organic Frameworks (MOFs). *Chem. Soc. Rev.* **2014**, *43* (16), 5415–5418. https://doi.org/10.1039/C4CS90059F.

(18) Xiao, J.-D.; Jiang, H.-L. Metal–Organic Frameworks for Photocatalysis and Photothermal Catalysis. *Acc. Chem. Res.* **2019**, *52* (2), 356–366. https://doi.org/10.1021/acs.accounts.8b00521.

(19) Wang, C.; An, B.; Lin, W. Metal–Organic Frameworks in Solid–Gas Phase Catalysis. *ACS Catal.* **2019**, *9* (1), 130–146. https://doi.org/10.1021/acscatal.8b04055.

(20) Cui, Y.; Zhang, J.; He, H.; Qian, G. Photonic Functional Metal–Organic Frameworks. *Chem. Soc. Rev.* **2018**, *47* (15), 5740–5785. https://doi.org/10.1039/C7CS00879A.

(21) Li, G.; Zhao, S.; Zhang, Y.; Tang, Z. Metal–Organic Frameworks Encapsulating Active Nanoparticles as Emerging Composites for Catalysis: Recent Progress and Perspectives. *Advanced Materials* **2018**, *30* (51), 1800702. https://doi.org/10.1002/adma.201800702.

(22) Banerjee, R.; Phan, A.; Wang, B.; Knobler, C.; Furukawa, H.; O'Keeffe, M.; Yaghi, O. M. High-Throughput Synthesis of Zeolitic Imidazolate Frameworks and Application to CO_2 Capture. *Science* **2008**, *319* (5865), 939–943. https://doi.org/10.1126/science.1152516.

(23) Zhang, X.; Zheng, Q.; He, H. Multicomponent Adsorptive Separation of CO_2, CH_4, N_2, and H_2 over M-MOF-74 and AX-21@M-MOF-74 Composite Adsorbents. *Microporous and Mesoporous Materials* **2022**, *336*, 111899. https://doi.org/10.1016/j.micromeso.2022.111899.

(24) Dong, Y.; Zhang, J.; Yang, Y.; Wang, J.; Hu, B.; Wang, W.; Cao, W.; Gai, S.; Xia, D.; Lin, K.; Fan, R. Multifunctional Nanostructured Host-Guest POM@MOF with Lead Sequestration Capability Induced Stable and Efficient Perovskite Solar Cells. *Nano Energy* **2022**, *97*, 107184. https://doi.org/10.1016/j.nanoen.2022.107184.

(25) Katayama, T.; Tanaka, S.; Tsuruoka, T.; Nagahama, K. Two-Dimensional Metal–Organic Framework-Based Cellular Scaffolds with High Protein Adsorption, Retention, and Replenishment Capabilities. *ACS Appl. Mater. Interfaces* **2022**, *14* (30), 34443–34454. https://doi.org/10.1021/acsami.2c08677.

(26) Moosavi, S. M.; Nandy, A.; Jablonka, K. M.; Ongari, D.; Janet, J. P.; Boyd, P. G.; Lee, Y.; Smit, B.; Kulik, H. J. Understanding the Diversity of the Metal-Organic Framework Ecosystem. *Nat Commun* **2020**, *11* (1), 4068. https://doi.org/10.1038/s41467-020-17755-8.

(27) Zhou, L.; Luo, X.; Gao, J.; Liu, G.; Ma, L.; He, Y.; Huang, Z.; Jiang, Y. Facile Synthesis of Covalent Organic Framework Derived Fe-COFs Composites as a Peroxidase-Mimicking Artificial Enzyme. *Nanoscale Advances* **2020**, *2* (3), 1036–1039. https://doi.org/10.1039/D0NA00025F.

(28) Liang, W.; Carraro, F.; Solomon, M. B.; Bell, S. G.; Amenitsch, H.; Sumby, C. J.; White, N. G.; Falcaro, P.; Doonan, C. J. Enzyme Encapsulation in a Porous Hydrogen-Bonded Organic Framework. *J. Am. Chem. Soc.* **2019**, *141* (36), 14298–14305. https://doi.org/10.1021/jacs.9b06589.

(29) Huang, X.-C.; Lin, Y.-Y.; Zhang, J.-P.; Chen, X.-M. Ligand-Directed Strategy for Zeolite-Type Metal–Organic Frameworks: Zinc(II) Imidazolates with Unusual Zeolitic Topologies. *Angewandte Chemie International Edition* **2006**, *45* (10), 1557–1559. https://doi.org/10.1002/anie.200503778.

(30) Wu, X.; Yue, H.; Zhang, Y.; Gao, X.; Li, X.; Wang, L.; Cao, Y.; Hou, M.; An, H.; Zhang, L.; Li, S.; Ma, J.; Lin, H.; Fu, Y.; Gu, H.; Lou, W.; Wei, W.; Zare, R. N.; Ge, J. Packaging and Delivering Enzymes by Amorphous Metal-Organic Frameworks. *Nat Commun* **2019**, *10* (1), 5165. https://doi.org/10.1038/s41467-019-13153-x.

(31) Shi, Y.; Xing, Y.; Gong, C.; Zhao, H. In Situ Encapsulation of Laccase in Mesoporous Amorphous ZIF-8 for Reactive Blue 19 Removal. *Water Environment Research* **2023**, *95* (5), e10879. https://doi.org/10.1002/wer.10879.

(32) Carraro, F.; Williams, J. D.; Linares-Moreau, M.; Parise, C.; Liang, W.; Amenitsch, H.; Doonan, C.; Kappe, C. O.; Falcaro, P. Continuous-Flow Synthesis of ZIF-8 Biocomposites with Tunable Particle Size. *Angewandte Chemie* **2020**, *132* (21), 8200–8204. https://doi.org/10.1002/ange.202000678.

(33) Fujita, M.; Kwon, Y. J.; Washizu, S.; Ogura, K. Preparation, Clathration Ability, and Catalysis of a Two-Dimensional Square Network Material Composed of Cadmium(II) and 4,4'-Bipyridine. *J. Am. Chem. Soc.* **1994**, *116* (3), 1151–1152. https://doi.org/10.1021/ja00082a055.

(34) Yepez, R.; García, S.; Schachat, P.; Sánchez-Sánchez, M.; González-Estefan, J. H.; González-Zamora, E.; Ibarra, I. A.; Aguilar-Pliego, J. Catalytic Activity of HKUST-1 in the Oxidation of Trans-Ferulic Acid to Vanillin. *New J. Chem.* **2015**, *39* (7), 5112–5115. https://doi.org/10.1039/C5NJ00247H.

(35) Hwang, Y. K.; Hong, D.-Y.; Chang, J.-S.; Seo, H.; Yoon, M.; Kim, J.; Jhung, S. H.; Serre, C.; Férey, G. Selective Sulfoxidation of Aryl Sulfides by Coordinatively Unsaturated Metal Centers in Chromium Carboxylate MIL-101. *Applied Catalysis A: General* **2009**, *358* (2), 249–253. https://doi.org/10.1016/j.apcata.2009.02.018.

(36) Nguyen, L. T. L.; Le, K. K. A.; Phan, N. T. S. A Zeolite Imidazolate Framework ZIF-8 Catalyst for Friedel-Crafts Acylation. *Chinese Journal of Catalysis* **2012**, *33* (4), 688–696. https://doi.org/10.1016/S1872-2067(11)60368-9.

(37) Tran, U. P. N.; Le, K. K. A.; Phan, N. T. S. Expanding Applications of Metal−Organic Frameworks: Zeolite Imidazolate Framework ZIF-8 as an Efficient Heterogeneous Catalyst for the Knoevenagel Reaction. *ACS Catal.* **2011**, *1* (2), 120–127. https://doi.org/10.1021/cs1000625.

(38) Chizallet, C.; Lazare, S.; Bazer-Bachi, D.; Bonnier, F.; Lecocq, V.; Soyer, E.; Quoineaud, A.-A.; Bats, N. Catalysis of Transesterification by a Nonfunctionalized Metal−Organic Framework: Acido-Basicity at the External Surface of ZIF-8 Probed by FTIR and Ab Initio Calculations. *J. Am. Chem. Soc.* **2010**, *132* (35), 12365–12377. https://doi.org/10.1021/ja103365s.

(39) Zhu, M.; Srinivas, D.; Bhogeswararao, S.; Ratnasamy, P.; Carreon, M. A. Catalytic Activity of ZIF-8 in the Synthesis of Styrene Carbonate from CO_2 and Styrene Oxide. *Catalysis Communications* **2013**, *32*, 36–40. https://doi.org/10.1016/j.catcom.2012.12.003.

(40) Jing, H.-P.; Wang, C.-C.; Zhang, Y.-W.; Wang, P.; Li, R. Photocatalytic Degradation of Methylene Blue in ZIF-8. *RSC Adv.* **2014**, *4* (97), 54454–54462. https://doi.org/10.1039/C4RA08820D.

(41) Vermoortele, F.; Vandichel, M.; Van de Voorde, B.; Ameloot, R.; Waroquier, M.; Van Speybroeck, V.; De Vos, D. E. Electronic Effects of Linker Substitution on Lewis Acid Catalysis with Metal–Organic Frameworks. *Angewandte Chemie International Edition* **2012**, *51* (20), 4887–4890. https://doi.org/10.1002/anie.201108565.

(42) Yang, D.; Odoh, S. O.; Borycz, J.; Wang, T. C.; Farha, O. K.; Hupp, J. T.; Cramer, C. J.; Gagliardi, L.; Gates, B. C. Tuning Zr_6 Metal–Organic Framework (MOF) Nodes as Catalyst Supports: Site Densities and Electron-Donor Properties Influence Molecular Iridium Complexes as Ethylene Conversion Catalysts. *ACS Catal.* **2016**, *6* (1), 235–247. https://doi.org/10.1021/acscatal.5b02243.

(43) Katz, M. J.; Klet, R. C.; Moon, S.-Y.; Mondloch, J. E.; Hupp, J. T.; Farha, O. K. One Step Backward Is Two Steps Forward: Enhancing the Hydrolysis Rate of UiO-66 by Decreasing [OH–]. *ACS Catal.* **2015**, *5* (8), 4637–4642. https://doi.org/10.1021/acscatal.5b00785.

(44) Vermoortele, F.; Bueken, B.; Le Bars, G.; Van de Voorde, B.; Vandichel, M.; Houthoofd, K.; Vimont, A.; Daturi, M.; Waroquier, M.; Van Speybroeck, V.; Kirschhock, C.; De Vos, D. E. Synthesis Modulation as a Tool To Increase the Catalytic Activity of Metal–Organic Frameworks: The Unique Case of UiO-66(Zr). *J. Am. Chem. Soc.* **2013**, *135* (31), 11465–11468. https://doi.org/10.1021/ja405078u.

(45) Winarta, J.; Shan, B.; Mcintyre, S. M.; Ye, L.; Wang, C.; Liu, J.; Mu, B. A Decade of UiO-66 Research: A Historic Review of Dynamic Structure, Synthesis Mechanisms, and Characterization Techniques of an Archetypal Metal–Organic Framework. *Crystal Growth & Design* **2020**, *20* (2), 1347–1362. https://doi.org/10.1021/acs.cgd.9b00955.

(46) Cavka, J. H.; Jakobsen, S.; Olsbye, U.; Guillou, N.; Lamberti, C.; Bordiga, S.; Lillerud, K. P. A New Zirconium Inorganic Building Brick Forming Metal Organic Frameworks with Exceptional Stability. *J. Am. Chem. Soc.* **2008**, *130* (42), 13850–13851. https://doi.org/10.1021/ja8057953.

(47) Shearer, G. C.; Chavan, S.; Ethiraj, J.; Vitillo, J. G.; Svelle, S.; Olsbye, U.; Lamberti, C.; Bordiga, S.; Lillerud, K. P. Tuned to Perfection: Ironing Out the Defects in Metal–Organic Framework UiO-66. *Chem. Mater.* **2014**, *26* (14), 4068–4071. https://doi.org/10.1021/cm501859p.

(48) Vermoortele, F.; Bueken, B.; Le Bars, G.; Van de Voorde, B.; Vandichel, M.; Houthoofd, K.; Vimont, A.; Daturi, M.; Waroquier, M.; Van Speybroeck, V.; Kirschhock, C.; De Vos, D. E. Synthesis Modulation as a Tool To Increase the Catalytic Activity of Metal–Organic Frameworks: The Unique Case of UiO-66(Zr). *J. Am. Chem. Soc.* **2013**, *135* (31), 11465–11468. https://doi.org/10.1021/ja405078u.

(49) Gairola, P.; Millot, Y.; Krafft, J.-M.; Averseng, F.; Launay, F.; Massiani, P.; Jolivalt, C.; Reboul, J. On the Importance of Combining Bulk- and Surface-Active Sites to Maximize the Catalytic Activity of Metal–Organic Frameworks for the Oxidative Dehydrogenation of Alcohols Using Alkyl Hydroperoxides as Hydride Acceptors. *Catal. Sci. Technol.* **2020**, *10* (20), 6935–6947. https://doi.org/10.1039/D0CY00901F.

(50) Liu, D.; Wang, C.; Zhou, Z.; Ye, C.; Yu, R.; Wang, C.; Du, Y. Ultra-Low Ru Doped MOF-Derived Hollow Nanorods for Efficient Oxygen Evolution Reaction. *Inorg. Chem. Front.* **2022**, *9* (23), 6158–6166. https://doi.org/10.1039/D2QI01764D.

(51) Zhang, Y.; Riduan, S. N.; Wang, J. Redox Active Metal– and Covalent Organic Frameworks for Energy Storage: Balancing Porosity and Electrical Conductivity.

Chemistry – A European Journal **2017**, *23* (65), 16419–16431. https://doi.org/10.1002/chem.201702919.

(52) Li, R.; Chen, T.; Lu, J.; Hu, H.; Zheng, H.; Zhu, P.; Pan, X. Metal–Organic Frameworks Doped with Metal Ions for Efficient Sterilization: Enhanced Photocatalytic Activity and Photothermal Effect. *Water Research* **2023**, *229*, 119366. https://doi.org/10.1016/j.watres.2022.119366.

(53) Ahmad, A.; Iqbal, N.; Noor, T.; Hassan, A.; Khan, U. A.; Wahab, A.; Raza, M. A.; Ashraf, S. Cu-Doped Zeolite Imidazole Framework (ZIF-8) for Effective Electrocatalytic CO_2 Reduction. *Journal of CO2 Utilization* **2021**, *48*, 101523. https://doi.org/10.1016/j.jcou.2021.101523.

(54) Cao, J.; Yang, Z.; Xiong, W.; Zhou, Y.; Peng, Y.; Li, X.; Zhou, C.; Xu, R.; Zhang, Y. One-Step Synthesis of Co-Doped UiO-66 Nanoparticle with Enhanced Removal Efficiency of Tetracycline: Simultaneous Adsorption and Photocatalysis. *Chemical Engineering Journal* **2018**, *353*, 126–137. https://doi.org/10.1016/j.cej.2018.07.060.

(55) Chen, C.; Meng, L.; Alalouni, M. R.; Dong, X.; Wu, Z.-P.; Zuo, S.; Zhang, H. Ultra-Highly Active Ni-Doped MOF-5 Heterogeneous Catalysts for Ethylene Dimerization. *Small n/a* (n/a), 2301235. https://doi.org/10.1002/smll.202301235.

(56) Jin, Y.; Wu, J.; Wang, J.; Fan, Y.; Zhang, S.; Ma, N.; Dai, W. Highly Efficient Capture of Benzothiophene with a Novel Water-Resistant-Bimetallic Cu-ZIF-8 Material. *Inorganica Chimica Acta* **2020**, *503*, 119412. https://doi.org/10.1016/j.ica.2020.119412.

(57) Phan, A.; Doonan, C. J.; Uribe-Romo, F. J.; Knobler, C. B.; O'Keeffe, M.; Yaghi, O. M. Synthesis, Structure, and Carbon Dioxide Capture Properties of Zeolitic Imidazolate Frameworks. *Acc. Chem. Res.* **2010**, *43* (1), 58–67. https://doi.org/10.1021/ar900116g.

(58) López-Cabrelles, J.; Romero, J.; Abellán, G.; Giménez-Marqués, M.; Palomino, M.; Valencia, S.; Rey, F.; Mínguez Espallargas, G. Solvent-Free Synthesis of ZIFs: A Route toward the Elusive Fe(II) Analogue of ZIF-8. *J. Am. Chem. Soc.* **2019**, *141* (17), 7173–7180. https://doi.org/10.1021/jacs.9b02686.

(59) Yu, L.; Ding, Q.; Liu, Y.; Sun, D.; Ding, J.; Zhu, G.; Bai, H.; Fan, W. An In-Situ Cation Exchange Approach to Stabilize Zn-MOF: Understanding the Role of Nickel Ions for Photoelectrochemical Performance. *International Journal of Hydrogen Energy* **2022**, *47* (18), 10277–10288. https://doi.org/10.1016/j.ijhydene.2022.01.118.

(60) Zhang, M.; Cao, A.; Zhang, H.; Yang, C. Defective MNiFeO (M = Cu, Zn, Co, Mn) NRs Derived from Cation-Exchanged Fe_2Ni-MOFs for Catalytic Nitroarene Hydrogenation. *Journal of Colloid and Interface Science* **2022**, *623*, 63–76. https://doi.org/10.1016/j.jcis.2022.04.177.

(61) Noh, J.; Kim, Y.; Park, H.; Lee, J.; Yoon, M.; Park, M. H.; Kim, Y.; Kim, M. Functional Group Effects on a Metal-Organic Framework Catalyst for CO_2 Cycloaddition. *Journal of Industrial and Engineering Chemistry* **2018**, *64*, 478–483. https://doi.org/10.1016/j.jiec.2018.04.010.

(62) Patel, P.; Parmar, B.; Kureshy, R. I.; Khan, N. H.; Suresh, E. Amine-Functionalized Zn(II) MOF as an Efficient Multifunctional Catalyst for CO_2 Utilization and Sulfoxidation Reaction. *Dalton Trans.* **2018**, *47* (24), 8041–8051. https://doi.org/10.1039/C8DT01297K.

(63) Luan, Y.; Zheng, N.; Qi, Y.; Yu, J.; Wang, G. Development of a SO3H-Functionalized UiO-66 Metal–Organic Framework by Postsynthetic Modification and Studies of Its Catalytic Activities. *European Journal of Inorganic Chemistry* **2014**, *2014* (26), 4268–4272. https://doi.org/10.1002/ejic.201402509.

(64) Zeng, Y.; Lan, T.; Li, M.; Yuan, G.; Li, F.; Liao, J.; Yang, J.; Yang, Y.; Liu, N. Removal of Co(II) from Aqueous Solutions by Pyridine Schiff Base-Functionalized Zirconium-Based MOFs: A Combined Experimental and DFT Study on the Effect of Ortho-, Meta-, and Para-Substitution. *J. Chem. Eng. Data* **2021**, *66* (1), 749–760. https://doi.org/10.1021/acs.jced.0c00852.

(65) Eddaoudi, M.; Kim, J.; Rosi, N.; Vodak, D.; Wachter, J.; O'Keeffe, M.; Yaghi, O. M. Systematic Design of Pore Size and Functionality in Isoreticular MOFs and Their Application in Methane Storage. *Science* **2002**, *295* (5554), 469–472. https://doi.org/10.1126/science.1067208.

(66) Hartmann, M.; Fischer, M. Amino-Functionalized Basic Catalysts with MIL-101 Structure. *Microporous and Mesoporous Materials* **2012**, *164*, 38–43. https://doi.org/10.1016/j.micromeso.2012.06.044.

(67) Banerjee, R.; Furukawa, H.; Britt, D.; Knobler, C.; O'Keeffe, M.; Yaghi, O. M. Control of Pore Size and Functionality in Isoreticular Zeolitic Imidazolate Frameworks and Their Carbon Dioxide Selective Capture Properties. *J. Am. Chem. Soc.* **2009**, *131* (11), 3875–3877. https://doi.org/10.1021/ja809459e.

(68) Devic, T.; Horcajada, P.; Serre, C.; Salles, F.; Maurin, G.; Moulin, B.; Heurtaux, D.; Clet, G.; Vimont, A.; Grenèche, J.-M.; Ouay, B. L.; Moreau, F.; Magnier, E.; Filinchuk, Y.; Marrot, J.; Lavalley, J.-C.; Daturi, M.; Férey, G. Functionalization in Flexible Porous Solids: Effects on the Pore Opening and the Host−Guest Interactions. *J. Am. Chem. Soc.* **2010**, *132* (3), 1127–1136. https://doi.org/10.1021/ja9092715.

(69) Tang, J.; Zhao, J.; Wang, S.; Zhang, L.; Zhao, M.; Huang, Z.; Hu, Y. Pre-Modification Strategy to Prepare a Novel Zr-Based MOF for Selective Adsorption of Palladium(II) from Solution. *Chemical Engineering Journal* **2021**, *407*, 127223. https://doi.org/10.1016/j.cej.2020.127223.

(70) Cho, K. Y.; An, H.; Do, X. H.; Choi, K.; Yoon, H. G.; Jeong, H.-K.; Lee, J. S.; Baek, K.-Y. Synthesis of Amine-Functionalized ZIF-8 with 3-Amino-1,2,4-Triazole by Postsynthetic Modification for Efficient CO_2-Selective Adsorbents and Beyond. *J. Mater. Chem. A* **2018**, *6* (39), 18912–18919. https://doi.org/10.1039/C8TA02797H.

(71) Fei, H.; Cahill, J. F.; Prather, K. A.; Cohen, S. M. Tandem Postsynthetic Metal Ion and Ligand Exchange in Zeolitic Imidazolate Frameworks. *Inorg. Chem.* **2013**, *52* (7), 4011–4016. https://doi.org/10.1021/ic400048g.

(72) Kaur, M.; Kumar, S.; Younis, S. A.; Yusuf, M.; Lee, J.; Weon, S.; Kim, K.-H.; Malik, A. K. Post-Synthesis Modification of Metal-Organic Frameworks Using Schiff Base Complexes for Various Catalytic Applications. *Chemical Engineering Journal* **2021**, *423*, 130230. https://doi.org/10.1016/j.cej.2021.130230.

(73) Kim, M.; F. Cahill, J.; Su, Y.; A. Prather, K.; M. Cohen, S. Postsynthetic Ligand Exchange as a Route to Functionalization of 'Inert' Metal–Organic Frameworks. *Chemical Science* **2012**, *3* (1), 126–130. https://doi.org/10.1039/C1SC00394A.

(74) Li, G.-L.; Kumar Tripathi, A.; Chan, H.; Chen, S.-T.; Chang, J.-T.; Nakagawa, T.; Wang, C.-Y. Recyclable Dehydrogenation/Regeneration of Ammonia Borane Nanoconfined in Amino-Functionalized ZIF-8 with 3-Amino-1,2,4-Triazole. *ACS Sustainable Chem. Eng.* **2023**, *11* (16), 6143–6152. https://doi.org/10.1021/acssuschemeng.2c06036.

(75) Lee, Y.-R.; Do, X. H.; Hwang, S. S.; Baek, K.-Y. Dual-Functionalized ZIF-8 as an Efficient Acid-Base Bifunctional Catalyst for the One-Pot Tandem Reaction. *Catalysis Today* **2021**, *359*, 124–132. https://doi.org/10.1016/j.cattod.2019.06.076.

(76) Lu, G.; Li, S.; Guo, Z.; Farha, O. K.; Hauser, B. G.; Qi, X.; Wang, Y.; Wang, X.; Han, S.; Liu, X.; DuChene, J. S.; Zhang, H.; Zhang, Q.; Chen, X.; Ma, J.; Loo, S. C. J.; Wei, W. D.; Yang, Y.; Hupp, J. T.; Huo, F. Imparting Functionality to a Metal–Organic Framework Material by Controlled Nanoparticle Encapsulation. *Nature Chem* **2012**, *4* (4), 310–316. https://doi.org/10.1038/nchem.1272.

(77) Li, X.; Zhang, Z.; Xiao, W.; Deng, S.; Chen, C.; Zhang, N. Mechanochemistry-Assisted Encapsulation of Metal Nanoparticles in MOF Matrices via a Sacrificial Strategy. *J. Mater. Chem. A* **2019**, *7* (24), 14504–14509. https://doi.org/10.1039/C9TA03578H.

(78) Yang, Y.; Dong, H.; Wang, Y.; Wang, Y.; Liu, N.; Wang, D.; Zhang, X. A Facile Synthesis for Porous CuO/Cu_2O Composites Derived from MOFs and Their Superior Catalytic Performance for CO Oxidation. *Inorganic Chemistry Communications* **2017**, *86*, 74–77. https://doi.org/10.1016/j.inoche.2017.09.027.

(79) Sun, L.; Yuan, Y.; Wang, F.; Zhao, Y.; Zhan, W.; Han, X. Selective Wet-Chemical Etching to Create TiO2@MOF Frame Heterostructure for Efficient Photocatalytic Hydrogen Evolution. *Nano Energy* **2020**, *74*, 104909. https://doi.org/10.1016/j.nanoen.2020.104909.

(80) Wu, L.-Y.; Mu, Y.-F.; Guo, X.-X.; Zhang, W.; Zhang, Z.-M.; Zhang, M.; Lu, T.-B. Encapsulating Perovskite Quantum Dots in Iron-Based Metal–Organic Frameworks (MOFs) for Efficient Photocatalytic CO_2 Reduction. *Angewandte Chemie International Edition* **2019**, *58* (28), 9491–9495. https://doi.org/10.1002/anie.201904537.

(81) Molina, M. A.; Díez-Jaén, J.; Sánchez-Sánchez, M.; Blanco, R. M. One-Pot Laccase@MOF Biocatalysts Efficiently Remove Bisphenol A from Water. *Catalysis Today* **2022**, *390–391*, 265–271. https://doi.org/10.1016/j.cattod.2021.10.005.

(82) Falcaro, P.; Ricco, R.; Yazdi, A.; Imaz, I.; Furukawa, S.; Maspoch, D.; Ameloot, R.; Evans, J. D.; Doonan, C. J. Application of Metal and Metal Oxide Nanoparticles@MOFs. *Coordination Chemistry Reviews* **2016**, *307*, 237–254. https://doi.org/10.1016/j.ccr.2015.08.002.

(83) Zhou, Y.-H.; Yang, Q.; Chen, Y.-Z.; Jiang, H.-L. Low-Cost CuNi@MIL-101 as an Excellent Catalyst toward Cascade Reaction: Integration of Ammonia Borane Dehydrogenation with Nitroarene Hydrogenation. *Chem. Commun.* **2017**, *53* (91), 12361–12364. https://doi.org/10.1039/C7CC06530B.

(84) Hermes, S.; Schröter, M.-K.; Schmid, R.; Khodeir, L.; Muhler, M.; Tissler, A.; Fischer, R. W.; Fischer, R. A. Metal@MOF: Loading of Highly Porous Coordination Polymers Host

Lattices by Metal Organic Chemical Vapor Deposition. *Angewandte Chemie International Edition* **2005**, *44* (38), 6237–6241. https://doi.org/10.1002/anie.200462515.

(85) Xiong, G.; Chen, X.-L.; You, L.-X.; Ren, B.-Y.; Ding, F.; Dragutan, I.; Dragutan, V.; Sun, Y.-G. La-Metal-Organic Framework Incorporating Fe_3O_4 Nanoparticles, Post-Synthetically Modified with Schiff Base and Pd. A Highly Active, Magnetically Recoverable, Recyclable Catalyst for CC Cross-Couplings at Low Pd Loadings. *Journal of Catalysis* **2018**, *361*, 116–125. https://doi.org/10.1016/j.jcat.2018.02.026.

(86) Zhu, Z.-H.; Liang, Z.-L.; Jiao, Z.-H.; Jiang, X.-L.; Xie, Y.; Xu, H.; Zhao, B. A Facile Strategy to Obtain Low-Cost and High-Performance Gold-Based Catalysts from Artificial Electronic Waste by $[Zr_{48}Ni_6]$ Nano-Cages in MOFs for CO_2 Electroreduction to CO. *Angewandte Chemie International Edition* **2022**, *61* (49), e202214243. https://doi.org/10.1002/anie.202214243.

(87) Wang, W.; Chen, S.; Cal, E. G.; Moro, M. M.; Moya, S.; Coy, E.; Wang, C.; Hamon, J.-R.; Astruc, D. ZIF-8-Based vs. ZIF-8-Derived Au and Pd Nanoparticles as Efficient Catalysts for the Ullmann Homocoupling Reaction. *Inorg. Chem. Front.* **2020**, *7* (20), 3945–3952. https://doi.org/10.1039/D0QI00831A.

(88) Ding, R.; Li, D.; Li, Y.; Yu, J.; Jia, M.; Xu, J. Bimetallic PdAu Nanoparticles in Amine-Containing Metal–Organic Framework UiO-66 for Catalytic Dehydrogenation of Formic Acid. *ACS Appl. Nano Mater.* **2021**, *4* (5), 4632–4641. https://doi.org/10.1021/acsanm.1c00266.

(89) Liang, W.; Wied, P.; Carraro, F.; Sumby, C. J.; Nidetzky, B.; Tsung, C.-K.; Falcaro, P.; Doonan, C. J. Metal–Organic Framework-Based Enzyme Biocomposites. *Chem. Rev.* **2021**, *121* (3), 1077–1129. https://doi.org/10.1021/acs.chemrev.0c01029.

(90) Qiu, Q.; Chen, H.; Wang, Y.; Ying, Y. Recent Advances in the Rational Synthesis and Sensing Applications of Metal-Organic Framework Biocomposites. *Coordination Chemistry Reviews* **2019**, *387*, 60–78. https://doi.org/10.1016/j.ccr.2019.02.009.

(91) Nadar, S. S.; Vaidya, L.; Rathod, V. K. Enzyme Embedded Metal Organic Framework (Enzyme–MOF): De Novo Approaches for Immobilization. *International Journal of Biological Macromolecules* **2020**, *149*, 861–876. https://doi.org/10.1016/j.ijbiomac.2020.01.240.

(92) Du, Y.; Jia, X.; Zhong, L.; Jiao, Y.; Zhang, Z.; Wang, Z.; Feng, Y.; Bilal, M.; Cui, J.; Jia, S. Metal-Organic Frameworks with Different Dimensionalities: An Ideal Host Platform for Enzyme@MOF Composites. *Coordination Chemistry Reviews* **2022**, *454*, 214327. https://doi.org/10.1016/j.ccr.2021.214327.

(93) Sheldon, R. A.; Pelt, S. van. Enzyme Immobilisation in Biocatalysis: Why, What and How. *Chem. Soc. Rev.* **2013**, *42* (15), 6223–6235. https://doi.org/10.1039/C3CS60075K.

(94) Koeller, K. M.; Wong, C.-H. Enzymes for Chemical Synthesis. *Nature* **2001**, *409* (6817), 232–240. https://doi.org/10.1038/35051706.

(95) Stepankova, V.; Bidmanova, S.; Koudelakova, T.; Prokop, Z.; Chaloupkova, R.; Damborsky, J. Strategies for Stabilization of Enzymes in Organic Solvents. *ACS Catal.* **2013**, *3* (12), 2823–2836. https://doi.org/10.1021/cs400684x.

(96) Bell, G.; Halling, P. J.; Moore, B. D.; Partridge, J.; Rees, D. G. Biocatalyst Behaviour in Low-Water Systems. *Trends in Biotechnology* **1995**, *13* (11), 468–473. https://doi.org/10.1016/S0167-7799(00)89004-6.

(97) Burton, S. G.; Cowan, D. A.; Woodley, J. M. The Search for the Ideal Biocatalyst. *Nat Biotechnol* **2002**, *20* (1), 37–45. https://doi.org/10.1038/nbt0102-37.

(98) Eş, I.; Vieira, J. D. G.; Amaral, A. C. Principles, Techniques, and Applications of Biocatalyst Immobilization for Industrial Application. *Appl Microbiol Biotechnol* **2015**, *99* (5), 2065–2082. https://doi.org/10.1007/s00253-015-6390-y.

(99) Libertino, S.; Aiello, V.; Scandurra, A.; Renis, M.; Sinatra, F. Immobilization of the Enzyme Glucose Oxidase on Both Bulk and Porous SiO_2 Surfaces. *Sensors* **2008**, *8* (9), 5637–5648. https://doi.org/10.3390/s8095637.

(100) Kim, H.; Kwon, J.-Y. Enzyme Immobilization on Metal Oxide Semiconductors Exploiting Amine Functionalized Layer. *RSC Adv.* **2017**, *7* (32), 19656–19661. https://doi.org/10.1039/C7RA01615H.

(101) Davis, S.; Burns, R. G. Covalent Immobilization of Laccase on Activated Carbon for Phenolic Effluent Treatment. *Appl Microbiol Biotechnol* **1992**, *37* (4), 474–479. https://doi.org/10.1007/BF00180972.

(102) Marzadori, C.; Miletti, S.; Gessa, C.; Ciurli, S. Immobilization of Jack Bean Urease on Hydroxyapatite: Urease Immobilization in Alkaline Soils. *Soil Biology and Biochemistry* **1998**, *30* (12), 1485–1490. https://doi.org/10.1016/S0038-0717(98)00051-0.

(103) Karakuş, E.; Pekyardımcı, Ş. Immobilization of Apricot Pectinesterase (Prunus Armeniaca L.) on Porous Glass Beads and Its Characterization. *Journal of Molecular Catalysis B: Enzymatic* **2009**, *56* (1), 13–19. https://doi.org/10.1016/j.molcatb.2008.04.003.

(104) Ribeiro, E. S.; de Farias, B. S.; Sant'Anna Cadaval Junior, T. R.; de Almeida Pinto, L. A.; Diaz, P. S. Chitosan–Based Nanofibers for Enzyme Immobilization. *International Journal of Biological Macromolecules* **2021**, *183*, 1959–1970. https://doi.org/10.1016/j.ijbiomac.2021.05.214.

(105) Sathishkumar, P.; Kamala-Kannan, S.; Cho, M.; Kim, J. S.; Hadibarata, T.; Salim, M. R.; Oh, B.-T. Laccase Immobilization on Cellulose Nanofiber: The Catalytic Efficiency and Recyclic Application for Simulated Dye Effluent Treatment. *Journal of Molecular Catalysis B: Enzymatic* **2014**, *100*, 111–120. https://doi.org/10.1016/j.molcatb.2013.12.008.

(106) Zhang, J.; Dai, Y.; Jiang, B.; Zhang, T.; Chen, J. Dual-Enzyme Co-Immobilization for the One-Pot Production of Glucose 6-Phosphate from Maltodextrin. *Biochemical Engineering Journal* **2020**, *161*, 107654. https://doi.org/10.1016/j.bej.2020.107654.

(107) Yang, Y. M.; Wang, J. W.; Tan, R. X. Immobilization of Glucose Oxidase on Chitosan–SiO2 Gel. *Enzyme and Microbial Technology* **2004**, *34* (2), 126–131. https://doi.org/10.1016/j.enzmictec.2003.09.007.

(108) Li, P.; Chen, Q.; Wang, T. C.; Vermeulen, N. A.; Mehdi, B. L.; Dohnalkova, A.; Browning, N. D.; Shen, D.; Anderson, R.; Gómez-Gualdrón, D. A.; Cetin, F. M.; Jagiello, J.; Asiri, A. M.; Stoddart, J. F.; Farha, O. K. Hierarchically Engineered Mesoporous Metal-

Organic Frameworks toward Cell-Free Immobilized Enzyme Systems. *Chem* **2018**, *4* (5), 1022–1034. https://doi.org/10.1016/j.chempr.2018.03.001.

(109) Pisklak, T. J.; Macías, M.; Coutinho, D. H.; Huang, R. S.; Balkus, K. J. Hybrid Materials for Immobilization of MP-11 Catalyst. *Top Catal* **2006**, *38* (4), 269–278. https://doi.org/10.1007/s11244-006-0025-6.

(110) Ren, Z.; Luo, J.; Wan, Y. Highly Permeable Biocatalytic Membrane Prepared by 3D Modification: Metal-Organic Frameworks Ameliorate Its Stability for Micropollutants Removal. *Chemical Engineering Journal* **2018**, *348*, 389–398. https://doi.org/10.1016/j.cej.2018.04.203.

(111) Ma, W.; Jiang, Q.; Yu, P.; Yang, L.; Mao, L. Zeolitic Imidazolate Framework-Based Electrochemical Biosensor for in Vivo Electrochemical Measurements. *Anal. Chem.* **2013**, *85* (15), 7550–7557. https://doi.org/10.1021/ac401576u.

(112) Liu, Q.; Chapman, J.; Huang, A.; Williams, K. C.; Wagner, A.; Garapati, N.; Sierros, K. A.; Dinu, C. Z. User-Tailored Metal–Organic Frameworks as Supports for Carbonic Anhydrase. *ACS Appl. Mater. Interfaces* **2018**, *10* (48), 41326–41337. https://doi.org/10.1021/acsami.8b14125.

(113) Yang, X.-G.; Zhang, J.-R.; Tian, X.-K.; Qin, J.-H.; Zhang, X.-Y.; Ma, L.-F. Enhanced Activity of Enzyme Immobilized on Hydrophobic ZIF-8 Modified by Ni^{2+} Ions. *Angewandte Chemie International Edition* **2023**, *62* (7), e202216699. https://doi.org/10.1002/anie.202216699.

(114) Hu, Y.; Dai, L.; Liu, D.; Du, W. Rationally Designing Hydrophobic UiO-66 Support for the Enhanced Enzymatic Performance of Immobilized Lipase. *Green Chem.* **2018**, *20* (19), 4500–4506. https://doi.org/10.1039/C8GC01284A.

(115) Zimpel, A.; Al Danaf, N.; Steinborn, B.; Kuhn, J.; Höhn, M.; Bauer, T.; Hirschle, P.; Schrimpf, W.; Engelke, H.; Wagner, E.; Barz, M.; Lamb, D. C.; Lächelt, U.; Wuttke, S. Coordinative Binding of Polymers to Metal–Organic Framework Nanoparticles for Control of Interactions at the Biointerface. *ACS Nano* **2019**, *13* (4), 3884–3895. https://doi.org/10.1021/acsnano.8b06287.

(116) Malhotra, A. Chapter 16 Tagging for Protein Expression. In *Methods in Enzymology*; Burgess, R. R., Deutscher, M. P., Eds.; Guide to Protein Purification, 2nd Edition; Academic Press, 2009; Vol. 463, pp 239–258. https://doi.org/10.1016/S0076-6879(09)63016-0.

(117) Niu, H.; Ding, M.; Sun, X.; Zhuang, W.; Liu, D.; Ying, H.; Zhu, C.; Chen, Y. Immobilization of a Polyphosphate Kinase 2 by Coordinative Self-Assembly of His-Tagged Units with Metal-Organic Frameworks and Its Application in ATP Regeneration from AMP. *Colloids and Surfaces B: Biointerfaces* **2019**, *181*, 261–269. https://doi.org/10.1016/j.colsurfb.2019.05.054.

(118) Jesionowski, T.; Zdarta, J.; Krajewska, B. Enzyme Immobilization by Adsorption: A Review. *Adsorption* **2014**, *20* (5), 801–821. https://doi.org/10.1007/s10450-014-9623-y.

(119) Jung, S.; Kim, Y.; Kim, S.-J.; Kwon, T.-H.; Huh, S.; Park, S. Bio-Functionalization of Metal–Organic Frameworks by Covalent Protein Conjugation. *Chem. Commun.* **2011**, *47* (10), 2904–2906. https://doi.org/10.1039/C0CC03288C.

(120) Mallin, H.; Höhne, M.; Bornscheuer, U. T. Immobilization of (R)- and (S)-Amine Transaminases on Chitosan Support and Their Application for Amine Synthesis Using Isopropylamine as Donor. *Journal of Biotechnology* **2014**, *191*, 32–37. https://doi.org/10.1016/j.jbiotec.2014.05.015.

(121) Pan, Y.; Li, H.; Farmakes, J.; Xiao, F.; Chen, B.; Ma, S.; Yang, Z. How Do Enzymes Orient When Trapped on Metal–Organic Framework (MOF) Surfaces? *J. Am. Chem. Soc.* **2018**, *140* (47), 16032–16036. https://doi.org/10.1021/jacs.8b09257.

(122) Gkaniatsou, E.; Sicard, C.; Ricoux, R.; Benahmed, L.; Bourdreux, F.; Zhang, Q.; Serre, C.; Mahy, J.-P.; Steunou, N. Enzyme Encapsulation in Mesoporous Metal–Organic Frameworks for Selective Biodegradation of Harmful Dye Molecules. *Angewandte Chemie International Edition* **2018**, *57* (49), 16141–16146. https://doi.org/10.1002/anie.201811327.

(123) Li, P.; Chen, Q.; Wang, T. C.; Vermeulen, N. A.; Mehdi, B. L.; Dohnalkova, A.; Browning, N. D.; Shen, D.; Anderson, R.; Gómez-Gualdrón, D. A.; Cetin, F. M.; Jagiello, J.; Asiri, A. M.; Stoddart, J. F.; Farha, O. K. Hierarchically Engineered Mesoporous Metal-Organic Frameworks toward Cell-Free Immobilized Enzyme Systems. *Chem* **2018**, *4* (5), 1022–1034. https://doi.org/10.1016/j.chempr.2018.03.001.

(124) Chen, Y.; Lykourinou, V.; Vetromile, C.; Hoang, T.; Ming, L.-J.; Larsen, R. W.; Ma, S. How Can Proteins Enter the Interior of a MOF? Investigation of Cytochrome c Translocation into a MOF Consisting of Mesoporous Cages with Microporous Windows. *J. Am. Chem. Soc.* **2012**, *134* (32), 13188–13191. https://doi.org/10.1021/ja305144x.

(125) Feng, D.; Liu, T.-F.; Su, J.; Bosch, M.; Wei, Z.; Wan, W.; Yuan, D.; Chen, Y.-P.; Wang, X.; Wang, K.; Lian, X.; Gu, Z.-Y.; Park, J.; Zou, X.; Zhou, H.-C. Stable Metal-Organic Frameworks Containing Single-Molecule Traps for Enzyme Encapsulation. *Nat Commun* **2015**, *6* (1), 5979. https://doi.org/10.1038/ncomms6979.

(126) Hsu, P.-H.; Chang, C.-C.; Wang, T.-H.; Lam, P. K.; Wei, M.-Y.; Chen, C.-T.; Chen, C.-Y.; Chou, L.-Y.; Shieh, F.-K. Rapid Fabrication of Biocomposites by Encapsulating Enzymes into Zn-MOF-74 via a Mild Water-Based Approach. *ACS Appl. Mater. Interfaces* **2021**, *13* (44), 52014–52022. https://doi.org/10.1021/acsami.1c09052.

(127) Maddigan, N. K.; Tarzia, A.; Huang, D. M.; Sumby, C. J.; Bell, S. G.; Falcaro, P.; Doonan, C. J. Protein Surface Functionalisation as a General Strategy for Facilitating Biomimetic Mineralisation of ZIF-8. *Chem. Sci.* **2018**, *9* (18), 4217–4223. https://doi.org/10.1039/C8SC00825F.

(128) Liang, K.; Ricco, R.; Doherty, C. M.; Styles, M. J.; Bell, S.; Kirby, N.; Mudie, S.; Haylock, D.; Hill, A. J.; Doonan, C. J.; Falcaro, P. Biomimetic Mineralization of Metal-Organic Frameworks as Protective Coatings for Biomacromolecules. *Nat Commun* **2015**, *6* (1), 7240. https://doi.org/10.1038/ncomms8240.

(129) Wang, L.; Zhi, W.; Wan, J.; Han, J.; Li, C.; Wang, Y. Recyclable β-Glucosidase by One-Pot Encapsulation with Cu-MOFs for Enhanced Hydrolysis of Cellulose to Glucose. *ACS Sustainable Chem. Eng.* **2019**, *7* (3), 3339–3348. https://doi.org/10.1021/acssuschemeng.8b05489.

(130) Lyu, F.; Zhang, Y.; Zare, R. N.; Ge, J.; Liu, Z. One-Pot Synthesis of Protein-Embedded Metal–Organic Frameworks with Enhanced Biological Activities. *Nano Lett.* **2014**, *14* (10), 5761–5765. https://doi.org/10.1021/nl5026419.

(131) Liao, F.-S.; Lo, W.-S.; Hsu, Y.-S.; Wu, C.-C.; Wang, S.-C.; Shieh, F.-K.; Morabito, J. V.; Chou, L.-Y.; Wu, K. C.-W.; Tsung, C.-K. Shielding against Unfolding by Embedding Enzymes in Metal–Organic Frameworks via a de Novo Approach. *J. Am. Chem. Soc.* **2017**, *139* (19), 6530–6533. https://doi.org/10.1021/jacs.7b01794.

(132) Liang, W.; Xu, H.; Carraro, F.; Maddigan, N. K.; Li, Q.; Bell, S. G.; Huang, D. M.; Tarzia, A.; Solomon, M. B.; Amenitsch, H.; Vaccari, L.; Sumby, C. J.; Falcaro, P.; Doonan, C. J. Enhanced Activity of Enzymes Encapsulated in Hydrophilic Metal–Organic Frameworks. *J. Am. Chem. Soc.* **2019**, *141* (6), 2348–2355. https://doi.org/10.1021/jacs.8b10302.

(133) Zou, Z.; Zhou, H.; Dai, L.; Liu, D.; Du, W. A Dual Stable MOF Constructed through Ligand Exchange for Enzyme Immobilization with Improved Performance in Biodiesel Production. *Renewable Energy* **2023**, *208*, 17–25. https://doi.org/10.1016/j.renene.2023.03.072.

(134) Silva, T. F. S.; Martins, L. M. D. R. S. Recent Advances in Copper Catalyzed Alcohol Oxidation in Homogeneous Medium. *Molecules* **2020**, *25* (3), 748. https://doi.org/10.3390/molecules25030748.

(135) Parmeggiani, C.; Cardona, F. Transition Metal Based Catalysts in the Aerobic Oxidation of Alcohols. *Green Chem.* **2012**, *14* (3), 547–564. https://doi.org/10.1039/C2GC16344F.

(136) Najafishirtari, S.; Friedel Ortega, K.; Douthwaite, M.; Pattisson, S.; Hutchings, G. J.; Bondue, C. J.; Tschulik, K.; Waffel, D.; Peng, B.; Deitermann, M.; Busser, G. W.; Muhler, M.; Behrens, M. A Perspective on Heterogeneous Catalysts for the Selective Oxidation of Alcohols. *Chemistry – A European Journal* **2021**, *27* (68), 16809–16833. https://doi.org/10.1002/chem.202102868.

(137) Brackman, W.; Gaasbeek, C. J. Studies in Homogeneous Catalysis.: Radicals of the Type as Catalysts for the Oxidation of Methanol by Cupric Complexes and as Promoters for Various Oxidations Catalysed by Copper. *Recueil des Travaux Chimiques des Pays-Bas* **1966**, *85* (3), 221–241. https://doi.org/10.1002/recl.19660850302.

(138) Hoover, J. M.; Stahl, S. S. Highly Practical Copper(I)/TEMPO Catalyst System for Chemoselective Aerobic Oxidation of Primary Alcohols. *J. Am. Chem. Soc.* **2011**, *133* (42), 16901–16910. https://doi.org/10.1021/ja206230h.

(139) Könning, D.; Hiller, W.; Christmann, M. One-Pot Oxidation/Isomerization of Z-Allylic Alcohols with Oxygen as Stoichiometric Oxidant. *Org. Lett.* **2012**, *14* (20), 5258–5261. https://doi.org/10.1021/ol302420k.

(140) Chaudhuri, P.; Hess, M.; Flörke, U.; Wieghardt, K. From Structural Models of Galactose Oxidase to Homogeneous Catalysis: Efficient Aerobic Oxidation of Alcohols. *Angewandte Chemie International Edition* **1998**, *37* (16), 2217–2220. https://doi.org/10.1002/(SICI)1521-3773(19980904)37:16<2217::AID-ANIE2217>3.0.CO;2-D.

(141) Jazdzewski, B. A.; Tolman, W. B. Understanding the Copper–Phenoxyl Radical Array in Galactose Oxidase: Contributions from Synthetic Modeling Studies. *Coordination Chemistry Reviews* **2000**, *200–202*, 633–685. https://doi.org/10.1016/S0010-8545(00)00342-8.

(142) Hoover, J. M.; Ryland, B. L.; Stahl, S. S. Mechanism of Copper(I)/TEMPO-Catalyzed Aerobic Alcohol Oxidation. *J. Am. Chem. Soc.* **2013**, *135* (6), 2357–2367. https://doi.org/10.1021/ja3117203.

(143) Adomeit, S.; Rabeah, J.; Surkus, A. E.; Bentrup, U.; Brückner, A. Effects of Imidazole-Type Ligands in CuI/TEMPO-Mediated Aerobic Alcohol Oxidation. *Inorg. Chem.* **2017**, *56* (1), 684–691. https://doi.org/10.1021/acs.inorgchem.6b02925.

(144) Marais, L.; Swarts, A. J. Biomimetic Cu/Nitroxyl Catalyst Systems for Selective Alcohol Oxidation. *Catalysts* **2019**, *9* (5), 395. https://doi.org/10.3390/catal9050395.

(145) Dhakshinamoorthy, A.; Alvaro, M.; Garcia, H. Aerobic Oxidation of Benzylic Alcohols Catalyzed by Metal−Organic Frameworks Assisted by TEMPO. *ACS Catal.* **2011**, *1* (1), 48–53. https://doi.org/10.1021/cs1000703.

(146) Peng, M. M.; Jeon, U. J.; Ganesh, M.; Aziz, A.; Vinodh, R.; Palanichamy, M.; Jang, H. T. Oxidation of Ethylbenzene Using Nickel Oxide Supported Metal Organic Framework Catalyst. *Bulletin of the Korean Chemical Society* **2014**, *35* (11), 3213–3218. https://doi.org/10.5012/bkcs.2014.35.11.3213.

(147) Qi, Y.; Luan, Y.; Yu, J.; Peng, X.; Wang, G. Nanoscaled Copper Metal–Organic Framework (MOF) Based on Carboxylate Ligands as an Efficient Heterogeneous Catalyst for Aerobic Epoxidation of Olefins and Oxidation of Benzylic and Allylic Alcohols. *Chemistry – A European Journal* **2015**, *21* (4), 1589–1597. https://doi.org/10.1002/chem.201405685.

(148) Asgharnejad, L.; Abbasi, A.; Najafi, M.; Janczak, J. One-, Two- and Three-Dimensional Coordination Polymers Based on Copper Paddle-Wheel SBUs as Selective Catalysts for Benzyl Alcohol Oxidation. *Journal of Solid State Chemistry* **2019**, *277*, 187–194. https://doi.org/10.1016/j.jssc.2019.06.011.

(149) Zwoliński, K. M.; Chmielewski, M. J. TEMPO-Appended Metal–Organic Frameworks as Highly Active, Selective, and Reusable Catalysts for Mild Aerobic Oxidation of Alcohols. *ACS Appl. Mater. Interfaces* **2017**, *9* (39), 33956–33967. https://doi.org/10.1021/acsami.7b09914.

(150) Ghasempour, H.; ZareKarizi, F.; Morsali, A.; Yan, X.-W. Development of a Highly Porous Fe-Based MOF Using Symmetrically Incompatible Building Blocks: Selective Oxidation of Benzyl Alcohols. *Applied Materials Today* **2021**, *24*, 101157. https://doi.org/10.1016/j.apmt.2021.101157.

(151) Peng, L.; Wu, S.; Yang, X.; Hu, J.; Fu, X.; Li, M.; Bai, L.; Huo, Q.; Guan, J. Oxidation of Benzyl Alcohol over Metal Organic Frameworks M-BTC (M = Co, Cu, Fe). *New J. Chem.* **2017**, *41* (8), 2891–2894. https://doi.org/10.1039/C7NJ00588A.

(152) Wu, X.; Guo, S.; Zhang, J. Selective Oxidation of Veratryl Alcohol with Composites of Au Nanoparticles and Graphene Quantum Dots as Catalysts. *Chem. Commun.* **2015**, *51* (29), 6318–6321. https://doi.org/10.1039/C5CC00061K.

(153) Yu, X.; Huo, Y.; Yang, J.; Chang, S.; Ma, Y.; Huang, W. Reduced Graphene Oxide Supported Au Nanoparticles as an Efficient Catalyst for Aerobic Oxidation of Benzyl Alcohol. *Applied Surface Science* **2013**, *280*, 450–455. https://doi.org/10.1016/j.apsusc.2013.05.008.

(154) Wang, T.; Shou, H.; Kou, Y.; Liu, H. Base-Free Aqueous-Phase Oxidation of Non-Activated Alcohols with Molecular Oxygen on Soluble Pt Nanoparticles. *Green Chemistry* **2009**, *11* (4), 562–568. https://doi.org/10.1039/B818560C.

(155) Harada, T.; Ikeda, S.; Hashimoto, F.; Sakata, T.; Ikeue, K.; Torimoto, T.; Matsumura, M. Catalytic Activity and Regeneration Property of a Pd Nanoparticle Encapsulated in a Hollow Porous Carbon Sphere for Aerobic Alcohol Oxidation. *Langmuir* **2010**, *26* (22), 17720–17725. https://doi.org/10.1021/la102824s.

(156) Zhao, J.; Hernández, W. Y.; Zhou, W.; Yang, Y.; Vovk, E. I.; Capron, M.; Ordomsky, V. Selective Oxidation of Alcohols to Carbonyl Compounds over Small Size Colloidal Ru Nanoparticles. *ChemCatChem* **2020**, *12* (1), 238–247. https://doi.org/10.1002/cctc.201901249.

(157) Gates, J. A.; Kesmodel, L. L. Methanol Adsorption and Decomposition on Clean and Oxygen Precovered Palladium (111). *Journal of Catalysis* **1983**, *83* (2), 437–445. https://doi.org/10.1016/0021-9517(83)90068-4.

(158) Jorgensen, S. W.; Madix, R. J. Hydrogen Transfer Pathways in the Oxidation of Methanol on Pd(100). *Surface Science* **1987**, *183* (1), 27–43. https://doi.org/10.1016/S0039-6028(87)80334-5.

(159) Besson, M.; Gallezot, P. Selective Oxidation of Alcohols and Aldehydes on Metal Catalysts. *Catalysis Today* **2000**, *57* (1), 127–141. https://doi.org/10.1016/S0920-5861(99)00315-6.

(160) Wang, D.; Villa, A.; Spontoni, P.; Su, D. S.; Prati, L. In Situ Formation of Au–Pd Bimetallic Active Sites Promoting the Physically Mixed Monometallic Catalysts in the Liquid-Phase Oxidation of Alcohols. *Chemistry – A European Journal* **2010**, *16* (33), 10007–10013. https://doi.org/10.1002/chem.201001330.

(161) Balcha, T.; Strobl, J. R.; Fowler, C.; Dash, P.; Scott, R. W. J. Selective Aerobic Oxidation of Crotyl Alcohol Using AuPd Core-Shell Nanoparticles. *ACS Catal.* **2011**, *1* (5), 425–436. https://doi.org/10.1021/cs200040a.

(162) Savara, A.; Chan-Thaw, C. E.; Rossetti, I.; Villa, A.; Prati, L. Benzyl Alcohol Oxidation on Carbon-Supported Pd Nanoparticles: Elucidating the Reaction Mechanism. *ChemCatChem* **2014**, *6* (12), 3464–3473. https://doi.org/10.1002/cctc.201402552.

(163) Sankar, M.; Nowicka, E.; Tiruvalam, R.; He, Q.; Taylor, S. H.; Kiely, C. J.; Bethell, D.; Knight, D. W.; Hutchings, G. J. Controlling the Duality of the Mechanism in Liquid-Phase Oxidation of Benzyl Alcohol Catalysed by Supported Au–Pd Nanoparticles. *Chemistry – A European Journal* **2011**, *17* (23), 6524–6532. https://doi.org/10.1002/chem.201003484.

(164) Yang, J.; Cao, K.; Gong, M.; Shan, B.; Chen, R. Atomically Decorating of MnOx on Palladium Nanoparticles towards Selective Oxidation of Benzyl Alcohol with High Yield. *Journal of Catalysis* **2020**, *386*, 60–69. https://doi.org/10.1016/j.jcat.2020.03.029.

(165) Chen, G.; Wu, S.; Liu, H.; Jiang, H.; Li, Y. Palladium Supported on an Acidic Metal–Organic Framework as an Efficient Catalyst in Selective Aerobic Oxidation of Alcohols. *Green Chem.* **2012**, *15* (1), 230–235. https://doi.org/10.1039/C2GC36618E.

(166) Chen, L.; Chen, H.; Luque, R.; Li, Y. Metal−organic Framework Encapsulated Pd Nanoparticles: Towards Advanced Heterogeneous Catalysts. *Chem. Sci.* **2014**, *5* (10), 3708–3714. https://doi.org/10.1039/C4SC01847H.

(167) Taher, A.; Susan, Md. A. B. H.; Begum, N.; Lee, I.-M. Amine-Functionalized Metal–Organic Framework-Based Pd Nanoparticles: Highly Efficient Multifunctional Catalysts for Base-Free Aerobic Oxidation of Different Alcohols. *New J. Chem.* **2020**, *44* (44), 19113–19121. https://doi.org/10.1039/D0NJ04138F.

(168) Nilekar, A. U.; Alayoglu, S.; Eichhorn, B.; Mavrikakis, M. Preferential CO Oxidation in Hydrogen: Reactivity of Core−Shell Nanoparticles. *J. Am. Chem. Soc.* **2010**, *132* (21), 7418–7428. https://doi.org/10.1021/ja101108w.

(169) Afanasyev, O. I.; Kuchuk, E.; Usanov, D. L.; Chusov, D. Reductive Amination in the Synthesis of Pharmaceuticals. *Chem. Rev.* **2019**, *119* (23), 11857–11911. https://doi.org/10.1021/acs.chemrev.9b00383.

(170) Liu, J.; Song, Y.; Ma, L. Earth-Abundant Metal-Catalyzed Reductive Amination: Recent Advances and Prospect for Future Catalysis. *Chemistry – An Asian Journal* **2021**, *16* (17), 2371–2391. https://doi.org/10.1002/asia.202100473.

(171) Sharma, M.; Mangas-Sanchez, J.; Turner, N. J.; Grogan, G. NAD(P)H-Dependent Dehydrogenases for the Asymmetric Reductive Amination of Ketones: Structure, Mechanism, Evolution and Application. *Advanced Synthesis and Catalysis* **2017**, *359* (12), 2011–2025. https://doi.org/10.1002/adsc.201700356.

(172) Hummel, W.; Schütte, H.; Schmidt, E.; Wandrey, C.; Kula, M. R. Isolation of L-Phenylalanine Dehydrogenase from Rhodococcus Sp. M4 and Its Application for the Production of l-Phenylalanine. *Applied Microbiology and Biotechnology* **1987**, *26* (5), 409–416. https://doi.org/10.1007/BF00253523.

(173) Steffen-Munsberg, F.; Vickers, C.; Kohls, H.; Land, H.; Mallin, H.; Nobili, A.; Skalden, L.; van den Bergh, T.; Joosten, H.-J.; Berglund, P.; Höhne, M.; Bornscheuer, U. T. Bioinformatic Analysis of a PLP-Dependent Enzyme Superfamily Suitable for Biocatalytic Applications. *Biotechnology Advances* **2015**, *33* (5), 566–604. https://doi.org/10.1016/j.biotechadv.2014.12.012.

(174) Hwang, B. Y.; Cho, B. K.; Yun, H.; Koteshwar, K.; Kim, B. G. Revisit of Aminotransferase in the Genomic Era and Its Application to Biocatalysis. *Journal of Molecular Catalysis B: Enzymatic* **2005**, *37* (1–6), 47–55. https://doi.org/10.1016/j.molcatb.2005.09.004.

(175) Guo, F.; Berglund, P. Transaminase Biocatalysis: Optimization and Application. *Green Chemistry* **2017**, *19* (2), 333–360. https://doi.org/10.1039/c6gc02328b.

(176) Galman, J. L.; Slabu, I.; Weise, N. J.; Iglesias, C.; Parmeggiani, F.; Lloyd, R. C.; Turner, N. J. Biocatalytic Transamination with Near-Stoichiometric Inexpensive Amine Donors Mediated by Bifunctional Mono- and Di-Amine Transaminases. *Green Chemistry* **2017**, *19* (2), 361–366. https://doi.org/10.1039/c6gc02102f.

(177) Savile, C. K.; Janey, J. M.; Mundorff, E. C.; Moore, J. C.; Tam, S.; Jarvis, W. R.; Colbeck, J. C.; Krebber, A.; Fleitz, F. J.; Brands, J.; Devine, P. N.; Huisman, G. W.; Hughes, G. J. Biocatalytic Asymmetric Synthesis of Chiral Amines from Ketones Applied to Sitagliptin Manufacture. *Science* **2010**, *329* (5989), 305–309. https://doi.org/10.1126/science.1188934.

(178) Gomm, A.; O'Reilly, E. Transaminases for Chiral Amine Synthesis. *Current Opinion in Chemical Biology* **2018**, *43* (Figure 1), 106–112. https://doi.org/10.1016/j.cbpa.2017.12.007.

(179) Clausen, A. M.; Dziadul, B.; Cappuccio, K. L.; Kaba, M.; Starbuck, C.; Hsiao, Y.; Dowling, T. M. Identification of Ammonium Chloride as an Effective Promoter of the Asymmetric Hydrogenation of a β-Enamine Amide. *Org. Process Res. Dev.* **2006**, *10* (4), 723–726. https://doi.org/10.1021/op050232o.

(180) Shin, J.-S.; Kim, B.-G. Kinetic Modeling of ω-Transamination for Enzymatic Kinetic Resolution of α-Methylbenzylamine. *Biotechnology and Bioengineering* **1998**, *60* (5), 534–540. https://doi.org/10.1002/(SICI)1097-0290(19981205)60:5<534:AID-BIT3>3.0.CO;2-L.

(181) Dawood, A. W. H.; Weiß, M. S.; Schulz, C.; Pavlidis, I. V.; Iding, H.; de Souza, R. O. M. A.; Bornscheuer, U. T. Isopropylamine as Amine Donor in Transaminase-Catalyzed Reactions: Better Acceptance through Reaction and Enzyme Engineering. *ChemCatChem* **2018**, *10* (18), 3943–3949. https://doi.org/10.1002/cctc.201800936.

(182) Bea, H.-S.; Lee, S.-H.; Yun, H. Asymmetric Synthesis of (R)-3-Fluoroalanine from 3-Fluoropyruvate Using Omega-Transaminase. *Biotechnol Bioproc E* **2011**, *16* (2), 291–296. https://doi.org/10.1007/s12257-010-0282-x.

(183) Rehn, G.; Adlercreutz, P.; Grey, C. Supported Liquid Membrane as a Novel Tool for Driving the Equilibrium of ω-Transaminase Catalyzed Asymmetric Synthesis. *Journal of Biotechnology* **2014**, *179*, 50–55. https://doi.org/10.1016/j.jbiotec.2014.03.022.

(184) Payer, S. E.; Schrittwieser, J. H.; Kroutil, W. Vicinal Diamines as Smart Cosubstrates in the Transaminase-Catalyzed Asymmetric Amination of Ketones. *European Journal of Organic Chemistry* **2017**, *2017* (17), 2553–2559. https://doi.org/10.1002/ejoc.201700253.

(185) Koszelewski, D.; Lavandera, I.; Clay, D.; Rozzell, D.; Kroutil, W. Asymmetric Synthesis of Optically Pure Pharmacologically Relevant Amines Employing ω-Transaminases. *Advanced Synthesis & Catalysis* **2008**, *350* (17), 2761–2766. https://doi.org/10.1002/adsc.200800496.

(186) Wang, B.; Land, H.; Berglund, P. An Efficient Single-Enzymatic Cascade for Asymmetric Synthesis of Chiral Amines Catalyzed by ω-Transaminase. *Chem. Commun.* **2012**, *49* (2), 161–163. https://doi.org/10.1039/C2CC37232K.

(187) Green, A. P.; Turner, N. J.; O'Reilly, E. Chiral Amine Synthesis Using ω-Transaminases: An Amine Donor That Displaces Equilibria and Enables High-Throughput Screening. *Angewandte Chemie International Edition* **2014**, *53* (40), 10714–10717. https://doi.org/10.1002/anie.201406571.

(188) Martínez-Montero, L.; Gotor, V.; Gotor-Fernández, V.; Lavandera, I. But-2-Ene-1,4-Diamine and But-2-Ene-1,4-Diol as Donors for Thermodynamically Favored

Transaminase- and Alcohol Dehydrogenase-Catalyzed Processes. *Advanced Synthesis & Catalysis* **2016**, *358* (10), 1618–1624. https://doi.org/10.1002/adsc.201501066.

(189) Richter, N.; Farnberger, J. E.; Pressnitz, D.; Lechner, H.; Zepeck, F.; Kroutil, W. A System for ω-Transaminase Mediated (R)-Amination Using L-Alanine as an Amine Donor. *Green Chem.* **2015**, *17* (5), 2952–2958. https://doi.org/10.1039/C4GC02363C.

(190) Höhne, M.; Kühl, S.; Robins, K.; Bornscheuer, U. T. Efficient Asymmetric Synthesis of Chiral Amines by Combining Transaminase and Pyruvate Decarboxylase. *ChemBioChem* **2008**, *9* (3), 363–365. https://doi.org/10.1002/cbic.200700601.

(191) Truppo, M. D.; Rozzell, J. D.; Moore, J. C.; Turner, N. J. Rapid Screening and Scale-up of Transaminase Catalysed Reactions. *Org. Biomol. Chem.* **2008**, *7* (2), 395–398. https://doi.org/10.1039/B817730A.

(192) Mallin, H.; Menyes, U.; Vorhaben, T.; Höhne, M.; Bornscheuer, U. T. Immobilization of Two (R)-Amine Transaminases on an Optimized Chitosan Support for the Enzymatic Synthesis of Optically Pure Amines. *ChemCatChem* **2013**, *5* (2), 588–593. https://doi.org/10.1002/cctc.201200420.

(193) Velasco-Lozano, S.; Benítez-Mateos, A. I.; López-Gallego, F. Co-Immobilized Phosphorylated Cofactors and Enzymes as Self-Sufficient Heterogeneous Biocatalysts for Chemical Processes. *Angewandte Chemie International Edition* **2017**, *56* (3), 771–775. https://doi.org/10.1002/anie.201609758.

(194) Velasco-Lozano, S.; Santiago-Arcos, J.; Mayoral, J. A.; López-Gallego, F. Co-Immobilization and Colocalization of Multi-Enzyme Systems for the Cell-Free Biosynthesis of Aminoalcohols. *ChemCatChem* **2020**, *12* (11), 3030–3041. https://doi.org/10.1002/cctc.201902404.

(195) Zhang, X.-J.; Fan, H.-H.; Liu, N.; Wang, X.-X.; Cheng, F.; Liu, Z.-Q.; Zheng, Y.-G. A Novel Self-Sufficient Biocatalyst Based on Transaminase and Pyridoxal 5′-Phosphate Covalent Co-Immobilization and Its Application in Continuous Biosynthesis of Sitagliptin. *Enzyme and Microbial Technology* **2019**, *130*, 109362. https://doi.org/10.1016/j.enzmictec.2019.109362.

(196) Planchestainer, M.; Contente, M. L.; Cassidy, J.; Molinari, F.; Tamborini, L.; Paradisi, F. Continuous Flow Biocatalysis: Production and in-Line Purification of Amines by Immobilised Transaminase from Halomonas Elongata. *Green Chem.* **2017**, *19* (2), 372–375. https://doi.org/10.1039/C6GC01780K.

(197) Feng, Y.; Wang, Z.; Luo, Z.; Chen, M.; He, F.; Liu, B.; Goldmann, S.; Zhang, L. Further Optimization of a Scalable Biocatalytic Route to (3R)-N-Boc-3-Aminoazepane with Immobilized ω-Transaminase. *Org. Process Res. Dev.* **2019**, *23* (3), 355–360. https://doi.org/10.1021/acs.oprd.8b00411.

(198) Yu, J.; Zong, W.; Ding, Y.; Liu, J.; Chen, L.; Zhang, H.; Jiao, Q. Fabrication of ω-Transaminase@Metal-Organic Framework Biocomposites for Efficiently Synthesizing Benzylamines and Pyridylmethylamines. *Advanced Synthesis & Catalysis* **2022**, *364* (2), 380–390. https://doi.org/10.1002/adsc.202100997.

(199) Rudroff, F.; Mihovilovic, M. D.; Gröger, H.; Snajdrova, R.; Iding, H.; Bornscheuer, U. T. Opportunities and Challenges for Combining Chemo- and Biocatalysis. *Nat Catal* **2018**, *1* (1), 12–22. https://doi.org/10.1038/s41929-017-0010-4.

(200) Cai, T.; Sun, H.; Qiao, J.; Zhu, L.; Zhang, F.; Zhang, J.; Tang, Z.; Wei, X.; Yang, J.; Yuan, Q.; Wang, W.; Yang, X.; Chu, H.; Wang, Q.; You, C.; Ma, H.; Sun, Y.; Li, Y.; Li, C.; Jiang, H.; Wang, Q.; Ma, Y. Cell-Free Chemoenzymatic Starch Synthesis from Carbon Dioxide. *Science* **2021**, *373* (6562), 1523–1527. https://doi.org/10.1126/science.abh4049.

(201) Świętochowska, D.; Łochowicz, A.; Ocal, N.; Pollegioni, L.; Charmantray, F.; Hecquet, L.; Szymańska, K. Co-Immobilization of D-Amino Acid Oxidase, Catalase, and Transketolase for One-Pot, Two-Step Synthesis of L-Erythrulose. *Catalysts* **2023**, *13* (1), 95. https://doi.org/10.3390/catal13010095.

(202) Kourist, R.; González-Sabín, J. Non-Conventional Media as Strategy to Overcome the Solvent Dilemma in Chemoenzymatic Tandem Catalysis. *ChemCatChem* **2020**, *12* (7), 1903–1912. https://doi.org/10.1002/cctc.201902192.

(203) Heuson, E.; Froidevaux, R.; Itabaiana, I.; Wojcieszak, R.; Capron, M.; Dumeignil, F. Optimisation of Catalysts Coupling in Multi-Catalytic Hybrid Materials: Perspectives for the next Revolution in Catalysis. *Green Chem.* **2021**, *23* (5), 1942–1954. https://doi.org/10.1039/D0GC04172F.

(204) Zhou, Y.; Wu, S.; Bornscheuer, U. T. Recent Advances in (Chemo)Enzymatic Cascades for Upgrading Bio-Based Resources. *Chem. Commun.* **2021**, *57* (82), 10661–10674. https://doi.org/10.1039/D1CC04243B.

(205) Júnior, A. A. da T.; Ladeira, Y. F. X.; França, A. da S.; Souza, R. O. M. A. de; Moraes, A. H.; Wojcieszak, R.; Itabaiana, I.; Miranda, A. S. de. Multicatalytic Hybrid Materials for Biocatalytic and Chemoenzymatic Cascades—Strategies for Multicatalyst (Enzyme) Co-Immobilization. *Catalysts* **2021**, *11* (8), 936. https://doi.org/10.3390/catal11080936.

(206) Anderson, M. Amine Transaminases in Multi-Step One-Pot Reactions. Doctoral Thesis, KTH Royal Institute of Technology, 2017.

(207) Slabu, I. Transaminase Mediated Cascade Reactions. Doctoral Thesis, University of Manchester, 2018. https://research.manchester.ac.uk/en/studentTheses/transaminase-mediated-cascade-reactions.

(208) Lorillière, M.; Sousa, M. D.; Bruna, F.; Heuson, E.; Gefflaut, T.; Berardinis, V. de; Saravanan, T.; Yi, D.; Fessner, W.-D.; Charmantray, F.; Hecquet, L. One-Pot, Two-Step Cascade Synthesis of Naturally Rare L-Erythro (3S,4S) Ketoses by Coupling a Thermostable Transaminase and Transketolase. *Green Chem.* **2017**, *19* (2), 425–435. https://doi.org/10.1039/C6GC02015A.

(209) Fuchs, M.; Tauber, K.; Sattler, J.; Lechner, H.; Pfeffer, J.; Kroutil, W.; Faber, K. Amination of Benzylic and Cinnamic Alcohols via a Biocatalytic, Aerobic, Oxidation–Transamination Cascade. *RSC Adv.* **2012**, *2* (15), 6262–6265. https://doi.org/10.1039/C2RA20800H.

(210) Martínez-Montero, L.; Gotor, V.; Gotor-Fernández, V.; Lavandera, I. Stereoselective Amination of Racemic Sec-Alcohols through Sequential Application of Laccases and

Transaminases. *Green Chem.* **2017**, *19* (2), 474–480. https://doi.org/10.1039/C6GC01981A.

(211) Tauber, K.; Fuchs, M.; Sattler, J. H.; Pitzer, J.; Pressnitz, D.; Koszelewski, D.; Faber, K.; Pfeffer, J.; Haas, T.; Kroutil, W. Artificial Multi-Enzyme Networks for the Asymmetric Amination of Sec-Alcohols. *Chemistry – A European Journal* **2013**, *19* (12), 4030–4035. https://doi.org/10.1002/chem.201202666.

(212) Sattler, J. H.; Fuchs, M.; Tauber, K.; Mutti, F. G.; Faber, K.; Pfeffer, J.; Haas, T.; Kroutil, W. Redox Self-Sufficient Biocatalyst Network for the Amination of Primary Alcohols. *Angewandte Chemie International Edition* **2012**, *51* (36), 9156–9159. https://doi.org/10.1002/anie.201204683.

(213) Tian, K.; Li, Z. A Simple Biosystem for the High-Yielding Cascade Conversion of Racemic Alcohols to Enantiopure Amines. *Angewandte Chemie International Edition* **2020**, *59* (48), 21745–21751. https://doi.org/10.1002/anie.202009733.

(214) Liardo, E.; Ríos-Lombardía, N.; Morís, F.; Rebolledo, F.; González-Sabín, J. Hybrid Organo- and Biocatalytic Process for the Asymmetric Transformation of Alcohols into Amines in Aqueous Medium. *ACS Catal.* **2017**, *7* (7), 4768–4774. https://doi.org/10.1021/acscatal.7b01543.

(215) Gairola, P. Association of Metal-Organic Framework and Transaminase for Chemoenzymatic Production of Amines. These de doctorat, Sorbonne université, 2019. https://www.theses.fr/2019SORUS107)

Chapter 2.

Materials and characterization methods

This chapter describes and gives the specifications of the chemicals and instruments used in this thesis. The different characterization techniques employed are briefly introduced and the protocols followed to apply them are described.

2.1. Materials

Table 2.1. Materials

Chemicals	Chemical formula	Specification	Supplier
(±)-1-phenylethanol	$C_8H_{10}O$	97%	Sigma-Aldrich
(S)-(-)-1-phenylethanamine	$C_8H_{11}N$	98%	Thermo scientific
1,2-diaminopropane	$C_3H_{10}N_2$	99%	Sigma-Aldrich
2,2,6,6-tetramethylpiperidinyl-1-oxy	$C_9H_{18}NO$	98%	Sigma-Aldrich
2-Imidazolecarboxaldehyde	$C_4H_4N_2O$	97%	Sigma-Aldrich
2-methylimidazole	$C_4H_6N_2$	99%	Sigma-Aldrich
3-amino-1,2,4-triazole	$C_2H_4N_4$	≥95%	Sigma-Aldrich
4-dimethylaminopyridine	$C_7H_{10}N_2$	≥99%	Sigma-Aldrich
acetonitrile	C_2H_3N	99.8+%	Alfa Aesar
acetophenone	C_8H_8O	99%	Sigma-Aldrich
benzaldehyde	C_7H_6O	99+%	Alfa Aesar
benzoic acid	$C_7H_6O_2$	99.50%	Sigma-Aldrich
benzyl alcohol	C_7H_8O	≥99%	Sigma-Aldrich
caffeine	$C_8H_{10}N_4O_2$	99%	Sigma-Aldrich
calcium nitrate tetrahydrate	$Ca(NO_3)_2{\cdot}4H_2O$	≥99%	Sigma-Aldrich
copper (II) chloride dihydrate	$CuCl_2{\cdot}2H_2O$	≥99%	Sigma-Aldrich
D-glucose	$C_6H_{12}O_6$	≥99.8%	Calbiochem
dimethyl sulfoxide	C_2H_6OS	Analytical grade	VWR
ethanol	C_2H_5O	99.98%	VWR
glucose dehydrogenase from *Pseudomonas sp.*	-	≥200 U/mg	Sigma-Aldrich

hydrogen chloride	HCl	37%	Carlo Erba
hydrogen tetrachloroaurate(III) trihydrate	$HAuCl_4 \cdot 3H_2O$	99%	Alfa Aesar
iron(III) nitrate nonahydrate	Fe(NO3)3·9H2O	≥98%	Sigma-Aldrich
isopropylamine	C_3H_9N	99.50%	Sigma-Aldrich
lactic dehydrogenase, recombinant from *E. coli*	-	≥90 U/mg	Sigma-Aldrich
L-alanine	$C_3H_7NO_2$	≥98.5%	Sigma-Aldrich
methanol	CH_4O	Analytical grade	VWR
nickel(II) nitrate hexahydrate	$Ni(NO_3)_2 \cdot 6H_2O$	94.5-105.5%	Sigma-Aldrich
nitric acid	HNO_3	70%	Sigma-Aldrich
oxygen	O_2		Air liquid
potassium carbonate	K_2CO_3	99%	Merck
potassium dihydrogen phosphate	KH_2PO_4	100%	Merck
potassium hydrogen phosphate	K_2HPO_4	99%	Merck
pyridoxal 5'-phosphate hydrate	$C_8H_{12}NO_7P$	≥98%	Sigma-Aldrich
sodium bicarbonate	$NaHCO_3$	99.7-100.3%	Sigma-Aldrich
sodium borohydride	$NaBH_4$	98%	Sigma-Aldrich
sodium carbonate	Na_2CO_3	99%	Sigma-Aldrich
sodium formate	HCOONa	97%	Thermo scientific
sodium pyruvate	$C_3H_3NaO_3$	99%	Alfa Aesar
sodium tetrachloropalladate(II)	Na_2PdCl_4	36% Pd	Thermo scientific
trifluoroacetic acid	$C_2HF_3O_2$	99%	Alfa Aesar
trisamine	$C_4H_{11}NO_3$		Sigma-Aldrich
zinc(II) nitrate hexahydate	$Zn(NO_3)_2 \cdot 6H_2O$	≥99%	Sigma-Aldrich
β-nicotinamide adenine dinucleotide, reduced disodium salt hydrate	$C_{21}H_{27}N_7Na_2O_{14}P_2 \cdot xH_2O$	≥97% (HPLC)	Sigma-Aldrich

2.2. Characterization techniques and protocols

Powder X-ray diffraction (PXRD)

To obtain crystallographic information on ZIF-8 and its derivatives, Powder X-ray diffraction (PXRD) was performed using a Bruker D8 Advance diffractor (Cu Kα =1.5406 Å).
The average crystal size of Cu nanoparticles in Cu/ZIF-8($NaBH_4$) and Cu/ZIF-8(H_2) was calculated using Scherrer's equation using the half peak width of the strongest diffraction peak:

$$D = \frac{K\lambda}{B\cos\theta}$$

where D is the particle size of the nanoparticles, λ is the wavelength of the incident X-rays, θ is the Bragg reflection angle of the selected diffraction peak, B is the radian corresponding to the half-height width of the diffraction peak and k is the Scherrer's constant with respect to the shape of the crystal, which is taken as 0.89 in the case of spherical particles.

N_2 physisorption analysis

To obtain information on the texture and pore properties of ZIF-8 and its derivatives, the N_2 physisorption analyses were performed using a Belsorp MAX instrument at the liquid N_2 temperature (77 K). The samples were pretreated in vacuum at 100 °C for 18 hours, and the surface parameters were calculated by Brunauer, Emmett et Teller (BET) method.

Transmission electron microscope (TEM)

To analyze the morphologies and the size distributions of the nanoparticles of the Cu/ZIF-8, Pd@ZIF-8, Au@ZIF-8 and PdAu@ZIF-8 catalysts, conventional transmission electron microscope (TEM) images of the samples above were obtained using a JEOL 1011 operating at 100 kV. To prepare the samples, 1 mg of sample was dispersed in 1 mL of ethanol. One drop

of sample suspension was dropped on a carbon film supported on a copper mesh. When the sample contains copper, the carbon film of Ni mesh is employed instead.

High-resolution transmission electron microscopy (HRTEM)

To analyze the morphology of the Cu/ZIF-8, PdAu@ZIF-8 catalysts and elemental distribution in PdAu@ZIF-8 catalysts, high-resolution transmission electron microscopy (HRTEM) was carried out using a JEOL 2100Plus UHR microscope operating at 200 kV. Samples were dispersed in ethanol, and the resulting solution dropped on to a carbon film supported on a nickel grid. Scanning transmission electron microscopy (STEM) images using a high-angle annular dark-field (HAADF) detector were also acquired. Analytic investigations were performed with an energy dispersive X-ray (EDX) spectrometer attached to the microscope column. Sample preparation using the same steps as for conventional TEM.

X-ray photoelectron spectroscopy (XPS)

To analyze the chemical nature of the element in Cu/ZIF-8, Pd@ZIF-8, Au@ZIF-8 and PdAu@ZIF-8 catalysts, XPS analyses were performed using an Omicron Argus X-ray photoelectron spectrometer, equipped with a monochromated AlKα radiation source (hν = 1486.6 eV) and a 280 W electron beam power. The emission of photoelectrons from the sample was analyzed at a takeoff angle of 45° under ultra-high vacuum conditions (≤10−9 mBar). Spectra were carried out with a 100 eV pass energy for the survey scan and 20 eV pass energy for the C 1s, O 1s, N 1s, Cu 2p and Zn 2p regions and element peak intensities were corrected by Scofield factors. The peak areas of Cu 2p were determined after subtraction of a U 2 TOUGAARD background. The spectra were fitted using Casa XPS v.2.3.15 software (Casa Software Ltd, U.K.) and applying a Gaussian/Lorentzian ratio G/L equal to 70/30.

Inductively coupled plasma atomic emission spectroscopy (ICP-OES)

The values for Zn and Cu contents in Cu/ZIF-8 and Pd and Au contents in Pd/Au@ZIF-8 were determined by inductively coupled plasma atomic emission spectroscopy (ICP-OES) using an Agilent ICP-OES 5100 SVDV equipment. 5 mg of sample was digested in 10 mL of nitric acid (2%). The standard was prepared on the same day with same diluent.

Hydrogen temperature-programmed reduction (H_2-TPR)

H_2-TPR was used to analyze the reduction temperature of the metal precursors of the copper, palladium and gold metal nanoparticles. The tests were performed on a Micromeritics AutoChem 2910 equipped with a thermal conductivity cell detector (TCD). H_2-TPR testing of the samples followed the following procedure: 50 mg of sample was taken and placed in a quartz U-tube sample. First, the samples were purged at room temperature for 20 minutes under a Helium stream, followed by heating to 400 °C at a rate of 5 °C/min under a H_2/Ar (5%, 100 mL/min) gas stream.

^{1}H nuclear magnetic resonance (NMR) spectroscopy

The reaction products of benzaldehyde with isopropylamine and benzylamine were identified by liquid state ^{1}H-NMR. ^{1}H NMR spectra were recorded on a Bruker Avance 400 NMR (400 MHz) spectrometer equipped with an autotunable broad band probe. Chemical shifts (δ) are reported in part per million (ppm).

The rate of partial exchange of the ZIF-8 2-methylimidazole linkers by 3-amino-1, 2, 4-triazole substituent linkers achieved in Chapter 6 to produce the surface-functionalized ZIF-8 derivative were analyzed by the ^{1}H-NMR of the digestion solution. The ^{1}H NMR spectra of ZIF-8 and ZIF-8A were acquired in diluted HNO_3 with D_2O (2% m/V) at 25 °C. 1 mg of ZIF-8 or ZIF-8A were digested in 1 mL of HNO_3 D_2O solution. The ligand exchange ratio was calculated from the relative ratio of the integral area (math.) of the peak of characteristic hydrogen atoms.

Zeta potential

To analyze the surface charge of free and immobilized ω-transaminase and ZIF-8 derivatives, Zeta potential experiments were performed on Litesizer™ 500 apparatus (Anton Paar) provided with 658 nm laser operating at 40 mW. The angle of backscattering light collection was set to 90°. The zeta potential measurements of PdAu@ZIF-8 and derivatives were performed in a Ω-shaped capillary cuvette with 150 V applied potential. The zeta potential measurements of free and immobilized ω-transaminase and ZIF-8 derivatives were performed at 30 V.

Chapter 3.

Catalysis of the oxidation of alcohol: copper nanoparticles supported on ZIF-8

3.1. Introduction

This chapter deals with the synthesis of ZIF-8-based Cu nanoparticle catalysts and their use for aerobic oxidation of benzyl alcohol in the presence of TEMPO. Cu(I/II) and 2,2,6,6-Tetramethylpiperidinyloxyl (TEMPO) system is one of the most studied homogeneous catalytic system for alcohol oxidation.[1–3] It appeared as a particularly interesting candidate to achieved the chemoenzymatic system targeted in this thesis because it is known to allow oxidation of alcohol to be achieved under mild temperature conditions and potentially in water (as reported for some transition metals including Cu /TEMPO system) (See Chapter 1, Section 1.2.1.1).[4,5] The ultimate goal of this thesis being the creation of chemoenzymatic heterogeneous catalysts, a challenge of this project was to realize the heterogeneous version of the homogeneous Cu/TEMPO system. The current direction for the heterogenization of Cu/TEMPO is mainly the heterogenization of either Cu complexes or TEMPO.[6–10] ZIF-8 has been investigated as a support for a variety of metal ions or nanoparticles (See Chapter 1, Section 1.1.1). Here, we firstly tried to heterogenized Cu^{2+} in the support ZIF-8, as a part of the framework by exchanging Zn^{2+} with Cu^{2+}.

Several strategies to introduce active Copper centers into ZIF-8 were tentatively followed:

Bottom-up "in-situ" introduction of the doping metal (see Chapter 1; Section 1.1.2.1.1). This is a direct method of introducing Cu sites. We synthesized Cu-doped ZIF-8 by replacing in the reaction mixture a part of $Zn(NO_3)_2$ with a certain percentage (10 mol% and 25 mol%) of $Cu(NO_3)_2$. Alternatively, other copper-based MOFs known to be stable in water were also synthesized to compare their catalytic activity with that of our Cu-doped ZIF-8. These MOFs were ZIF-202 ($Cu(imidazole)_4$),[11] Cu-AD-SA($Cu_2(AD)_2(SA)$, AD= adenine, SA= succinic acid).[12] However, none of them were active for benzyl alcohol oxidation (See table 3.1). Since the Cu/TEMPO catalytic mechanism relies on the coordination of Cu(I/II) with the TEMPO and benzyl alcohol, the Cu-doped ZIF-8 and the tested Cu-based MOFs may not expose sufficiently coordinated unsaturated Cu sites. Indeed, copper centers at the nodes of the crystal structure of these MOFs (including our Cu-doped ZIF-8) are coordinatively saturated and may

not be accessible. Therefore, we turned our attention to the top-down strategy (i.e., post-synthesis modification).

Table 3.1. Benzyl alcohol oxidation over Cu containing MOFs

Catalyst	Catalyst loading/mg	T/°C	Time/h	Yield benzaldehyde/%
Cu-doping-ZIF-8(25%)	27	60	24	3.3
Cu-doping-ZIF-8(10%)	50	60	24	2.2
ZIF-202	50	70	24	0
Cu-AD-SA	30	70	24	1

Conditions: Benzyl alcohol 108mg (100 mM), solvent 10mL, TEMPO 8 mg (5 mM), DMAP 60mg (50 mM), O_2 flow, acetonitrile.

Top-down introduction of the doping metal by cation exchange (See Chapter 1, Section 1.1.2.1.1). In this strategy, we introduce Cu^{2+} to the priory synthesized ZIF-8 by a step of impregnation. In this case, the introduced Cu^{2+} can be either replacing a part of the Zn^{2+} cations (intra-framework position) or adsorbed within the pores of the ZIF-8 (extra-framework position). Both situations are most probably occurring. The obtained Cu-ZIF-8 led to excellent catalytic oxidation activity of benzyl alcohol (Table 3.2). However, the stability of the catalyst was low; indeed, significant leaching of copper cations occurred during the test. Subsequently, various strategies to stabilize the introduced Cu site were attempted, including varying the counter anions of Cu cations ($CuCl_2$ instead of $Cu(NO_3)_2$, see Table 3.2 Cu-ZIF-8(Cl)), ligand exchange (partially replacing 2-MeIM with 3-amino-1,2,4-triazole, see table 3.1 Cu-ZIF-8A), and converting the introduced copper cations into copper oxide (See table 3.1 CuO-ZIF-8). However, all strategies failed to avoid Cu leaching.

Table 3.2. Benzyl alcohol oxidation over Cu-ZIF-8

Catalyst	Catalyst loading/mg	Solvent	Time/h	Yield benzaldehyde/%
Cu-ZIF-8	20	water	4	18.5
Cu-ZIF-8	20	CH_3CN	6	81.2
Cu-ZIF-8(Cl)	20	CH_3CN	6	61
Cu-ZIF-8A	20	CH_3CN	6	83
CuO-ZIF-8	20	CH_3CN	6	0

Conditions: Benzyl alcohol 108mg (100 mM), solvent 10 mL, TEMPO 8 mg (5 mM), DMAP 60 mg (50 mM), 60 °C, air atmosphere.

Finally, a strategy proved to overcome these issues was to reduce the copper cations introduced within ZIF-8 pores and framework after impregnation in order to form copper metal NPs trapped within the hybrid MOF framework. To our delight, the copper NPs thus produced efficiently catalyzed the oxidation benzyl alcohol in the presence of TEMPO. Reports in the literature indeed demonstrated that Cu^{2+} species existing on either copper oxide or partially oxidized Cu^0 NPs act as active sites similarly to homogeneous copper complexes in the alcohol oxidation catalyzed in the presence of TEMPO under mild conditions (See supporting information of the article). This was however the first time that the formation of Cu^0 NPs occluded in a MOF framework was used as a strategy to heterogenized Cu^{2+} active species. We showed that the stability of this catalyst strongly depends on the method of copper II reduction. This study was published in an article attached to this chapter. The main results displayed in this article are summarized in the following.

3.2. Article synopsis

In this article, we created a stable heterogeneous made of Cu nanoparticle (NP) supported on ZIF-8 for the aerobic oxidation of benzyl alcohol with 2,2,6,6-Tetramethylpiperidinyloxyl (TEMPO) as co-catalyst under mild conditions using molecular oxygen as a green oxidant. In particular, the catalysts obtained by two different conventional reduction methods were

characterized and compared by X-ray diffraction (XRD), transmission electron microscopy (TEM), N_2 adsorption-desorption isotherms, and X-ray photoelectron spectroscopy (XPS): (i) the wet route using an aqueous solution of $NaBH_4$, and (ii) the dry route using a H_2 gas flow (the reduction temperature was determined by the H_2-temperature-programmed reduction (H_2-TPR)).

The in-depth physicochemical characterization and comparison of the resulting two types of Cu/ZIF-8 materials reveal significant differences: the reduction with $NaBH_4$ led to the formation of 16 nm sized Cu^0 nanoparticles (NP) mainly localized on the external surface of the ZIF-8 crystals together with ZnO nanocrystallites, while the reduction under H_2 flow results in Cu^0 nanoparticles with a mean size of 22 nm embedded within the bulk of ZIF-8 crystals. More, when $NaBH_4$ was used to reduce cupric ions, ZnO particles were highlighted by high-resolution microscopy imaging. Formation of ZnO impurities was confirmed by the photoluminescence analysis of ZIF-8 after $NaBH_4$ treatment. In contrast, ZnO was not detected on ZIF-8 treated with H_2. Both types of the Cu^0 NPs supported on ZIF-8 were found to be active as catalysts towards the aerobic oxidation of benzyl alcohol under moderate temperature (T < 80°C) and using air as sustainable O_2 source. Benzaldehyde yields of 66% and selectivity superior to 90% were obtained with Cu/ZIF-8 catalyst prepared under H_2 flow after 24h under these conditions. The same material could be recycled 5 times without loss of activity, unlike the catalysts synthesized with $NaBH_4$, as a result of the leaching of the surface copper NPs over the consecutive catalytic cycles. Finally, the most stable catalyst was successfully implemented in a tandem "one-pot" catalytic system associating benzyl alcohol oxidation and Knoevenagel condensation to synthesize benzylidene malononitrile.

In the article, the calculation of yield and conversion follows formulas:

$$Conversion(\%) = \frac{C_{0(substrate)} - C_{t(substrate)}}{C_{0(substrate)}} * 100$$

$$Yield(\%) = \frac{C_{t(product)}}{C_{0(substrate)}} * 100$$

In Table 2 of the article, there was a mistake that filling the percentage of the Cu species of Cu nanoparticles obtained by different reduction methods in the blanks. We make the following errata here.

Table 2 Atomic Percentages of the N, Zn, and Cu Elements in Cu/ZIF-8(H_2) and Cu/ZIF-8(NaBH4)

catalysts	XPS signal					Percentage in Cu species (%)	
	N1s	Zn2p	Cu2p	O1s	Cu2p/N1s	Cu(II)	Cu(0) or Cu(I)
ZIF-8	20.7	7.4		4.34			
Cu/ZIF-8(H_2)	19.1	4.2	0.8	7.47	0.19	23	77
Cu/ZIF-8($NaBH_4$)	15.8	2.9	2.4	12.76	0.83	93	7

In Table 3 of the article, an anomalous yield higher than the conversion rate can be observed. This is due to systematic errors in the experiment. For better understanding, the data in the table has been updated here by adding the standard deviation of the yield.

Table 3. Catalytic Oxidation of Benzyl Alcohol

catalysts	time (h)	conversion (%)	benzaldehyde yield (%)
ZIF-8	24		
Cu/ZIF-8($NaBH_4$)	24	61±3	58±3
Cu/ZIF-8(H_2)	24	62±5	66±3

Conditions: Benzyl alcohol 108mg (100 mM), acetonitrile 10 mL, TEMPO 8 mg (5 mM), DMAP 60 mg (50 mM),70 ℃, air atmosphere.

While this catalyst displays satisfactory activity with air as the oxidant at temperatures as low as 50 °C, it exhibits no activity in an aqueous phase. This limitation poses challenges for chemoenzymatic cascade reactions due to the requisite of aqueous solvents by ω-transaminases.

Our attention then focused on the second most promising catalytic system dedicated to alcohol oxidation under mild conditions identified in the literature (See Chapter 1, Section 1.2.1.2), namely PdAu NPs.

The next chapter focuses on the immobilization of PdAu NPs on ZIF-8 and on the characterization of PdAu@ZIF-8 catalyst with various Pd to Au ratio and on the monitoring and comparison of their catalytic performances.

References

(1) Hoover, J. M.; Stahl, S. S. Highly Practical Copper(I)/TEMPO Catalyst System for Chemoselective Aerobic Oxidation of Primary Alcohols. J. Am. Chem. Soc. 2011, 133 (42), 16901–16910. https://doi.org/10.1021/ja206230h.

(2) Hoover, J. M.; Ryland, B. L.; Stahl, S. S. Mechanism of Copper(I)/TEMPO-Catalyzed Aerobic Alcohol Oxidation. J. Am. Chem. Soc. 2013, 135 (6), 2357–2367. https://doi.org/10.1021/ja3117203.

(3) Gamez, P.; E. Arends, I. W. C.; Reedijk, J.; A. Sheldon, R. Copper(II)-Catalysed Aerobic Oxidation of Primary Alcohols to Aldehydes. Chemical Communications 2003, 0 (19), 2414–2415. https://doi.org/10.1039/B308668B.

(4) Liu, W.; Yang, J.; Cai, J. Aerobic Alcohol Oxidation Catalyzed by CuO-Rectorite/TEMPO in Water. Res Chem Intermed 2019, 45 (2), 549–561. https://doi.org/10.1007/s11164-018-3618-3.

(5) Zhu, X.; Yang, D.; Wei, W.; Jiang, M.; Li, L.; Zhu, X.; You, J.; Wang, H. Magnetic Copper Ferrite Nanoparticles/TEMPO Catalyzed Selective Oxidation of Activated Alcohols to Aldehydes under Ligand- and Base-Free Conditions in Water. RSC Adv. 2014, 4 (110), 64930–64935. https://doi.org/10.1039/C4RA14152K.

(6) Taher, A.; Kim, D. W.; Lee, I.-M. Highly Efficient Metal Organic Framework (MOF)-Based Copper Catalysts for the Base-Free Aerobic Oxidation of Various Alcohols. RSC Adv. 2017, 7 (29), 17806–17812. https://doi.org/10.1039/C6RA28743C.

(7) Deng, J.; Ben Tayeb, K.; Dong, C.; Simon, P.; Marinova, M.; Dubois, M.; Morin, J.-C.; Zhou, W.; Capron, M.; Ordomsky, V. V. TEMPO-Ru-BEA Composite Material for the Selective Oxidation of Alcohols to Aldehydes. ACS Catalysis 2022, 12 (15), 8925–8935.

(8) Li, L.; Matsuda, R.; Tanaka, I.; Sato, H.; Kanoo, P.; Jeon, H. J.; Foo, M. L.; Wakamiya, A.; Murata, Y.; Kitagawa, S. A Crystalline Porous Coordination Polymer Decorated with Nitroxyl Radicals Catalyzes Aerobic Oxidation of Alcohols. J. Am. Chem. Soc. 2014, 136 (21), 7543–7546. https://doi.org/10.1021/ja5019095.

(9) Wei, Z.; Ru, S.; Zhao, Q.; Yu, H.; Zhang, G.; Wei, Y. Highly Efficient and Practical Aerobic Oxidation of Alcohols by Inorganic-Ligand Supported Copper Catalysis. Green Chem. 2019, 21 (15), 4069–4075. https://doi.org/10.1039/C9GC01248F.

(10) GUPTA, M.; SHARMA, P.; GUPTA, M.; GUPTA, R. Silica Functionalized Cu(II) Catalysed Selective Oxidation of Benzyl Alcohols Using TEMPO and Molecular Oxygen as an Oxidant. J Chem Sci 2015, 127 (8), 1485–1489. https://doi.org/10.1007/s12039-015-0902-2.

(11) Nguyen, N. T. T.; Lo, T. N. H.; Kim, J.; Nguyen, H. T. D.; Le, T. B.; Cordova, K. E.; Furukawa, H. Mixed-Metal Zeolitic Imidazolate Frameworks and Their Selective Capture of Wet Carbon Dioxide over Methane. Inorg. Chem. 2016, 55 (12), 6201–6207. https://doi.org/10.1021/acs.inorgchem.6b00814.

(12) Wang, L.; Wang, K.; An, H.-T.; Huang, H.; Xie, L.-H.; Li, J.-R. A Hydrolytically Stable Cu(II)-Based Metal−Organic Framework with Easily Accessible Ligands for Water Harvesting. ACS Appl. Mater. Interfaces 2021, 13 (41), 49509–49518. https://doi.org/10.1021/acsami.1c15240.

ACS APPLIED MATERIALS & INTERFACES

www.acsami.org

Research Article

Copper Nanoparticles Supported on ZIF-8: Comparison of Cu(II) Reduction Processes and Application as Benzyl Alcohol Oxidation Catalysts

Yifan Zan, Ferdaous Ben Romdhane, Antoine Miche, Christophe Méthivier, Jean-Marc Krafft, Claude Jolivalt,* and Julien Reboul*

Cite This: *ACS Appl. Mater. Interfaces* 2023, 15, 38716−38728

Read Online

ACCESS | Metrics & More | Article Recommendations | Supporting Information

ABSTRACT: We report the synthesis of a stable heterogeneous catalyst based on copper metal nanoparticles with oxidized surface supported on ZIF-8 for the oxidation of benzyl alcohol under mild temperature and using air as a sustainable oxygen source as well as for the implementation of the tandem "one-pot" catalytic system allowing the sustainable synthesis of benzylidene malononitrile. The influence of the reduction process applied to form the nanoparticle upon the catalyst texture and its performances was extensively examined. After ZIF-8 impregnation with a copper chloride precursor, the reduction of cupric ions into Cu^0 nanoparticles was carried out according to two procedures: (i) by soaking the solid into a solution of $NaBH_4$ and (ii) by submitting it to a flow of gaseous H_2 at 340 °C. The in-depth physicochemical characterization and comparison of the resulting two types of Cu/ZIF-8 materials reveal significant differences: the reduction with $NaBH_4$ led to the formation of 16 nm sized Cu^0 nanoparticles (NP) mainly localized on the external surface of the ZIF-8 crystals together with ZnO nanocrystallites, while the reduction under H_2 flow resulted in Cu^0 nanoparticles with a mean size of 22 nm embedded within the bulk of ZIF-8 crystals. More, when $NaBH_4$ was used to reduce cupric ions, ZnO particles were highlighted by high-resolution microcospy imaging. Formation of ZnO impurities was confirmed by the photoluminescence analysis of ZIF-8 after $NaBH_4$ treatment. In contrast, ZnO was not detected on ZIF-8 treated with H_2. Both types of Cu^0 NPs supported on ZIF-8 were found to be active as catalysts toward the aerobic oxidation of benzyl alcohol under moderate temperature (T < 80 °C) and using air as a sustainable O_2 source. Benzaldehyde yield of 66% and selectivity superior to 90% were obtained with the Cu/ZIF-8 catalyst prepared under H_2 flow after 24 h under these conditions. The same material could be recycled 5 times without loss of activity, unlike the catalysts synthesized with $NaBH_4$, as a result of the leaching of the surface copper NPs over the consecutive catalytic cycles. Finally, the most stable catalyst was successfully implemented in a tandem "one-pot" catalytic system associating benzyl alcohol oxidation and Knoevenagel condensation to synthesize benzylidene malononitrile.

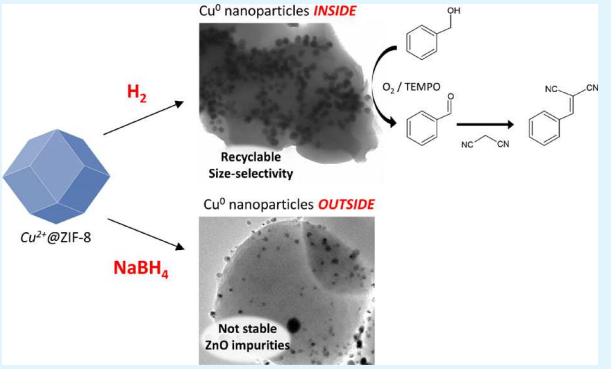

KEYWORDS: *copper nanoparticles, ZIF-8, Cu(II) reduction process, nanoparticle location, aerobic alcohol oxidation, ZnO impurities*

1. INTRODUCTION

Copper-based catalysts are of high potential interest among transition metals for the development of economic and sustainable oxidation catalytic systems. They afford promising alternatives to the classic oxidation methods using stoichiometric quantities of toxic inorganic oxidants, such as manganese dioxide, chromium(VI), and the Swern or Dess−Martin reagents,[1] and to more virtuous but still highly expensive catalytic systems based on the use of precious metals, such as gold and platinum.[2,3] A variety of copper(II) complexes were recently reported allowing the oxidation of alcohols under mild conditions using O_2 or hydroperoxide as sustainable alternative oxidants.[4] Among these catalytic systems, copper complexes associated with a nitroxyl cocatalyst, typically the commercially available and stable 2,2,6,6−tetramethylpiperidine-1-oxyl radical (TEMPO), were shown to be particularly efficient for the selective aerobic oxidation of benzylic, allylic, and aliphatic alcohols under mild temperatures and using pure O_2 or even ambient air.[5] However, these copper complexes imply the use of relatively expensive specific organic ligands, whose synthesis can be

Received: June 20, 2023
Accepted: July 19, 2023
Published: July 31, 2023

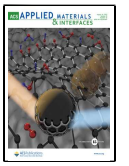

https://doi.org/10.1021/acsami.3c08906
ACS Appl. Mater. Interfaces 2023, 15, 38716−38728

tedious.[6] Furthermore, the homogeneous character of these copper catalytic systems inherently entails problems related to their separation and recycling, as well their stability. These issues were recently addressed by combining TEMPO with copper oxide or surface-oxidized copper metal nanoparticles supported on various supports, resulting in robust and active heterogeneous catalytic systems.[7−10] Metal−organic frameworks (MOFs) were shown to be excellent support for metallic and metal oxide nanoparticles mainly because their extremely high surface area promotes the efficient dispersion of metal precursors within the crystal bulk, resulting in highly dispersed nanoparticles after a metal cation reduction step. Among them, ZIF-8, a prototypical MOF composed of a zinc-imidazolate framework, was particularly studied as a support for a variety of metal nanoparticles (Au, Pd, Ru, Cu, etc.)[11] due to its high surface area, its three-dimensional structure made of interconnected nanocages, and relative stability in a wide range of reaction conditions, including basic aqueous media. Herein, we report the immobilization of copper metal nanoparticles (NPs) on ZIF-8 and their use as stabilized copper-based heterogeneous catalyst systems capable of selectively oxidizing benzylic alcohols in the presence of TEMPO and an organic base (4-dimethylaminopyridine, DMAP) under mild temperature and with air as the oxidant source. Particular attention was given to the method used to reduce the copper cations dispersed within the pores of ZIF-8. Two traditional reduction methods were compared: (i) a wet route using an aqueous $NaBH_4$ solution and (ii) a dry route achieved under H_2 flow at the reduction temperature of the metal precursors (H_2-TPR) (Scheme 1). The resulting two types of catalysts were carefully characterized, and their performances in the oxidation of benzyl alcohol were compared. Finally, a tandem catalytic system, combining alcohol oxidation and Knoevenagel catalysis in a one-pot synthesis process, was implemented with the most promising Cu/ZIF catalyst relative to the oxidation step, taking advantage of Cu NP activity and of the basic properties of both ZIF-8 imidazolate linkers and DMAP required in the Knoevenagel coupling step.

Scheme 1. Schematic Representation of the Formation of Cu/ZIF-8 Nanocomposites Following the Two Cu^{2+} Reduction Methods Compared in This Work: (a) Using $NaBH_4$ and (b) Using H_2

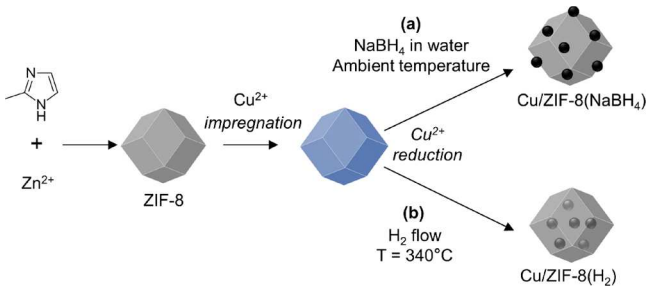

2. EXPERIMENTAL SECTION

2.1. Chemicals. Chemicals were from commercial sources and used without any further purification. Copper(II) chloride dihydrate ($CuCl_2{\cdot}2H_2O$, ≥99%), zinc nitrate hexahydrate ($Zn(NO_3)_2{\cdot}6H_2O$, ≥99%), 2-methylimidazole (2-mim, 99%), sodium borohydride ($NaBH_4$, 98%), 2,2,6,6-tetramethylpiperidinyl-1-oxy (TEMPO, 98%), 4-dimethylaminopyridine (DMAP, ≥99%), benzyl alcohol (≥99%), and caffeine were purchased from Sigma-Aldrich. Benzaldehyde (99+%) and acetonitrile (99.8+%) were purchased from Alfa Aesar. Methanol (analytical grade) and ethanol (99.98%) were purchased from VWR.

2.2. Synthesis of ZIF-8. ZIF-8 was synthesized following a procedure described by Astruc et al. in the literature with minor modifications.[12] In brief, 13.3 mmol of $Zn(NO_3)_2{\cdot}6H_2O$ was dissolved in 100 mL of methanol. Then, 50 mmol of 2-methylimidazole dissolved in 100 mL of methanol was added slowly. The mixture was maintained at 30 °C and aged for 24 h. The product was collected by centrifugation and washed three times with 30 mL of methanol. The obtained material was heated at 100 °C under vacuum overnight, and the obtained ZIF-8 solid was stored at room temperature before further use.

2.3. Synthesis of Cu/ZIF-8. The Cu^{2+}/ZIF-8 was prepared by soaking 114 mg of ZIF-8 in 10 mL of a 0.25 mmol $CuCl_2{\cdot}2H_2O$ solution in methanol. The suspension was stirred for 24 h. The purple solid (Cu^{2+}/ZIF-8) was then harvested by filtration and washed with 30 mL of methanol.

Cu^{2+}/ZIF-8 was then reduced either with $NaBH_4$ or H_2 to produce metal copper NPs. Reduction with $NaBH_4$ was achieved by redispersing Cu^{2+}/ZIF-8 into 10 mL of water and adding 5 mL of fresh aqueous solution of $NaBH_4$ (240 mM, 4 equiv) dropwise under vigorous stirring. The stirring lasted for 4 h. A deep blue powder was collected by filtration. Reduction with H_2 was achieved by treating Cu^{2+}/ZIF-8 with 100 mL/min H_2 flow at 340 °C for 20 min.

Regardless of the reduction method, the collected Cu/ZIF-8 particles were washed with 10 mL of methanol three times. Then, they were dried at 90 °C under vacuum overnight before their characterization and catalytic assessment. Solids reduced with $NaBH_4$ are denoted as Cu/ZIF-8($NaBH_4$), and those reduced under H_2 gaseous flow are denoted as Cu/ZIF-8(H_2).

2.4. Characterization. Powder X-ray diffraction (PXRD) of ZIF-8, Cu^{2+}/ZIF-8, Cu/ZIF-8($NaBH_4$), and Cu/ZIF-8(H_2) was performed using a Bruker D8 Advance diffractometer (Cu Kα = 1.5406 Å). N_2 physisorption analyses were performed using a Belsorp MAX instrument. The samples were pretreated by vacuum at 100 °C for 18 h, and the textural parameters were calculated according to the Brunauer, Emmett, and Teller (BET) method.

Imaging of the samples was performed by conventional transmission electron microscopy (TEM) using a JEOL 1011 operating at 100 kV. High-resolution transmission electron microscopy (HRTEM) was carried out using a JEOL 2100Plus UHR microscope operating at 200 kV. Samples were dispersed in ethanol, and the resulting solution dropped onto a carbon film supported on a nickel grid. Scanning transmission electron microscopy (STEM) images using a high-angle annular dark-field (HAADF) detector were also recorded. Analytic investigations were performed with an energy dispersive X-ray (EDX) spectrometer attached to the microscope column.

XPS analyses were performed using an Omicron Argus X-ray photoelectron spectrometer, equipped with a monochromated Al Kα radiation source ($h\nu$ = 1486.6 eV) and a 280 W electron beam power. The emission of photoelectrons from the sample was analyzed at a takeoff angle of 45° under ultrahigh vacuum conditions (≤10−9 mbar). Spectra were recorded with a 100 eV pass energy for the survey scan and 20 eV pass energy for the C 1s, O 1s, N 1s, Cu 2p, and Zn 2p regions, and element peak intensities were corrected by Scofield factors. The peak areas of Cu 2p were determined after subtraction of a U 2 TOUGAARD background. The spectra were fitted using CasaXPS v.2.3.15 software (Casa Software Ltd., U.K.) and applying a Gaussian/Lorentzian ratio G/L equal to 70/30.

Zn and Cu contents of the synthesized catalysts were determined by inductively coupled plasma atomic emission spectroscopy (ICP-OES) using an Agilent ICP-OES 5100 SVDV equipment. The hydrogen temperature-programmed reduction (H_2-TPR) of ZIF-8 and Cu^{2+}/ZIF-8 was performed using a Micromeritics AutoChem 2910.

Photoluminescence measurements were performed with a Horiba Jobin Yvon Fluorolog 3 spectrofluorimeter equipped with a 450 W Xe lamp as an excitation source. Solids ZiF-8, ZIF-8 treated with $NaBH_4$

https://doi.org/10.1021/acsami.3c08906
ACS Appl. Mater. Interfaces 2023, 15, 38716−38728

($ZiF\text{-}8(NaBH_4)$), and ZIF-8 treated with H_2 ($ZiF\text{-}8(H_2)$) were placed in a Suprasil quartz cell with 5 mm external diameter and 4 mm internal diameter. Excitation was set at λ_{exc} = 335 nm, and the emission spectrum was recorded between 350 and 650 nm.

2.5. Catalytic Aerobic Oxidation of Alcohols. The catalytic aerobic oxidation of alcohols to the corresponding aldehydes was performed in a 5 mL round-bottom flask sealed with a septum equipped with a balloon. In a typical reaction, 0.2 mmol (1 wt %) of alcohol, 0.01 mmol (5 mol % to the substrate) of TEMPO, and 0.1 mmol of DMAP were dissolved in 2 mL of acetonitrile. Then, 5 mg of catalyst (based on copper, 10 mol % to the substrate) was added. The suspension was treated under ultrasound for 2 min to disperse the catalyst within the reaction solution. The reaction was performed under stirring at 600 rpm at constant temperatures maintained by oil bath. The atmosphere was set to oxygen or air by filling the balloon connected to the reaction vessel with the corresponding gas. In the case of O_2, the flask was blown by O_2 before adding the catalyst. After the catalytic test, the catalyst was recovered by centrifugation and washed with 2 mL of methanol three times. The recyclability test was achieved after reactivating the catalyst at 90 °C under vacuum. The reaction solution was analyzed by high-performance liquid chromatography (HPLC, 1260 Infinity II by Agilent) equipped with a Beckman Coulter ultrasphere ODS column (150 × 4.6 mm, 5 μm) and a diode-array detector (DAD). The mobile phase was the mixture of acetonitrile and water (v:v = 50:50). The concentrations of reactants and products were determined using calibration curves and caffeine as an internal standard to correct deviations due to solvent volume changes because of its partial evaporation.

One-pot sequential oxidation/Knoevenagel condensation reaction was achieved by mixing in a 10 mL round-bottom flask 0.2 mmol (1 wt %) of benzyl alcohol, 0.01 mmol (5 mol % to the substrate) of TEMPO, 0.1 mmol of DMAP, and 2 mL of acetonitrile. Then, 5 mg of catalyst (based on copper, 10 mol % to the substrate) was added and dispersed by ultrasonication (1 min). A balloon filled with air was connected to the round flask, and the reaction was allowed to proceed under magnetic stirring at T= 70 °C until the alcohol conversion reached an almost constant value. An amount of 0.33 mmol of malononitrile was then added to the reaction mixture that was placed under stirring at T= 70 °C. The same protocol was also achieved without the addition of DMAP.

3. RESULTS AND DISCUSSION

3.1. Synthesis and Characterization of the Catalysts. The copper nanoparticles supported on ZIF-8 crystals were prepared according to the procedure illustrated in Scheme 1. The diffraction pattern of the purple powder recovered after ZIF-8 impregnation with the copper chloride solution agrees with that of the pristine ZIF-8 (Figure 1). It shows that impregnation does not affect the crystal structure of ZIF-8. On the other hand, a drastic reduction of BET specific surface area from 1621 to 745 cm^2g^{-1} and of pore volume (from 0.64 to 0.43 cm^3g^{-1}) were evidenced by N_2 sorption analysis at 77 K after $CuCl_2$ impregnation, suggesting the partial filling of ZIF-8 pores by the Cu^{2+} precursor (Figure 2 and Table 1).

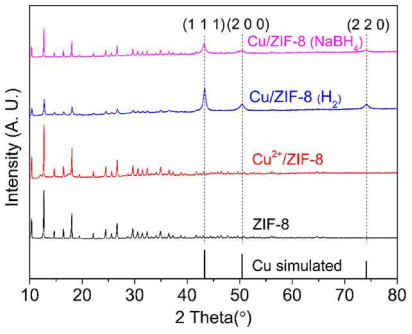

Figure 1. XRD patterns of ZIF-8, Cu^{2+}/ZIF-8, $Cu/ZIF\text{-}8(NaBH_4)$, and $Cu/ZIF\text{-}8(H_2)$. The simulated XRD pattern of Cu^0 is also shown for comparison.

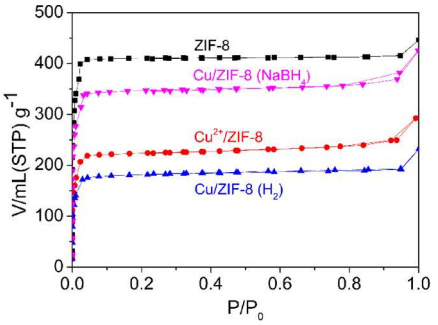

Figure 2. N_2 adsorption isotherms of ZIF-8, Cu^{2+}/ZIF-8, $Cu/ZIF\text{-}8(NaBH_4)$, and $Cu/ZIF\text{-}8(H_2)$.

Table 1. Textural Properties of ZIF-8, Cu^{2+}/ZIF-8, $Cu/ZIF\text{-}8(NaBH_4)$, and $Cu/ZIF\text{-}8(H_2)$

samples	A_{BET} (cm^2 g^{-1})[a]	V_P (cm^3g^{-1})[b]	d_{Cu} (nm)[c]
ZIF-8	1621	0.64	
Cu^{2+}/ZIF-8	745	0.43	
$Cu/ZIF\text{-}8(NaBH_4)$	1302	0.62	16 (18)
$Cu/ZIF\text{-}8(H_2)$	638	0.33	22 (18)

[a]BET surface area. [b]Pore volume. [c]Average Cu crystallite size determined using TEM analysis (the average size determined by the Scherrer equation using the (111) peak is indicated into brackets).

Reducibility of copper species adsorbed within ZIF-8 pores was then studied by TPR analysis (Figure S1). The TPR profile of the impregnated material shows only one well-defined peak centered at T = 340 °C, incidentally proving the existence of only one type of Cu^{2+} species strongly interacting with the framework of ZIF-8. The purple color of the material after impregnation supports the hypothesis of Cu^{2+} cations strongly interacting with the imidazolate linkers of the hybrid network, namely, by the formation of coordination bonds, as copper-imidazolate complexes with a purple color were reported in the literature.[13] The impregnated Cu^{2+}/ZIF-8 was then further reduced by two methods (Scheme 1): either (a) under a stream of H_2 at T= 340 °C (the reduction temperature determined by TPR analysis) or (b) by immersing the impregnated ZIF-8 in an aqueous solution of $NaBH_4$ under stirring. The obtained solids are denoted as $Cu/ZIF\text{-}8(H_2)$ or $Cu/ZIF\text{-}8(NaBH_4)$, respectively, in the following. Copper contents of $Cu/ZIF\text{-}8(NaBH_4)$ and $Cu/ZIF\text{-}8(H_2)$ were 21.7 and 22.4 wt % as measured by ICP-OES analysis.

After reduction, the PXRD patterns of both $Cu/ZIF\text{-}8(H_2)$ and $Cu/ZIF\text{-}8(NaBH_4)$ clearly show three additional peaks at 43.4°, 55.5°, and 74°, which can be assigned to the (111), (200), and (220) planes of Cu^0, respectively, indicating the successful formation of Cu^0 nanoparticles with both reduction methods (Figure 2). It is also noteworthy that a significant decrease of the ZIF-8 diffraction peak intensity was observed, suggesting losses of crystallinity of the MOF. The discrepancy is even more pronounced in the case of the use of H_2 as a reducing agent. For the latter materials, reduction under H_2 flow results in a reduction of the BET surface area and pore volume to 638 m^2g^{-1} and 0.33 cm^3g^{-1}, respectively (Figure 2,

https://doi.org/10.1021/acsami.3c08906
ACS Appl. Mater. Interfaces 2023, 15, 38716−38728

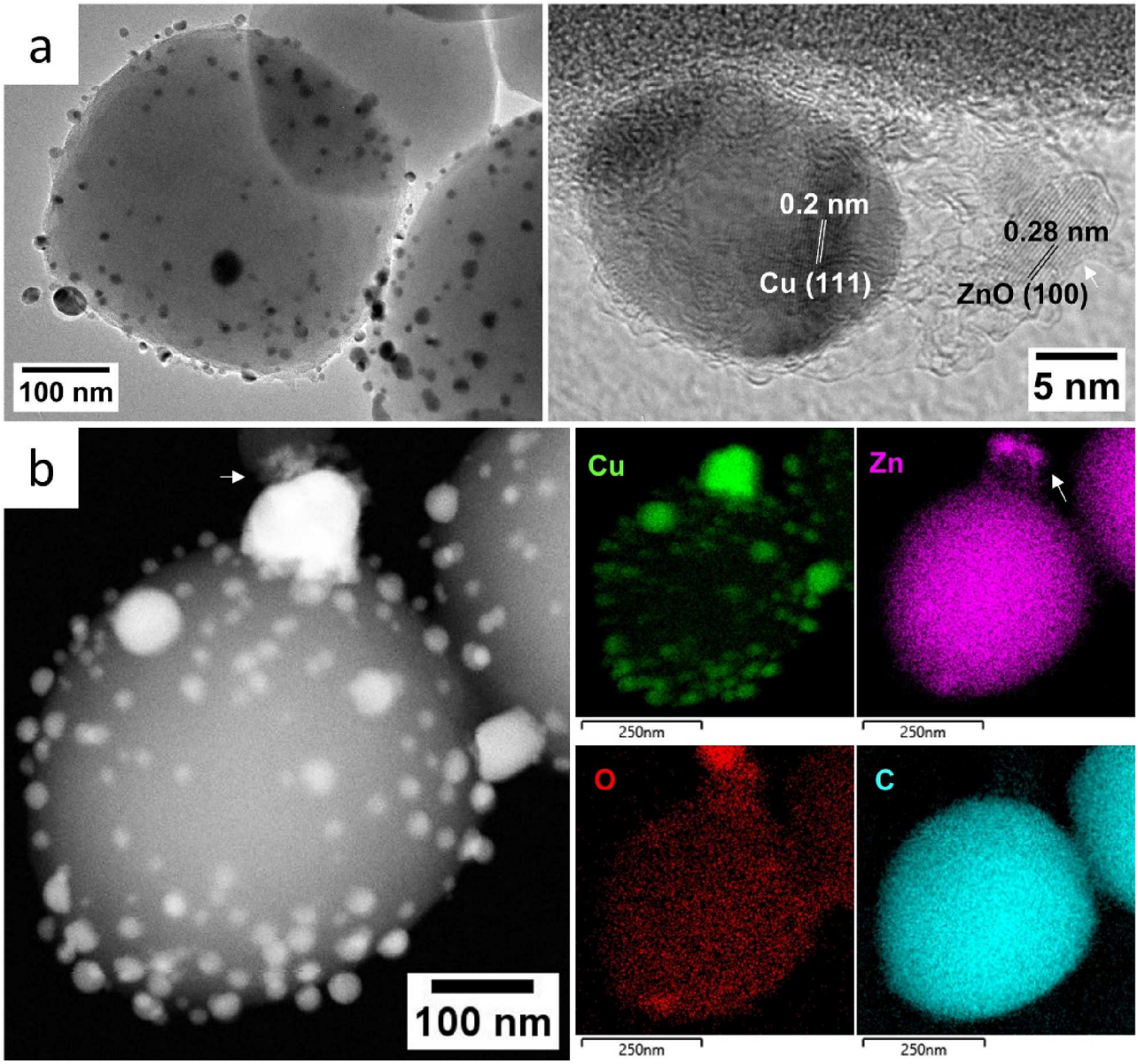

Figure 3. (a) TEM (left) and HRTEM (right) images and (b) HAADF image and corresponding Cu, Zn, O, and C EDX element mapping of Cu/ZIF-8($NaBH_4$). The white arrows indicate where the ZnO nanocrystallite aggregates are located.

Table 1). In contrast, the opposite trend is observed when $NaBH_4$ is used as the reductant. In this case, surface area and pore volume of the reduced material increase to 1302 m^2g^{-1} and 0.62 cm^3g^{-1}, respectively (Figure 2 and Table 1), i.e., textural parameters very close to those determined for ZIF-8 alone. Such a result would be in line with the assumption that in the case of Cu/ZIF-8(H_2) materials, the Cu^0 NPs are located inside the ZIF-8 porosity whereas for Cu/ZIF-8($NaBH_4$), NPs are on the external surface of ZIF-8.

TEM imaging was then performed to investigate the morphology, size, dispersion, and localization of copper nanoparticles in the two Cu/ZIF-8($NaBH_4$) and Cu/ZIF-8(H_2) samples (Figures 3 and 4). A representative image of Cu/ZIF-8($NaBH_4$) is shown in Figure 3a, highlighting the presence of particles dispersed on the external surface of the ZIF-8 crystals whose size is mainly in the range of 5 to 80 nm with a mean size of 16 nm (histogram shown in Figure S2a). HRTEM images of most of these nanoparticles (Figure 3a right) display lattice fringes with interplanar spacings of 0.21 nm corresponding to the (100) planes of metal copper (JCPDS 04-0836). The formation of the Cu^0 nanoparticles dispersed on the external surface of ZIF-8 is confirmed by HAADF, the Cu nanoparticles clearly appearing as bright dots, and STEM-EDX mapping (Figure 3b). Noteworthy, HRTEM imaging also highlights some nanocrystals with ill-defined shape in addition to the Cu^0 nanoparticles. These latter particles are characterized by lattice fringes with interplanar spacings of 0.28 nm corresponding to the (100) atomic plane of wurtzite ZnO (JCPDS 36-1451) (additional HRTEM images of Cu/ZIF-8($NaBH_4$) are available in Figure S3, and a STEM image showing ZnO nanocrystallites on ZIF-8 is given in Figure S4).

In order to clarify the role of $NaBH_4$ in the formation of ZnO only during the reduction process, imaging of ZIF-8 crystals alone (i.e., without any cupric ions) after soaking in pure water or in a $NaBH_4$ aqueous solution was compared

https://doi.org/10.1021/acsami.3c08906
ACS Appl. Mater. Interfaces 2023, 15, 38716−38728

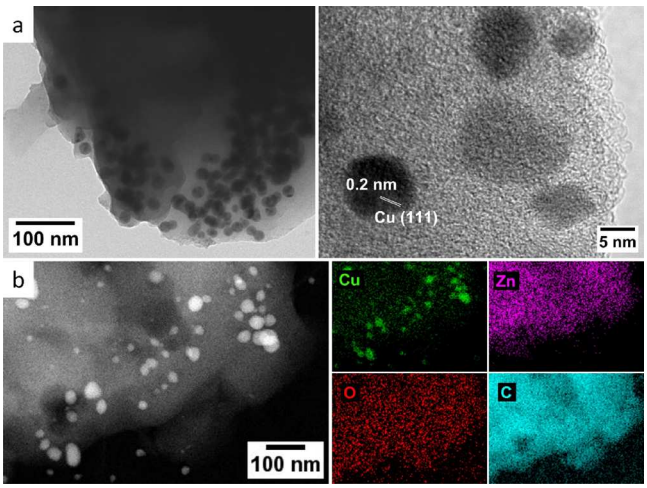

Figure 4. (a) TEM and HRTEM images and (b) HAADF image and corresponding Cu, Zn, O, and C EDX element mappings of Cu/ZIF-8(H_2).

(Figure S5). No ZnO particles were detected on ZIF-8 soaked in pure water, while ZnO crystallites were observed on the ZIF-8 treated with $NaBH_4$. In such conditions, ZIF-8 partly dissolve, leading to the formation of ZnO particles as a result of the presence of strongly basic and nucleophilic metaborate anions (BO_2^-) produced during the hydrolysis of $NaBH_4$ (according to the reaction $BH_4^- + 2H_2O \rightarrow BO_2^- + 4H_2$).[14] An increase of the pH from 8.3 to 10 was indeed measured during the $NaBH_4$ reduction process of cupric ions. However, no discrepancy of ZIF-8 crystallinity was observed by PXRD of the MOF. Furthermore, no ZnO could be detected by this characterization method (Figure S6). It can be hypothesized that either the ZnO content of the sample is too low, or crystallites are too small to be detected by XRD analysis. This may explain why the formation of such surface ZnO nanoparticles has never been reported so far in studies dealing with the synthesis of metal nanoparticles supported on ZIF-related materials using $NaBH_4$ as the reducting agent.[15−20] Formation of ZnO impurities under $NaBH_4$ was confirmed by photoluminescence (PL) spectroscopy (Figure S7). This technique is a powerful tool for assessing MOF purity and specifically for identifying the presence of ZnO impurities in MOF samples, with the advantage of a higher sensitivity compared to powder XRD characterization.[21] At ambient temperature, ZIF-8 exhibits a luminescence at 434 nm upon excitation at 335 nm, which could be attributed to the $\pi^*-\pi$ transition of the 2-methylimidazolate linkers.[22] After the reduction process using $NaBH_4$, the emission spectrum of ZIF-8 displays an additional broad PL emission peak centered on 516 nm, strongly suggesting the presence of nanoscale ZnO particles. It is indeed known that the photoluminescence of ZnO nanoparticles shows an emission peak at approximately 500 nm upon excitation at 350 nm as a result of the presence of defects (oxygen vacancies) on the ZnO surface. This surface-related emission is particularly intense for ZnO particles with high surface-to-volume.[23] To summarize, reduction of copper cations with an aqueous solution of $NaBH_4$ results in their migration toward the outside of the MOF crystals, where the formation of the copper nanoparticles takes place. It is accompanied by the formation of ZnO nanocrystallites as impurities. The presence of such nanoscale semiconductor impurities in the ZIF-8 sample should be avoided as their intrinsic physicochemical properties[24] may interfere with the targeted applications of the ZIF-based materials.

The morphology of Cu/ZIF-8(H_2) is drastically different from that observed with Cu/ZIF-8($NaBH_4$). Conventional TEM images of this sample show well-dispersed nanoparticles with a mean size of 22 nm mostly located within the bulk of the ZIF-8 crystal (Figure 4a, a size histogram and additional HRTEM images are available in Figures S2b and S8, respectively). The chemical composition of the nanoparticles is confirmed by the lattice fringes with interplanar spacings of 0.20 corresponding to the (111) planes of metal copper (JCPDS 04-0836) observed on nanoparticles by HRTEM (Figure 4a). The HAADF image and the corresponding element mapping also confirm the chemical composition of the nanoparticles and their dispersal within the MOF (Figure 4b). Contrary to $NaBH_4$, H_2 used as the reduction agent under the experimental conditions used in this study does not trigger the formation of ZnO impurities. Indeed, ZnO impurities were indeed not detected on Cu/ZIF-8(H_2) by HRTEM analysis. In addition, the photoluminescence spectrum of H_2-treated ZIF-8 did not display any additional PL emission peak at approximately 500 nm upon excitation at 335 nm (Figure S7). These analyses therefore show that H_2 reduction (i) promotes the formation of copper nanoparticles mostly located within the bulk of the ZIF-8 crystals and (ii) does not lead to the formation of any ZnO nanoparticles.

However, determining the location of copper nanoparticles, either within the bulk or onto the external surface of ZIF-8 crystals, is a difficult issue to address by the observation of two-dimensional TEM or STEM images alone. Therefore, herein, the nanoparticles location depending on the reduction method was further investigated using X-ray photoelectron spectroscopy (XPS) analysis.

First, the chemical state analysis of Cu/ZIF-8(H_2) and Cu/ZIF-8($NaBH_4$) NPs was performed. The main peaks in the survey spectra were assigned to C 1s, Cu 2p, O 1s, N 1s, and Zn 2p (see Table 2 and Figure 5a,c).

Theoretically, the Cu 2p XPS signal is composed of two contributions, namely, Cu $2p_{1/2}$ and Cu $2p_{3/2}$, with a relative peak intensity of 1/2 and a binding energy (BE) difference of 20 eV (Figure S9). As expected, the positions of the Cu $2p_{1/2}$ and Cu $2p_{3/2}$ signals were found here at 953 and 933 eV, respectively, for Cu/ZIF-8(H_2) with a relative intensity of 0.47 and at 954.3 and 934.6 eV for Cu/ZIF-8($NaBH_4$) with a

Table 2. Atomic Percentages of the N, Zn, and Cu Elements in Cu/ZIF-8(H_2) and Cu/ZIF-8($NaBH_4$)

			Cu_{2p} signal				
	N_{1s}	Zn_{2p}	Cu_{2p}	O_{1s}	Cu_{2p}/N_{1s}	Cu(II)	Cu(0) or Cu(I)
ZIF-8	20.7	7.4		4.34			
Cu/ZIF-8(H_2)	19.1	4.2	0.8	7.47	0 0.19	77	23
Cu/ZIF-8($NaBH_4$)	15.8	2.9	2.4	12.76	0.83	7	93

https://doi.org/10.1021/acsami.3c08906
ACS Appl. Mater. Interfaces 2023, 15, 38716−38728

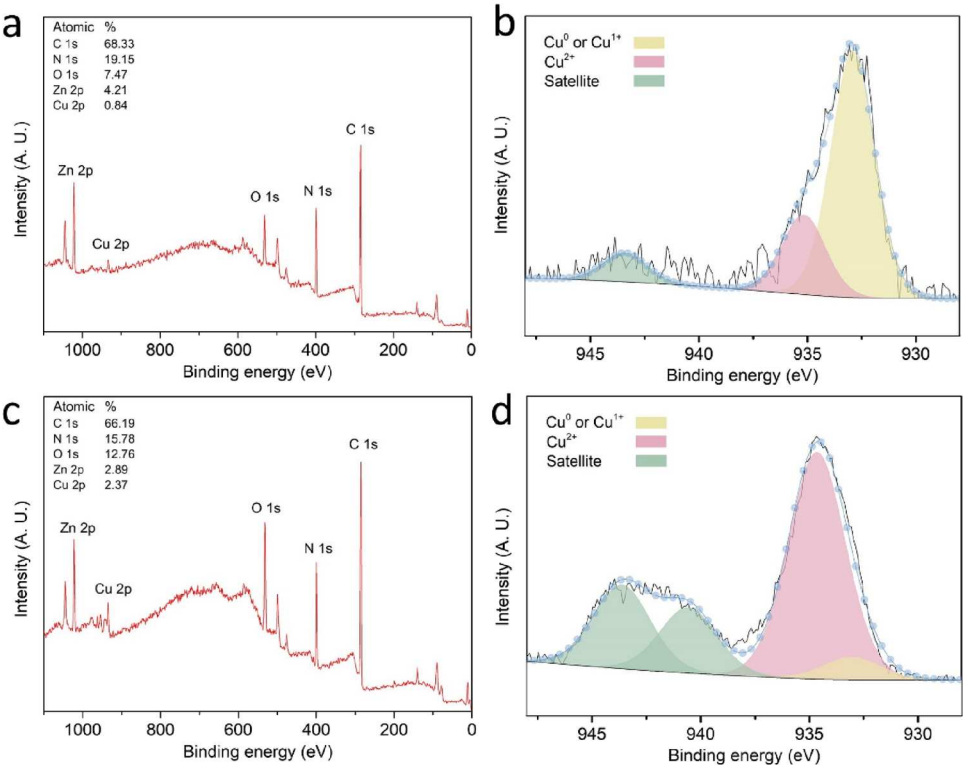

Figure 5. Full XPS spectra (a, c) and high-resolution XPS spectra of Cu $2p_{3/2}$ (b, d) of Cu/ZIF-8(H_2) (a, b) and of Cu/ZIF-8($NaBH_4$) (c, d).

relative intensity of 0.45. One obvious difference when comparing the signals of Cu/ZIF-8(H_2) to those of Cu/ZIF-8($NaBH_4$) is that their ratios between the atomic percentages of Cu 2p and N 1s (Cu_{2p} /N_{1s}, in Table 2) are very different, namely, 0.19 and 0.83, respectively (for similar copper contents close to 22%, as quantified from ICP-OES measurements). Such a result is an indication that Cu nanoparticles in Cu/ZIF-8($NaBH_4$) are more preferentially located on the surface of the ZIF-8 crystals compared to the Cu/ZIF-8(H_2) solid.

As an attempt toward an in-depth analysis of the copper speciation, the Cu $2p_{3/2}$ signal of Cu NPs was fitted using CasaXPS software. The main peak at around 933 eV was separated into two contributions, the lower one being assigned to the Cu(0) and/or Cu_2O (cuprous oxide, Cu(I)) species around 933 eV,[25] while at higher BE, 935.2 (±0.1) eV was assigned to divalent Cu(II), whose speciation could be $Cu(OH)_2$ (copper hydroxide) and/or CuO (cupric oxide) (Figure 5b,d). Such a signal decomposition clearly shows that the Cu/ZIF-8($NaBH_4$) sample contains much more Cu(II) species than Cu(0) or Cu(I) species compared to the Cu/ZIF-8(H_2). Also, both the peak shape and the main peak to shake-up peak separation of the Cu $2p_{3/2}$ signal of the Cu/ZIF-8($NaBH_4$) sample indicate that the speciation of the Cu(II) compound is likely to be $Cu(OH)_2$. However, this could not be confirmed by a check of the O 1s signal. The corresponding peak around 531.7 (±0.1) eV has a full width at half-maximum that could allow a deconvolution into several contributions, but the total O 1s intensity is too high to account only for oxidized copper species. This excess of oxygen may be explained by the contamination of the samples, as often observed in XPS spectra of real-world solids. Moreover, inspection of the C 1s spectrum, as well as the C 1s/N 1s atomic percentage ratio, which is higher than that expected for ZIF-8, confirms that significant oxygen containing carbon species are present in the solids. Notably, the formation of the ZnO particles on the surface of ZIF-8 after Cu(II) reduction as observed on the TEM images (Figure 3) should also result in an excess of oxygen. As suggested by Biesinger, the quantification of the relative [Cu(0) + Cu(I)] and Cu(II) species contents on a sample surface can be calculated from the main emission line of Cu $2p_{3/2}$ and the shake-up satellite intensity knowing the main peak/shakeup satellite peak areas for the pure corresponding Cu(II) sample.[25] Here, it can be assumed that the partial oxidation of the Cu(0) NP surface in both Cu/ZIF-8(H_2) and Cu/ZIF-8($NaBH_4$) is likely to occur after the reduction step when the samples are stored in contact with ambient O_2 and H_2O. In this scenario, adsorbed water molecules dissociate and form surface hydroxyls groups resulting in a thin layer of mainly $Cu(OH)_2$ on the nanoparticle surface. Consequently, assuming that the oxidized copper species evidenced on CuZIF-8 surface are mainly formed of copper hydroxide, whose main peak/shakeup satellite peak area is 1.57, the percentage of Cu(II) on the Cu NP surface could be quantified to 10% and 93% for Cu/ZIF-8(H_2) and Cu/ZIF-8($NaBH_4$), respectively, in line with the assumption that Cu NPs are more readily oxidized when located on the surface of ZIF-8 crystals like in the case of Cu/ZIF-8($NaBH_4$). Notably, the different conditions used to synthesize the Cu NPs may also explain these differences of surface oxidation extent. Indeed, the wet reduction process achieved in the aqueous solution of $NaBH_4$ is expected to be more favorable to the oxidation of the Cu NP than the dry process under gaseous dihydrogen flow.

Overall, the above results (TEM and XPS analyses) evidence that Cu NPs are more deeply embedded inside the ZIF-8 crystals for Cu/ZIF-8(H_2) than in the case of Cu/ZIF-8($NaBH_4$). To explain this trend, we speculate that the wet

https://doi.org/10.1021/acsami.3c08906
ACS Appl. Mater. Interfaces 2023, 15, 38716−38728

conditions provided by the aqueous $NaBH_4$ solution, all the more that it is achieved under vigorous stirring conditions, favor the outward diffusion of cupric cations adsorbed within the ZIF-8 pores, leading to the formation of Cu^0 NPs on the external surface of the crystals. Such an assumption is in line with the significant increase of the porous volume and BET surface area observed by N_2 sorption analysis after reduction, which become close to those of the parent ZIF-8 (Figure 2 and Table 1). Conversely, the dry gaseous condition inherent to the use of H_2 promotes the fast reduction of cupric cations localized within the ZIF-8 porosity after the impregnation process, leading to the growth of copper NPs mostly positioned within the pores.

3.2. Catalytic Activity and Heterogeneity Test: Effect of the Reduction Method. *3.2.1. Oxidation of Benzyl Alcohol in Air.* Selective oxidation of benzyl alcohol was selected as model reaction to monitor and compare the catalytic activities of Cu/ZIF-8(H_2) and Cu/ZIF-8($NaBH_4$) as well as to optimize the reaction conditions.

Reactions were performed in the presence of TEMPO and DMAP. TEMPO is a free radical that is classically used in the aerobic oxidation of alcohols, while DMAP mainly acts as an organic base cocatalyst. Reactions were performed in acetonitrile as a solvent, at 70 °C for 24 h in the presence of air as an oxidation agent. The conversion extent of benzyl alcohol and the benzaldehyde yield are shown in Table 3.

Table 3. Catalytic Oxidation of Benzyl Alcohol[a]

catalysts	time (h)	conversion (%)	benzaldehyde yield (%)
ZIF-8	24		
Cu/ZIF-8($NaBH_4$)	24	61	58
Cu/ZIF-8(H_2)	24	62	66

[a]Test conditions: 5 mg of catalyst (10 mol %), 5 mM TEMPO, 100 mM benzyl alcohol, 1 atm of air, 2 mL of acetonitrile, 70 °C, and for 24 h.

The control experiment using pure ZIF-8 did not yield any benzaldehyde formation after 24 h of reaction at 70 °C. In contrast, using Cu/ZIF-8(H_2) and Cu/ZIF-8($NaBH_4$) as catalysts led to benzyl alcohol conversions of 62 and 61%, respectively (benzaldehyde yields reach 66 and 58% after 24 h with Cu/ZIF-8(H_2) and Cu/ZIF-8($NaBH_4$), respectively). These results demonstrate the critical role of copper as a catalyst. No benzylic acid was detected, indicating that no overoxidation reaction occurs. Notably, Figure 6 shows that the kinetic profiles of the first 6 h of reaction catalyzed with Cu/ZIF-8(H_2) and Cu/ZIF-8($NaBH_4$) are different. Indeed, using Cu/ZIF-8(H_2) induces a lag time of 3 h, presumably due to some diffusional limitations of the alcohol inside the pores of ZIF-8 whose size (from 3.4 Å for the pristine ZIF-8 to 6.9 Å for its open form[26]) is close to that of benzyl alcohol (molecular length ca. 7.9 Å, width ca. 5.3 Å[27]), thus slowing down benzyl alcohol diffusion toward copper nanoparticles trapped within the bulk ZIF-8 crystals. Conversely, when using Cu/ZIF-8($NaBH_4$) as a catalyst, benzaldehyde yield increases almost linearly with the reaction time. In this case, because the nanoparticles are likely located on the surface of the ZIF-8 crystals, they are directly accessible to the reactant, so that there is no diffusional barrier to overcome. The difference between reaction kinetics when comparing the two catalysts is even more significant when a bulkier substrate is employed instead of benzyl alcohol. Indeed, for the 3,5-di-*tert*-butyl-4-hydroxybenzyl alcohol, a bulky derivative of benzyl alcohol, the oxidation yield of the corresponding aldehyde after 2 h of reaction remains below 10% with Cu/ZIF-8(H_2) while a benzaldehyde yield of 43% is obtained with Cu/ZIF-8($NaBH_4$) after the same reaction time. Cu/ZIF-8(H_2) therefore fully takes advantage of the sieving effect of ZIF-8. Indirectly, these results confirm the effect of the copper reduction procedure on the location of the Cu NPs: thermal treatment under H_2 flow promotes the Cu^0 nanoparticle growth within the bulk of ZIF-8 crystals, which promotes a size selectivity relative to the oxidation substrate.

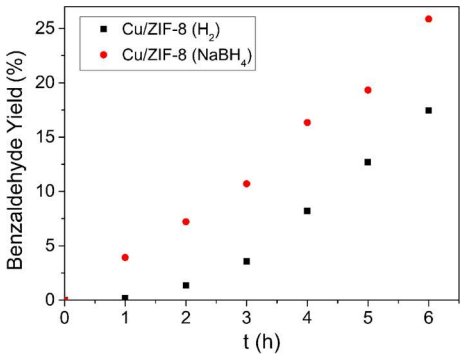

Figure 6. Kinetic profiles of the benzaldehyde reaction catalyzed with Cu/ZIF-8($NaBH_4$) and Cu/ZIF-8(H_2). Reaction conditions: 5 mg of catalyst (10 mol %), 5 mM TEMPO, 100 mM benzyl alcohol, 1 atm of air, 2 mL of acetonitrile, and 60 °C.

The stability and the heterogeneous character of the two catalysts Cu/ZIF-8(H_2) and Cu/ZIF-8($NaBH_4$) were then monitored and compared. Cu/ZIF-8(H_2) and Cu/ZIF-8($NaBH_4$) catalysts were removed from the hot reaction medium by means of filtration using a 0.45 μm filtration membrane after 5 and 3 h of reaction, respectively, and the catalytic activity of the filtrate for benzyl alcohol oxidation was further monitored (Figure 7).

The absence of reaction in the reaction mixture after the catalyst removal with both catalysts indicates the absence of active sites leaching during the reaction course. This result points out the fully heterogeneous character of both Cu/ZIF-8(H_2) and Cu/ZIF-8($NaBH_4$) catalysts. The recyclability of the two types of catalysts was also evaluated and compared by reusing the catalysts five times subsequently. The catalysts were removed by centrifugation between two consecutive tests and thoroughly washed with acetonitrile. Figure 8 shows the benzaldehyde yield plotted as a function of time for each type of catalyst during the first 5 h of reaction. Similar benzaldehyde yields were obtained for the first four cycles with Cu/ZIF-8(H_2) indicating the excellent stability of this catalyst (Figure 8a). In contrast, benzaldehyde yield decreases after each cycle with Cu/ZIF-8($NaBH_4$) (Figure 8b). Elemental ICP-OES analyses of the two catalysts before and after the five consecutive cycles confirm the lower stability of Cu/ZIF-8($NaBH_4$) compared to Cu/ZIF-8(H_2). Copper content in Cu/ZIF-8($NaBH_4$) drops from 22 wt % for the freshly synthesized material to 10% after the fifth cycle. Such a decrease is not observed in the case of Cu/ZIF-8(H_2) for which the copper content remains almost stable, decreasing only slightly from 22 wt % for the fresh catalyst to 19 wt % after 5 cycles. PXRD characterization of the catalysts after the fifth cycle also evidences the difference in stability of the two types of catalysts (Figure S10). While the intensities of the

https://doi.org/10.1021/acsami.3c08906
ACS Appl. Mater. Interfaces 2023, 15, 38716−38728

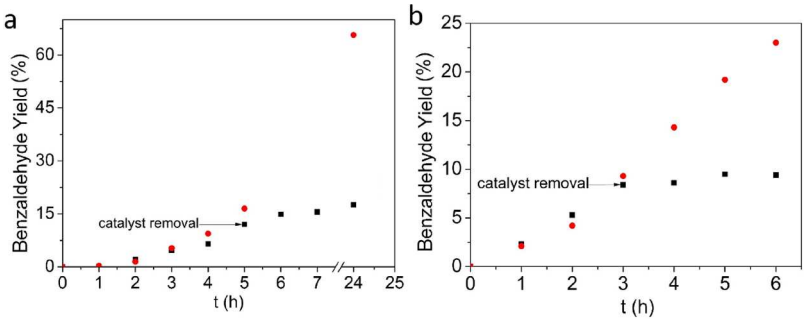

Figure 7. Assessment of heterogeneous catalysis: (a) Cu/ZIF-8(H_2) was removed after 5 h of reaction; (b) Cu/ZIF-8($NaBH_4$) was removed after 3 h of reaction. Reaction conditions: 5 mg of catalyst (10 mol %), 5 mM TEMPO, 100 mM benzyl alcohol, 1 atm of air, 2 mL of acetonitrile, and 60 °C.

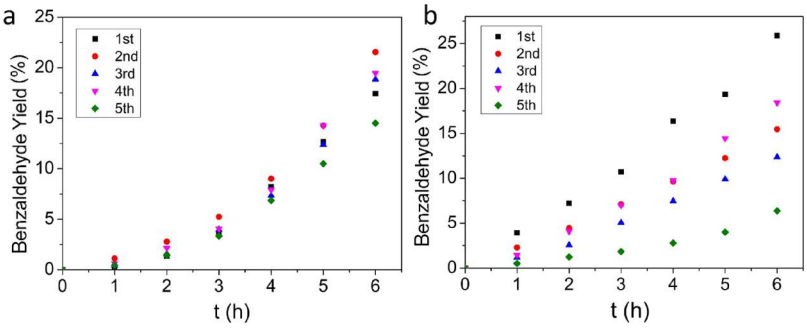

Figure 8. Recycling tests with (a) Cu/ZIF-8(H_2) and (b) Cu/ZIF-8($NaBH_4$) as catalysts. Reaction conditions: 5 mg of catalyst (10 mol %), 5 mM TEMPO, 100 mM benzyl alcohol, 1 atm of air, 2 mL of acetonitrile, and 60 °C.

Scheme 2. Possible Mechanism for the Aerobic Oxidation of Benzyl Alcohol Catalyzed by Cu(II) Sites on the Surface of Cu/ZIF-8 Copper Nanoparticles with TEMPO as the Cocatalyst

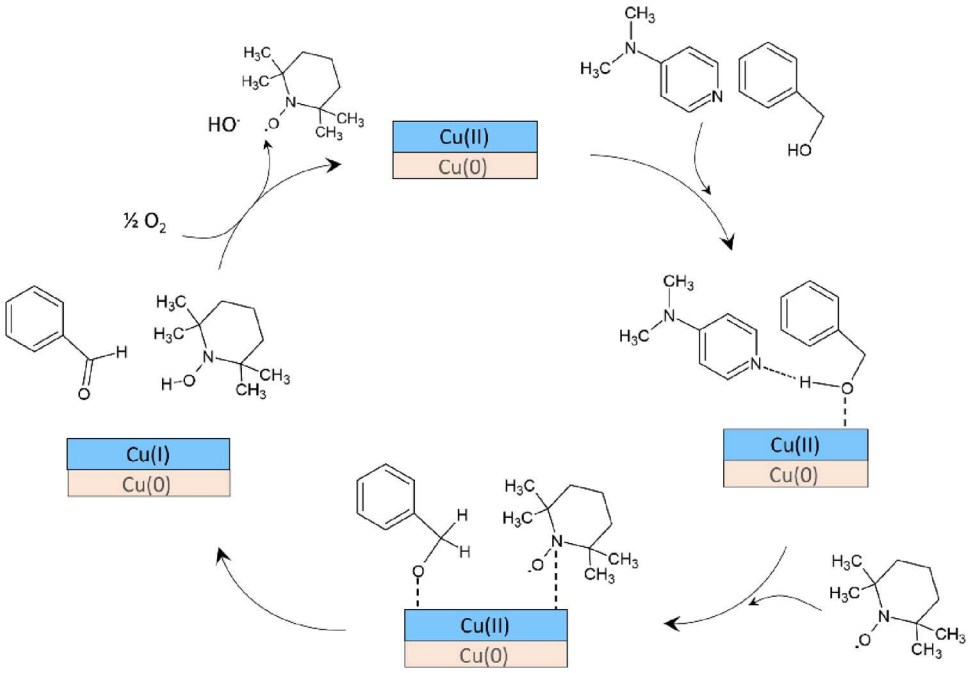

diffraction peaks assigned to ZIF-8 seemed not to be affected by the catalytic tests, the three diffraction peaks observed on the XRD profile of the fresh Cu/ZIF-8($NaBH_4$) representing the (111), (200), and (220) planes of Cu^0 (at 43.39°, 55.50°, and 74.08°, respectively) almost completely disappeared after the five consecutive catalytic tests, corroborating the leaching of copper species as measured by ICP-OES analysis. In contrast, XRD peaks attributed to ZIF-8 and Cu^0 in the Cu/ZIF-8(H_2) diffraction pattern remain unchanged after cycling the catalyst, confirming its stability. Furthermore, the N_2 physisorption curves of Cu/ZIF-8($NaBH_4$) and Cu/ZIF-8(H_2) measured after cycling are similar to those of the

https://doi.org/10.1021/acsami.3c08906
ACS Appl. Mater. Interfaces 2023, 15, 38716−38728

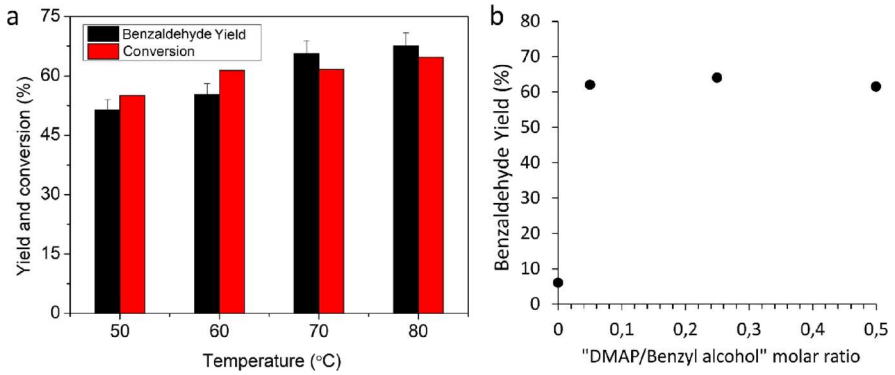

Figure 9. Cu/ZIF-8(H_2) activity as a function of (a) the reaction temperature and (b) the molar ratio between DMAP and benzyl alcohol. Reaction conditions: (a) 5 mg of Cu/ZIF-8(H_2) (10 mol %), 5 mM TEMPO, 100 mM benzyl alcohol, 1 atm of air, 2 mL of acetonitrile, 24 h; (b) 5 mg of Cu/ZIF-8(H_2) (10 mol %), 5 mM TEMPO, 100 mM benzyl alcohol, 1 atm of air, 2 mL of acetonitrile, T = 70 °C, 24 h.

freshly synthesized catalysts (Figure S11), which is also consistent with the putative location of copper NPs: when located on the Cu/ZIF-8($NaBH_4$) external surface, their leaching has no influence on the textural properties of ZIF-8 whereas in the case of Cu/ZIF-8(H_2) material, unchanged textural properties are in good accordance with the good stability of the catalyst. In this case, the hybrid ZIF-8 network entrapping Cu NPs efficiently stabilizes them and prevents copper species from leaching during both the reaction course and the separation/washing processes.

By trapping the Cu NPs within ZIF-8 bulk, this strategy hence allows for efficient heterogenization and recycling of Cu(II) sites that are believed to be the active sites that catalyze the aerobic oxidation of alcohols in the presence of TEMPO. A mechanism for the oxidation of benzyl alcohol is proposed in the following, based on previous reports focused on the homogeneous catalysis of aerobic alcohol oxidation involving copper sites and TEMPO (Scheme 2).[5] As indicated by XPS analysis, the surface of the copper nanoparticles before the catalysis test is decorated with copper(II) species (CuO and $Cu(OH)_2$). The alcohol is therefore first expected to coordinate to the surface copper(II) atoms, facilitating the deprotonation of the alcohol to form a Cu(II)-alkoxide. Alcohol deprotonation may be achieved either by vicinal copper hydroxide groups, the closest nitrogen atoms of the 2-methyl-imidazolate MOF linkers, or the additional organic base DMAP. A minimum amount of DMAP was however shown to be necessary for the alcohol oxidation to proceed efficiently (Figure 9b), suggesting that this basic compound is mainly responsible for the alcohol deprotonation. A hydrogen transfer from the α-carbon of the alcohol to TEMPO, which is also coordinated to the surface copper(II) cations, then results in the formation of the carbonyl product and in the generation of surface copper(I) cations. The aerobic oxidation of both TEMPOH and surface copper(I) finally results in the regeneration of TEMPO and surface copper(II) cations, hence terminating the catalytic cycle. In this process, the critical role of TEMPO and O_2 was evidenced experimentally since they are mandatory for the reaction to proceed.

Cu/ZIF-8(H_2) is therefore the most promising of the two catalysts. Its activity was then studied as the function of different experimental parameters.

3.2.2. Optimization of the Reaction Conditions with Cu/ZIF-8(H_2) as the Catalyst. The effect of the reaction temperature was first monitored. Figure 9a shows that the benzaldehyde yield determined after 24 h of reaction increases from 51 to 66% with an increase of temperature from 50 to 70 °C. Benzaldehyde yield remains then constant when the temperature is further increased to 80 °C. Then, the reaction was conducted with four different DMAP to benzyl alcohol molar ratios. Figure 9b shows that benzyl alcohol takes place only above a DMAP to benzyl alcohol molar ratio of 0.05. The benzaldehyde yield obtained after 24 h of reaction is indeed only 6% when the reaction is achieved without DMAP, while it reaches around 65% for a DMAP to benzyl alcohol molar ratio higher than 0.05. Hence, the copper-coordinated imidazolate linkers located close to the copper nanoparticles within the ZIF-8 framework do not provide sufficiently strong basic sites to deprotonate benzyl alcohol and favor the formation of the active Cu(II)-alkoxide intermediate necessary for the generation of benzaldehyde, as described by Stahl and collaborators.[28] The presence of a minimum amount of the strong organic base DMAP is therefore required.

The reaction was also tested in different solvents (Table 4). Benzaldehyde yield was monitored as a function of time within three solvents: water, acetonitrile, and ethanol or without any solvent. The highest activity of Cu/ZIF-8(H_2) is obtained in acetonitrile, with a benzaldehyde yield of 78% (selectivity >99%). Ethanol and water however do not allow the production of benzaldehyde. The reaction carried out without additional solvent, where benzaldehyde is used both as substrate and solvent, leads to a yield equal to 57%. The catalyst is however degraded during the reaction, which is mainly catalyzed under homogeneous conditions.

Table 4. Influence of Solvent and Oxygen Source on Benzyl Alcohol Yield[a]

solvent	oxidant	yield (%)	conversion (%)
water	O_2	0	29
ethanol	O_2	3	10
neat	O_2	57	59
acetonitrile	O_2	78	77
acetonitrile	air	66	62

[a]Reaction conditions: 5 mg of Cu/ZIF-8(H_2) (10 mol %), 5 mM TEMPO, 100 mM benzyl alcohol, 1 atm of gas phase, 2 mL of solvent (when used), T= 70 °C, 24 h.

Finally, pure O_2 was compared to air as a green and cheap source of oxygen (Table 4). When employing molecular O_2, Cu/ZIF-8(H_2) showed only a 15% higher benzyl alcohol conversion (77%) than with air and a similarly high yield (78%

https://doi.org/10.1021/acsami.3c08906
ACS Appl. Mater. Interfaces 2023, 15, 38716−38728

compared to 66%, respectively). Using air instead of pure O_2 therefore does not significantly penalize the catalysis performances of Cu/ZIF-8(H_2), which are still satisfying.

Based on these results, the best reaction conditions for benzyl alcohol oxidation, considering both reaction efficiency and sustainability, are the following: in acetonitrile as solvent, at a temperature T= 70 °C, with a molar ratio of DMAP to benzyl alcohol equal to 0.05 and using air as a sustainable oxygen source. Cu/ZIF-8(H_2) therefore provides a new heterogeneous and recyclable system allowing for the aerobic oxidation of benzyl alcohol. Its performances are comparable to those of other heterogeneous copper-based systems catalyzing alcohol oxidation with TEMPO as the cocatalyst and O_2 as the oxidant reported in the literature. However, compared to these catalysts, Cu/ZIF-8(H_2) combined several advantages: it does not require the chemical modification of the support surface or the use of expensive organic linkers, it is stable, and it works under relatively mild temperature and using atmospheric air as the oxygen source instead of pure O_2 (Table S1). Moreover, this catalytic system integrates different reactive sites (the N-sites of the ZIF-8 organic linkers) making possible its use for tandem catalysis. The optimal reaction conditions were hence used to set the stepwise benzyl alcohol oxidation and Knoevenagel condensation described in the next section.

3.2.3. Stepwise Benzyl Alcohol Oxidation and Knoevenagel Condensation. The catalytic behavior of Cu/ZIF-8(H_2) was investigated in a stepwise process coupling benzyl alcohol oxidation with the Knoevenagel reaction, an important C−C coupling reaction widely used in the synthesis of fine chemicals (Scheme 3).[29] This "one-pot" process is expected to enhance the sustainability of the synthesis of benzylidene malononitrile, a highly valuable molecule regarding its role as molecular building block for the construction of various nitrogenous heterocycles with versatile biological activities.[30,31]

Scheme 3. Reaction Scheme Displaying the Stepwise Reaction: (A) Benzyl Alcohol Oxidation into Benzaldehyde Followed by (B) the Knoevenagel Condensation of Benzaldehyde with Malononitrile to Form the Benzylidene Malononitrile[a]

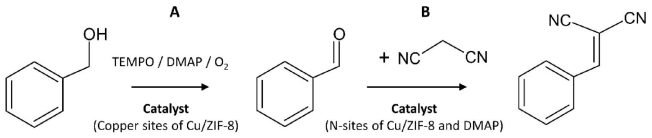

[a]The catalytic sites for the two reactions are indicated.

The rational for this approach relies on the fact that, in addition to the Cu sites responsible for the alcohol oxidation, the Cu/ZIF-8(H_2)/TEMPO/DMA system also contains two types of chemical basic sites that were recently reported to efficiently catalyze the Knoevenagel reaction: (i) the basic N-moieties of the ZIF-8 framework[32] and (ii) DMAP.[33] Here, both ZIF-8 and DMAP were first independently tested as catalysts for the Knoevenagel condensation of benzaldehyde with malononitrile under the optimized conditions of benzyl alcohol oxidation set before.

The use of ZIF-8 alone results in benzyl alcohol conversion and BIM yield higher than 95% after 5 h of reaction (Figure 10a). With DMAP alone, benzyl alcohol is fully converted and the yield of BIM reaches 94% after 1 h of reaction (Figure 10b). However, the yield of BIM decreases after reaching this maximum. We hypothesize that this drop is due to the reaction of BIM with the malononitrile dimer to form polyfunctionality substituted benzenes and pyridine derivatives as side products. Both dimerization of malononitrile added as a 2-fold excess compared to benzaldehyde and the reaction of the dimer with BIM were indeed shown to be achieved in basic media and at temperatures close to that used in this study.[34,35] This decrease of BIM yield is however not observed when ZIF-8 alone is used as a catalyst, suggesting that ZIF-8 is selective toward the Knoevenagel reaction under the reaction conditions set in this study (Figure 10a).

The stepwise process coupling benzyl alcohol oxidation with the Knoevenagel reaction was then achieved with Cu/ZIF-8(H_2) as the catalyst (Scheme 3).

In a first attempt, all reagents involved in the two reactions were added at once into the reaction mixture in order to perform the tandem reaction in a one-step process. However, the combination did not allow for the oxidation of benzyl alcohol to occur. A similar result was reported by Hinde and collaborators, who also studied the association of alcohol oxidation and subsequent Knoevenagel condensation but with a different catalytic system.[36] The deleterious effect of malononitrile over the oxidation of benzyl alcohol during the alcohol oxidation step is probably due to the poisoning of the copper nanoparticle surface. Alternatively, malononitrile was therefore added only after completion of the benzyl oxidation

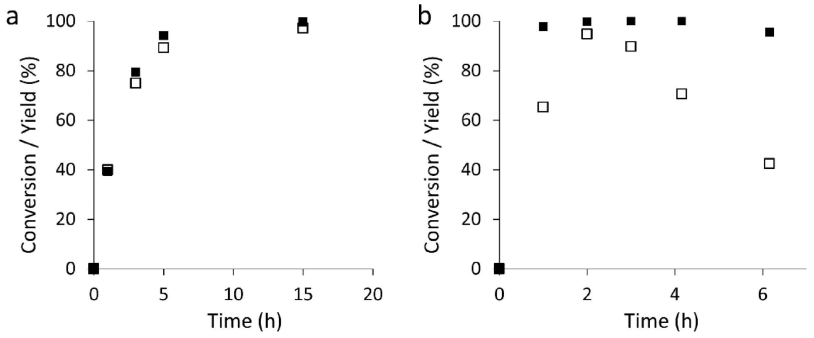

Figure 10. Activities of (a) ZIF-8 and (b) DMAP as catalysts for the Knoevenagel condensation of benzaldehyde with malononitrile. Filled squares correspond to the benzaldehyde conversion and empty squares represent the benzylidene malononitrile yield. Reaction conditions: (a) 5 mg of ZIF-8, 190 mM malononitrile, 100 mM benzaldehyde, 2 mL of acetonitrile, and 70 °C; (b) 5.7 mM DMAP, 190 mM malononitrile, 100 mM benzaldehyde, 2 mL of acetonitrile, and 70 °C.

https://doi.org/10.1021/acsami.3c08906
ACS Appl. Mater. Interfaces 2023, 15, 38716−38728

step (at t= 26 h). Resulting yields of benzyl alcohol, benzaldehyde, and benzylidene malononitrile as a function of time are shown in Figure 11.

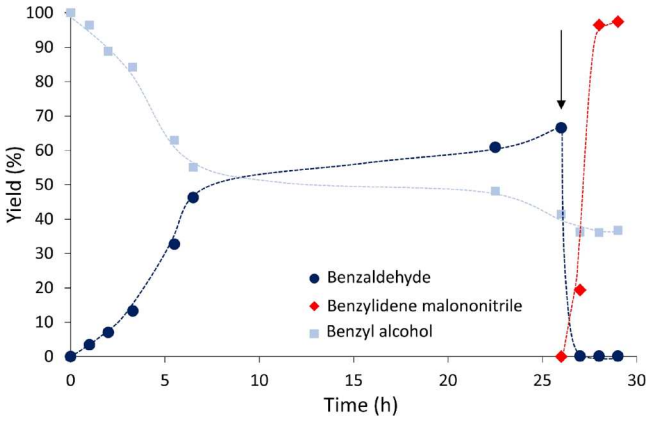

Figure 11. Time course for the one-pot tandem reaction. Malononitrile was added after 26 h of benzyl alcohol oxidation (indicated by the arrow). Colored dotted lines were drawn to guide the eyes. Reaction conditions: 5 mg of Cu/ZIF-8(H_2), 5 mM TEMPO, 100 mM benzyl alcohol, 5.7 mM DMAP, 190 mM malononitrile, 1 atm of air, 2 mL of acetonitrile, and 70 °C.

A benzaldehyde yield of 65% is reached after 26 h. Then, the addition of malononitrile to the reaction mixture leads to the consumption of benzaldehyde that occurs concomitantly to the production of benzylidene malononitrile. The latter product is obtained with a yield higher than 95% relative to benzaldehyde after only 2 h of reaction that is a yield equal to 65% when it is calculated based on the benzyl alcohol. The same tandem reaction is achieved without DMAP. The yield of benzaldehyde then reaches 16% after 66 h and the yield of benzylidene malononitrile is 5% after addition of the malononitrile based on the benzyl alcohol quantity introduced at the start of the reaction. This result confirms the critical role of DMAP in the catalysis of benzyl alcohol oxidation (Figure 9b).

4. CONCLUSIONS

Surface-oxidized-Cu^0 nanoparticles supported on ZIF-8 crystals with a significant activity toward the oxidation of benzyl alcohol were synthesized by the impregnation of ZIF-8 with a copper precursor followed by the reduction of Cu^{2+} into Cu^0 nanoparticles. The oxidation of the nanoparticle surface then occurred during the storage of the catalysts under ambient conditions. Two procedures were followed and compared for the reduction of the Cu^{2+} cations into Cu^0: (i) a dried treatment at high temperature under H_2 flow and (ii) a wet treatment in an aqueous solution of $NaBH_4$. Only the dry reduction procedure under a H_2 atmosphere allowed for the synthesis of well-dispersed Cu^0 nanoparticles located within the bulk of the ZIF-8 crystals. The entrapment of the copper nanoparticles within the microporous hybrid network conferred to the catalysts (Cu/ZIF-8(H_2)) a high stability and a potential for selective catalysis based on the molecular size of the substrates. In contrast, the use of $NaBH_4$ led to the formation of copper nanoparticles exclusively located on the external surface of the ZIF-8 crystals. It is noteworthy that copper nanoparticles were observed along with ZnO impurities generated by the partial degradation of the MOF during the $NaBH_4$ treatment. The resulting catalyst Cu/ZIF-8($NaBH_4$) presented a lower stability than Cu/ZIF-8(H_2). To our knowledge, the effect of the procedure of metal precursor reduction over (i) the location of the final metal nanoparticles on MOF and (ii) the purity of the sample was not reported yet. Finally, the most stable and pure catalyst (Cu/ZIF-8(H_2)) was successfully applied to implement a one-pot cascade chemical process where the benzyl alcohol oxidation into benzaldehyde is subsequently transformed into benzylidene malononitrile by a Knoevenagel condensation step catalyzed by both DMAP and the basic imidazolate linkers of the ZIF-8 framework.

■ ASSOCIATED CONTENT

Supporting Information

The Supporting Information is available free of charge at https://pubs.acs.org/doi/10.1021/acsami.3c08906.

H_2-TPR analysis of Cu^{2+}/ZIF-8; the size histograms of Cu nanoparticles in Cu/ZIF-8($NaBH_4$) and Cu/ZIF-8(H_2); additional HRTEM images of Cu/ZIF-8-($NaBH_4$); local atomic composition analyses of the ZnO nanoparticles in Cu/ZIF-8($NaBH_4$); HTEM images and PXRD analyses of ZIF-8 crystals dispersed in water without $NaBH_4$ and in an aqueous solution of $NaBH_4$; photoluminescence spectra of ZIF-8, ZIF-8 after $NaBH_4$ treatment and ZIF-8 treated with H_2; additional TEM images of copper nanoparticles in Cu/ZIF-8(H_2); XPS signals on the Cu 2p BE range and the calculation used to quantify Cu(II) on the copper nanoparticle surface; comparison of the XRD patterns and N_2 adsorption isotherms of Cu/ZIF-8($NaBH_4$) and Cu/ZIF-8(H_2) before and after five catalysis cycles; a table comparing the different supported copper-based catalysts (supported single sites and copper nanoparticles) used for the aerobic oxidation of benzyl alcohol reported in the literature with Cu/ZIF-8(H_2) (PDF)

■ AUTHOR INFORMATION

Corresponding Authors

Claude Jolivalt − *Sorbonne Université, CNRS, Laboratoire de Réactivité de Surface (LRS), Paris 75005, France;* orcid.org/0000-0002-0318-5421; Email: claude.jolivalt@sorbonne-universite.fr

Julien Reboul − *Sorbonne Université, CNRS, Laboratoire de Réactivité de Surface (LRS), Paris 75005, France;* orcid.org/0000-0002-5716-9603; Email: julien.reboul@sorbonne-universite.fr

Authors

Yifan Zan − *Sorbonne Université, CNRS, Laboratoire de Réactivité de Surface (LRS), Paris 75005, France;* orcid.org/0000-0003-3134-5303

Ferdaous Ben Romdhane − *Fédération de Chimie et Matériaux de Paris-Centre (FCMat), Paris 75005, France*

Antoine Miche − *Sorbonne Université, CNRS, Laboratoire de Réactivité de Surface (LRS), Paris 75005, France*

Christophe Méthivier − *Sorbonne Université, CNRS, Laboratoire de Réactivité de Surface (LRS), Paris 75005, France*

Jean-Marc Krafft − *Sorbonne Université, CNRS, Laboratoire de Réactivité de Surface (LRS), Paris 75005, France*

Complete contact information is available at: https://pubs.acs.org/10.1021/acsami.3c08906

Author Contributions

The manuscript was written through contributions of all authors. All authors have given approval to the final version of the manuscript.

Funding

The work was funded by the doctoral school ED 397 of Sorbonne University

Notes

The authors declare no competing financial interest.

■ ACKNOWLEDGMENTS

The authors thank the Ministère de l'Enseignement Supérieur, de la Recherche et de l'Innovation for providing the financial support for the work of Y.Z. This work was supported by Sorbonne Université, Centre National de la Recherche Scientifique (CNRS) and Région Ile de France.

■ REFERENCES

(1) Arends, I. W. C. E.; Sheldon, R. A. *Modern Oxidation Methods*, 2nd ed.; Backvall, J.-E., Ed.; Wiley VCH: Weinheim, Germany, 2010.

(2) Ferraz, C. P.; Garcia, M. A. S.; Teixeira-Neto, É.; Rossi, L. M. Oxidation of Benzyl Alcohol Catalyzed by Gold Nanoparticles Under Alkaline Conditions: Weak vs. Strong Bases. *RSC Adv.* **2016**, *6*, 25279−25285.

(3) Durndell, L. J.; Cucuzzella, C.; Parlett, C. M. A.; Isaacs, M. A.; Wilson, K.; Lee, A. F. Platinum Catalysed Aerobic Selective Oxidation of Cinnamaldehyde to Cinnamic Acid. *Catal. Today* **2019**, *333*, 161−168.

(4) Silva, T. F. S.; Martins, L. M. D. R. S. Recent Advances in Copper Catalyzed Alcohol Oxidation in Homogeneous Medium. *Molecules* **2020**, *25* (3), 748−762.

(5) Ryland, B. L.; Stahl, S. S. Practical Aerobic Oxidations of Alcohols and Amines with Homogeneous Copper/TEMPO and Related Catalyst Systems. *Angew. Chem. Int. Ed.* **2014**, *53* (34), 8824−8838.

(6) Silva, T. F. S.; Martins, L. M. D. R. S. Recent Advances in Copper Catalyzed Alcohol Oxidation in Homogeneous Medium. *Molecules* **2020**, *25*, 748−762.

(7) Xu, B.; Senthilkumar, S.; Zhong, W.; Shen, Z.; Lu, C.; Liu, X. Magnetic Core−Shell Fe_3O_4@Cu_2O and Fe_3O4@Cu_2O−Cu Materials as Catalysts for Aerobic Oxidation of Benzylic Alcohols Assisted by TEMPO and N-methylimidazole. *RSC Adv.* **2020**, *10*, 26142−26150.

(8) Ibrahem, I.; Iqbal, M. N.; Verho, O.; Eivazihollagh, A.; Olsén, P.; Edlund, H.; Tai, C. W.; Norgren, M.; Johnston, E. V. Copper Nanoparticles on Controlled Pore Glass and TEMPO for the Aerobic Oxidation of Alcohols. *ChemNanoMat* **2018**, *4*, 71−75.

(9) Buxaderas, E.; Graziano-Mayer, M.; Volpe, M.; Radivoy, G. Bimetallic Cu-Pd Nanoparticles Supported on Bio-silica as an Efficient Catalyst for Selective Aerobic Oxidation of Benzylic Alcohols. *Synthesis* **2016**, *49*, 1387−1393.

(10) Ju, S.; Yusuf, M.; Jang, S.; Kang, H.; Kim, S.; Park, K. H. Simple Transformation of Hierarchical Hollow Structures by Reduction of Metal−Organic Frameworks and Their Catalytic Activity in the Oxidation of Benzyl Alcohol. *Chem. Eur. J.* **2019**, *25*, 7852−7859.

(11) Zhang, K.; Shang, H.; Li, B.; Wang, Z.; Lu, Y.; Wang, X. Structural Design of Metal Catalysts Based on ZIFs: From Nanoscale to Atomic Level. *Nano Select* **2021**, *2*, 1902−1925.

(12) Wang, W.; Chen, S.; Guisasola Cal, E.; Martínez Moro, M.; Moya, S.; Coy, E.; Wang, C.; Hamon, J. R.; Astruc, D. ZIF-8-based vs. ZIF-8-Derived Au and Pd Nanoparticles as Efficient Catalysts for the Ullmann Homocoupling reaction. *Inorg. Chem. Front.* **2020**, *7*, 3945−3952.

(13) Kamaraj, K.; Kim, E.; Galliker, B.; Zakharov, L. N.; Rheingold, A. L.; Zuberbühler, A. D.; Karlin, K. D. Copper(I) and Copper(II) Complexes Possessing Cross-Linked Imidazole-Phenol Ligands: Structures and Dioxygen Reactivity. *J. Am. Chem. Soc.* **2003**, *125* (20), 6028−6029.

(14) Abdelhamid, H. N. A Review on Hydrogen Generation from the Hydrolysis of Sodium Borohydride. *Int. J. Hydrogen Energy* **2021**, *46* (1), 726−765.

(15) Zhou, Y. H.; Cao, X.; Ning, J.; Ji, C.; Cheng, Y.; Gu, J. Pd-Doped Cu Nanoparticles Confined by ZIF-67@ZIF-8 for Efficient Dehydrogenation of Ammonia Borane. *Int. J. Hydrogen Energy* **2020**, *45* (56), 31440−31451.

(16) Lv, X. W.; Wang, L.; Wang, G.; Hao, R.; Ren, J. T.; Liu, X.; Duchesne, P. N.; Liu, Y.; Li, W.; Yuan, Z. Y.; Ozin, G. A. ZIF-supported AuCu Nanoalloy for Ammonia Electrosynthesis from Nitrogen and Thin Air. *J. Mater. Chem. A* **2020**, *8*, 8868−8874.

(17) Guo, C.; Liang, C.; Qin, X.; Gu, Y.; Gao, P.; Shao, M.; Wong, W. t. Zeolitic Imidazolate Framework Cores Decorated with Pd Nanoparticles and Coated Further with Metal−Organic Framework Shells (ZIF-8@Pd@MOF-74) as Nanocatalysts for Chemoselective Hydrogenation Reactions. *ACS Appl. Nano Mater.* **2020**, *3* (7), 7242−7251.

(18) Feng, Y.; Yan, G.; Wang, T.; Jia, W.; Zeng, X.; Sperry, J.; Sun, Y.; Tang, X.; Lei, T.; Lin, L. Cu^1−Cu^0 Bicomponent CuNPs@ZIF-8 for Highly Selective Hydrogenation of Biomass Derived 5-Hydroxymethylfurfural. *Green Chem.* **2019**, *21*, 4319−4323.

(19) Tuan, D. D.; Lin, K. Y. A. Ruthenium Supported on ZIF-67 as an Enhanced Catalyst for Hydrogen Generation from Hydrolysis of Sodium Borohydride. *Chem. Eng. J.* **2018**, *351*, 48−55.

(20) Kang, N.; Shen, R.; Li, B.; Fu, F.; Espuche, B.; Moya, S.; Salmon, L.; Pozzo, J. L.; Astruc, D. Dramatic Acceleration by Visible Light and Mechanism of AuPd@ZIF-8-catalyzed Ammonia Borane Methanolysis for Efficient Hydrogen Production. *J. Mater. Chem. A* **2023**, *11*, 5245−5256.

(21) Feng, P. L.; Perry, J. J.; Nikodemski, S.; Jacobs, B. W.; Meek, S. T.; Allendorf, M. D. Assessing the Purity of Metal-Organic Frameworks Using Photoluminescence: MOF-5, ZnO Quantum Dots, and Framework Decomposition. *J. Am. Chem. Soc.* **2010**, *132*, 15487−15489.

(22) Liu, S.; Xiang, Z.; Hu, Z.; Zheng, X.; Cao, D. Zeolitic Imidazolate Framework-8 as a Luminescent Material for the Sensing of Ions and Small Molecules. *J. Mater. Chem.* **2011**, *21*, 6649−6653.

(23) Kumbhakar, P.; Singh, D.; Tiwary, C. S.; Mitra, A. K. Chemical Synthesis and Visible Photoluminescence Emission from Monodispersed ZnO Nanoparticles. *Chalcogenide Lett.* **2008**, *5* (12), 387−394.

(24) Parihar, V.; Raja, M.; Paulose, R. A Brief Review of Structural, Electrical and Electrochemical Properties of Zinc Oxide Nanoparticles. *Rev. Adv. Mater. Sci.* **2018**, *53*, 119−130.

(25) Biesinger, M. C. Advanced Analysis of Copper X-ray Photoelectron Spectra. *Surf. Interface Anal.* **2017**, *49* (13), 1325−1334.

(26) Yu, T.; Cai, Q.; Lian, G.; Bai, Y.; Zhang, X.; Zhang, X.; Liu, L.; Zhang, S. Mechanisms Behind High CO_2/CH_4 Selectivity using ZIF-8 Metal Organic Frameworks with Encapsulated Ionic Liquids: A Computational Study. *Chem. Eng. J.* **2021**, *419*, No. 129638.

(27) Moreno, I.; Dummer, N. F.; Edwards, J. K.; Alhumaimess, M.; Sankar, M.; Sanz, R.; Pizarro, P.; Serrano, D. P.; Hutchings, G. J. Selective Oxidation of Benzyl Alcohol Using In Situ Generated H_2O_2 over Hierarchical Au−Pd Titanium Silicalite Catalysts. *Catal. Sci. Technol.* **2013**, *3*, 2425−2434.

(28) Hoover, J. M.; Ryland, B. L.; Stahl, S. S. Copper/TEMPO-Catalyzed Aerobic Alcohol Oxidation: Mechanistic Assessment of Different Catalyst Systems. *ACS Catal.* **2013**, *3* (11), 2599−2605.

(29) van Beurden, K.; de Koning, S.; Molendijk, D.; van Schijndel, J. The Knoevenagel Reaction: a Review of the Unfinished Treasure Map to Forming Carbon−Carbon Bonds. *Green Chem. Lett. Rev.* **2020**, *13* (4), 349−364.

(30) Sidhu, A.; Sharma, J. R.; Rai, M. Chemoselective Reaction of Malononitrile with Imine-Ones and Antifungal Potential of Products. *Indian J. Chem.* **2010**, *49*, no−250.

(31) Maltsev, S. S.; Mironov, M. A.; Bakulev, V. A. Synthesis of Cyclopentene Derivatives by the Cyclooligomerization of Isocyanides

https://doi.org/10.1021/acsami.3c08906
ACS Appl. Mater. Interfaces 2023, 15, 38716−38728

with Substituted Benzylidenemalononitriles. *Mendeleev Commun.* **2006**, *16*, 201−202.
(32) Amarante, S. F.; Freire, M. A.; Mendes, D. T. S. L.; Freitas, L. S.; Ramos, A. L. D. Evaluation of Basic Sites of ZIFs Metal Organic Frameworks in the Knoevenagel Condensation Reaction. *Appl. Catal. A: Gen.* **2017**, *548*, 47−51.
(33) Shkoor, M.; Bayari, R. DMAP-Catalyzed Reaction of Diethyl 1,3-Acetonedicarboxylate with 2-Hydroxybenzylideneindenediones: Facile Synthesis of Fluorenone-Fused Coumarins. *Synlett* **2021**, *32* (8), 795−799.
(34) Mittelbach, M. An Improved and Facile Synthesis of 2-Amino-1,1,3-Tricyanopropene. *Monatsh. Chem.* **1985**, *116*, 689−691.
(35) Al-Mousawi, S. M.; Moustafa, M. S.; Elnagdi, M. H. Green Synthetic Approaches: Solventless Synthesis of Polyfunctionally Substituted Aromatics as Potential Versatile Building Blocks in Organic Synthesis Utilizing Enaminones and Enaminonitriles as Precursors. *Green Chem. Lett. Rev.* **2011**, *4* (2), 185−193.
(36) Hinde, C. S.; Webb, W. R.; Chew, B. K. J.; Tan, H. R.; Zhang, W. H.; Hor, T. S. A.; Raja, R. Utilisation of Gold Nanoparticles on Amine-Functionalised UiO-66 (NH_2-UiO-66) Nanocrystals for Selective Tandem Catalytic Reactions. *Chem. Commun.* **2016**, *52*, 6557−6560.

NOTE ADDED AFTER ASAP PUBLICATION

Due to a production error, this paper was published ASAP on July 31, 2023, with incorrect wording in the Conclusions section. The corrected version was reposted on August 2, 2023.

https://doi.org/10.1021/acsami.3c08906
ACS Appl. Mater. Interfaces 2023, 15, 38716−38728

Supporting Information.

Copper nanoparticles supported on ZIF-8: comparison of Cu(II) reduction processes and application as benzyl alcohol oxidation catalysts

Yifan Zan[1], Ferdaous Ben Romdhane[2], Antoine Miche[1], Christophe Méthivier[1], Jean-Marc Krafft[1], Claude Jolivalt[1], Julien Reboul[1*]*

[1] Sorbonne Université, CNRS, Laboratoire de Réactivité de Surface (LRS), 4 Place Jussieu, 75005 Paris, France

[2] Fédération de Chimie et Matériaux de Paris- Centre (FCMat), 4 Place Jussieu, 75005 Paris, France

Corresponding author's email adresses :

Julien.reboul@sorbonne-universite.fr

Claude.jolivalt@sorbonne-universite.fr

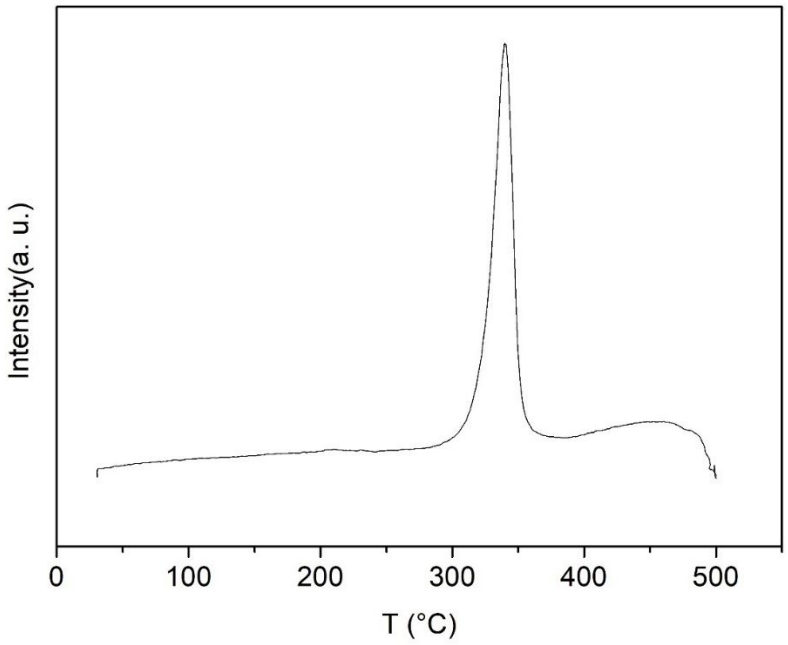

Figure S1. H_2-TPR analysis of Cu^{2+}/ZIF-8.

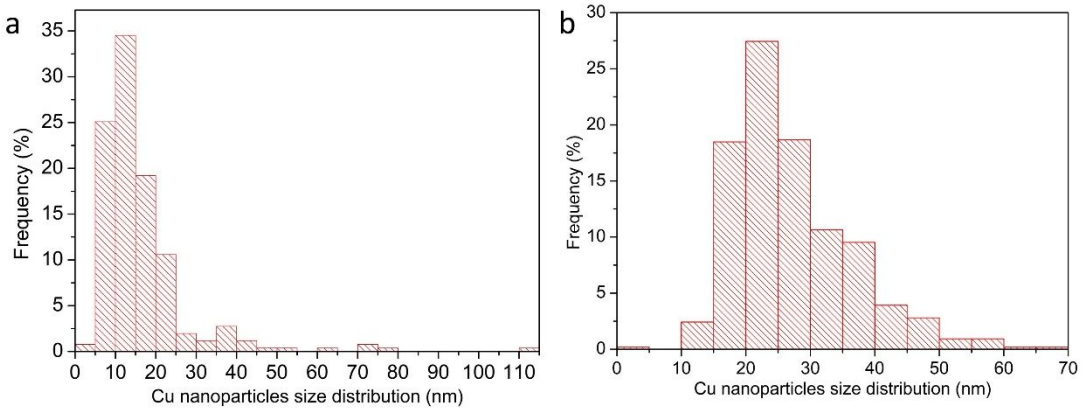

Figure S2. Size histograms of Cu nanoparticles in (a) Cu/ZIF-8($NaBH_4$) and (b) Cu/ZIF-8(H_2).

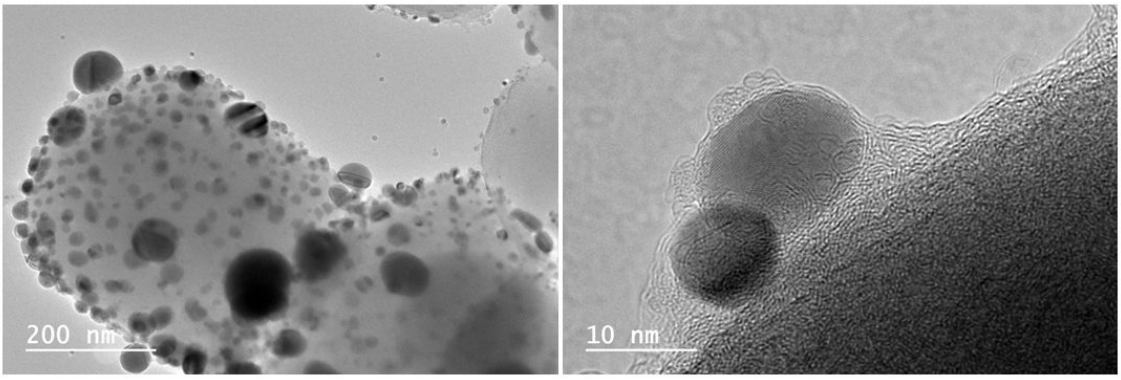

Figure S3. Additional HRTEM images of Cu/ZIF-8($NaBH_4$).

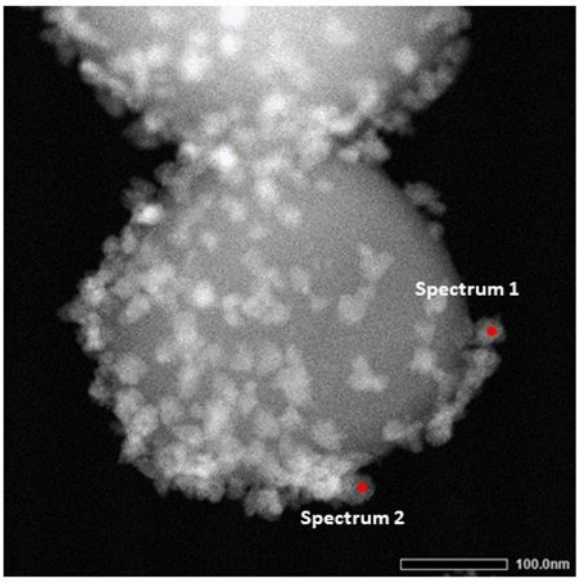

Figure S4. STEM image of Cu/ZIF-8($NaBH_4$) indicating the two areas where EDX measures were achieved.

Local atomic composition analyses of the ZnO nanoparticles performed on the two areas pointed on Fig S4.

Atoms	N	O	Cu	Zn	Total
Spectrum 1	0.00	62.31	0.69	37.00	100.00
Spectrum 2	0.00	63.55	0.32	36.14	100.00

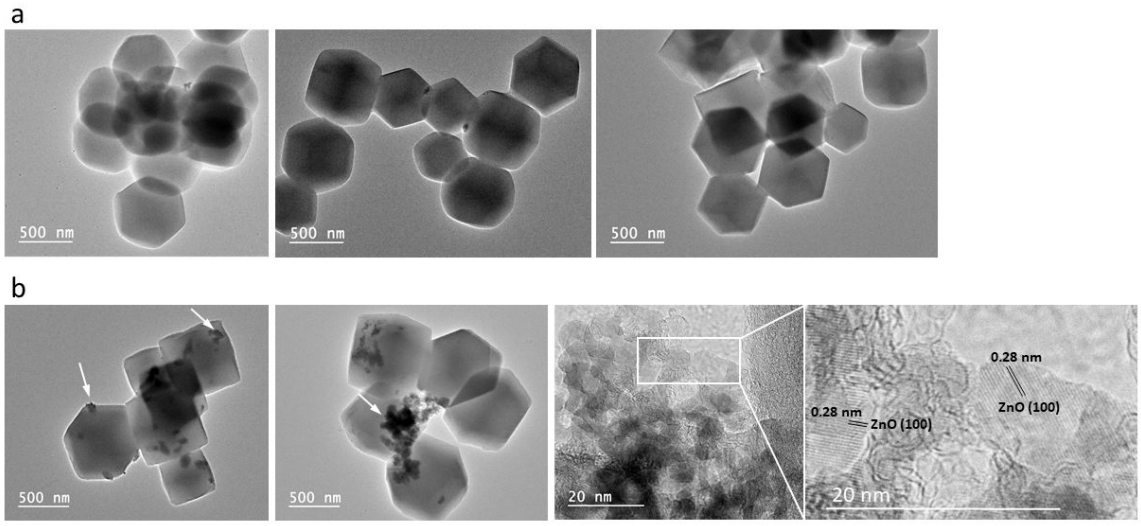

Figure S5. HTEM images of (a) ZIF-8 after dispersion in water (without $NaBH_4$) and (b) ZIF-8 after dispersion in an aqueous solution of $NaBH_4$.

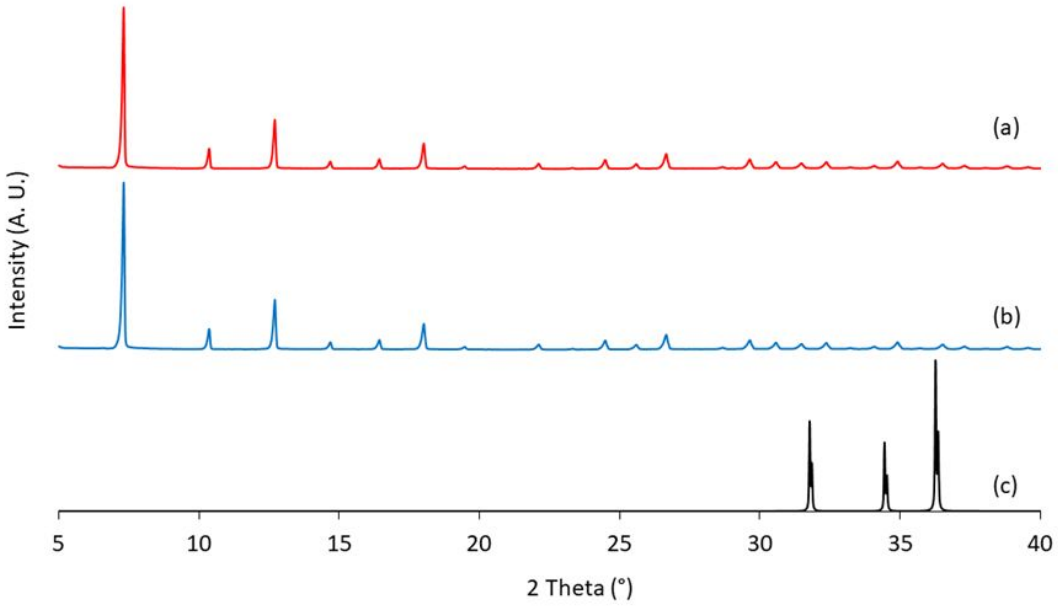

Figure S6. PXRD profiles of (a) ZIF-8 dispersed in an aqueous solution of $NaBH_4$, (b) ZIF-8 dispersed in water (without $NaBH_4$) and (c) calculated profiles of ZnO.

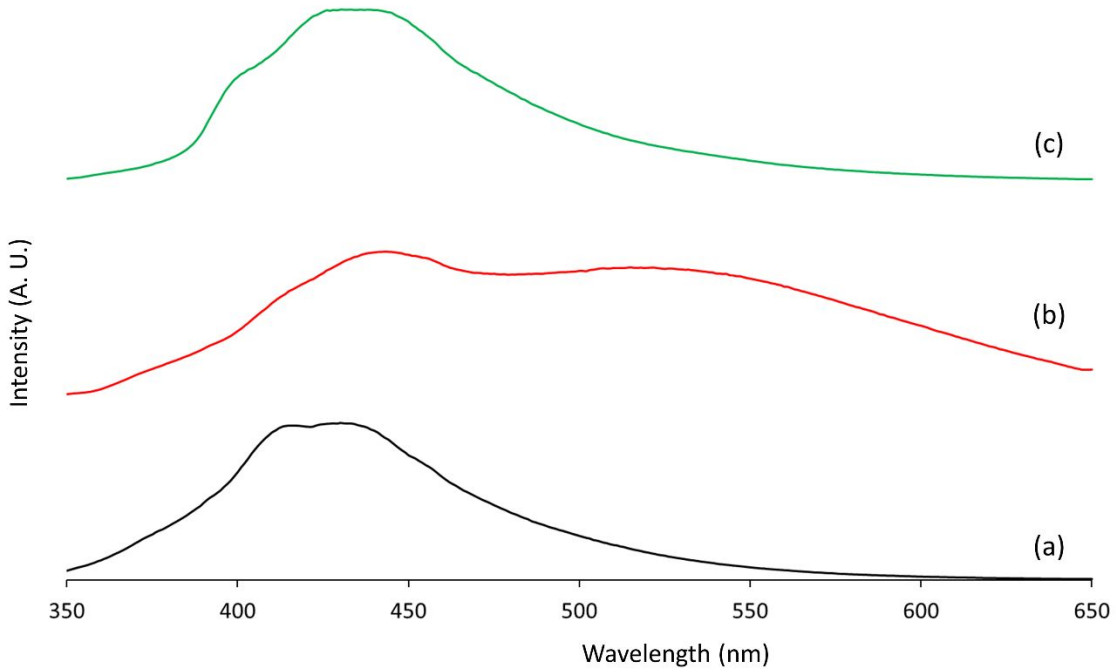

Figure S7. Comparison of the emission spectra for (a) ZIF-8, (b) ZIF-8 treated with $NaBH_4$ and (c) ZIF-8 treated with H_2.

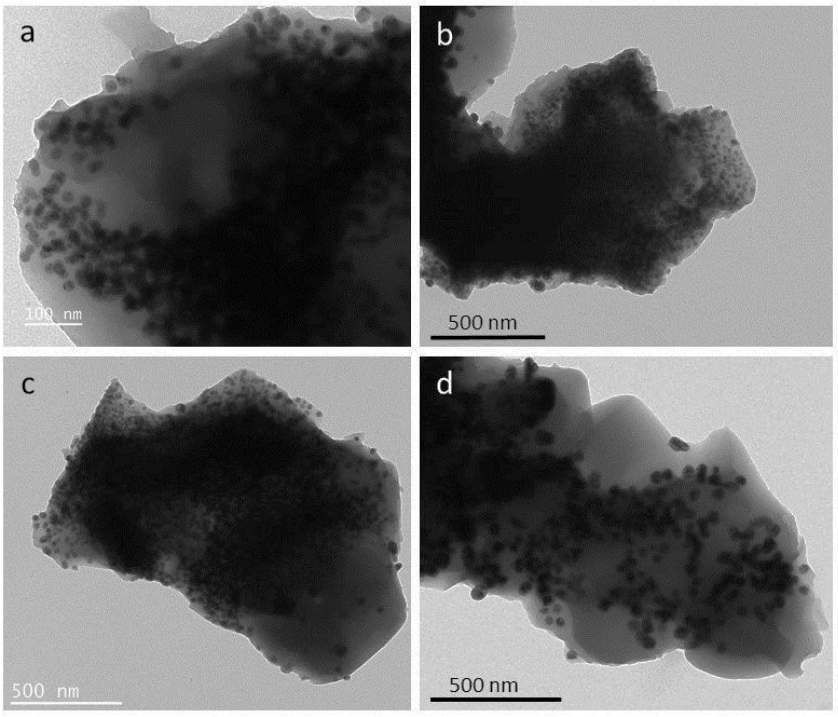

Figure S8. (a-d) Additional TEM images of copper nanoparticles in Cu/ZIF-8(H_2).

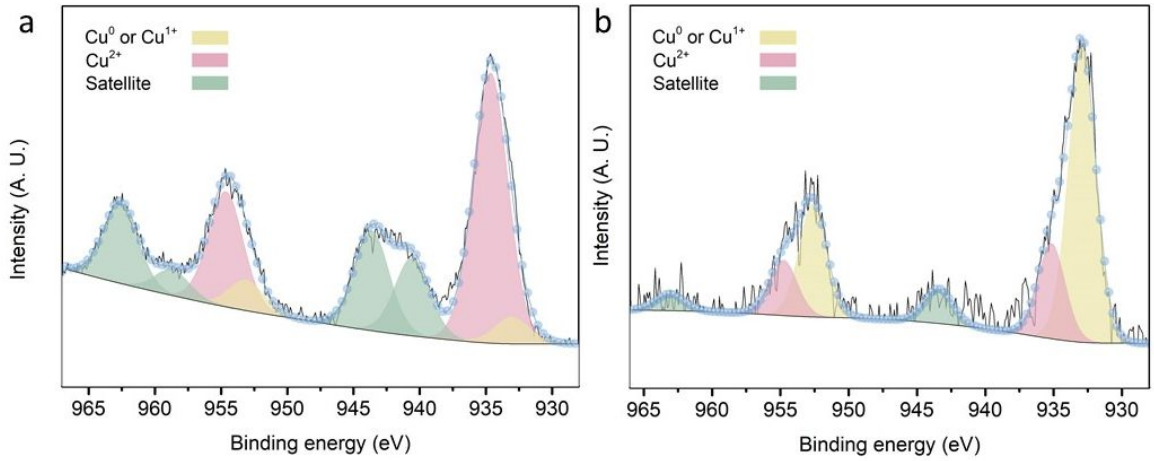

Figure S9. XPS signals on Cu 2p BE range of (a) Cu/ZIF-8($NaBH_4$) and (b) Cu/ZIF-8(H_2).

Quantification of Cu(II) on the copper nanoparticle surface: details of the calculation as given in the reference [1].

%Cu(II) = (B + (A1)/(A+B) x 100

= B(1 + (A1s/Bs))/(A+B) x 100

Where B is the area of the shake-up peak and A is the total area of the main peak. Assuming that the oxidized copper species evidenced on CuZIF-8 surface are mainly formed of copper hydroxide, the main peak/shake-up satellite peak area (A1s/Bs) is equal to 1.57.[1]

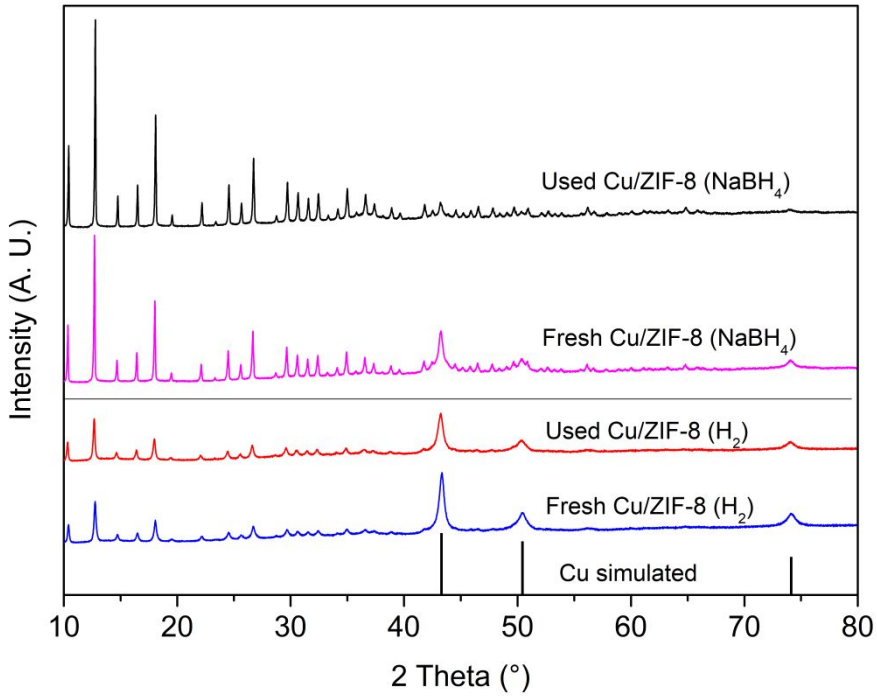

Figure S10. Comparation of XRD patterns of Cu/ZIF-8($NaBH_4$) and Cu/ZIF-8(H_2) before and after 5 catalysis cycles (named “used Cu/ZIF-8”).

Supported Cu single sites					
Catalytic system	**Reaction conditions**	**n_{Cu} : $n_{benz.\ alc.}$ (mmol)**	**Yield**	**Selectivity**	**Ref.**
Cu(I)-Y zeolite / TEMPO	T = 60°C ; ethanol ; 18h ; air atm. ; No additional base added	0.34 : 1	>99%	>99%	2
$Cu_3(BTC)_2$ (MOF) / TEMPO	T = 75°C ; CH_3CN ; 22h ; pure O_2 atm. ; Na_2CO_3	2.4 : 1	91%	>98%	3
Cu(II)/MOF-NH_2 / TEMPO	T = 70°C ; CH_3CN ; 6h ; air atm. ; No additional base added	0.01 : 1	100%	100%	4
$[Cu(DPIO)_2(SiF_6)]$ (TEMPO-decorated MOF)	T = 80°C ; $C_2D_2Cl_4$; 24h ; air atm ; tert-butyl nitrite	0.07 : 1	79%	nc[a]	5
$(NH_4)_4[CuMo_6O_{18}(OH)_6]\cdot 5H_2O$ (POM) / No TEMPO	T = 60°C ; H_2O/CH_3CN ; 15h ; pure O_2 atm. ; No additional base added	0.01 : 1	90%	99%	6
SiO_2-Cu(II) / TEMPO	T = 110°C ; Toluene ; 3h ; pure O_2 atm ; K_2CO_3	0.05 : 1	93%	nc	7
MCM-41-bpy-Cu(I) / TEMPO	T = 50°C ; ethanol ; 15h ; air atm ; $NH_3.H_2O$	0.10 : 1	95%	100%	8
MCM-41-2,6-bis[(N-phenyl)amido]-4-	T = 80°C ; toluene ;	nc	80%	100%	9

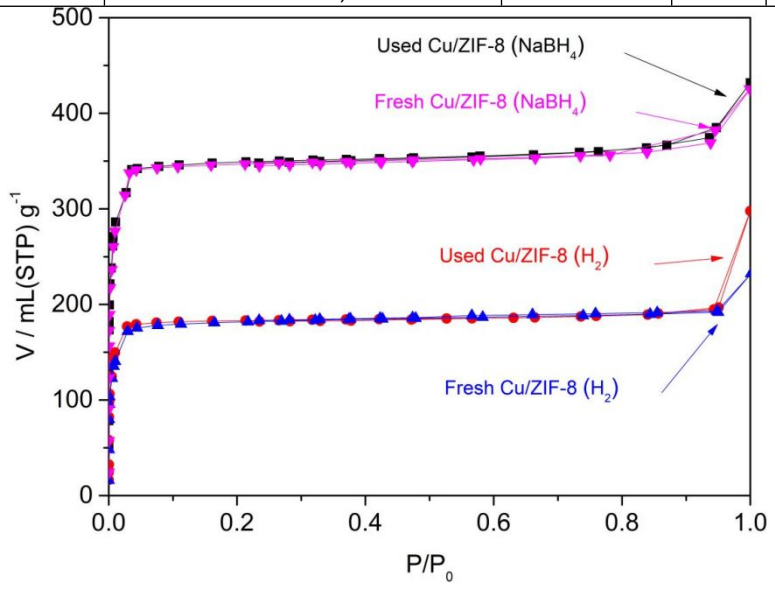

Figure S11. Comparation of N_2 adsorption isothermals of Cu/ZIF-8 ($NaBH_4$) and Cu/ZIF-8 (H_2) before and after 5 cycles (named "used Cu/ZIF-8").

Table S1. Comparison of supported *copper*-based catalysts (supported single sites and copper nanoparticles) for the *aerobic* oxidation of benzyl alcohol reported in the literature with Cu/ZIF-8(H_2).

methylphenol-Cu(II) / TEMPO	16h ; pure O_2 atm ; No additional base added				
Supported copper oxide or surface-oxidized Cu(0) nanoparticles					
Catalytic system	**Reaction conditions**	**n_{Cu} : $n_{benz.\ alc.}$ (mmol)**	**Yield**	**Selec.**	**Ref.**
CuO-rectorite (clay-mineral) / TEMPO	T = 50°C ; H_2O ; 24h ; pure O_2 atm ; K_2CO_3	0.019 : 1	90%	100%	10
Cu_2O-Fe_3O_4 / TEMPO	T = 25°C ; CH_3CN ; 18h ; pure O_2 atm. ; N-methylimidazole	0.02 : 1	>99%	>99%	11
$CuFe_2O_4$ / TEMPO	T = 100°C ; H_2O ; 24h ; pure O_2 atm. ; No additional base added	0.10 : 1	95%	nc	12
Cu NPs supported on MOF-derived carbon / TEMPO	T = 70°C ; CH_3CN ; 9h ; pure O_2 atm. ; N-methylimidazole	0.05 : 1	94%	nc	13
Cu NPs supported on MOF-derived composite / TEMPO	T = 75°C ; DMF ; 0.5h ; pure O_2 atm. ; Na_2CO_3	0.7 : 1	99%	99%	14
Cu NPs supported on nitrogen-doped carbon / TEMPO	T = 60°C ; CH_3CN ; 5h ; pure O_2 atm. ; N-methylimidazole	0.01 : 1	>99%	>99%	15
Cu NPs supported on organized mesoporous polymer / No TEMPO	T = 150°C ; CH_3CN ; 24h ; pure O_2 (1 MPa) ; No additional base added	0.01 : 1	86%	100%	16
Cu NPs supported on aminopropyl-functionalized porous glass / TEMPO	T = 50°C ; No solvent ; 5.5h ; pure O_2 atm. ; No additional base added	0.05 : 1	95%	nc	17
Cu NPs supported on polyacrylamide-SBA-15 / TEMPO	T = 69°C ; n-hexane ; 3h ; pure O_2 atm. ; No additional base added	0.178 : 1	80%	100%	18
Cu NP supported on ZIF-8 / TEMPO	T = 70°C ; CH_3CN ; 24h ; air atm. ; 4-dimethylaminopyridine	0.1 : 1	66%	100%	**This work**

[a] nc : not communicated

References :

[1] Biesinger M. C. Advanced Analysis of Copper X-ray Photoelectron Spectra. *Surf. Interface Anal.* **2017**, 49 (13), 1325-1334. DOI: 10.1002/sia.6239

[2] Senthilkumar, S.; Zhong, W.; Natarajan, M.; Lu, C.; Xu, B.; Liu X. A Green Approach for Aerobic Oxidation of Benzylic Alcohols Catalysed by CuI–Y Zeolite/TEMPO in Ethanol Without Additional Additives. *New J. Chem.* **2021**, 45, 705-713. DOI : 10.1039/D0NJ03776A

[3] Dhakshinamoorthy, A.; Alvaro, M.; Garcia, H. Aerobic Oxidation of Benzylic Alcohols Catalyzed by Metal-Organic Frameworks Assisted by TEMPO. *ACS Catal.* **2011**, 1, 48-53. DOI : 10.1021/cs1000703

[4] Taher, A.; Kim, D. W.; Lee, I.-M. Highly Efficient Metal Organic Framework (MOF)-ased Copper Catalysts for the Base-Free Aerobic Oxidation of Various Alcohols. *RSC Adv.* **2017**, 7, 17806-17812. DOI: 10.1039/c6ra28743c

[5] Li, L.; Matsuda, R.; Tanaka, I.; Sato, H.; Kanoo, P.; Jeon, H. J.; Foo, M. L.; Wakamiya, A.; Murata, Y.; Kitagawa, S. A Crystalline Porous Coordination Polymer Decorated with Nitroxyl Radicals Catalyzes Aerobic Oxidation of Alcohols. *J. Am. Chem. Soc.* **2014**, 136, 7543−7546. DOI : 10.1021/ja5019095

[6] Wei, Z.; Ru, S.; Zhao, Q.; Yu, H.; Zhang, G.; Wei, Y. Highly Efficient and Practical Aerobic Oxidation of Alcohols by Inorganic-Ligand Supported Copper Catalysis. *Green Chem.* **2019**, 21, 4069-4075. DOI: 10.1039/c9gc01248f

[7] Gupta, M.; Sharma, P.; GUPTA, Gupta, M. R. Silica Functionalized Cu(II) Catalysed Selective Oxidation of Benzyl Alcohols Using TEMPO and Molecular Oxygen as an Oxidant. *J. Chem. Sci.* **2015**, 127 (8), 1485-1489. DOI 10.1007/s12039-015-0902-2

[8] Zhao, H.; Chen, Q.; Wei, L.; Jiang, Y.; Cai, M. A Highly Efficient Heterogeneous Aerobic Alcohol Oxidation Catalyzed by Immobilization of Bipyridine Copper(I) Complex in MCM-41. *Tetrahedron* **2015**, 71, 8725-8731. DOI: 10.1016/j.tet.2015.09.054

[9] Samanta, S.; Das, S.; Samanta, P. K.; Dutta, S.; Biswas, P. A Mononuclear Copper(II) Complex Immobilized in Mesoporous Silica: an Efficient Heterogeneous Catalyst for the Aerobic Oxidation of Benzylic Alcohols. *RSC Adv.* **2013**, 3, 19455-19466. DOI: 10.1039/c3ra41417e

[10] Liu, W.; Yang, J.; Cai, J. Aerobic Alcohol Oxidation Catalyzed by CuO-Rectorite/TEMPO in Water. *Res. Chem. Intermed.* **2019**, 45, 549-561. DOI : 10.1007/s11164-018-3618-3

[11] Xu, B.; Senthilkumar, S.; Zhong, W.; Shen, Z.; Lu, C.; Liu, X. Magnetic Core-Shell Fe_3O_4@Cu_2O and Fe_3O_4@Cu_2O–Cu Materials as Catalysts for Aerobic Oxidation of Benzylic Alcohols Assisted by TEMPO and N-methylimidazole. *RSC Adv.* **2020**, 10, 26142-26150. DOI: 10.1039/d0ra04064a

[12] Zhu, X., Yang, D.; Wei, W.; Jiang, M.; Li, L.; Zhu, X.; You, J.; Wang, H. Magnetic Copper Ferrite Nanoparticles/TEMPO Catalyzed Selective Oxidation of Activated Alcohols to Aldehydes under Ligand- and Base-Free Conditions in Water. *RSC Adv.* **2014**, 4, 64930-64935. DOI: 10.1039/c4ra14152k

[13] Kim, B. R.; Oh, J. S.; Kim, J.; Lee, C. Y. Robust Aerobic Alcohol Oxidation Catalyst Derived from Metal–Organic Frameworks. *Catal. Lett.* **2016**, 146, 734-743. DOI : 10.1007/s10562-016-1700-2

[14] Ju, S.; Yusuf, M.; Jang, S.; Kang, H.; Kim, S.; Park, K. H. Simple Transformation of Hierarchical Hollow Structures by Reduction of Metal–Organic Frameworks and Their Catalytic Activity in the Oxidation of Benzyl Alcohol. *Chem. Eur. J.* **2019**, 25, 7852-7859. DOI : 10.1002/chem.201900231

[15] Tobita, F.; Yasukawa, T.; Yamashita, Y.; Kobayashi, Sh. Aerobic Oxidation of Alcohols Enabled by Nitrogen-doped Copper Nanoparticle Catalysts. *Catal. Sci. Technol.* **2022**, 12, 1043-1048. DOI: 10.1039/d1cy01777b

[16] Kong, L.; Zhao, J.; Han, S.; Zhang, T.; He, L.; Zhang, P.; Dai, S. Facile Synthesis of Copper Containing Ordered Mesoporous Polymers via Aqueous Coordination Self-Assembly for Aerobic Oxidation of Alcohols. *Ind. Eng. Chem. Res.* **2019**, 58, 6438−6445. DOI : 10.1021/acs.iecr.9b00669

[17] Ibrahem, I.; Naeem Iqbal, M.; Verho, O.; Eivazihollagh, A.; Olsén, P.; Edlund, H.; Tai, C.-W.; Norgren, M.; Johnston, E. V. Copper Nanoparticles on Controlled Pore Glass and TEMPO for the Aerobic Oxidation of Alcohols. *ChemNanoMat* **2018**, 4, 71-75. DOI: 10.1002/cnma.201700309

[18] Kalbasi, R. J.; Abbas Nourbakhsh, A.; Zia, M. Aerobic Oxidation of Alcohols Catalyzed by Copper Nanoparticle-Polyacrylamide/SBA-15 as Novel Polymer-Inorganic Hybrid. *J. Inorg. Organomet. Polym.* **2012**, 22, 536-542. DOI 10.1007/s10904-011-9580-9

Chapter 4.

PdAu nanoparticles supported on ZIF-8 as catalyst for base free aerobic alcohol oxidation in water

4.1. Introduction

Noble metal nanoparticles (NPs) catalysts, such as gold, palladium, and platinum, have been extensively studied for the aerobic oxidation of alcohols.[1–4] Their significant advantage over Cu/TEMPO systems is their excellent efficiency toward oxidation in aqueous phase.[5–7] In addition, their high activity often allows operation at lower catalyst loadings and lower reaction temperatures. It was also found that the combination of noble metals would provide enhanced activity due to the synergistic effect including electron effect, bifunctional effect, ensemble effect, etc. between metal atoms of different elements, for example, Au-Pd, Au-Pt, Au-Ag, etc.[8–11] For instance, the Pd based catalyst are efficient for hydrogenation but in some cases poorly selective. Adding Au enhances the selectivity.[12] Au-Pd bimetallic NPs were shown to be highly active for the oxidation of saturated and unsaturated alcohols such as benzyl alcohols and have shown significantly enhanced activity relative to monometallic Au and Pd catalysts.[5,13,14] Moreover, bimetallic nanoparticles can work without any base addition.[15,16] Bimetallic Au-Pd catalysts therefore allow to achieve alcohol oxidation under mild conditions (close to room temperature, neutral pH and in water) that are compatible with those of enzymes. This makes them good candidates for their involvement in chemoenzymatic catalytic systems. However, an optimal Pd/Au ratio was not clearly established in the literature. This optimal composition may depend on different parameters including the nature of the NP support. To our knowledge, the synthesis of PdAu NPs supported on ZIF-8 with the aim of catalyzing the reaction of alcohol oxidation was not reported yet. In this chapter, the effort therefore focused on the synthesis and characterization of ZIF-8-supported NPs with various Pd/Au ratio and on the study of the effect of the Pd/Au ratio over the activity of the catalysts. The characterization of the synthesized NPs@ZIF-8 catalysts was achieved by means of XRD, N_2 adsorption, TEM, STEM, ICP-OES, and XPS analyses. The assessment of their catalysis performances for the aerobic oxidation of primary and secondary alcohols was carried out using benzyl alcohol and 1-phenylethanol as model substrates.

4.2. Methods

4.2.1. Synthesis of hybrid metallic nanoparticles@ZIF-8 catalysts

ZIF-8 (100 mg, synthesized according to the method described in section 3.2.1 and dried at 90°C) was dispersed in 10 mL of a 4.4 mM metal precursor solution in methanol. In the case of Pd@ZIF-8 (Pd nanoparticles on ZIF-8) and Au@ZIF-8, the precursors are Na_2PdCl_4 and $HAuCl_4 \cdot 3H_2O$, respectively. For the bimetallic nanoparticles synthesis (PdAu@ZIF-8), the precursor solution in methanol consists of a mixture of Na_2PdCl_4 and $HAuCl_4 \cdot 3H_2O$ (molar %: molar %) = 75:25, 50:50 or 25:75, molar proportions. Overall, the total concentration of the 2 metals is 4.4 mM. (See Table 4.1) The suspension was stirred for 24 hours at room temperature. The as-impregnated particles [M]-ZIF-8 (non-reduced samples, [M] refers to Pd, Au or the mixture PdAu) were then recovered by filtration and washed with 30 mL methanol. Finally, the samples were dried under vacuum at 90°C overnight and stored at room temperature before use.

Table 4.1. Initial concentration of precursors in the impregnation solutions

Sample	Pd concentration (mM)	Au Concentration (mM)	Initial Pd/Au (molar % : molar %)
Pd@ZIF-8	4.4	0	-
Au@ZIF-8	0	4.4	-
Pd_9Au_1@ZIF-8	3.3	1.1	75/25
Pd_2Au_1@ZIF-8	2.2	2.2	50/50
Pd_1Au_3@ZIF-8	1.1	3.3	25/75

Nanoparticles formation was induced by flowing 100 mL/min of H_2 for 20 minutes through approximately 100 mg of [M]-ZIF-8 placed in a U-shaped quartz reactor. The reduction temperature was first determined according to a temperature programmed reduction (TPR) experiment performed on the metal-impregnated ZIF-8 (See Figure 4.1).

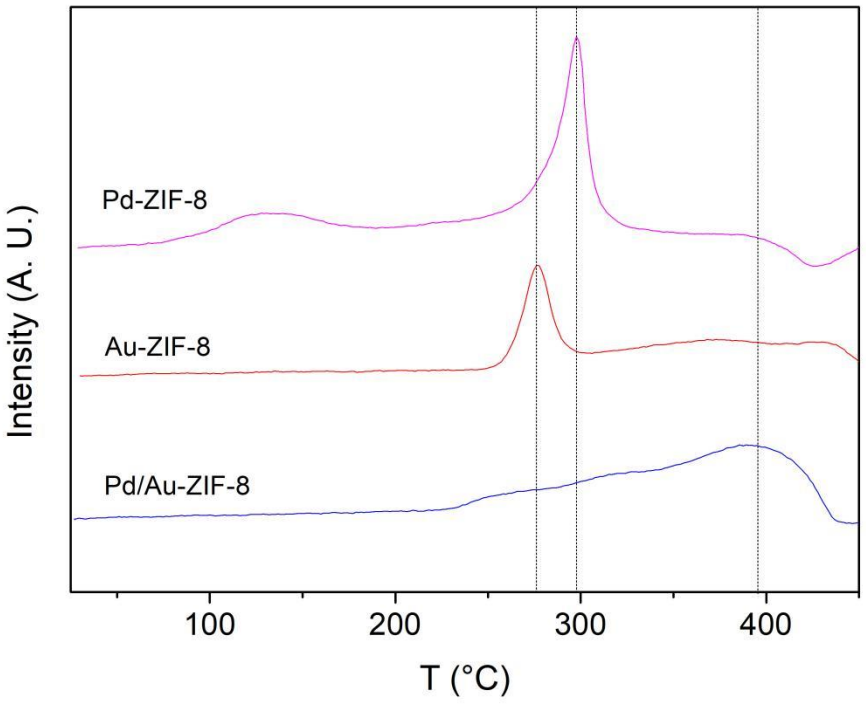

Figure 4.1 TPR patterns of Pd-ZIF-8, Au-ZIF-8, and Pd_2Au_1-ZIF-8
Conditions: Ramp: 5°C/min. 100 mL/min of 5% H_2/Ar flow.

The TPR profiles of non-reduced Pd-ZIF-8 and Au-ZIF-8 showed a H_2 consumption peak with a maximum at 299 °C and 275 °C, respectively, which is attributed to the reduction of Pd^{2+} and Au^{3+} precursors. The reduction temperature of gold and palladium supported on ZIF-8 is higher relative to that previously reported on metal oxide (Pd on SiO_2 170°C), zeolite (Pd on TS-1, 51°C) and other supports [17–20]. The reduction of Pd and Au precursors on ZIF-8 therefore requires particularly high energy, which indicates strong metal-support interactions. TPR profile of Pd-ZIF-8 displays one additional broad reduction peaks at lower temperature, T = 125 °C, suggesting the presence of a proportion of Pd^{2+} precursor that interacts less strongly with the ZIF-8 pore surface or that would be adsorbed on the external surface of the crystals. The TPR profile of the (50/50) bimetallic PdAu-ZIF-8 exhibits no sharp H_2 consumption signal. However, a significant increase of the signal intensity is observed in the 250-430°C range, as if Au-III) and Pd(II) were continuously reduced in this range. Finally, the temperature selected for the formation of the metal nanoparticles based on these TPR results was T = 300 °C because

it allows reducing at least partly Pd^{2+} and Au^{3+} precursors in both mono- and bi-metallic [M]-ZIF-8 without degrading ZIF-8 structure, according to the litterature.[21] The as-reduced samples [M]@ZIF-8 (Pd@ZIF-8, Au@ZIF-8 and PdAu@ZIF-8) were finally dried at 70 °C under vacuum overnight before characterization and catalytic evaluation.

4.2.2. Catalytic aerobic oxidation of alcohols

In a typical experiment, the catalytic aerobic oxidation of benzyl alcohol to benzaldehyde or 1-(±)-phenylethanol (1-PE) to acetophenone (AP) were performed in a 15 mL test tube sealed with a plastic lid. Unless stated in the text, 0.2 mmol alcohol was dissolved in 2 mL of water. Then, 5 mg of catalyst was added. Before sealing the tested tube, the suspension was bubbled with a O_2 flow for 10 minutes. The suspension was then ultrasonicated for 1 minute to disperse the catalyst. The reaction was performed under stirring at 600 rpm at a given temperature controlled with an oil bath. After the reaction was completed, the catalyst was recovered by centrifugation and washed with 2 mL of methanol 3 times. The recovered catalyst is reactivated by vacuum under 90 °C between each cycle of the recycling test. The products of the reaction were analyzed by high performance liquid chromatography (HPLC, Infinity II by Agilent) equipped with a SiELC Primesep 100 column (150 x 4.6 mm, 5µm) and a diode-array detector (DAD). The mobile phase was acetonitrile: 0.1 % v/v trifluoroacetic acid in water (v:v=30: 70). The detection of substrates and products were performed at the wavelength 254 nm and 230 nm and their quantification used a calibration curve method. Conversions and yields are calculated according to the formula:

$$Conversion(\%) = \frac{C_{0(substrate)} - C_{t(substrate)}}{C_{0(substrate)}} * 100$$

$$Yield(\%) = \frac{C_{t(product)}}{C_{0(substrate)}} * 100$$

4.3. Results and discussion

4.3.1. Synthesis and characterization of the catalysts

The monometallic Pd and Au nanoparticles, as well as bimetallic PdAu NPs with different initial Pd/Au ratio, encapsulated inside ZIF-8 according to the method described above were first thoroughly characterized by means of several physico-chemical technics.

4.3.1.1. Elemental composition

The elemental content of gold and palladium in all samples was analyzed by ICP-OES. (See Table 4.2) For monometallic Pd@ZIF-8 and Au@ZIF-8, the Pd and Au contents are 4.46 ± 0.05 wt.% and 4.07 ± 0.05 wt.%, respectively. The incorporation yield of Pd is therefore 100% in Pd@ZIF-8 whereas it is only 51% for Au in Au@ZIF-8. It suggests that during the synthesis, the loss of gold is noteworthy. For the bimetallic samples, the yields all are lower than expected from the results obtained for monometallic NPs. For samples with initial Pd to Au ratios of 75/25, 50/50, and 25/75, the yields of Pd are 94%, 87%, and 41%, respectively. The yields of Au are 35%, 43%, and 44%, respectively. Based on ICP results, the proportions of Pd to Au in the 3 bimetallic samples are calculated as 89/11, 67/33, and 25/75. For easily understanding, the samples are named according to the Pd to Au atomic proportions obtained from ICP. The samples with Pd/Au atomic proportions 89/11, 67/33, and 25/75 are named as Pd_9Au_1, Pd_2Au_1, and Pd_1Au_3, respectively. The different yields of Pd and Au elements reflect the different strengths of interaction between these 2 elements and ZIF-8. Clearly, Pd exhibits a stronger affinity for ZIF-8, resulting in its relatively higher yield. On the other hand, the lower yield of gold can be attributed to the following reasons: i) Not all of the Au precursors are absorbed by ZIF-8 during the impregnation process. ii) Some of the metal NPs are purged onto the tube furnace wall by the H_2 flow during the reduction process. One piece of evidence in favor of the above hypothesis is the pink mirror formation observed on the wall of the furnace tube after the reduction reaction, indicating the shedding of Au^0.

Table 4.2. ICP element analysis

	Pd (±0.05 wt.%)	Pd Yield%	Au (±0.05 wt.%)	Au Yield%	Initial atomic Pd/Au proportions	ICP atomic Pd/Au proportions
Pd@ZIF-8	4.46	100	0.05	-	-	-
Au@ZIF-8	0.06	-	4.07	51	-	-
Pd_9Au_1@ZIF-8	3.13	94	0.69	35	75/25	89/11
Pd_2Au_1@ZIF-8	1.93	87	1.73	43	50/50	67/33
Pd_1Au_3@ZIF-8	0.46	41	2.63	44	25/75	25/75

4.3.1.2. Structural and textural properties

Crystal structures of the reduced materials (M@ZIF-8 series) were investigated by powder X-Ray diffraction (PXRD) (Figure 4.2a). The PXRD patterns are all similar to that of the as-synthesized ZIF-8 indicating that the impregnation nor the reductions step affect the crystal structure of the MOF. The diffraction peaks assignment relative to metal NPs is not obvious for all M@ZIF-8, which can be attributed to the small size of the NPs (< 5 nm). In case of Au@ZIF-8, a broad peak can be observed at 2 θ= 38.8° that corresponds to the {111} plane of Au (JCPDS no. 00-004-0784) (overlaid with one diffraction peak of ZIF-8), thus confirming the presence of Au NPs in this sample (Figure 4.2b). This peak is also observed on the bimetallic sample with the highest Au proportion, ca Pd_1Au_3@ZIF-8 but not for the bimetallic samples with lower Au proportion. It suggests that either there are no pure Au NPs in the sample as a consequence of the formation of PdAu alloy, or/and the Au or alloy NPs are too small to be detected by this technic.

For Pd@ZIF-8, the most intense peak at 2θ = 40° relative to the {111} lattice planes of the Pd crystal (JCPDS no. 00-046-1043) are missing. Instead, two peaks at 2θ = 41.2° and 44.1° attributed to the {111} and {200} planes of the alloy PdZn (JCPDS no. 00-006-0620) can be observed in the pattern. The presence of such an alloy – and its corresponding {111} plane has

already been reported in works describing Pd deposition on ZnO by a wet impregnation method using a Pd precursor, followed by a reduction step at 250 °C using a H_2 flow.[22,23] In these reports, PdZn alloy form on the reduction of Pd/ZnO composites heated in hydrogen. This well-known approach works due to the partial reducibility of ZnO under reductive conditions. The strong interaction between metallic palladium or palladium hydride and the support leads to hydrogen spillover during reduction. This enables the reduction of the ZnO in the vicinity of the palladium particles and the formation of the intermetallic compound ZnPd under relatively mild temperatures from 250°C to 300°C. In this process, ZnO alone cannot be reduced by hydrogen under such low temperatures. Pd NPs are necessary to activate H_2 and thereby produce reactive atomic hydrogen capable of reducing zinc species under mild temperatures.[24] Interestingly, this phenomenon has never been reported for the reduction of Zn^{2+} centers composing MOF frameworks, to our knowledge. This PdZn {111} peak is only detected for Pd@ZIF-8 sample. Interestingly, a new broad peak is observed at 2 θ= 40.9° on the diffractogram of Pd_9Au_1@ZIF-8 suggesting the formation of a Pd/Au alloy phase, consistent with the literature.[25] However, for both Pd_1Au_3@ZIF-8 and Pd_2Au_1@ZIF-8, ca the bimetallic samples with Pd content lower than Pd_9Au_1@ZIF-8,the peak at 2θ = 40.9° is not observed. In that case, the PXRD data do not allow to conclude about the presence of bimetallic Pd/Au alloy or small monometallic Au and Pd NPs.

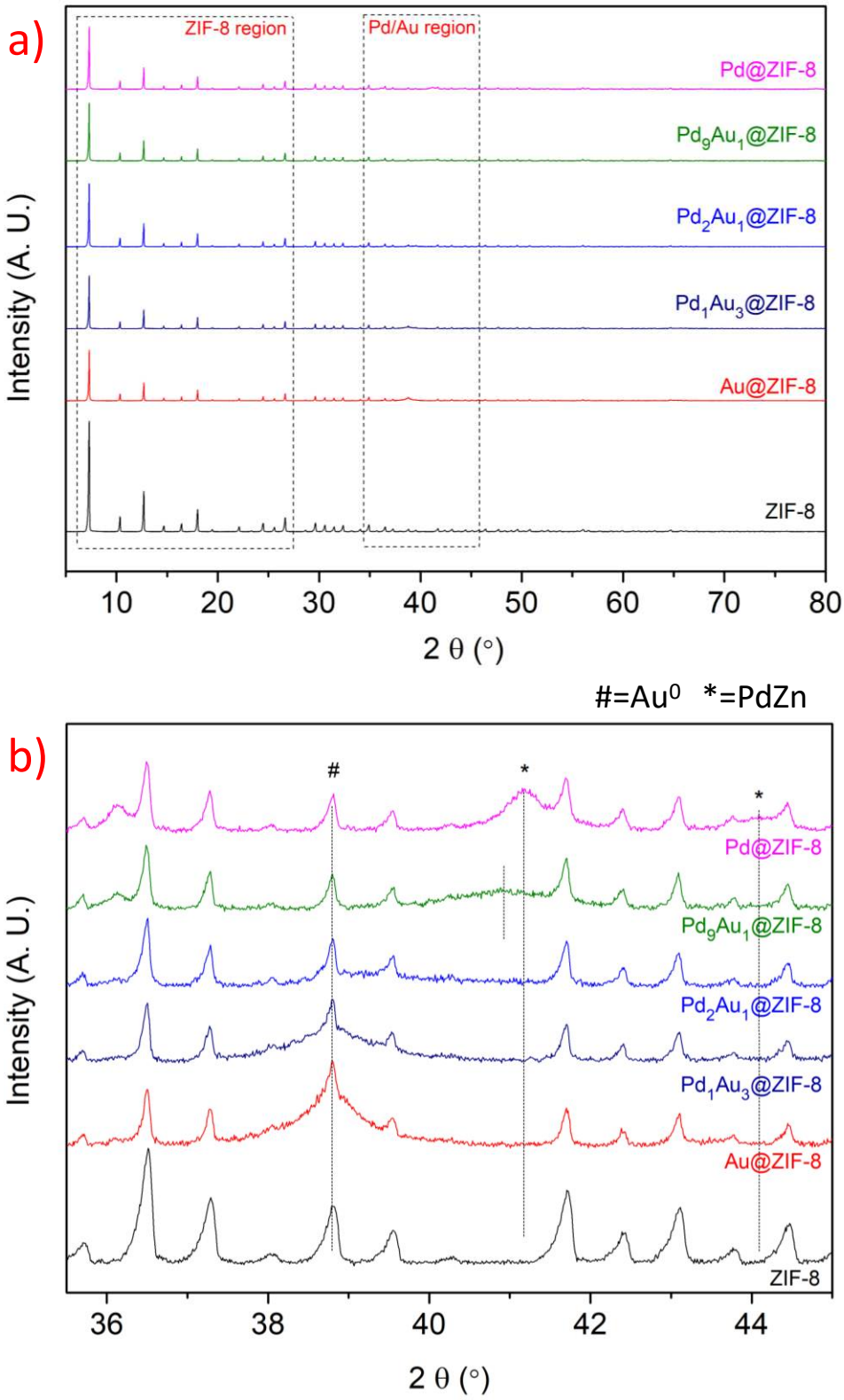

Figure 4.2. a) PXRD patterns of Pd@ZIF-8, Pd_9Au_1@ZIF-8, Pd_2Au_1@ZIF-8 Pd_1Au_3@ZIF-8, Au@ZIF-8, as-synthesized ZIF-8, and simulated ZIF-8; b) zoom-up on the 2-θ range of 35.5 to 45° corresponding to the metal nanoparticles. 38.8° = Au {111}, 41.2° = PdZn {111}, 44.1° = PdZn {200}

In summary, the PXRD patterns confirmed the formation of a metallic phase in both Pd@ZIF-8 and Au@ZIF-8 samples. This analysis also suggests the formation of a bimetallic alloy in the Pd_9Au_1@ZIF-8materials. This X-ray diffraction study revealed that, in the sample containing the pure Pd NPs, a part of the Zn^{2+} centers in ZIF-8 was reduced to form PdZn alloys. Supported PdZn alloys were shown to efficiently catalyze the aerobic oxidation of benzyl alcohol by the group of Pr. Graham J. Hutchings.[26] The presence of Zn in the metal nanoparticles should therefore not be detrimental to the catalysis objectives of this work.

The N_2 adsorption and desorption isotherms measured at 77 k are shown in figure 4.3. The as-synthesized ZIF-8 exhibited a large Brunauer-Emmett-Teller (BET) surface areas of 1442 m^2/g consistent with that already reported in the literature. All samples loaded with metal nanoparticles also showed permanent porosity (Table 4.3). The S_{BET} of Pd@ZIF-8, Pd_9Au_1@ZIF-8, Pd_2Au_1@ZIF-8, Pd_1Au_3@ZIF-8, and Au@ZIF-8 are 867, 1192, 1314, 685, and 363 m^2/g, respectively. Au@ZIF-8 shows both the lowest pore volume and the lowest BET surface area of the series, followed by Pd_1Au_3@ZIF-8. Samples with lower gold content, Pd_2Au_1@ZIF-8 and Pd_9Au_1@ZIF-8 show pore volumes and BET surface area close to those of ZIF-8 alone, although lower, which is expected in the presence of metal NPs inside the MOF. The PXRD patterns show a significant decrease in the crystallinity of ZIF-8 after the NPs synthesis process, and the extent of the decrease in peak intensity also correlates with the decrease in pore volume. As expected, the metal nanoparticles grow within the ZIF-8 at the expense of its crystallinity, surface area and pore volume. Among them, Au@ZIF-8 shows the smallest pore volume, followed by Pd_1Au_3@ZIF-8 whose XRD pattern displays peaks with a drastically reduced intensity. Moreover, the decrease of pore volume may be attributed to the formation of some NPs, which results in the blockage of the pores, as often reported in articles dealing with MOFs supported NPs.[10,27] There is no significant correlation between the metal content and the pore volumes and BET surface areas determined by N_2 sorption analysis. The reason for that is currently unclear. It is supposed to be the cumulative consequences of both crystallinity changes of ZIF-8 during the impregnation and reduction steps as well as the localization of the NPs, either within the bulk crystal or on the external surface of the ZIF-8.

This location difference is indeed known to affect both pore accessibility and MOF crystallinity in very different ways (See article in Chapter 3). In addition, hysteresis loops were observed in the isotherms of Pd_2Au_1@ZIF-8 as well as Pd_9Au_1@ZIF-8 As the hysteresis loops appear at high pressure (P/P0 = 0.6-0.9), this is an indication of the presence of some mesoporosity due to the partial dissolution of ZIF-8 during the impregnation process.

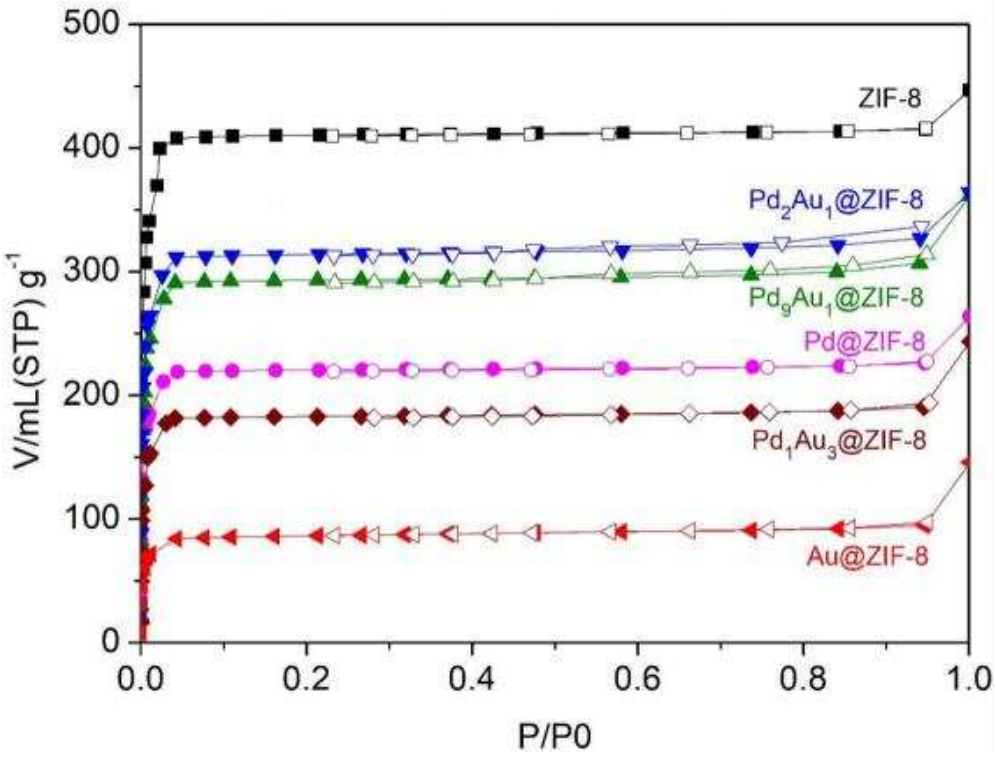

Figure 4.3. N_2 sorption isotherms of Pd@ZIF-8, Pd_9Au_1@ZIF-8, Pd_2Au_1@ZIF-8, Pd_1Au_3@ZIF-8, Au@ZIF-8, as-synthesized ZIF-8 at 77K

Table 4.3. Analysis of N_2 sorption isotherms

	S_{BET} ($cm^3.g^{-1}$)	$V_{microporous}$ ($cm^3.g^{-1}$)
ZIF-8	1442	0.69
Pd_2Au_1@ZIF-8	1314	0.54
Pd_9Au_1@ZIF-8	1192	0.52
Pd@ZIF-8	867	0.43
Pd_1Au_3@ZIF-8	685	0.34
Au@ZIF-8	363	0.21

4.3.1.3. TEM morphology analysis

The morphology of the [M]@ZIF-8 (reduced materials) series was studied by TEM (Figure 4.4). The dimension of ZIF-8 particles is about 0.5±0.1 μm. All the samples basically exhibit the typical rhombic dodecahedral morphology of ZIF-8. However, the crystals of ZIF-8 supporting NPs became rough compared to the ZIF-8 ones. Stairstep structure morphologies observed on the surface of the crystals. It suggests that the reduction of H_2 damaged the surface of ZIF-8 crystals. This is in accordance with the decrease of crystallinity and pore volumes previously mentioned (Table 4.3). In all samples, NPs seems to be localized both within and on the external surface of the crystals of ZIF-8. External nanoparticles tend to have larger sizes. The average particle size of NPs was calculated by measuring the particle size of at least 250 NPs on TEM images. The mean size of particles in Pd@ZIF-8, Pd_9Au_1@ZIF-8, Pd_2Au_1@ZIF-8, Pd_1Au_3@ZIF-8, Au@ZIF-8 are 6.0 ± 2.4 nm, 5.2 ± 2.7 nm, 5.1 ± 2.6 nm, 5.2 ± 3.0 nm, and 4.8 ± 4.8 nm, respectively. In the latter case, the presence of some large particles (diameter > 20 nm) can also be observed, thus increasing the standard deviation. Consequently, the median size of the particles is given in Table 4.4 to avoid this bias. Noteworthy, the median particle sizes of all bimetallic samples are between the average particle size of monometallic nanoparticles, ca 3.6 nm and 5.4 nm for monometallic Au and Pd NPs, respectively. The average particle size increases with the increase of the Pd proportion, in accordance with the literature.[28]

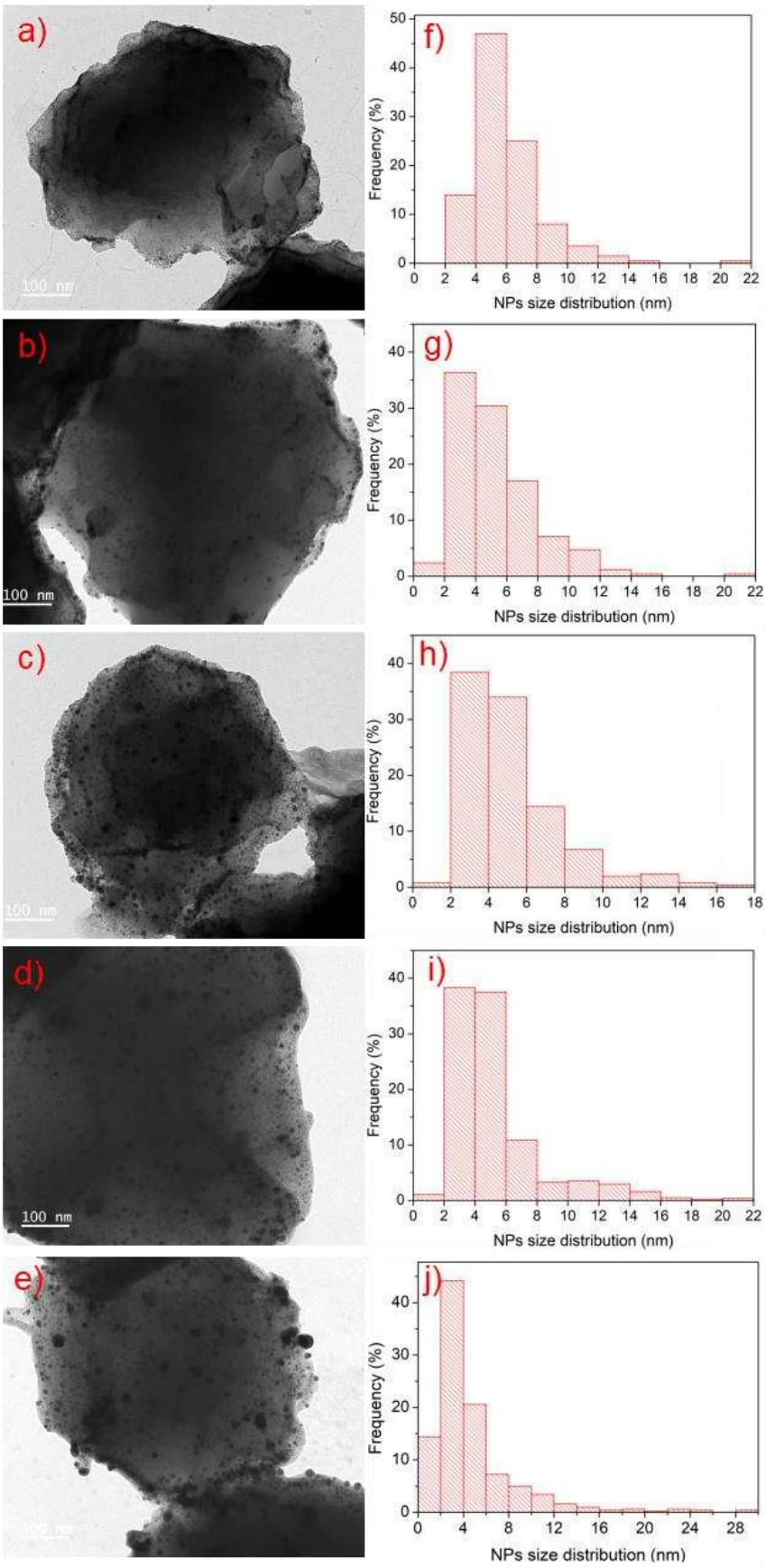

Figure 4.4. TEM images and NPs size distribution histogram. a), f) Pd@ZIF-8; b), g) Pd_9Au_1@ZIF-8; c), h) Pd_2Au_1@ZIF-8; d), i) Pd_1Au_3@ZIF-8; e), j) Au@ZIF-8

Table 4.4. Mean and median sizes of the nanoparticles

Sample	Mean size (nm)	Median size (nm)
Pd@ZIF-8	6.0±2.4	5.4
Pd_9Au_1@ZIF-8	5.2±2.7	4.4
Pd_2Au_1@ZIF-8	5.1±2.6	4.5
Pd_1Au_3@ZIF-8	5.2±3.0	4.4
Au@ZIF-8	4.8±4.8	3.6

High-resolution TEM (HRTEM), energy-dispersive X-ray Spectroscopy (EDX), and high-angle annular dark field scanning transmission electron microscopy (HAADF-STEM) analyses were achieved to further confirm the location of NPs, their chemical composition and the formation of alloy-phase nanoparticles in the sample Pd_9Au_1@ZIF-8 (See Figure 4. 5 and 4.6). This sample was selected because its XRD analysis already suggests the formation of a PdAu alloy (Figure 4.2b), which must be confirmed. In accordance with the TEM images in Figure 4.4b, most of the metal NPs are encapsulated within the ZIF-8 crystals and few NPs are observed on the surface or in the shallow layer of ZIF-8 (Figure 4.5 a). The observed NPs inside ZIF-8 have an average size of 5 ± 3 nm. However, in the shallow layer of ZIF-8 crystal, larger-size NPs are observed. These nanoparticles have an average size of 10 nm. In addition, NPs in the shallow layer are poorly dispersed and a pronounced particles aggregation is observed. The reason for the preferential location of larger NPs on the edge of ZIF-8 crystals is still unclear. One explanation could be related to some mass transfer diffusion limitation of the Au and Pd precursors inside the ZIF-8 matrix because of the relatively small pore windows of ZIF-8 (3.4 Å). Thus, larger nanoparticles preferentially form at the crystal edges or external surface, where the concentration of the metal precursors is the highest, and smaller NPs forms deeper within the crystal bulk, where the precursor concentration is the lowest. This diffusion limitation may however be bridged over by enhancing the impregnation duration to give to the metal precursors the time to diffuse within the whole porosity of the ZIF-8 crystals (this issue could however not be addressed within the frame of this PhD course because of lack of time). An alternative

explanation for difference in regional size distribution as a function of the particle localization may also be related to the reduction process. During the reduction process under H_2 flow at T = 300 °C, the most exposed superficial zones of ZIF-8 crystals may undergo local structural collapse. This partial collapse of the framework may affect the stability of metal precursors confined in these crystal areas that are consequently more prompt to aggregate and form large NPs.

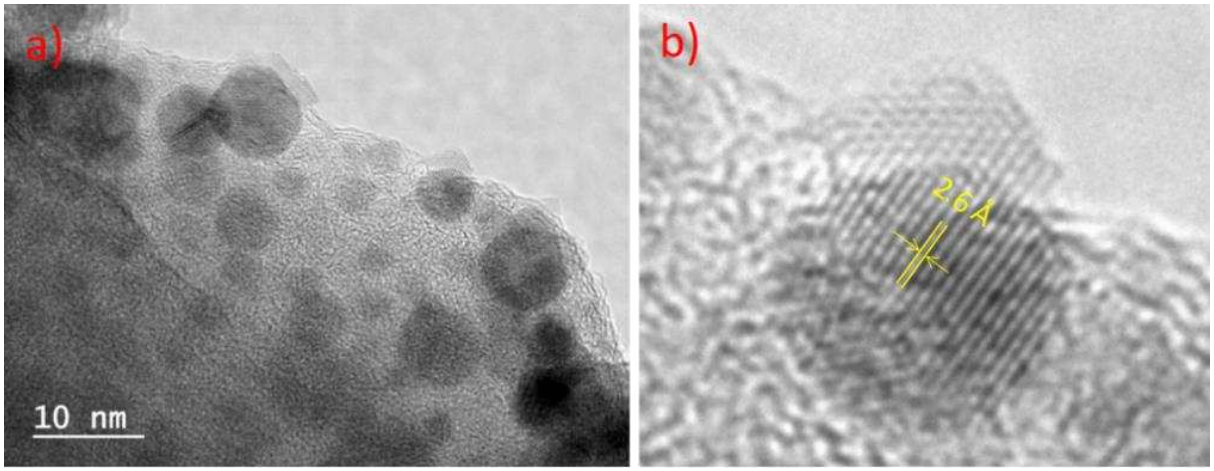

Figure 4.5. HRTEM of Pd_9Au_1@ZIF-8

HRTEM also shows the lattice parameters of the Pd/Au NPs (See Figure 4.5 b). The interplanar spacing is 2.6 Å, a value that cannot be attributed to either pure gold, pure palladium or the gold/palladium alloy because the interplanar spacing of both gold and palladium NPs {111} planes are 2.4 Å and 2.2 Å, respectively. We suspect that this broadened crystal interplanar spacing is related to the formation of PdO. PdO is known to grow on the Pd {111} surfaces and due to the mismatch of the lattice parameters of the two phases, the interplanar spacing expands.[29] The d-spacings of 2.6 Å likely corresponds to the {101} plane of a tetragonal PdO.

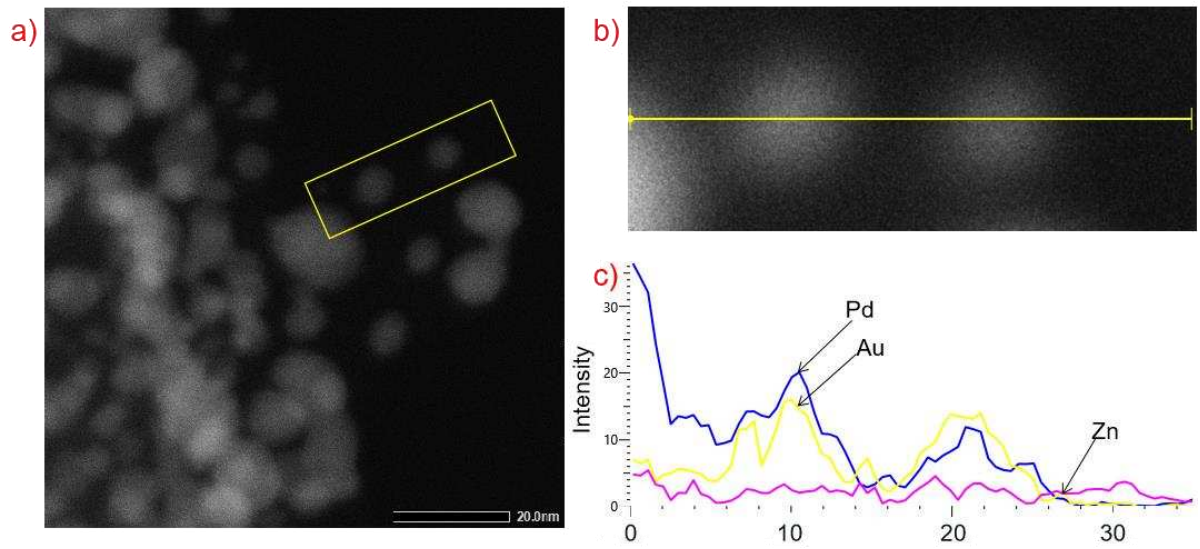

Figure 4.6. a), b) HAADF-STEM image of Pd_9Au_1@ZIF-8; c) the linear EDX elemental distribution of Pd (blue), Au (yellow), Zn (purple)

In order to identify a potential alloy phase, we performed EDX elemental linear analysis focusing on two NPs. To avoid any interference due to NPs superposition, we have selected isolated NPs on the HAADF-STEM image for further EDX analysis of its elementary composition along a yellow line (See Figure 4.6 b and c). On the other hand, the simultaneous signal of Au and Pd elements in the same position as the two selected NPs confirm the presence of a Pd/Au alloy phase. This result is indeed in line with the PXRD pattern of this sample (Figure 4.2). The atomic quantification of Pd to Au ratio on the in the two NPs is 57/43, which deviated from the results of ICP elemental analysis (89/11) in the overall sample, which can result from the presence of monometallic Pd NPs for example. Local atomic composition of five additional randomly selected NPs by EDX analysis supports this hypothesis since a large range of Pd/Au atomic ratio values (Figure 4.7) are determined, including one pure gold NP. A higher amount of data should be acquired to get a global and more reliable description of the Pd and Au atomic composition of the solid.

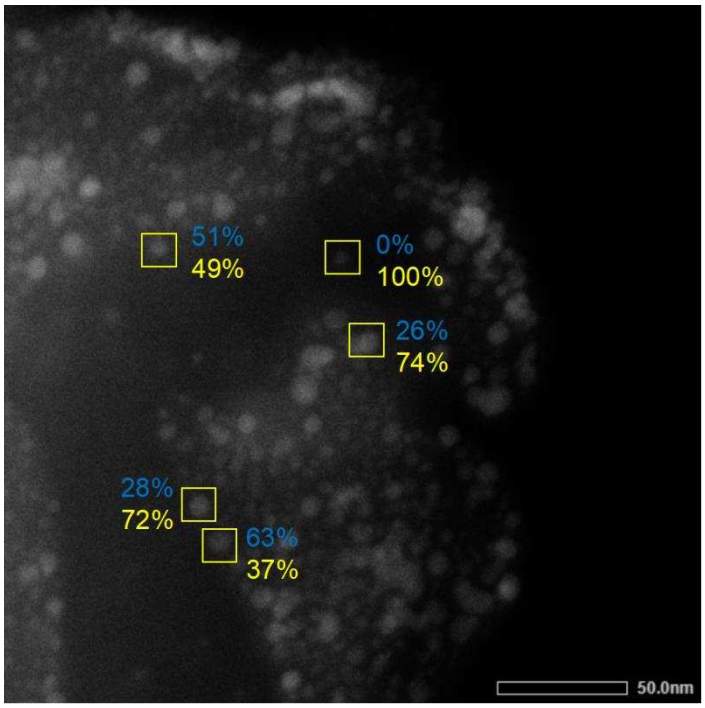

Figure 4.7. Atomic ratio of Pd (blue) and Au (yellow) determined by STEM-EDX elemental analysis

The 2D-EDX elemental mappings of Zn, Pd, Au, and Cl on Pd_9Au_1@ZIF-8 are displayed in Figure 4.8. The overall atomic quantification of Pd/Au ratio on region Figure 4.8a is 87/13, which is very close to the results of ICP elemental analysis (89/11).

In accordance to the TEM and HRTEM images (Figures 4.4 and 4.5), Pd/Au NPs are well dispersed within the ZIF-8 crystals. However, while the distribution of Au in ZIF-8 crystals is uniform, Pd signal intensity is higher at the edges of the ZIF-8 crystal. Therefore, it suggests that the NPs at the edges of ZIF-8 crystals have a higher Pd content. In addition, one can note that the mapping of the Cl element overlaps with that of the Pd element, thus being more concentrated at the edges of the ZIF-8 crystals. It can thus be assumed that the simultaneous presence of Cl and Pd on the external surface of ZIF-8 could be representative of palladium (II) chloride complexes, as a result of the uncomplete reduction of the Pd(II) species [$(Na^+)_2$, $(PdCl_4)^{2-}$].

The H_2-TPR analysis of [Pd/Au]-ZIF-8 (Figure 4.1) indeed shows that at least two reduction events occur at temperatures above the temperature applied to reduce the palladium and gold precursors (T = 300 °C). These two reduction events, at T = 320 °C and T = 390 °C, may

correspond to the reduction of palladium chloride species located at two types of strongly stabilizing environment in the pores of ZIF-8. These unreduced species are therefore remaining within the ZIF-8 framework after the reduction at T = 300 °C.

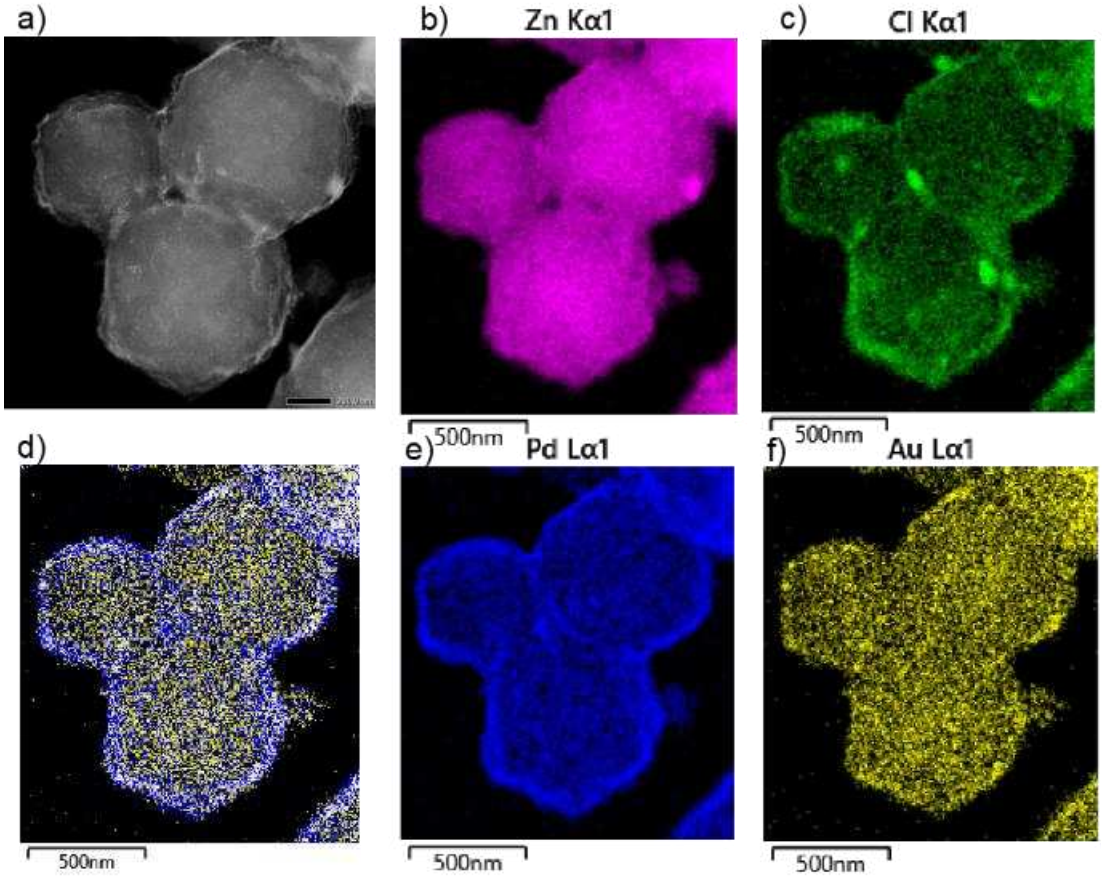

Figure 4.8. a) HAADF-STEM image of Pd_9Au_1@ZIF-8 crystals; the 2D-EDX elemental mapping of b) Zn, c) Cl, e) Pd, f) Au; d) the overlap of Pd and Au mappings

4.3.1.4. XPS analysis

Chemical state of metal NPs was investigated by X-ray photoelectron spectroscopy (XPS). The main peaks of the survey spectra of ZIF-8 can be assigned as C 1s, N 1s, O 1s, and Zn 2p (See Figure 4.9 and Table 4.5). C, N, and Zn are the component elements of ZIF-8, while O was presumed to come from contamination of the samples. For Pd@ZIF-8, Au@ZIF-8, and all PdAu@ZIF-8, the main peaks displayed on the survey spectra are assigned to C 1s, N 1s, O 1s, Zn 2p, Cl 2p, Pd 3d, and Au 4f. Compared to the survey spectra of pure ZIF-8, Pd 3d, Au 4f

and Cl 2p signals are observed as additional signals. The Cl 2p signal may result from unreduced precursors or reduction by-products that were not removed after reduction of the Au and Pd precursors.

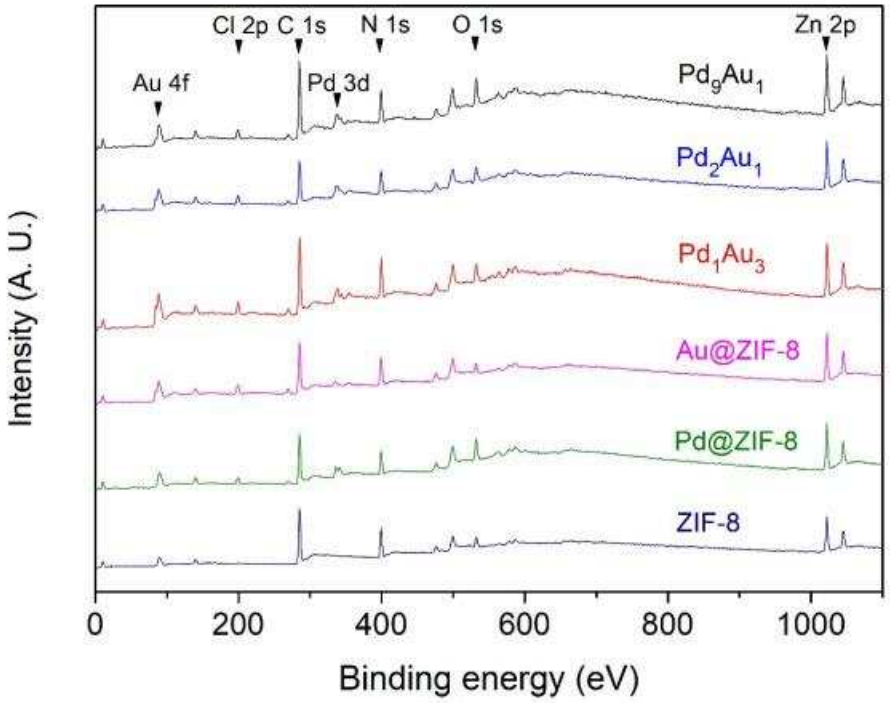

Figure 4.9. XPS survey of ZIF-8, Pd@ZIF-8, Au@ZIF-8, Pd_1Au_3@ZIF-8, Pd_2Au_1@ZIF-8, and Pd_9Au_1@ZIF-8

Table 4.5. Atomic percentage of the elements by XPS

Sample	Atomic %						
	C 1s	N 1s	O 1s	Zn 2p	Cl 2p	Pd 3d	Au 4f
ZIF-8	67.55	20.75	4.34	7.37	0	0	0
Pd@ZIF-8	55.83	17.3	11.04	9.58	4.28	1.96	0
Au@ZIF-8	56.99	20.18	4.65	9.32	6.16	0	2.7
Pd_9Au_1@ZIF-8	58.34	16.18	10.21	8.44	4.3	1.77	0.77
Pd_2Au_1@ZIF-8	52.71	17.39	9.7	9.55	5.46	2.22	2.98
Pd_1Au_3@ZIF-8	58.08	18.21	7.46	7.88	5.29	1.08	2

The XPS spectra of the Pd 3d orbitals were fitted by Casa XPS software (Experimental XPS data are shown in table 4.5). In agreement with theory, the Pd XPS signal of Pd@ZIF-8 is a doublet : Pd $3d_{3/2}$ at 340.3 eV and Pd $3d_{5/2}$ at 335.1 eV, with a binding energy splitting of 5.2 eV and a relative intensity of about 0.67 (Figure 4.10 a).[30] In all PdAu@ZIF-8 samples, the binding energy is similar to that of Pd@ZIF-8 with a deviation of ± 0.2 eV. Due to the proximity between the binding energy of the Au 4d orbital and that of the Pd $3d_{5/2}$ orbital, the two signals are overlaid.

An additional small Pd 3d doublet is also observed and can be set at ca. 338.2 eV ($3d_{5/2}$) and 343.5 eV ($3d_{3/2}$) after decomposition of the signal. This doublet is characteristic of Pd^{2+} while the doublet at 335.1 eV and 340.3 eV can be ascribed to Pd^0. Both doublets are observed for all the samples but the Pd^{2+} proportion is much higher for mixed Pd/Au@ZIF-8 NPs than for Pd@ZIF-8: around 8 at% for Pd@ZIF-8 while Pd^{2+} proportion increases from 42.2 at% to 75.8 at% for the most Au-rich sample (Experimental XPS data are shown in table 4.6). Oxidized Pd (PdO) is expected to exist on the surface of the nanoparticles, the samples being exposed to air under the storage conditions and during the drying step. The formation of PdO in the samples was already suggested by the HRTEM analysis of Pd_9Au_1@ZIF-8 (Figure 4.5). However, the amount of PdO surface species reported in the literature are commonly shown to decrease with the increase of the Au/Pd ratio, the presence of Au preventing the oxidation of surface Pd atoms.[28,31,32] In our study, the opposite trend is observed. This may be explained by the uncomplete reduction of the Pd precursors at T = 300 °C in the case of bimetallic NPs, that may leave unreduced particularly stabilized Pd^{2+} species. Indeed, the hydrogen consumption temperature range observed on the H_2 TPR profiles of the Pd/Au-impregnated ZIF-8 extends to over the reduction temperature 300°C suggesting that, at this temperature, a part of the adsorbed metal cations is still not reduced (Figure 4.1). The reason why Pd^{2+} would be more stabilized within ZIF-8 in the case of the concomitant Au and Pd impregnation is not understood.

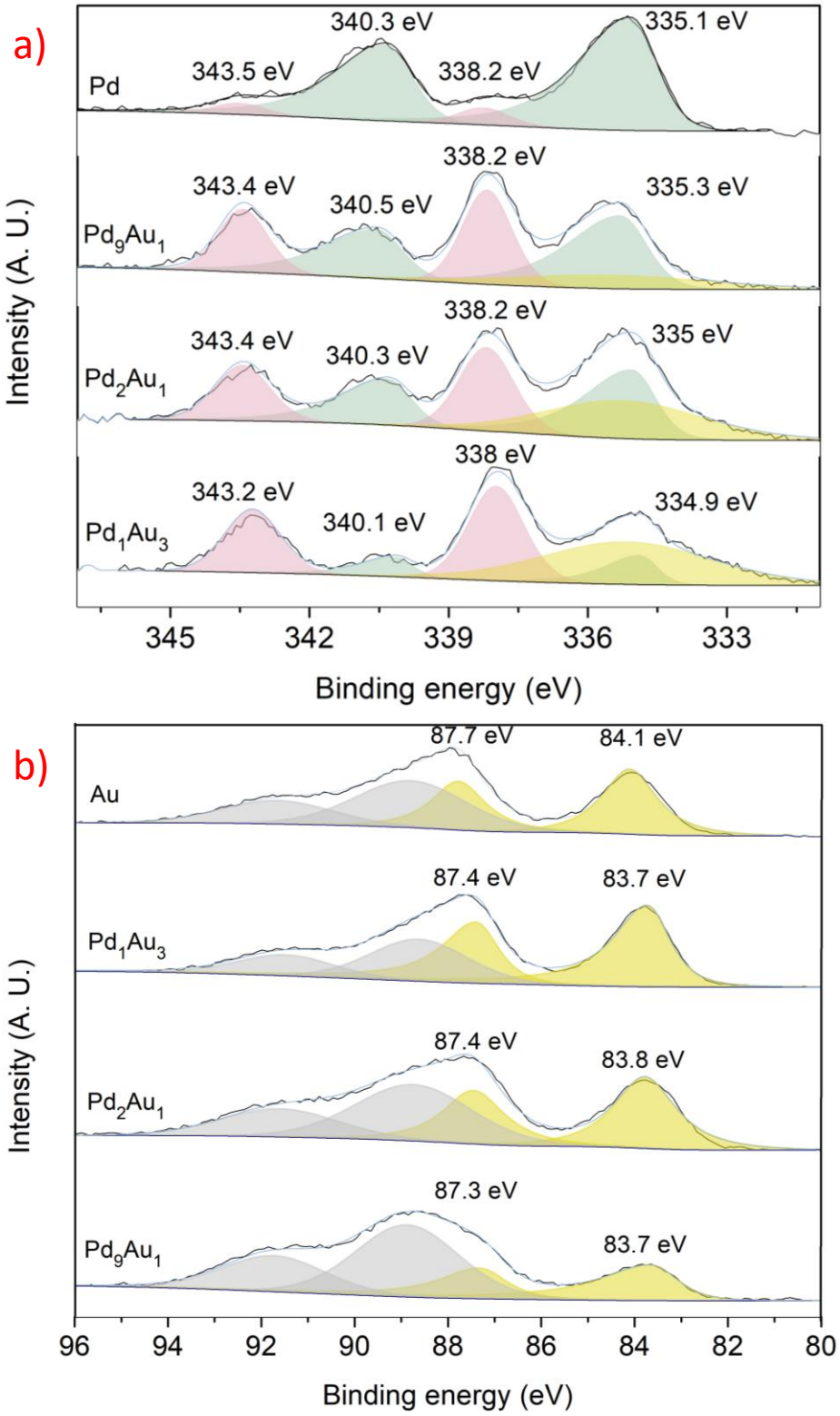

Figure 4.10. XPS core level spectra of catalysts a) Pd 3d and Au 4d orbitals of Pd@ZIF-8, Pd_9Au_1@ZIF-8, Pd_2Au_1@ZIF-8, and Pd_1Au_3@ZIF-8; b) Au 4f and Zn 3p orbitals of Au@ZIF-8, Pd_1Au_3@ZIF-8, Pd_2Au_1@ZIF-8, and Pd_9Au_1@ZIF-8. The green peaks are related to metallic Pd species. The pink peaks are related to the Pd^{2+} species. The yellow peaks are related to metallic Au species. The grey peaks are related to metallic Zn species.

Table 4.6. Binding energy and percentage of Pd $3d_{5/2}$ orbitals in Pd containing samples

Sample	Pd $3d_{5/2}$			
	Pd^0		Pd^{2+}	
	BE (eV)	(at. %)	BE (eV)	(at. %)
Pd@ZIF-8	335.1	91.9	338.2	8.1
Pd_9Au_1@ZIF-8	335.3	57.8	338.2	42.2
Pd_2Au_1@ZIF-8	335	54.2	338.2	45.8
Pd_1Au_3@ZIF-8	334.9	24.2	338	75.8

The XPS spectra of the Au 4f orbitals were also fitted by Casa XPS software. In Au@ZIF-8, it can be noticed that the signal of the Au 4f orbitals can be divided into Au $4f_{5/2}$ at the binding energy of 87.8 eV and Au $4f_{7/2}$ at 84.1 eV (Figure 4.10 b). The Δ_{BE} and relative peak intensities were 3.7 eV and 0.75, respectively, in agreement with the literature.[13] Due to the proximity between the binding energy of the Zn 3p orbital and that of the Au 4f orbital, the two signals are overlaid.

The maximum of the main peak is observed at 84.1 eV for Au@ZIF-8, which is almost equal to the binding energy assigned to Au^0 species in the literature (binding energy = 84.0 eV).[33] This slight shift is common in Au NPs, and could be related to the size of NPs.[34] No peak corresponding to Au^{3+} species commonly observed at the binding energy of 86.5 eV and Au^{1+} at 85.6 eV are detected. Therefore, these XPS data suggest that in Au@ZIF-8, all Au in the top surface of ZIF-8 crystal (not more than 11 nm depth from the surface, as it is the probing depth of XPS) is only Au^0 species. Hence, the Au precursor, $HAuCl_4$, has been completely reduced by the H_2 flow. In that case, it is likely that some chlorine remains in the sample due to insufficient rinsing at the end of the material synthesis.

For all the bimetallic catalysts, only one of the two 4f doublet contributions, Au $4f_{7/2}$, can be exploited to characterize Au^0 since the Au $4f_{5/2}$ signal is overlapped with the one of Zinc. Compared to Au@ZIF-8, a decrease in the Au $4f_{7/2}$ binding energy is observed for all the bimetallic NPs (Figure 4.10b). Indeed, the Au $4f_{7/2}$ binding energies in Pd_9Au_1@ZIF-8,

Pd_2Au_1@ZIF-8 and Pd_1Au_3@ZIF-8 are 83.7, 83.8, and 83.7 eV, respectively, instead of 84.1 eV in Au@ZIF-8.

This shift, has been reported in the literature for PdAu alloys.[35–39] This is explained by charge transfer within the PdAu NPs due to the higher electronegativity of Au compared to Pd. This results thus strongly supports the hypothesis of a PdAu alloy formation inside ZIF-8. However, it should be noticed that our experimental data do not allow to point out unambiguously any significant modification of the Pd^0 XPS signal in the PdAu@ZIF-8 samples which would corroborate the presence of the PdAu alloy. Indeed, as far as the Pd $3d_{5/2}$ around 335.1 eV signal is concerned, the overlapping with the Au 4d signal prevent from a precise deconvolution of the signal whereas for the Pd $3d_{3/2}$ signal around 340.3 eV, the signal to noise ratio is rather low, thus preventing any precise localization of the peak maximum. In all case, if it exists, the effect of the PdAu on the binding energy of Pd remains too small to be detected.

Table 4.7. Comparison of atomic ratio Pd/Zn and Au/Zn obtained by different techniques

Sample	ICP/OES measurements		XPS data	
	at. Pd/Au	at. Au/Zn	at. Pd/Au	at. Au/Zn
Pd@ZIF-8	0.0784		0.20	
Au@ZIF-8		0.0488		0.29
Pd_9Au_1@ZIF-8	0.0649	0.0077	0.21	0.091
Pd_2Au_1@ZIF-8	0.0409	0.0198	0.23	0.31
Pd_1Au_3@ZIF-8	0.0102	0.0311	0.13	0.25

Finally, we compare the atomic ratio Pd to Zn or Au to Zn obtained by XPS (a method probing the top surface-layer (11 nm depth) of the solid), to those obtained using ICP, in order to get insights into the composition of the NPs as a function of their localization into ZIF-8. For all the supported NPs type, the comparison between proportions of Pd and Au determined by XPS and ICP suggests that Pd content is higher than that of Au within the bulk crystal (See Table 4.7). The lowest difference is observed for the Pd@ZIF-8 NPs. In that case in the top layer of the particles the Pd/Zn atomic ration is about two-fold higher than the overall one given from

ICP experiments. In the other case, the difference can reach a tenfold higher ratio. This calculation of course shows that the NPs are located preferentially at the surface of the ZIF-8 particles, in line with the microscopy images.

4.3.2. Catalytic aerobic oxidation of alcohols

Palladium-gold (PdAu) nanoparticles have shown significantly enhanced activity relative to monometallic Au and Pd catalysts.[40–42] The catalytic activity of the monometallic and bimetallic NPs@ZIF-8 for the oxidation of primary and secondary alcohols was tested in batch reactions using benzyl alcohol and 1-phenylethanol as model substrates.

The metal contents of the catalysts determined by ICP analysis are recalled in Table 4.8, in view of the discussion, for a better understanding of the results. Notably, differences in the total metal contents depending on the Pd/Au ratio must be considered.

Table 4.8. ICP element analysis of the catalysts

Samples	Pd (±0.05 wt.%)	Au (±0.05 wt.%)	Total metal wt.%
Pd@ZIF-8	4.46	0.05	4.51
Au@ZIF-8	0.06	4.07	4.13
Pd_9Au_1@ZIF-8	3.13	0.69	3.82
Pd_2Au_1@ZIF-8	1.93	1.73	3.66
Pd_1Au_3@ZIF-8	0.46	2.63	3.09

The reaction was carried out at 50 °C in water during 24h without any base additions. O_2 was bubbled through the reaction mixture for 10 minutes before each test. The conversion and yield of benzaldehyde are shown in Figure 4.11.

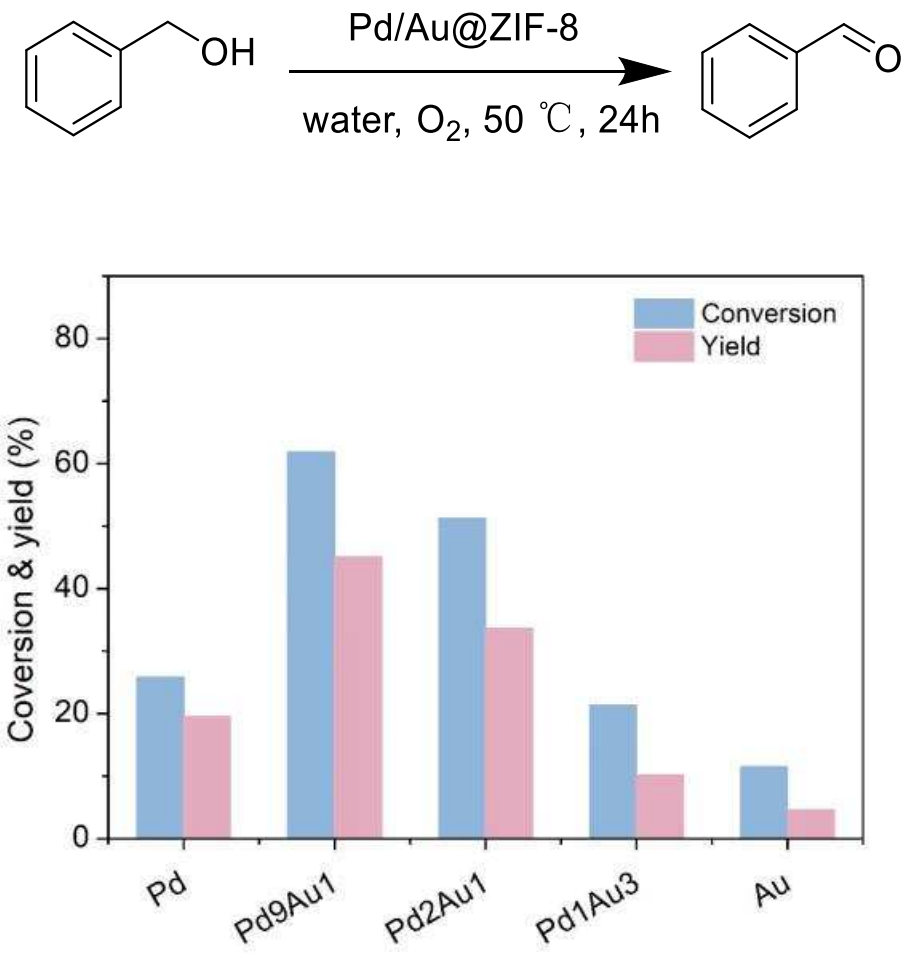

Figure 4.11. catalytic oxidation of benzyl alcohol over PdAu@ZIF-8 series catalysts. Conditions: Benzyl alcohol 100 mM, catalyst loading 5 mg (1 mol% based on the initial amount of metal), water 2 mL, 50 °C, O_2, 24h.

Interestingly, the catalytic activities of mono- and bimetallic catalysts vary with the Au and Pd content following a volcano-type behavior when going from a pure metal to the other (Figure 4.11). With Pd@ZIF-8 as a catalyst, the conversion and yield of benzaldehyde after 24h are 26% and 19%, respectively. With Au@ZIF-8, the conversion and yield are 11% and 5%, less than that of Pd@ZIF-8. Unsupported Pd NPs and Au NPs reported in the literature tend to be active under mild conditions.[43] However, it was reported that the activity is diminished after being immobilized on supports.[44] In addition, most noble metal-catalyzed alcohol oxidation requires the deprotonation of the hydroxyl group to form the alcoholate under alkaline conditions.[45] Therefore, base-free conditions are often more challenging and may explain these low performances. However, the activity increases with the formation of bimetallic NPs. For

Pd_1Au_3@ZIF-8 with high gold content, the catalytic activity was only slightly increased compared to the pure gold catalyst Au@ZIF-8 with 21% of conversion and 10% benzaldehyde yield, respectively. One should note that this relatively low activity improvement was obtained with a catalyst whose total metal content is lower (3.09 wt% for Pd_1Au_3@ZIF-8 against 4.13 wt% for Au@ZIF-8, Table 4.9). This means that alloying Au with a relatively small amount of Pd is enough to noticeably increases the NPs activity. Increasing the Pd proportion in the NPs further improves the NPs activity. For Pd_9Au_1@ZIF-8 and Pd_2Au_1@ZIF-8, the conversion and benzaldehyde yield are significantly improved compared to the pure gold catalyst. The conversion and yield are 62% and 45% for Pd_9Au_1@ZIF-8, 51% and 34% For Pd_2Au_1@ZIF-8. This is even more noticeable that, again, the total metal contents in these two catalysts are lower than in Au@ZIF-8 (Table 4.9). There is a consensus that PdAu bimetallic alloy catalysts have better activity than monometallic catalysts, especially when the palladium has a higher ratio.[13,14,46] The observed volcano-like activity derives from the balance between the number of active sites on the NP surface and the ease of the product desorption. These two parameters were shown to be extremely sensitive to the Pd content.[47] The enhanced activity with the increase of Pd content is thought to be attributed to both the metal distribution and the electronic structure of the bimetallic nanoparticles. A generally accepted mechanism of oxidation of benzyl alcohol over Pd- and PdAu-contained catalysts is first to form the Pd alcoholate intermediate through the interaction of the O–H bond of the alcohol with a Pd site, followed by the β-hydride elimination.[15,16] In this pathway, the hydroxyl groups of the alcohols are deprotonated and then absorbed by Pd. The β-H of substrates then transfer to the surface of Pd to form the H-Pd species together with the formation of the carbonyl compound. The O_2 finally re-oxidizes the surface H-Pd species to generate water.

Only Pd sites (sites with no Au) are active for benzyl alcohol adsorption, and thus, activity is proportional to the number of surfaces Pd ensembles (i.e., at least 6 Pd atoms on the surface) capable to accommodate benzyl alcohol. The gold atom itself is weakly active in catalyzing the alcohol oxidation reaction but combine with Pd, it participates to the increase of the alcohol

affinity with Pd sites. Indeed, there is a partial electron transfer from Pd^0 to Au^0 in the gold-palladium alloy nanoparticles, which reduces the electron cloud density of Pd^0 and therefore enhances its affinity for the alcohols.[16] However, an excessive benzyl alcohol adsorption subsequently results in an increase of the desorption energy required to clean the surface from the aldehyde product. Furthermore, the β-H-transfer from the alcohol to the Pd-rich systems (and the Pd-only system) is the most energy-demanding step, implying that the reaction are slow in these cases.[47] Therefore, there exists an optimal Pd/Au ratio for which benzyl alcohol adsorption can efficiently occur everywhere over the NP surface and for which desorption is still feasible and the H-transfer is not too energy demanding. In our study, where PdAu NP are supported on ZIF-8, the optimal appears to be Pd_9Au_1. The difference regarding the conversion and yield reveals that benzaldehyde is not the only product of this oxidation reaction. Possible by-products include benzoic acid and toluene, but are not observed in the HPLC.[48–50]

Secondary alcohols are generally considered to be more inert than primary alcohols in terms of oxidation reactions. However, the oxidation product has great potential for application due to its pre-chiral nature. Noteworthy, the goal of this PhD thesis is the synthesis of chiral amines taking advantage of the high enantioselectivity of the ω-transaminase. The employ of secondary alcohol is therefore important. We selected 1-PE to test the activity of PdAu@ZIF-8 series catalysts for the oxidation of secondary alcohol. The conversion of 1-PE and yield of AP are shown in Figure 4.12.

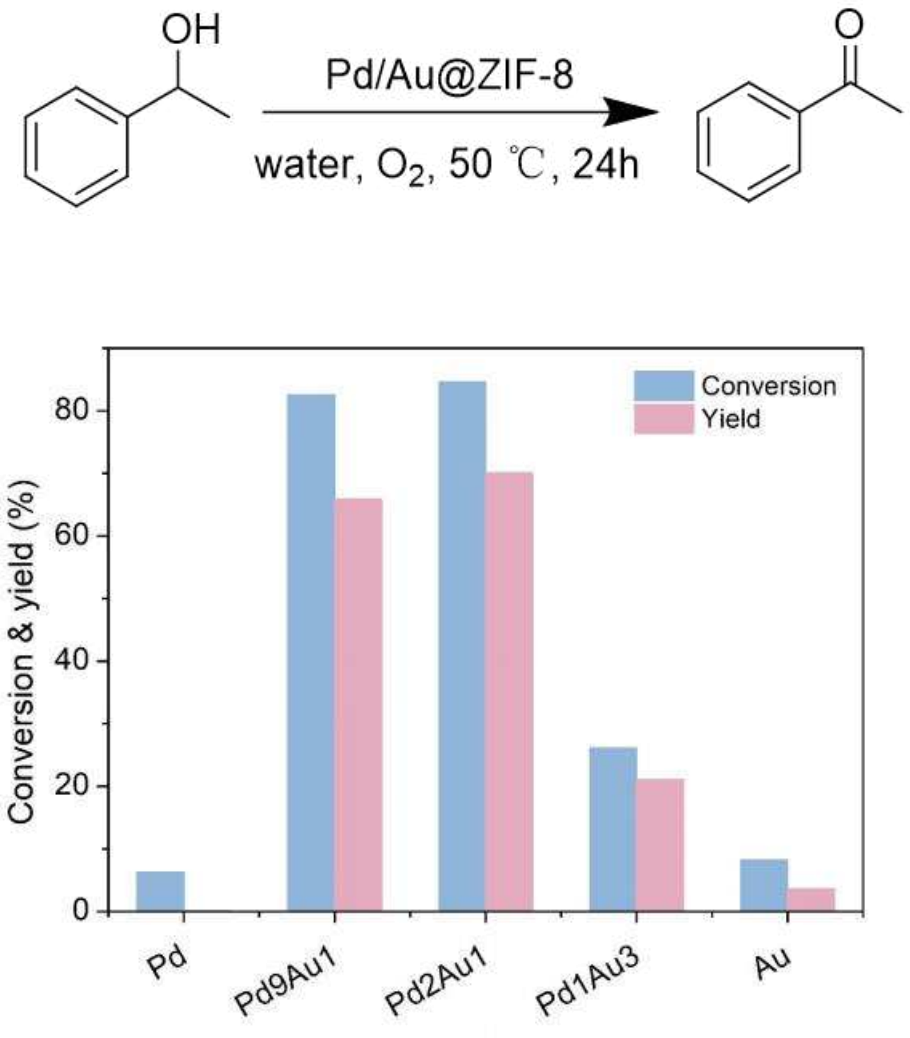

Figure 4. 12. catalytic oxidations of 1-phenyethanol over PdAu@ZIF-8 series catalysts
Conditions: 1-phenyethanol 100 mM, catalyst loading 5 mg (1 mol% based on the initial amount of metal), water 2 mL, T=50 °C, O_2, t=24 h

The oxidation reaction conversions of 1-PE were very low, 6% and 8%, with Pd@ZIF-8 and Au@ZIF-8, respectively. No AP is detected in the presence of Pd@ZIF-8 as a catalyst while only 3% yield of AP was calculated in the Au@ZIF-8 catalytic test. Considering the low reactivity of 1-phenylethanol toward oxidation and the base-free reaction medium, such a low conversion was expected. By contrast, the bimetallic catalysts exhibit excellent activity. For the two Pd-rich Pd_9Au_1@ZIF-8 and Pd_2Au_1@ZIF-8, the conversion reaches up to 83% and 85%, respectively. The yields are 66% and 70%, indicating a poor influence of Au NPs on the selectivity. The Au-rich Pd_1Au_3@ZIF-8 allows a lower conversion and yield: 26% and 21%,

respectively. The lower performances of this catalyst should however be regarded by considering its lower metal content compared to the two other bimetallic catalysts. What is interesting is that the significant enhancement of activity using the best bimetallic catalysts is even stronger than that of benzyl alcohol, leading to a higher final conversion of the alcohol: 85% for 1-phenylethanol compared to 62% for benzyl alcohol using Pd_9Au_1@ZIF-8.

4.4. Conclusion

We developed a PdAu bimetallic alloy nanoparticle supported on ZIF-8. According to XRD and N_2 adsorption, the synthesized PdAu@ZIF-8 displays the high crystallinity and porosity typical of ZIF-8. The TEM images of PdAu@ZIF-8 shows the PdAu NPs are homogeneous in size (4-6 nm). The PdAu NPs are generally well dispersed in ZIF-8 crystals, whatever is the Au/Pd composition. Through HRTEM and EDX mapping, the PdAu are confirmed to form the alloy. The chemical nature and oxidation states of the PdAu NPs were analyzed by XPS. In all samples, Au is present as a metallic species, while Pd is present in both 2+ and 0 valent states. It is hypothesized that the genesis of Pd^{2+} involves incomplete reduction as well as surface oxidation by exposure to air. The PdAu@ZIF-8 catalyst has excellent catalytic activity for the aerobic oxidation of alcohols in water and under mild temperature and pH conditions. Among them, the highest catalytic activity was achieved when the Pd to Au ratio is 9:1. PdAu@ZIF-8 catalysts are shown to catalyze both primary and secondary alcohols. The activity was tested by oxidation reactions with benzyl alcohol and 1-phenylethanol, and the conversion could reach up to 62% and 83%, respectively after 24 h at T = 50 °C. More importantly, the catalyst is active under aqueous phase conditions and no strong base addition is required, which provides sufficient flexibility for the adaptation to the conditions of the amination reaction catalyzed by transaminases. Therefore, Pd_9Au_1@ZIF-8 will be selected as the transaminase immobilization supporter for cascade catalytic oxidative amination reactions.

References

(1) Stratakis, M.; Garcia, H. Catalysis by Supported Gold Nanoparticles: Beyond Aerobic Oxidative Processes. *Chem. Rev.* **2012**, *112* (8), 4469–4506. https://doi.org/10.1021/cr3000785.

(2) Qian, L.; Zheng, G. Recent Advances of Metal Nanoclusters for Aerobic Oxidation. *Mater. Today Nano* **2020**, *11*, 100080. https://doi.org/10.1016/j.mtnano.2020.100080.

(3) Mallat, T.; Baiker, A. Oxidation of Alcohols with Molecular Oxygen on Solid Catalysts. *Chem. Rev.* **2004**, *104* (6), 3037–3058. https://doi.org/10.1021/cr0200116.

(4) Zhao, J. P.; Hernández, W. Y.; Zhou, W. J.; Yang, Y.; Vovk, E. I.; Wu, M.; Naghavi, N.; Capron, M.; Ordomsky, V. Nanocell Type Ru@quinone Core-Shell Catalyst for Selective Oxidation of Alcohols to Carbonyl Compounds. *Appl. Catal. Gen.* **2020**, *602*, 117693. https://doi.org/10.1016/j.apcata.2020.117693.

(5) Zou, H.; Wang, R.; Dai, J.; Wang, Y.; Wang, X.; Zhang, Z.; Qiu, S. Amphiphilic Hollow Porous Shell Encapsulated Au@Pd Bimetal Nanoparticles for Aerobic Oxidation of Alcohols in Water. *Chem. Commun.* **2015**, *51* (78), 14601–14604. https://doi.org/10.1039/C5CC05686A.

(6) García-Suárez, E. J.; Tristany, M.; García, A. B.; Collière, V.; Philippot, K. Carbon-Supported Ru and Pd Nanoparticles: Efficient and Recyclable Catalysts for the Aerobic Oxidation of Benzyl Alcohol in Water. *Microporous Mesoporous Mater.* **2012**, *153*, 155–162. https://doi.org/10.1016/j.micromeso.2011.12.023.

(7) Karimi, B.; Behzadnia, H.; Bostina, M.; Vali, H. A Nano-Fibrillated Mesoporous Carbon as an Effective Support for Palladium Nanoparticles in the Aerobic Oxidation of Alcohols "on Pure Water." *Chem. – Eur. J.* **2012**, *18* (28), 8634–8640. https://doi.org/10.1002/chem.201200373.

(8) Singh, A. K.; Xu, Q. Synergistic Catalysis over Bimetallic Alloy Nanoparticles. *ChemCatChem* **2013**, *5* (3), 652–676. https://doi.org/10.1002/cctc.201200591.

(9) Jin, X.; Zhao, M.; Vora, M.; Shen, J.; Zeng, C.; Yan, W.; Thapa, P. S.; Subramaniam, B.; Chaudhari, R. V. Synergistic Effects of Bimetallic PtPd/TiO_2 Nanocatalysts in Oxidation of Glucose to Glucaric Acid: Structure Dependent Activity and Selectivity. *Ind. Eng. Chem. Res.* **2016**, *55* (11), 2932–2945. https://doi.org/10.1021/acs.iecr.5b04841.

(10) Gu, X.; Lu, Z.-H.; Jiang, H.-L.; Akita, T.; Xu, Q. Synergistic Catalysis of Metal–Organic Framework-Immobilized Au–Pd Nanoparticles in Dehydrogenation of Formic Acid for Chemical Hydrogen Storage. *J. Am. Chem. Soc.* **2011**, *133* (31), 11822–11825. https://doi.org/10.1021/ja200122f.

(11) Duan, M.; Jiang, L.; Zeng, G.; Wang, D.; Tang, W.; Liang, J.; Wang, H.; He, D.; Liu, Z.; Tang, L. Bimetallic Nanoparticles/Metal-Organic Frameworks: Synthesis, Applications and Challenges. *Appl. Mater. Today* **2020**, *19*, 100564. https://doi.org/10.1016/j.apmt.2020.100564.

(12) van der Hoeven, J. E. S.; Jelic, J.; Olthof, L. A.; Totarella, G.; van Dijk-Moes, R. J. A.; Krafft, J.-M.; Louis, C.; Studt, F.; van Blaaderen, A.; de Jongh, P. E. Unlocking Synergy in Bimetallic Catalysts by Core–Shell Design. *Nat. Mater.* **2021**, *20* (9), 1216–1220. https://doi.org/10.1038/s41563-021-00996-3.

(13) Chen, Y.; Lim, H.; Tang, Q.; Gao, Y.; Sun, T.; Yan, Q.; Yang, Y. Solvent-Free Aerobic

Oxidation of Benzyl Alcohol over Pd Monometallic and Au–Pd Bimetallic Catalysts Supported on SBA-16 Mesoporous Molecular Sieves. *Appl. Catal. Gen.* **2010**, *380* (1), 55–65. https://doi.org/10.1016/j.apcata.2010.03.026.

(14) Silva, T. A. G.; Teixeira-Neto, É.; Borges, L. R.; Neves-Garcia, T.; Braga, A. H.; Rossi, L. M. From AuPd Nanoparticle Alloys towards Core-Shell Motifs with Enhanced Alcohol Oxidation Activity. *ChemCatChem* **2023**, *15* (11), e202300180. https://doi.org/10.1002/cctc.202300180.

(15) Zhu, X.; Guo, Q.; Sun, Y.; Chen, S.; Wang, J.-Q.; Wu, M.; Fu, W.; Tang, Y.; Duan, X.; Chen, D.; Wan, Y. Optimising Surface d Charge of AuPd Nanoalloy Catalysts for Enhanced Catalytic Activity. *Nat. Commun.* **2019**, *10* (1), 1428. https://doi.org/10.1038/s41467-019-09421-5.

(16) Balcha, T.; Strobl, J. R.; Fowler, C.; Dash, P.; Scott, R. W. J. Selective Aerobic Oxidation of Crotyl Alcohol Using AuPd Core-Shell Nanoparticles. *ACS Catal.* **2011**, *1* (5), 425–436. https://doi.org/10.1021/cs200040a.

(17) Modelska, M.; Binczarski, M. J.; Kaminski, Z.; Karski, S.; Kolesinska, B.; Mierczynski, P.; Severino, C. J.; Stanishevsky, A.; Witonska, I. A. Bimetallic Pd-Au/SiO_2 Catalysts for Reduction of Furfural in Water. *Catalysts* **2020**, *10* (4), 444. https://doi.org/10.3390/catal10040444.

(18) Di, Z.; Chen, H.; Zhang, R.; Wang, H.; Jia, J.; Wei, Y. Significant Promotion of Reducing Treatment on Pd/TS-1 Zeolite for Formaldehyde Catalytic Purification at Ambient Temperature. *Appl. Catal. B Environ.* **2022**, *304*, 120843. https://doi.org/10.1016/j.apcatb.2021.120843.

(19) Byun, M. Y.; Park, D.-W.; Lee, M. S. Effect of Oxide Supports on the Activity of Pd Based Catalysts for Furfural Hydrogenation. *Catalysts* **2020**, *10* (8), 837. https://doi.org/10.3390/catal10080837.

(20) Gualteros, J. A. D.; Garcia, M. A. S.; da Silva, A. G. M.; Rodrigues, T. S.; Cândido, E. G.; e Silva, F. A.; Fonseca, F. C.; Quiroz, J.; de Oliveira, D. C.; de Torresi, S. I. C.; de Moura, C. V. R.; Camargo, P. H. C.; de Moura, E. M. Synthesis of Highly Dispersed Gold Nanoparticles on Al_2O_3, SiO_2, and TiO_2 for the Solvent-Free Oxidation of Benzyl Alcohol under Low Metal Loadings. *J. Mater. Sci.* **2019**, *54* (1), 238–251. https://doi.org/10.1007/s10853-018-2827-x.

(21) James, J. B.; Lin, Y. S. Kinetics of ZIF-8 Thermal Decomposition in Inert, Oxidizing, and Reducing Environments. *J. Phys. Chem. C* **2016**, *120* (26), 14015–14026. https://doi.org/10.1021/acs.jpcc.6b01208.

(22) Tew, M. W.; Emerich, H.; van Bokhoven, J. A. Formation and Characterization of PdZn Alloy: A Very Selective Catalyst for Alkyne Semihydrogenation. *J. Phys. Chem. C* **2011**, *115* (17), 8457–8465. https://doi.org/10.1021/jp1103164.

(23) Bahruji, H.; Bowker, M.; Hutchings, G.; Dimitratos, N.; Wells, P.; Gibson, E.; Jones, W.; Brookes, C.; Morgan, D.; Lalev, G. Pd/ZnO Catalysts for Direct CO_2 Hydrogenation to Methanol. *J. Catal.* **2016**, *343*, 133–146. https://doi.org/10.1016/j.jcat.2016.03.017.

(24) Armbrüster, M.; Behrens, M.; Föttinger, K.; Friedrich, M.; Gaudry, É.; Matam, S. K.; Sharma, H. R. The Intermetallic Compound ZnPd and Its Role in Methanol Steam

Reforming. *Catal. Rev.* **2013**, *55* (3), 289–367. https://doi.org/10.1080/01614940.2013.796192.

(25) Kaszkur, Z. Direct Observation of Chemisorption Induced Changes in Concentration Profile in Pd–Au Alloy Nanosystems via in Situ X-Ray Powder Diffraction. *Phys. Chem. Chem. Phys.* **2004**, *6* (1), 193–199. https://doi.org/10.1039/B308177J.

(26) Nowicka, E.; Althahban, S.; Leah, T. D.; Shaw, G.; Morgan, D.; Kiely, C. J.; Roldan, A.; Hutchings, G. J. Benzyl Alcohol Oxidation with Pd-Zn/TiO_2: Computational and Experimental Studies. *Sci. Technol. Adv. Mater.* **2019**, *20* (1), 367–378. https://doi.org/10.1080/14686996.2019.1598237.

(27) Jiang, H.-L.; Akita, T.; Ishida, T.; Haruta, M.; Xu, Q. Synergistic Catalysis of Au@Ag Core−Shell Nanoparticles Stabilized on Metal−Organic Framework. *J. Am. Chem. Soc.* **2011**, *133* (5), 1304–1306. https://doi.org/10.1021/ja1099006.

(28) Wu, P.; Cao, Y.; Zhao, L.; Wang, Y.; He, Z.; Xing, W.; Bai, P.; Mintova, S.; Yan, Z. Formation of PdO on Au–Pd Bimetallic Catalysts and the Effect on Benzyl Alcohol Oxidation. *J. Catal.* **2019**, *375*, 32–43. https://doi.org/10.1016/j.jcat.2019.05.003.

(29) Zhang, D.; Jin, C.; Tian, H.; Xiong, Y.; Zhang, H.; Qiao, P.; Fan, J.; Zhang, Z.; Li, Z. Y.; Li, J. An In Situ TEM Study of the Surface Oxidation of Palladium Nanocrystals Assisted by Electron Irradiation. *Nanoscale* **2017**, *9* (19), 6327–6333. https://doi.org/10.1039/C6NR08763A.

(30) Brun, M.; Berthet, A.; Bertolini, J. C. XPS, AES and Auger Parameter of Pd and PdO. *J. Electron Spectrosc. Relat. Phenom.* **1999**, *104* (1), 55–60. https://doi.org/10.1016/S0368-2048(98)00312-0.

(31) Olmos, C. M.; Chinchilla, L. E.; Rodrigues, E. G.; Delgado, J. J.; Hungría, A. B.; Blanco, G.; Pereira, M. F. R.; Órfão, J. J. M.; Calvino, J. J.; Chen, X. Synergistic Effect of Bimetallic Au-Pd Supported on Ceria-Zirconia Mixed Oxide Catalysts for Selective Oxidation of Glycerol. *Appl. Catal. B Environ.* **2016**, *197*, 222–235. https://doi.org/10.1016/j.apcatb.2016.03.050.

(32) Yang, X.; Chen, D.; Liao, S.; Song, H.; Li, Y.; Fu, Z.; Su, Y. High-Performance Pd–Au Bimetallic Catalyst with Mesoporous Silica Nanoparticles as Support and Its Catalysis of Cinnamaldehyde Hydrogenation. *J. Catal.* **2012**, *291*, 36–43. https://doi.org/10.1016/j.jcat.2012.04.003.

(33) Darrah Thomas, T.; Weightman, P. Valence Electronic Structure of AuZn and AuMg Alloys Derived from a New Way of Analyzing Auger-Parameter Shifts. *Phys. Rev. B* **1986**, *33* (8), 5406–5413. https://doi.org/10.1103/PhysRevB.33.5406.

(34) Peters, S.; Peredkov, S.; Neeb, M.; Eberhardt, W.; Al-Hada, M. Size-Dependent XPS Spectra of Small Supported Au-Clusters. *Surf. Sci.* **2013**, *608*, 129–134. https://doi.org/10.1016/j.susc.2012.09.024.

(35) Lin, H.; Muzzio, M.; Wei, K.; Zhang, P.; Li, J.; Li, N.; Yin, Z.; Su, D.; Sun, S. PdAu Alloy Nanoparticles for Ethanol Oxidation in Alkaline Conditions: Enhanced Activity and C1 Pathway Selectivity. *ACS Appl. Energy Mater.* **2019**, *2* (12), 8701–8706. https://doi.org/10.1021/acsaem.9b01674.

(36) Zamora Zeledón, J. A.; Stevens, M. B.; Gunasooriya, G. T. K. K.; Gallo, A.; Landers, A.

T.; Kreider, M. E.; Hahn, C.; Nørskov, J. K.; Jaramillo, T. F. Tuning the Electronic Structure of Ag-Pd Alloys to Enhance Performance for Alkaline Oxygen Reduction. *Nat. Commun.* **2021**, *12* (1), 620. https://doi.org/10.1038/s41467-021-20923-z.

(37) Lv, G.; Zhang, Z.; Liu, S.; Tao, F.; Wang, J.; Meng, Y.; Yang, Y. Atom Level Revelation of the Synergistic Effect between Pd and Au Atoms in PdAu Nanoalloy Catalyst for Aerobic Oxidation of 5-Hydroxymethylfurfural. *Chem. Eng. J.* **2023**, *453*, 139816. https://doi.org/10.1016/j.cej.2022.139816.

(38) Zhu, X.; Guo, Q.; Sun, Y.; Chen, S.; Wang, J.-Q.; Wu, M.; Fu, W.; Tang, Y.; Duan, X.; Chen, D.; Wan, Y. Optimising Surface d Charge of AuPd Nanoalloy Catalysts for Enhanced Catalytic Activity. *Nat. Commun.* **2019**, *10* (1), 1428. https://doi.org/10.1038/s41467-019-09421-5.

(39) Nascente, P. A. P.; de Castro, S. G. C.; Landers, R.; Kleiman, G. G. X-Ray Photoemission and Auger Energy Shifts in Some Gold-Palladium Alloys. *Phys. Rev. B* **1991**, *43* (6), 4659–4666. https://doi.org/10.1103/PhysRevB.43.4659.

(40) Chang, J.-B.; Liu, C.-H.; Liu, J.; Zhou, Y.-Y.; Gao, X.; Wang, S.-D. Green-Chemistry Compatible Approach to TiO_2-Supported PdAu Bimetallic Nanoparticles for Solvent-Free 1-Phenylethanol Oxidation under Mild Conditions. *Nano-Micro Lett.* **2015**, *7* (3), 307–315. https://doi.org/10.1007/s40820-015-0044-6.

(41) Enache, D. I.; Edwards, J. K.; Landon, P.; Solsona-Espriu, B.; Carley, A. F.; Herzing, A. A.; Watanabe, M.; Kiely, C. J.; Knight, D. W.; Hutchings, G. J. Solvent-Free Oxidation of Primary Alcohols to Aldehydes Using Au-Pd/TiO2 Catalysts. *Science* **2006**, *311* (5759), 362–365. https://doi.org/10.1126/science.1120560.

(42) Dimitratos, N.; Lopez-Sanchez, J. A.; Lennon, D.; Porta, F.; Prati, L.; Villa, A. Effect of Particle Size on Monometallic and Bimetallic (Au,Pd)/C on the Liquid Phase Oxidation of Glycerol. *Catal. Lett.* **2006**, *108* (3), 147–153. https://doi.org/10.1007/s10562-006-0036-8.

(43) Klis, F. van der; Gootjes, L.; Verstijnen, N. H.; Haveren, J. van; Es, D. S. van; Bitter, J. H. Carbohydrate Structure–Activity Relations of Au-Catalysed Base-Free Oxidations: Gold Displaying a Platinum Lustre. *RSC Adv.* **2022**, *12* (15), 8918–8923. https://doi.org/10.1039/D2RA00255H.

(44) Rösler, C.; Esken, D.; Wiktor, C.; Kobayashi, H.; Yamamoto, T.; Matsumura, S.; Kitagawa, H.; Fischer, R. A. Encapsulation of Bimetallic Nanoparticles into a Metal–Organic Framework: Preparation and Microstructure Characterization of Pd/Au@ZIF-8. *Eur. J. Inorg. Chem.* **2014**, *2014* (32), 5514–5521. https://doi.org/10.1002/ejic.201402409.

(45) Tsunoyama, H.; Sakurai, H.; Negishi, Y.; Tsukuda, T. Size-Specific Catalytic Activity of Polymer-Stabilized Gold Nanoclusters for Aerobic Alcohol Oxidation in Water. *J. Am. Chem. Soc.* **2005**, *127* (26), 9374–9375. https://doi.org/10.1021/ja052161e.

(46) Nishimura, S.; Yakita, Y.; Katayama, M.; Higashimine, K.; Ebitani, K. The Role of Negatively Charged Au States in Aerobic Oxidation of Alcohols over Hydrotalcite Supported AuPd Nanoclusters. *Catal. Sci. Technol.* **2013**, *3* (2), 351–359. https://doi.org/10.1039/C2CY20244A.

(47) Silva, T. A. G.; Teixeira-Neto, E.; López, N.; Rossi, L. M. Volcano-like Behavior of Au-

Pd Core-Shell Nanoparticles in the Selective Oxidation of Alcohols. *Sci. Rep.* **2014**, *4* (1), 5766. https://doi.org/10.1038/srep05766.

(48) Meenakshisundaram, S.; Nowicka, E.; J. Miedziak, P.; L. Brett, G.; L. Jenkins, R.; Dimitratos, N.; H. Taylor, S.; W. Knight, D.; Bethell, D.; J. Hutchings, G. Oxidation of Alcohols Using Supported Gold and Gold – Palladium Nanoparticles. *Faraday Discuss.* **2010**, *145* (0), 341–356. https://doi.org/10.1039/B908172K.

(49) Savara, A.; Chan-Thaw, C. E.; Sutton, J. E.; Wang, D.; Prati, L.; Villa, A. Molecular Origin of the Selectivity Differences between Palladium and Gold–Palladium in Benzyl Alcohol Oxidation: Different Oxygen Adsorption Properties. *ChemCatChem* **2017**, *9* (2), 253–257. https://doi.org/10.1002/cctc.201601295.

(50) Crombie, C. M.; Lewis, R. J.; Taylor, R. L.; Morgan, D. J.; Davies, T. E.; Folli, A.; Murphy, D. M.; Edwards, J. K.; Qi, J.; Jiang, H.; Kiely, C. J.; Liu, X.; Skjøth-Rasmussen, M. S.; Hutchings, G. J. Enhanced Selective Oxidation of Benzyl Alcohol via In Situ H2O2 Production over Supported Pd-Based Catalysts. *ACS Catal.* **2021**, *11* (5), 2701–2714. https://doi.org/10.1021/acscatal.0c04586.

Chapter 5.

One-pot oxidation and amination of alcohols over PdAu@ZIF-8 and ω-transaminases

5.1. Introduction

In chapter 3 & 4, we developed and discussed ZIF-8 based Cu/ZIF-8/TEMPO and PdAu@ZIF-8 as heterogeneous catalysts for aerobic oxidation of alcohols. For benzyl alcohol and 1-phenylethanol, the above catalysts showed good catalytic activity, stability and recyclability. For the aim of this thesis, i.e., the creation of chemoenzymatic heterogeneous catalysts based on MOFs, the alcohol oxidation catalysts need to possess not only the properties of conventional catalysts, but also the compatibility with the reaction conditions suitable for ω-transaminase (ω-TA) activity. However, when dealing with chemoenzymatic catalytic systems, the optimal reaction conditions for each sub-reaction do not necessarily match with the optimal reaction conditions for each of the subreactions alone.[1–3] Therefore, the key to the creation of a chemoenzymatic catalytic system lies in a precise knowledge of the reaction conditions of each individual sub-reactions to be able to find a compromise for maximizing the overall yield in case the optima conditions are not the same, but remain compatible to some extent.[4,5] This chapter focuses on exploring and optimizing the reaction conditions for the enzyme-catalyzed "one-pot" amination of alcohols.

One of the characteristics of an enzyme is its substrate specificity. For ω-TAs, not all carbonyl compounds and amine donors can serve as substrates.[6] The carbonyl compounds and amine donors should not only be sized to meet the requirements of being able to enter the ω-TA catalytic pocket and match the stereoselectivity of the enzyme (as far as the amine donor is concerned), but also not undergo other side reactions in the chosen reaction conditions.[7,8] Consequently, the influence of both pH and buffers toward the enzymatic activity as well as the activity of PdAu@ZIF-8 was tested. Moreover, a challenge for the application of ω-TA lies in the thermodynamic limitations toward the biocatalytic amination (described in Section 1.2.2.2). In this regard, we tested two carbonyl compounds, benzaldehyde derived from a primary alcohol and acetophenone derived from a secondary alcohol, as substrates for ω-TA and three amine donors: isopropylamine (IPA), 1,2-diaminopropane (DAP) and L-alanine. In order to shift the thermodynamic equilibrium of the reaction toward the target reaction, two strategies

were investigated: (i) the use of an excess of amine donor and (ii) the removal of the carbonyl compound formed, either by its spontaneous chemical conversion (with DAP, so-called “smart” amine donor) or its evaporation (with IPA), or the use of an auxiliary enzymatic system (with alanine). Finally, a preliminary investigation of the "one-pot" amination reaction of 1-PE catalyzed by the combination of PdAu@ZIF-8 and ω-TA 3HMU was carried out. The chemoenzymatic system was first investigated by simply mixing Pd_9Au_1@ZIF-8 and ω-TA 3HMU in solution. The feasibility of a fully heterogenized system were attempted by the subsequent immobilization of 3HMU on PdAu@ZIF-8.

5.2. Methods

5.2.1. Enzyme activity assay

In this study, the determination of ω-TA activity was conducted using (S)-α-methylbenzylamine (S-MBA) as the amine donor and pyruvic acid as the amine acceptor. The protocol was adapted from S. Schätzle et al.[9]

The activity assay of the free transaminases (ω-TAs), i.e solubilized ω-TAs, were performed at 37 °C in Tris HCl buffer (50 mM, pH 8.5). (See Scheme 5.1) In a typical assay of free ω-TA, the reaction solution contains 2.5 mM of S-MBA (from a 25 mM stock solution of S-MBA in 2.5% v/v DMSO), 2.5 mM of sodium pyruvate, 0.1 mM of PLP and 0.001 to 0.01 mg/mL ω-TA. The kinetics of the reaction was analyzed using a UV spectrophotometer at 254 nm to extract the slope (Δ OD/ Δt), then used to calculate the initial rate of the enzymatic reaction relative to the formation of acetophenone (AP) deduced from (Δ OD/ Δt) thanks to Beer-Lambert's law. One unit (U) of ω-TA activity was defined as the amount of ω-TA required for the production of 1 μmol of AP per minute at the assessed conditions.

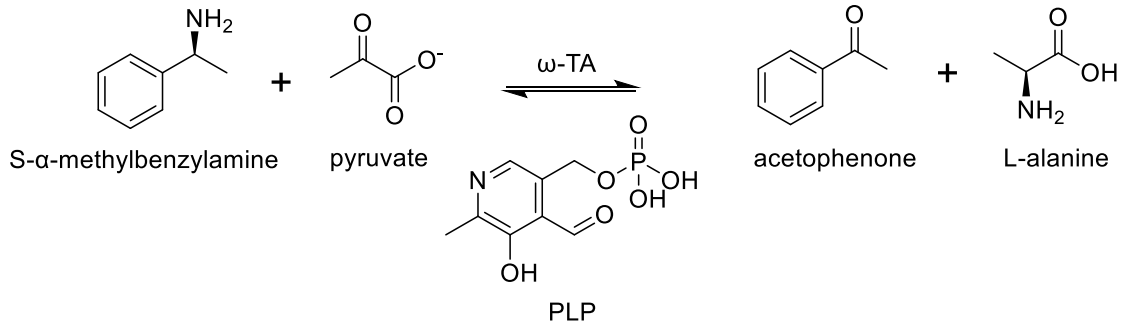

Scheme 5.1. Measurement of ω-TAs activity by monitoring the rate of formation of acetophenone spectrophotometrically at 254 nm.

The pH influence study on soluble ω-TA activity was performed at 37 °C using different buffers including NaH_2PO_4/Na_2HPO_4 (50mM, pH 7.0), Tris HCl (50 mM, pH 7.3, 7.9, 8.5), and $NaHCO_3/Na_2CO_3$ (50 mM, pH 9.0, 9.5, 10.0. 10.5) to cover the pH range from 7.0 to 10.5.

5.2.2. Synthesis of (S)-α-methylbenzylamine from acetophenone using free ω-transaminase with GDH/LDH system

In a 1.5 mL glass vial, acetophenone (50 mM), D-glucose (150 mM), L-alanine (250 mM), pyridoxal 5'-phosphate hydrate (PLP, 0.1 mM), β-nicotinamide adenine dinucleotide, reduced disodium salt hydrate (NADH, 1 mM), dimethyl sulfoxide (DMSO, 5%), lactic dehydrogenase (LDH), recombinant produced in *E. coli* (2 mg/mL), glucose dehydrogenase (GDH) from *Pseudomonas species*(0.1 mg/mL) and ω-transaminase (ω-TA, 2 mg/mL) was mixed in Tris HCl buffer (100 mM, pH 8.5) to give a total volume of 500 µL. The concentrations indicated above are the final concentrations in the 500 µL. The solution was incubated at 37 °C. At the end of the reaction, the liquid products of the reaction were filtered and analyzed by high performance liquid chromatography (HPLC, Infinity II by Agilent) equipped with a SiELC Primesep 100 column (150 x 4.6 mm, 5µm) and a diode-array detector (DAD). The mobile phase was acetonitrile: 0.1 v/v% trifluoroacetic acid in water (v:v=30:70). The detection of substrates and products were performed at the wavelength 254 nm and 230 nm and their quantification used a calibration curve method.

5.2.3. Amination of acetophenone or benzaldehyde using free ω-transaminase with isopropylamine or 1,2- diaminopropane, a "smart" amine donor

In a 1.5 mL glass vial, acetophenone or benzaldehyde (50 mM), pyridoxal 5'-phosphate hydrate (PLP, 0.1 mM), and free ω-transaminase (ω-TA, 2 mg/mL) were dissolved in a Tris HCl buffer (50 mM, pH 8.5 containing 50 mM of isopropylamine or 1,2-diaminopropane) to give a total volume of 500 μL. In the case of the buffer-free conditions, the Tris HCl buffer is replaced by amine donor solution (isopropylamine or 1,2-diaminopropane, 200 mM or 1M). The reaction took place at 37 °C. After the catalytic reaction, the liquid products were analyzed by the HPLC method as described in section 5.2.2.

5.2.4. Aerobic oxidation of 1-(±)-phenylethanol with PdAu@ZIF-8 in the presence of an auxiliary enzymatic system

The procedure of aerobic oxidation of 1-(±)-phenylethanol (1-PE) over PdAu@ZIF-8 (In this chapter, PdAu@ZIF-8 stands for Pd_9Au_1@ZIF-8 unless stated) followed the same procedure as described in section 4.2.2. In the experiments on the influence of pH, 0.2 mmol of 1-PE was dissolved in 2 mL of several buffers: including phosphate buffer (Na_2HPO_4/NaH_2PO_4, 100 mM pH 7.0), Tris HCl buffer (100 mM at pH 8.5), Carbonate buffer ($Na_2CO_3/NaHCO_3$, 100 mM pH 9.2). Then, the solution was bubbled with a O_2 flow for 10 minutes. 5 mg of PdAu@ZIF-8 was added. The suspension was then ultrasonicated for 1 minute to disperse the catalyst.

In the case of the auxiliary enzymatic conditions, 0.2 mmol of 1-PE was dissolved in 2 mL of water. The key components (substrates, PLP, equilibrium shift auxiliaries) of the enzymatic reaction were added one by one to test their effects on the oxidation reaction in water, i.e. PLP, L-alanine, IPA, glucose, etc. The catalytic reaction followed the same steps as described in the previous paragraph.

The reaction was maintained at 50 °C for 24 h. After the catalytic reaction, the suspension was centrifuged. The catalyst was collected and washed with water. The liquid products were

analyzed by the same HPLC method with Section 5.2.2. The detection of substrates and products were performed at the wavelength 254 nm and their quantification used a calibration curve method.

5.2.5. The one-pot/one-step synthesis of (S)-α-methylbenzylamine over PdAu@ZIF-8 and free 3HMU

The one-pot/one-step synthesis of (S)-α-methylbenzylamine reaction was carried in a 1.5 mL glass vial containing 1-(±)-phenylethanol (100 mM), D-glucose (150 mM), L-alanine (250 mM), PLP (0.1 mM), NADH (1 mM), DMSO (5%), lactic dehydrogenase, LDH (2 mg/mL), GDH (0.1 mg/mL) and ω-TA (4 mg/mL) in Tris HCl buffer (50 mM, pH 8.5) to give a total volume of 500 µL. Then, 1.25 mg of PdAu@ZIF-8 was added and the glass vial was saturated with O_2. The glass vials were stirred in an incubator at 50 °C at 60 rpm for 24 hours. After the catalytic reaction, the suspension was centrifuged. The solid was collected by filtration and washed with water. The supernatant was analyzed by the same HPLC method with Section 5.2.2.

5.2.6. The one-pot/two-step synthesis of (S)-α-methylbenzylamine over PdAu@ZIF-8 and 3HMU

The one-pot/two-step synthesis of (S)-α-methylbenzylamine was carried in 2 steps. The oxidation of 1-(±)-phenylethanol was first performed in a 15 mL glass test tube sealed by a plastic lid. 0.1 mmol of 1-(±)-phenylethanol was dissolved in 1 mL of water, giving an initial concentration of 100 mM. Before adding the substrate, water was saturated by O_2 bubbling for 10 minutes. Subsequently 2.5 mg of Pd_9Au_1@ZIF-8 was added. The reaction was performed at 50 °C for 24 h. After, the catalyst and supernatant were separated by centrifugation. 20 µL of supernatant was used for yield and conversion analysis. 250 µl of supernatant was transferred to a 1.5 ml glass vial with a lid and mixed with D-glucose (150 mM), L-alanine (250 mM), PLP (0.1 mM), NADH (1 mM), DMSO (5%), lactic dehydrogenase, LDH (2 mg/mL), GDH (0.1 mg/mL) and ω-TA (2 mg/mL) in Tris HCl buffer (100 mM, pH 8.5). Finally, the total volume

of the reaction solution was 500 μL (the concentrations mentioned above are final concentrations). The solution was spun at 37°C for 20 h at 40 rpm before being centrifuged and filtered. This mixture was analyzed the same HPLC method with section 5.2.2. The conversion and yield were calculated separately for the two reaction steps. The conversion and yield of the alcohol oxidation reaction were calculated from the initial concentration of 1-(±)-phenylethanol and acetophenone, while the yield of the amination reaction (second step) was calculated from the concentrations of (S)-α-methylbenzylamine and acetophenone.

5.3. Results and discussion

5.3.1. Biocatalyzed amination using ω-TA

5.3.1.1. Properties of ω-TAs used in this work

The two different recombinant ω-TAs, from *Chromobacterium violaceum* and *Silicibacter (or Rueguria) pomeroyi*, used in this work were a generous gift from Pr. Uwe Bornscheuer (Institute of Biochemistry at Greifswald University) and used as received. In the following, *Silicibacter (or Rueguria) pomeroyi*, ω-TA is named according to the PDB name corresponding to its 3D structure, ie 3HMU, whereas for ω-TA from *Chromobacterium violaceum* will be named *Cv*-ω-TA.

3HMU was first described as a transaminase in 2013,[10] although 3HMU crystallographic structure was register in the PDB in 2009 by Toro et al.[11] The 3D-structure of *Chromobacterium violaceum* ω-TA has been released from the Protein Data Base in 2012 (PDB name 4A6T).[12]

The alignment of the sequences of 3HMU and *Cv*-ω-TA share 51 % sequence identity, namely in the catalytic site (lysine 290, Asp256 which binds the pyridine ring nitrogen of PLP via a hydrogen bond coordination and Thr 321 whose main chain amide nitrogen atom forms a hydrogen bond with one of the phosphate oxygens of PLP). These residues are identical in both two structures and close residues highly conserved (See Figure 5.1).

Figure 5.1. Sequence alignment of3HMU and 4A6T (*Cv*-ω-TA) ω-TAs sequences (performed with the multiple sequence alignment tool from Clustal Omega

The two enzymes have been expressed and produced as recombinant proteins in *E. coli* BL21. A typical purification protocol uses a chelating chromatography step (IMAC) followed by a desalting one using an exclusion column and storage in a Tris HCl buffer pH 7.5-8.5 in the presence of 0.1 M PLP.[10,13] We have checked the purity of the enzymes we received from Pr. Bornscheuer by SDS Page electrophoresis (See Figure 5.2). Migration of both 3HMU and Cv ω-TA are very close from the molecular mass marker representative of 52.2 kDa, which is consistent with the expected mass of the monomeric chain of the protein reported in the literature, ie 51.7 and 51.2 kDa for 3HMU and *Cv*-ω-TA, respectively.

In the first batch 3HMU concentration is slightly higher than in the second one, although the first batch 3HMU is less pure. The 3HMU used in this Chapter is from the first batch.

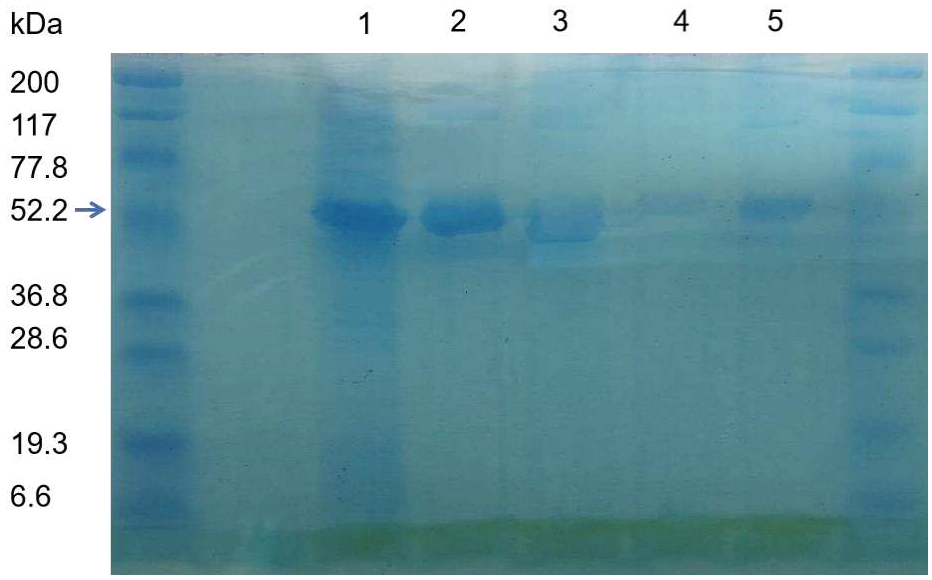

Figure 5.2. SDS Page electrophoresis of ω-TAs. lane 1: 3HMU 1st batch, lane 2: 3HMU 2nd batch, lane 5: *Cv*-ω-TA

5.3.1.1.1. ω-TA from *Silicibacter pomeroyi* (3HMU)

The crystallographic structure of 3HMU shows that the enzyme is a homodimer, each chain has a molecular weight of 51.7 kDa for 472 residues (including 6 His at the C-terminal end of the protein when the recombinant protein is expressed *in E. coli,* although only Chain A of the 3HMU PDB structure gives the coordinates of three of them (See Figure 5.3 left). The overall folding of the enzyme shows a typical overall structure of a protein of PLP fold class I enzyme, although 3HMU lacks the PLP molecule in its crystal structure. Instead, a sulfate ion from the crystallization buffer is coordinated in the position where the phosphate group of PLP is located in other ω-TAs.

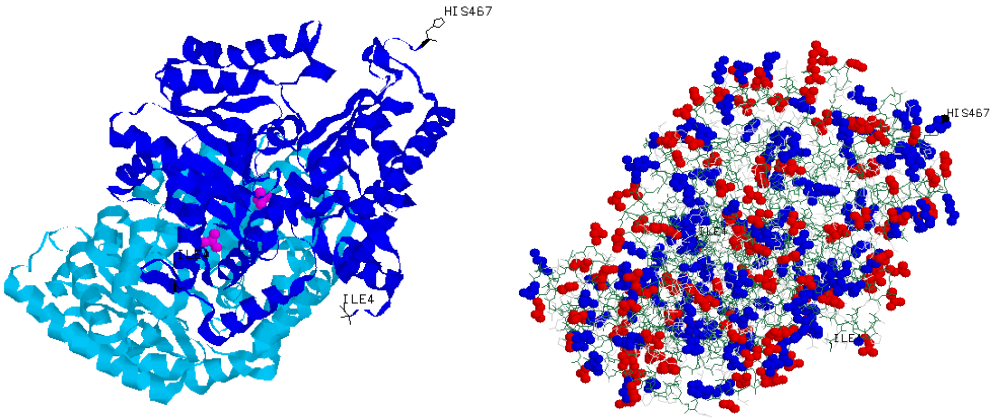

Figure 5.3. 3D structure of *R. pomeroyi* (3HMU) as a homodimer. Left: Backbone of the Chain A (in intense blue) et Chain B (in light blue). Sulfate ions are in pink. Right: Wireframe in light green are backbones of chains A and B. Blue balls are lysine, histidine and arginine residues. Red balls are aspartate or glutamate residues. Drawn with Rasmol 2.6.

3HMU calculated isoelectric point (using ProtParam tool in ExPASy) is 5.57, with basic and acidic residues homogeneously distributed mainly on the protein surface (See Figure 5.3 right). Another observation made from the work of Steffen-Munsberg et al. is the S-selectivity of 3HMU. In addition, S-α-methylbenzylamine (S-MBA), which is often used as a benchmark substrate for many ω-TAs, is a good substrate for 3HMU.[10]

Table 5.1. Overview of some characteristics of the polypeptide chain of *Silicibacter pomeroyi* (3HMU) and *Chromobacterium violaceum* (4A6T) ω-TAs proteins.

Microorganism (PDB name)	Molecular mass (kDa)	Number of residues	Isoelectric point	Number of residues per chain	
				Basic residues Arg/His/ Lys	Acidic residues Asp/Glu
S. pomeroyi (3HMU)	51.7	472	5.57	63 24/23/16	60 20/40
C. Violaceum (4A6T)	51.2	459	6.13	66 30/15/21	58 25/33

The specific activity of the 3HMU batch used in this chapter and chapter 6 were found to be 3.7 U/mg and 0.49 U/mg in Tris HCl buffer of pH 8.5 (50 mM) at 37°C using the activity test conditions described in section 5.2.1. It must be noticed that a higher activity was reported by Uwe Bornscheuer 's group with the same enzyme, ca 14.9 U/mg in slightly different conditions, ca pH 9.5 and 30°C.[10,14] The lower purity (See SDS Page) of the batch we have used could explain this discrepancy.

5.3.1.1.2. *Chromobacterium violaceum* ω-TA (*Cv*-ω-TA)

The isolation of *Cv*-ω-TA from *Chromobacterium violaceum* was first reported in 2007.[15] Now *Cv*-ω-TA stands out as a highly recognized ω-TA. Its characteristics including substrate diversity, 3-dimensional structure, and reaction kinetics stability, have been comprehensively investigated.[15–19]

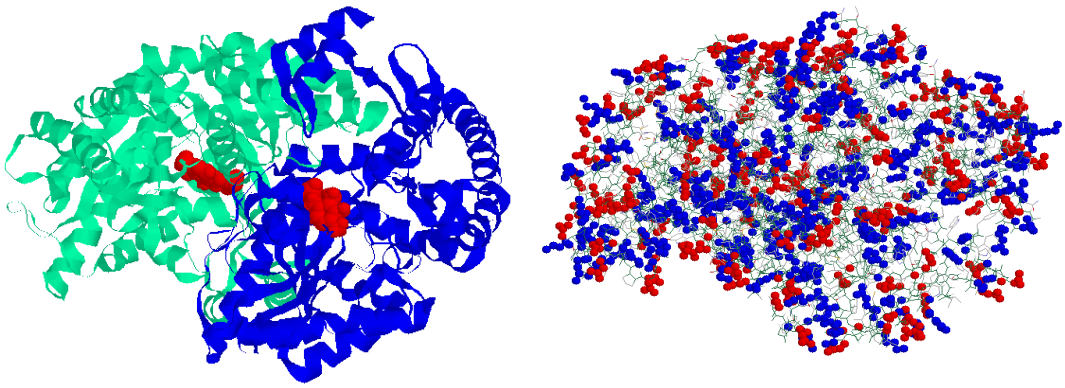

Figure 5.4. 3D structure of *C. violaceum* ω-TA (4A6T) as a homodimer. Left: Backbone of the Chain A (in intense blue) et Chain B (in light green). PLP (one in each monomer) are in red Right: wireframe in light green are backbones of chains A and B. Blue balls are lysine, histidine and arginine residues. Red balls are aspartate or glutamate residues. Drawn with Rasmol 2.6.

Cv-ω-TA is a homodimer with a molecular weight of approximately 100 kDa. each monomer has an active site at the dimer interface involving amino acid residues of both subunits.[12] The value of the isoelectric point of *Cv*-ω-TA is 6.13, higher than the one calculated for 3HMU ω-TA (5.57), due to a higher proportion of basic residues. The specific activity of *Cv*-ω-TA on S-MBA transamination is ca. 1.2 U/mg.[15,16] Notably, PLP plays an important role in the stability

of dimeric and tetrameric (S)-selective transaminases including *Cv*-ω-TA.[20,21]

5.3.1.2. Influence of pH on ω-TAs

Typically, there exists an optimum pH at which enzyme activity is maximized. ω-transaminases usually show the highest specific activity under weakly basic conditions.[22–24] Since a single buffer could only cover a narrow pH range, three different buffers were used to test the targeted pH range including sodium dihydrogen phosphate/disodium hydrogen phosphate (50mM, pH 7.0), Tris HCl (50 mM, pH 7.3, 7.9, 8.5), and sodium carbonate/sodium bicarbonate (50 mM, pH 9.0, 9.5, 10.0, 10.5). The activities of both ω-TAs at different pHs are shown in Figure 5.5.

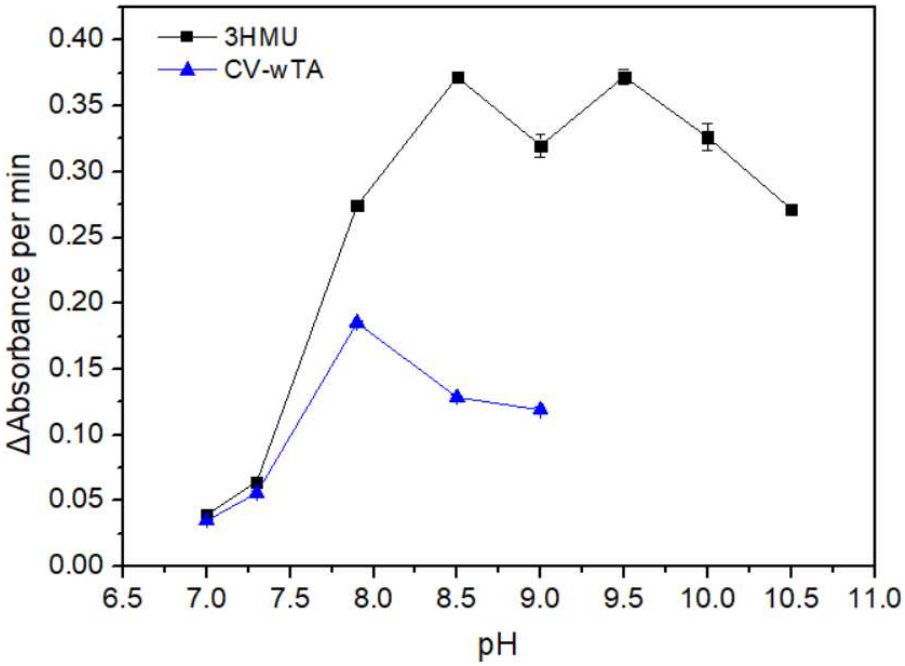

Figure 5.5. Effect of different pHs on the activity of 3HMU and *Cv*-ω-TA

The 2 ω-TAs show volcano-like activity-pH correlation curves, with a maximum working pH. Among the 2 ω-TAs, 3HMU has the highest activity at all pHs. The highest and second highest activities are obtained at pH 8.5 and pH 9.5, respectively. An unexpected decrease in activity is observed at pH 9.0 compared to pH 8.5 and pH 9.5. The explanation could be that pH 9.0 is the critical buffering pH of Tris HCl buffer, and therefore the buffering capacity of this buffer is not sufficient to maintain the pH of the solution, resulting in a shift to a higher pH after the

addition of the basic reaction substrate S-MBA. Unfortunately, pH of the reaction mixture was not checked before the activity measurement. The activity of 3HMU at pH 9.0 is similar to that at pH 10, which is consistent with the above explanation. 3HMU is also active outside the optimum working pH, but its activity is much weaker at near-neutral pH. Moreover, although 3HMU is also active at pH 10.5, a rapid decrease in the acetophenone formation rate was observed on the $OD_{254\,nm} = f(t)$ during the activity test, indicating the inactivation of 3HMU at high pH.

For *Cv*-ω-TA, the highest activity is recorded at pH 7.9. The activity of *Cv*-ω-TA decreases rapidly with increasing pH.

Overall, the optimal working pH of both ω-TAs is in the weak alkaline range, which is compatible with the use of ZIF-8 as a support for enzyme immobilization. Although ZIF-8 is one of the aqueous phase stable MOFs, its stability is very sensitive to pH. Indeed, ZIF-8 decomposes rapidly at a weak acidic environment around pH 6, while basic conditions are favorable for the preservation of its crystal structure.[25,26] The overlap between a stable pH for ZIF-8 and an optimal ω-TAs working pH at values suitable for an efficient oxidation of alcohols is therefore compatible with a one-pot chemoenzymatic-catalyzed oxidation-amination cascade reaction starting from an alcohol which could take place in the pH range 8.5-9.0.

5.3.1.3. Biocatalyzed amination of benzaldehyde

Although S-MBA is used as a model amine donor in the activity test protocol of ω-TAs, what makes economic sense in real industrial production is the reverse reaction to produce S-MBA. As described in section 1.2.2, the reaction to produce S-MBA is thermodynamically unfavorable. Therefore, in order to shift the chemical reaction equilibrium in the desired direction, the conventional strategy is to increase the substrate (the amine donor) concentration and/or decrease the product (the corresponding carbonyl derivative) concentration. For example, the product could be evaporated or transferred to an immiscible organic phase or irreversibly converted to other substances by chemical methods.

Isopropylamine (IPA) was first investigated as an inexpensive and readily available nonchiral

amine donor. The transamination reaction co-product is acetone, a low boiling point compound that can be easily evaporated from the solvent. Generally, excess IPA is required to drive the transfer of amino groups from amine donor to the targeted product side (See Scheme 5.2).

The enzymatic amination reaction of benzaldehyde, a primary alcohol oxidation product, with IPA as the amine donor was investigated. A five-fold molar IPA excess was used, as referred to the work of Pr. Uwe T. Borncheuer's group on IPA as an amine donor for transamination.[27] The conversion and yield of benzaldehyde transamination over the two studied ω-TAs are shown in Table 5.3.

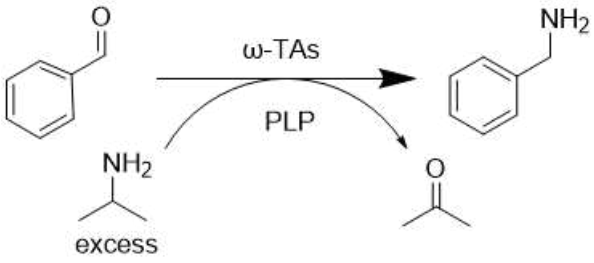

Scheme 5.2. Biocatalyzed benzaldehyde amination using IPA as an amine donor

Table 5.3. Enzymatic transamination of benzaldehyde

Enzyme	Time (h)	Conversion (%)	Yield benzylamine (%)
3HMU	24	70	34
Cv-ω-TA	24	-	-

Test conditions: IPA 20 mM, benzaldehyde 4 mM, PLP 0.2 mM, ω-TA 0.02mg/mL, Tris HCl buffer (pH 8.5 or 8.0 50 mM), T=37 °C

In the case of 3HMU, a conversion of 70% could be achieved after 24 h of reaction. This indicates that IPA is an acceptable amine donor for 3HMU. However, the yield of benzylamine (BLM) is only half of the conversion (34 %), which means that part of BLM is converted into by-products. This is confirmed by the presence of additional peaks observed on the corresponding HPLC chromatogram. In order to study the process of the reaction in detail, we

plotted the yield and conversion curves as a function of time, as shown in Figure 5.6. It can be seen from the figure that the conversion is higher than the substrate yield at any stage of the reaction. In the first 20 min of the reaction, the slope of the conversion curve is greater than the slope of the benzylamine yield, which indicates that side reactions start to occur at the beginning of the reaction. After 24 hours (1440 minutes), the BLM yield remains similar to the value at 30 minutes while the conversion reaches 70%, indicating that the selectivity of the reaction towards the aldehyde formation decreases with time.

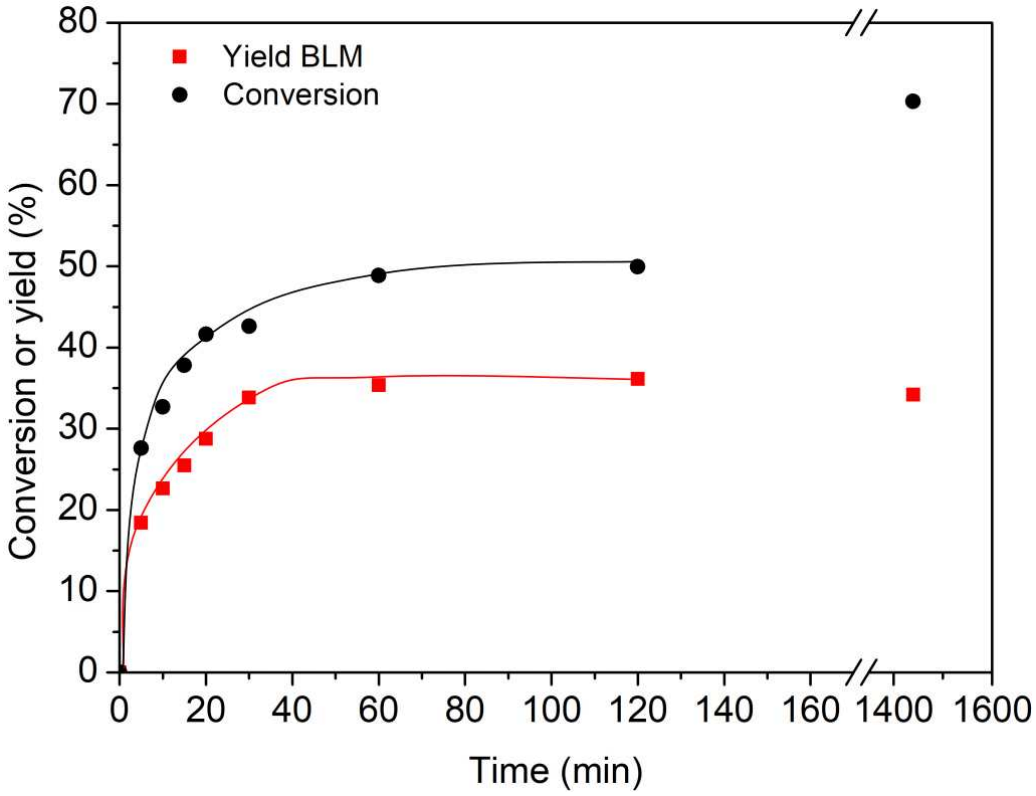

Figure 5.6. BLM yield and Benzaldehyde conversion using IPA as amine donor

Thus, the reaction involves a complex process of multiple side reactions. Since the side reaction start from the beginning, the by-products may come from side reaction between benzaldehyde and IPA or BLM formed by biocatalysis. Indeed, benzaldehyde could react with IPA or BLM to form an imine, also known as a Schiff base. Imine formation is reversible in water and the hydrolysis of imines to form aldehydes and amines occurs favorably under aqueous phase conditions. Therefore, the synthesis of imines usually takes place in organic solvents.[28]

However, it has been reported that imines could be synthesized and remain stable in the aqueous phase at room temperature without any catalyst.[29–31] To assess this hypothesis, we tested the reactions between benzaldehyde and IPA on one side and benzaldehyde and BLM on the other side in aqueous phase at room temperature without the addition of ω-TAs and PLP. It was checked that all 3 reactants are fully soluble in water in the tested concentrations. Pictures of the reaction solutions are shown in Figure 5.7. When IPA was added dropwise to the benzaldehyde solution, the solution became slightly turbid, indicating the spontaneous formation of a small amount of slightly soluble material. After sufficient shaking, the solution became transparent again, indicating that the reaction product could be dissolved in water (tube on the right position in Figure 5.7). In contrast, when BLM was added dropwise to the benzaldehyde solution, the solution became turbid rapidly and a stable emulsion was formed (tube on the left in Figure 5.7). In summary, it indicates that benzaldehyde may react with both IPA and BLM and forms a soluble Schiff base with IPA and an insoluble one with BLM (As suggested in Scheme 5.3).

Figure 5.7. Mixture of benzaldehyde and BLM (left) and benzaldehyde and IPA (right)

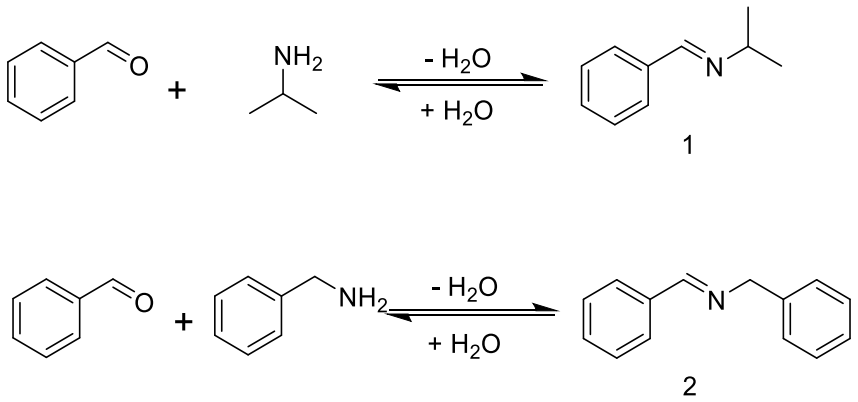

Scheme 5.3. Possible side reactions of benzaldehyde with amine donors and transamination reaction products

In order to identify the reaction products, HPLC and ^{1}H-NMR were used (Figure 5.8). After reaction between benzaldehyde (retention time (t_R) 6.7 min) and IPA (not detected by HPLC), a third peak can be observed at a retention time of 14 min. This peak is the only additional peak, which is presumably attributed to the imine formed by benzaldehyde with IPA, which is consistent with the retention phenomena which take place in reverse phase chromatography. In case of the benzaldehyde with BLM reaction, the only additional peak which can be observed is at about 25 min, which could be presumably attributed to the imine formed from benzaldehyde with benzylamine.

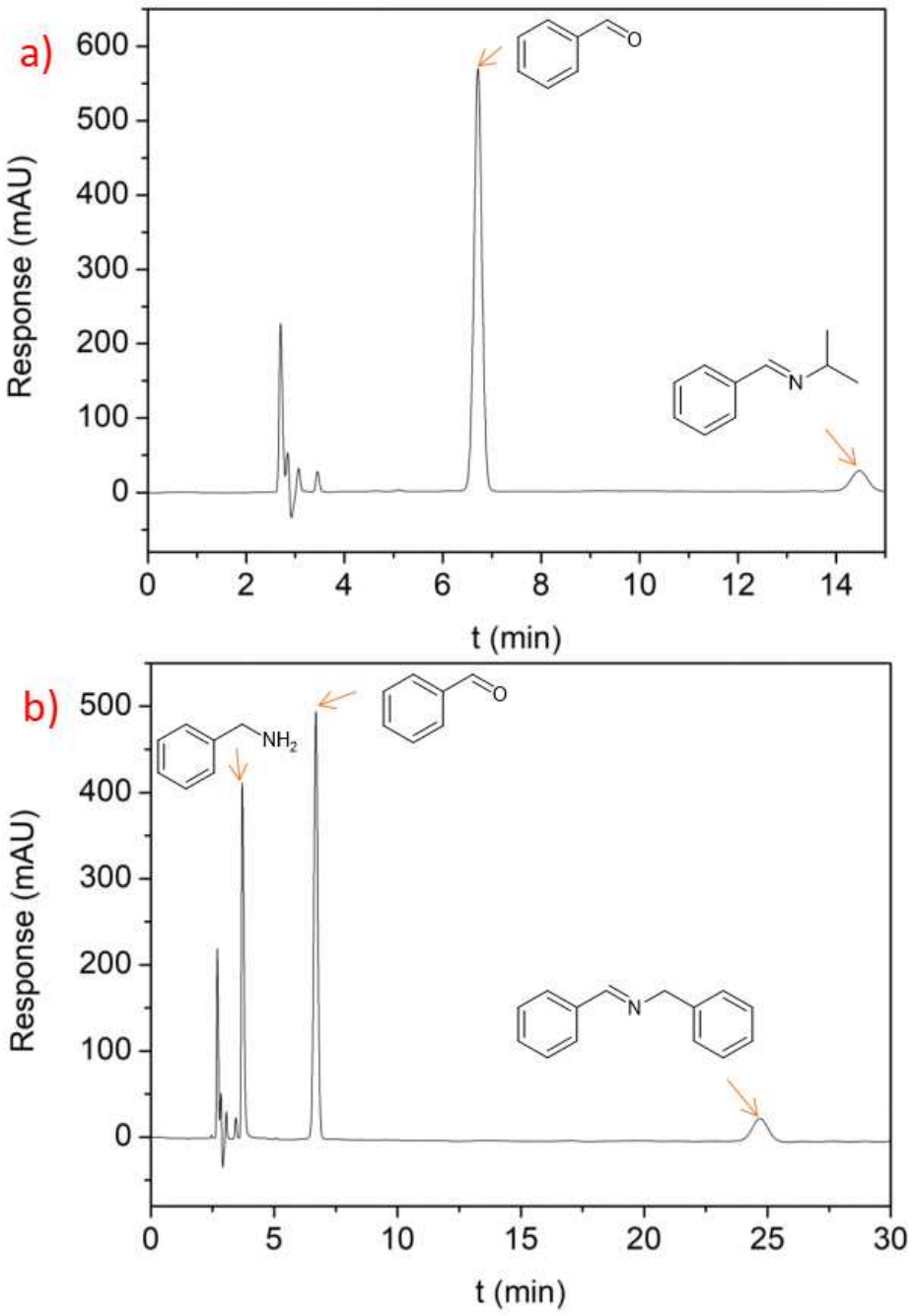

Figure 5.8. HPLC chromatography of mixture of a) benzaldehyde and IPA and b) benzaldehyde and BLM

In order to verify the above assumptions and further identify the reaction products, the above experiments were repeated using D_2O as a solvent and the mixtures were directly analyzed by ^{1}H-NMR. The NMR spectra of benzaldehyde, BLM and their mixtures are shown in Figure 5.9a.

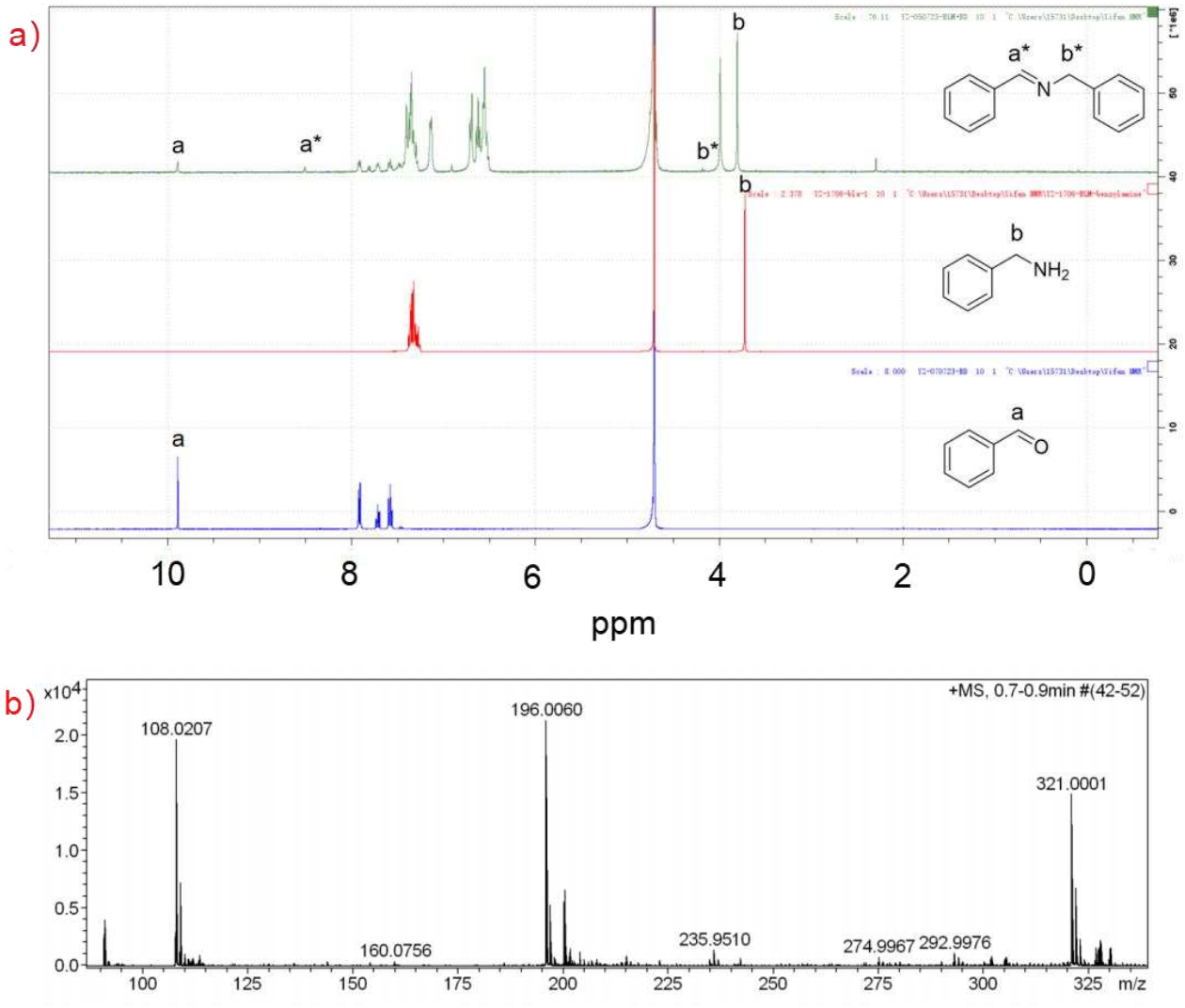

Figure 5.9. a) The ^{1}H-NMR spectra of benzaldehyde, BLM, and the mixture of them in D_2O b) ESI-HRMS of the mixture of benzaldehyde and BLM in water.

In the ^{1}H-NMR spectrum of benzaldehyde, the peak at chemical shift 9.887 ppm is attributed to the characteristic proton **a** of the aldehyde function. The ratio of the intensity of the peak at 9.881 to the ones at 7.511 to 7.922 ppm (assigned to the aromatic protons of benzaldehyde) is about 1:5, which is in line with the structural formula of benzaldehyde. In the ^{1}H-NMR spectrum of BLM, the peak at chemical shift 3.716 is attributed to the characteristic proton **b**. In the mixture of both compounds (green spectrum), these two peaks are observed, although the proton **a** signal is very much weaker as expected from the initial concentration of benzaldehyde. Additional peaks are observed, including a* at 8.441 ppm and b* at 4.165 ppm, that are consistent with the Schiff base **2** structure as well as data reported in the literature.[32] In

addition, the benzaldehyde/BLM mixture was analyzed by ESI-HRMS (see Figure 5.9b). The strong signal at m/z of 196 is likely consistent with Schiff base **2** (molar weight=195). Combining ^{1}H-NMR and ESI-HRMS analysis, we can conclude that at room temperature, benzaldehyde and benzylamine spontaneously form Schiff base **2** in water.

The ^{1}H-NMR spectra of benzaldehyde, isopropylamine (IPA), and their mixture are presented in Figure 5.10. In the ^{1}H-NMR spectrum of IPA, the peaks at chemical shifts of 3.074 and 1.023 ppm are attributed to the protons **b** and **c** respectively. Additionally, the peaks at chemical shifts of 8.366, 3.589, and 1.175 ppm can reasonably be assigned to protons a*, b*, and c* of Schiff base **1**, respectively, in accordance with literature.[32] Therefore, the formation of Schiff base 1 from benzaldehyde and IPA is confirmed.

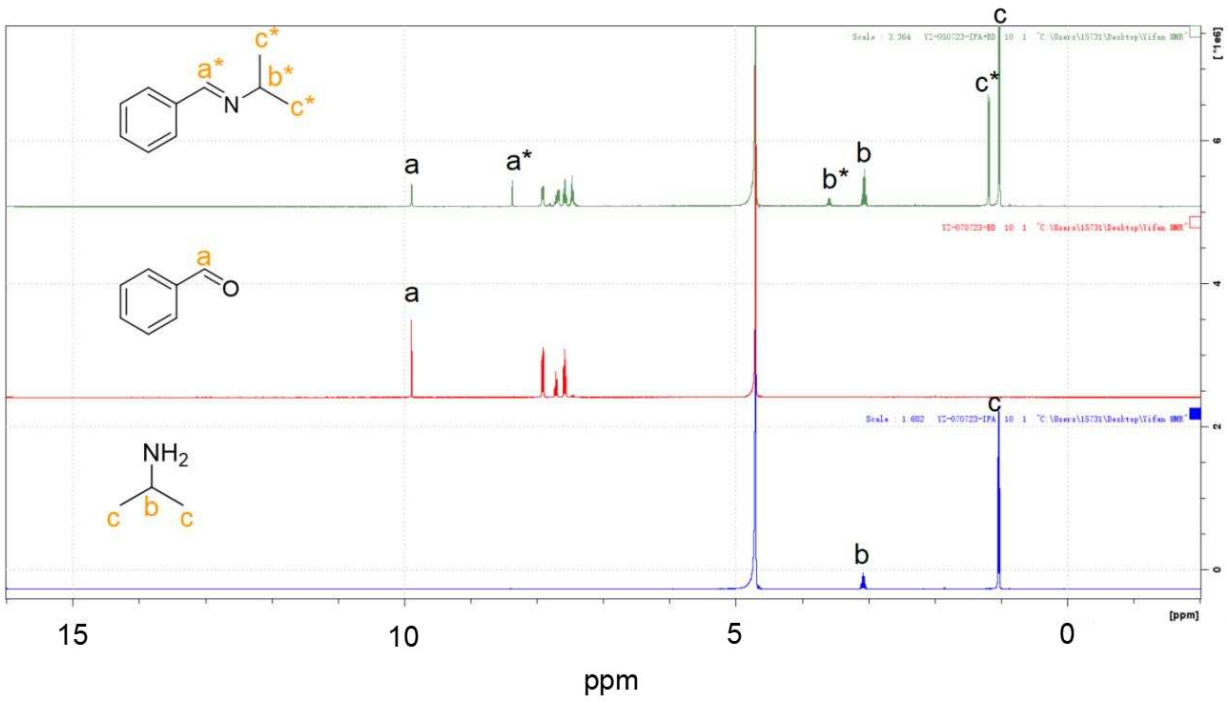

Figure 5.10. The ^{1}H-NMR spectra of benzaldehyde, IPA, and the mixture of them in D_2O

The reaction of benzaldehyde with BLM and IPA to form the corresponding imines is in agreement with the literature,[29–31] although the reaction is thermodynamically reversible and the hydrolysis of imines is favored in the aqueous phase. However, since the reaction product of benzaldehyde with BLM **2** is insoluble in water, its precipitation from the aqueous phase

leads to a thermodynamic trap that favors the imine **2** formation.[29]

To summarize, it was evidenced that benzaldehyde reacts with both IPA and its biocatalyzed amination derivative to form two imines as side-products, whose formation is driven by their low water solubility. Consequently, these side reactions limit the transamination reaction yield. Therefore, aldehydes such as benzaldehyde are not suitable as substrates to efficiently synthesize the corresponding amines by a transaminase biocatalyzed amination. Compared to aldehydes, ketones poorly react with amines in water to form imines and require acid catalyst,[33,34] whereas ω-TAs works under weakly basic conditions. Therefore, ketones as ω-TAs substrates are more suitable than aldehydes. Consequently, we used acetophenone from the oxidation of 1-PE as a model compound to study its transamination reaction catalyzed by ω-TAs, particularly the effect of the nature of the amine donor and the nature of the w-TA.

5.3.1.4. Biocatalyzed amination of acetophenone

Ketones are oxidation products of secondary alcohols. Asymmetric ketones are pre-chiral, meaning that the corresponding chiral amine is formed after the transamination reaction. In this section, we use acetophenone as a model compound to study ω-TAs for the asymmetric transamination reaction of ketones. Since for acetophenone the equilibrium of the enzymatic reaction is not in favor of S-MBA formation, we used an excess of IPA (2-fold molar) as the amine donor (As shown in Scheme 5.4a). Meanwhile, another cheap and readily available diamine, 1,2-propanediamine (DAP), was also used as a smart amine donor to drive the reaction toward the formation of S-MBA (Scheme 5.4b). The carbonyl compound formed from the deamination of 1,2-propanediamine are aminopropanone or α-aminopropanal. These two coproducts undergo a reversible reaction to produce the corresponding two pyrazine derivative isomers. The latest then undergo a spontaneous oxidative aromatization to a pyrazine thereby driving the reversible reaction into a thermodynamic trap.[35] Overall, the acetophenone amination efficiency toward the targeted S-MBA using the two strategies described above for equilibrium shifting are given in Table 5.4.

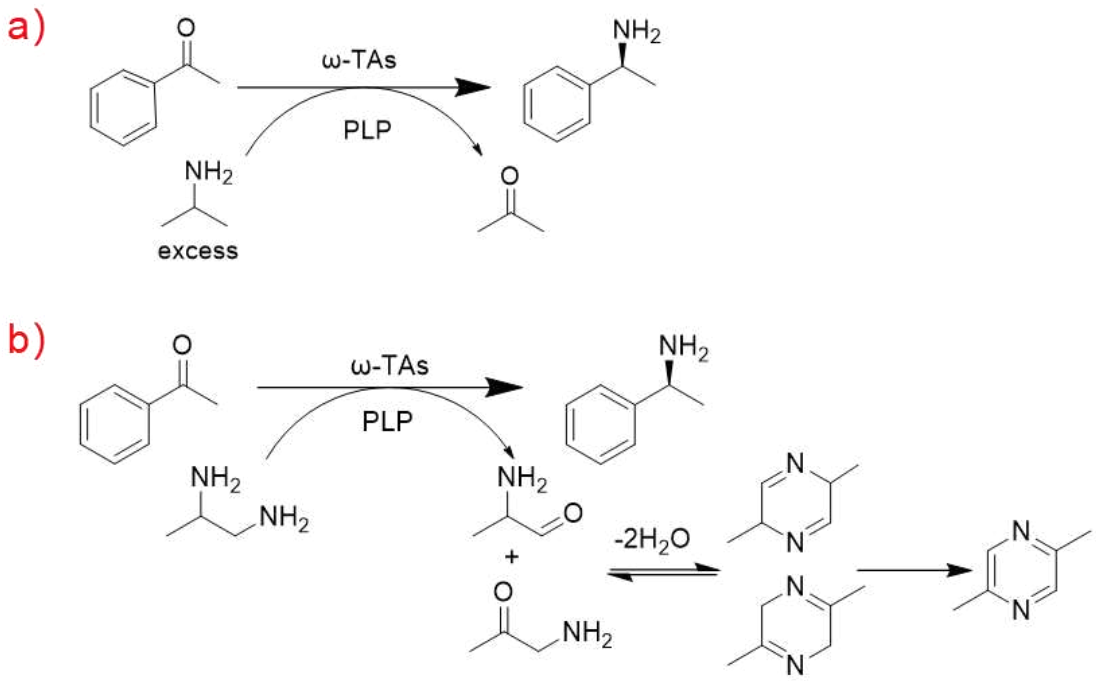

Scheme 5.4. Acetophenone amination using a) IPA and b) DAP as amine donors and strategies for shifting reaction equilibrium

Table 5.4. Conversion and S-MBA yield of transamination using IPA and DAP as amine donor

Enzyme	Buffer pH	Amine donors	Conversion AP (%)	Yield S-MBA (%)
3HMU	Tris HCl 8.5	IPA	0	0
3HMU	Tris HCl 8.5	DAP	0	0
Cv-ω-TA	Tris HCl 8.0	IPA	0	0
Cv-ω-TA	Tris HCl 8.0	DAP	0	0

Test conditions: IPA or DAP 50mM, AP 25 mM, PLP 0.2 mM, ω-TA 4 mg/mL, Tris HCl buffer (pH 8.5 100 mM)，T = 37 °C, t=24 h.

None of the strategies described above to shift the transamination equilibrium allowed the formation of S-MBA from acetophenone. This could have been anticipated since transamination reactions of ketones reported in the literature typically require more than 5-fold amine donor to amine acceptor concentration ratio to drive equilibrium shifts.[8,36–38] However, in our case, an

increase of IPA or DAP concentration would lead to an increase of the pH of the reaction solution, thus to a deactivation of ω-TA. Indeed, the Tris/HCl concentration would not be sufficient to buffer the solution. Alternatively, in other attempts achieved with IPA, no buffer was used. Instead, pH was set to pH 8 or 8.5 by adding hydrochloric acid in the reaction mixture containing IPA before adding ω-TA (See Table 5.5).

Table 5.5. Conversion and S-MBA yield of transamination using IPA as amine donor

Enzyme	IPA concentration (M)	pH	Conversion AP (%)	Yield S-MBA (%)
3HMU	0.2	8.5	21	17
3HMU	1	8.5	32	29
Cv-ω-TA	0.2	8.0	20	1
Cv-ω-TA	1	8.0	9	0

Test conditions: AP 50 mM, PLP 0.2 mM, ω-TA 4 mg/mL, T = 37 °C, t=24 h

In such conditions, the acetophenone conversion and S-MBA yield of the AP transamination reaction using 3HMU are 21% and 17%, respectively, when the concentration of IPA reaches 4-fold that of AP, indicating that IPA is an acceptable amine donor for 3HMU. As the concentration of IPA is increased to 20-fold that of AP, the acetophenone conversion and S-MBA yield are 32% and 29%, respectively. The influence of the amine donor concentration increase is thus rather low. For *Cv*-ω-TA, the acetophenone conversion of the AP transamination reaction are 20% and 9% in the presence of 200 mM and 1 M of IPA, respectively. However, no or negligeable amount of S-MBA is obtained with both concentrations of IPA, which may indicate that the transfer of the amino group is blocked because IPA is not a suitable amine donor for *Cv*-ω-TA.

As an alternative method to shift the transamination equilibrium, we have also tested the use of

an auxiliary multi-enzymes cascade reaction widely used in the literature.[23,24] In that case, L-alanine, a cheap and easily available amino acid, was used as an amine donor. Its amination product is pyruvate. It is then converted to lactate by lactate dehydrogenase (LDH), a process that relies on the oxidation of the cofactor NADH (As shown in Scheme 5.5). NAD^+ is then reduced thank to the oxidation of glucose catalyzed by glucose dehydrogenase (GDH). First, the influence of pH on the overall system was checked (See Table 5.6).

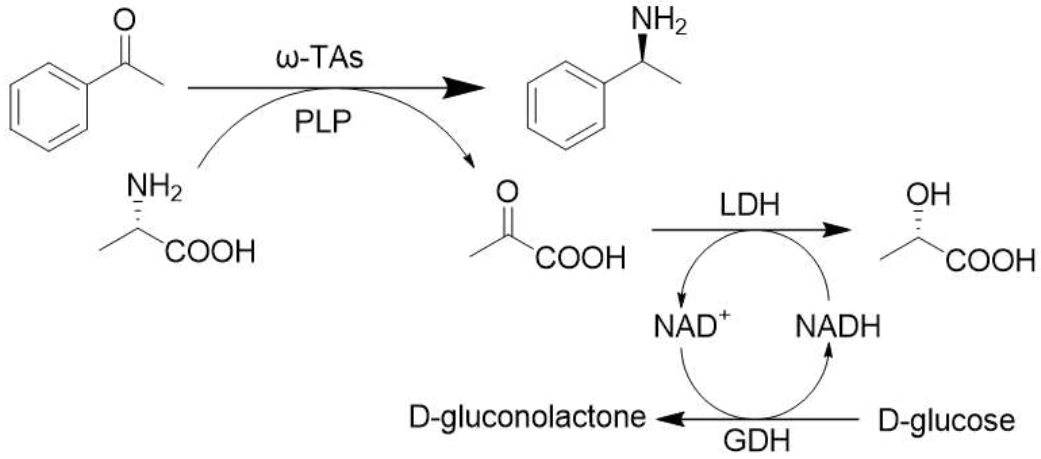

Scheme 5.5. Chemical reaction equations for L-alanine as amine donors and the strategy of shifting of equilibrium of transamination over LDH/GDH system

Table 5.6. Conversion and S-MBA yield of transamination using L-alanine as amine donor

Enzyme	Buffer	pH	Conversion (%)	Yield S-MBA (%)	Selectivity S-MBA (%)
3HMU	Phosphate buffer	7.0	80	76	95%
3HMU	Tris HCl	8.5	80	77	96%
3HMU	Carbonate buffer	9.2	55	37	67%
Cv-ω-TA	Phosphate buffer	7.0	41	25	61%
Cv-ω-TA	Tris HCl	8.5	18	11	61%
Cv-ω-TA	Carbonate buffer	9.2	15	3	20%

Test conditions: AP 50 mM, PLP 0.1 mM, ω-TAs 4 mg/mL, buffer 100 mM, T=37 °C, t=20 h

In the presence of 3HMU, the AP conversion in phosphate buffer pH 7.0, Tris HCl pH 8.0, and carbonate buffer pH 9.2 are 80%, 80%, and 55%, respectively. The yields of S-MBA are 76%, 77%, and 37%, respectively. The high AP conversions and S-MBA yields obtained in the LDH/GDH system compared to the use of excess amine donor IPA indicate that the LDH/GDH cascade enzymatic reaction is more effective for shifting the equilibrium of the transamination reaction. Also, the conversion and S-MBA yields obtained at pH 7.0 and pH 8.5 are very close to each other. This is not consistent with the results of 3HMU activity assessment but highlights the influence of pH of the auxiliary enzymatic system (LDH/GDH). The conversion and S-MBA yield in pH 9.2 buffer are lower than those in pH 7.0 and pH 8.5. We speculate that this is related to the reduced lifetime of 3HMU at high pH and in the presence of high concentration of amine. More, the S-MBA selectivities are very close at pH 7.0 and pH 8.5 (95% and 96%), but the S-MBA selectivity is significantly lower in carbonate buffer at pH 9.2 (67%).

For *Cv*-ω-TA, the conversion of its catalyzed AP transamination reaction in PBS at pH 7.0, tris HCl at pH 8.0, and $NaHCO_3/Na_2CO_3$ pH 9.2 are 41 %, 18 %, and 15 %, respectively. The yields of S-MBA are 25%, 11%, and 3%, respectively. Again, the best results are observed at pH 7.0, a pH lower than the one of maximal activity of *Cv*-ω-TA alone. This behavior is thus similar to that observed with 3HMU. It is worth noting that the S-MBA selectivities are significantly lower compared to 3HMU for all pH tested, which suggests that some side reactions are likely to occur. Unfortunately, no additional peak was observed on the HPLC chromatogram, so that this hypothesis was not confirmed.

In conclusion, different amine donors were used in the AP amination reaction catalyzed by ω-TAs and two equilibrium shift strategies were tested. In Tris/HCl buffer pH 8.5, 29% and 77% S-MBA yields are obtained with 3HMU when using 20-fold excess IPA concentration or L-alanine combined with the LDH/GDH system, respectively. For the chemoenzymatic cascade-catalyzed amination of alcohols described in the next part, L-alanine as an amine donor, in combination with LDH/GDH auxiliary system will be selected because of the satisfactory S-MBA yield obtained with this system and its broader buffer pH compatibility.

5.3.2. Attempts of cascade chemoenzymatic catalysis systems

5.3.2.1. Assessing pH and buffer type compatibility of PdAu@ZIF-8 catalyzed oxidation and transamination steps

In Chapters 3 and 4, we developed ZIF-8-based Cu@ZIF-8/TEMPO and PdAu@ZIF-8 catalysts for the aerobic and mild condition oxidation of alcohols. PdAu@ZIF-8 is more suitable than Cu@ZIF-8/TEMPO as a catalytic system for the chemoenzymatic cascade reaction due to its aqueous phase compatibility and good activity towards secondary alcohols (Cu@ZIF-8/TEMPO is only efficient in organic solvents).

The aerobic oxidation reaction of the model compound 1-phenylethanol (1-PE) catalyzed by PdAu@ZIF-8 at pHs and using buffers shown to be efficient toward transamination in section 5.3.2 as well as in water alone was investigated. The conversion and AP yields are shown in Figure 5.6.

First it appears that the higher the pH is, the higher are the 1-PE conversion and AP yield. Such a result is expected since high pHs favor the deprotonation of the hydroxyl group of the alcohol to form the alcoholate, which is known to favor its oxidation.[39,40]

However, the 1-PE conversion and AP yield obtained in water with a pH adjusted to 7, 83% and 66%, respectively, are higher than those obtained at the same pH in the phosphate buffer. This result indicates that pH is not the only parameter affecting the catalyst performances. The nature of the buffering species may also have an effect on the catalyst functioning.

The poor activity observed in phosphate buffer could indeed be explained by the formation of insoluble phosphates species on palladium and gold metal NPs or oxides, thus leading to their catalytic deactivation.[41–43] Therefore, phosphate poisoning of PdAu NPs is the probable reason for the decreased activity of PdAu@ZIF-8 in phosphate buffer. Another potential explanation could be the decomposition of ZIF-8 crystals in the phosphate solution, leading to the formation of insoluble particles of zinc phosphate, which loses the pore structure.[44,45] The supported PdAu NPs then take greater risk of leaching due to the loss of protection of ZIF-8.

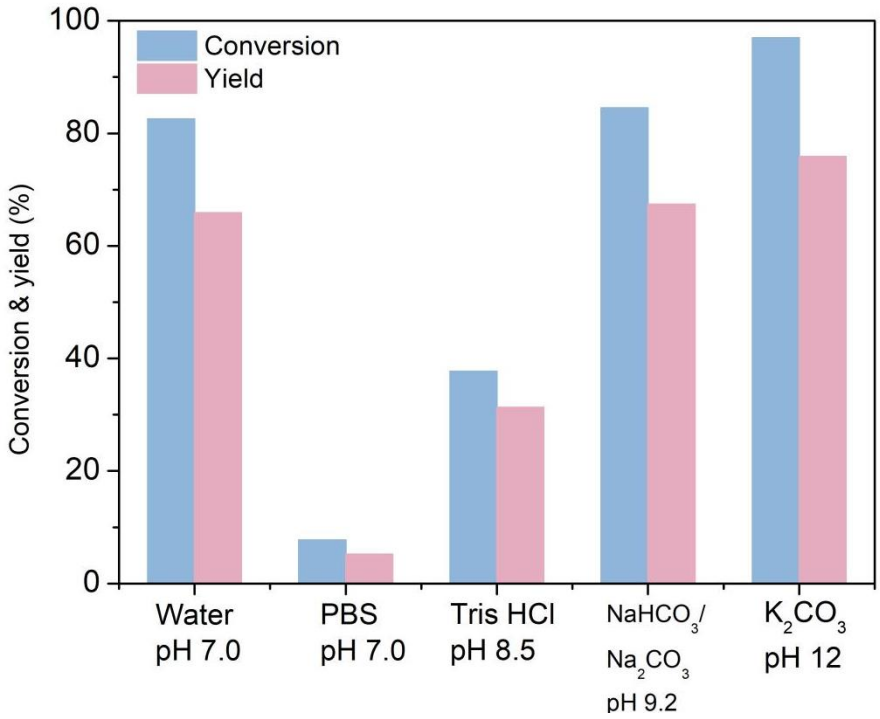

Figure 5.11. 1-PE aerobic oxidation over PdAu@ZIF-8 in different buffers
Test conditions: water or buffers 2 mL, 1-PE 100 mM, T=50 °C, t=24 h, O_2

Similarly, at pH 8.5 in Tris/HCl buffer, 1-PE conversion and AP yield are only 38% and 31%, respectively, which is a disappointing result since even weakly basic pH should be favorable for aerobic oxidation of alcohols.[39,40] It can be hypothesized that such a low conversion results from the inhibition of catalytic activity of PdAu@ZIF-8 in the presence of Tris HCl buffer, ie 2-Amino-2-(hydroxymethyl)-1,3-propanediol (2-AHP) and its corresponding ammonium salt. It is hypothesized that 2-AHP poisoning the metal surface through interactions with its amino groups.

Indeed it is known that competitive adsorption caused by the strong interaction of amine groups with PdAu NPs can lead to active site occupancy, thus reducing substrate accessibility.[46,47] For example, the catalytic activity of Pd NPs is inhibited after immobilization on amine-modified supports.[48] More, it has been reported that the reversible adsorption of aniline onto PdAu alloy nanoparticles inhibits the activity of catalyzing the oxidation of benzyl alcohol.[49] Thus, the adsorption of 2-AHP on PdAu alloy nanoparticles is one of the presumed reasons for the inhibition of PdAu@ZIF-8 activity in Tris HCl buffer. Another suspected factor for the

inhibition of PdAu@ZIF-8 activity is a possible competition of 2-AHP with 2-methylimidazole for the coordination with Zn^{2+} in ZIF-8. In order to study the effect of both water, Tris HCl, phosphate and carbonate buffers on the structure of ZIF-8, we immersed 50 mg of ZIF-8 in 20 mL water in the above buffers for 24h under stirring at 600 rpm at room temperature. To calculate the crystal loss, we measured the concentration of 2-methylimidazole (2-MeIM) in the supernatant by detecting the UV spectrum at 235 nm (See Table 5.7). 2-MeIM is detected in all supernatants including water. This is surprising because ZIF-8 is known for its stability in water. However, the leaching of ZIF-8 is most slight in water compared to buffers. The leaching in Tris HCl is higher compared to water. In phosphate and carbonate buffers, the leaching of 2-MeIM was close to 1/3 of the total mass. Besides leaching test, the PXRD patterns of ZIF-8 before and after immersion for 24 hours are shown in Figure 5.7. There is no significant change in the PXRD pattern of ZIF-8 before and after 24 h immersion in water and Tris HCl buffer. Only one tiny additional diffraction peak is observed at the $2\theta = 11°$, suggesting that ZIF-8 undergoes a slight amount of phase transition in water, but remains generally stable. In contrast, the PXRD pattern of ZIF-8 changes significantly after 24 h immersion in both phosphate buffer pH at 7.0 and carbonate buffer at pH 9.2. For phosphate buffer at pH 7.0, the characteristic peaks of the ZIF-8 phase disappeared, replaced by the characteristic peaks of zinc potassium phosphate ($KZnPO_4$, JCPDS 00-034-0194). The PXRD pattern after 24 h immersion in carbonate buffer at pH 9.2 matches with PXRD pattern of Zinc bis(2-MeIM) carbonate ($(H_3CCNC_2H_2N)_2ZnCO_3$, JCPDS 00-066-1415). The work of L. Huang et al. reports that, in the aqueous phase, ZIF-8 irreversibly generates a mixture of zinc carbonate crystals and 2-MeIM crystals with CO_2 leading to a complete loss of pore structure.[50] The authors attributed the decomposition of ZIF-8 to the acidic environment created by CO_2 dissolved in water. However, this study shows that ZIF-8 decomposition occurs even in basic bicarbonate buffer. In summary, ZIF-8 is unstable in phosphate and bicarbonate buffers and irreversibly generates the corresponding zinc salt, which is consistent with literature reports.[45] However, despite the phase changes, PdAu@ZIF-8 is completely inactivated only in phosphate buffer at pH 7.0. This suggests that the decomposition of the ZIF-8 structure and the loss of porous structure are not

the main reasons for its inactivation in phosphate buffer at pH 7.0. Therefore, the poisoning of PdAu NPs by phosphate should be the main cause of their inactivation.

Table 5.7. Leaching test of ZIF-8 in different buffers

Solvent	pH	$C_{(2\text{-MeIM})}$ (μg/mL)	Leaching rate (%)
Water	7.0	237	9.4
Phosphate buffer	7.0	758	30.4
Tris HCl	8.5	355	14.2
Carbonate buffer	9.2	696	27.8

Test conditions: ZIF-8 50 mg, solvent volume 20 mL, T=25 °C, t=24h

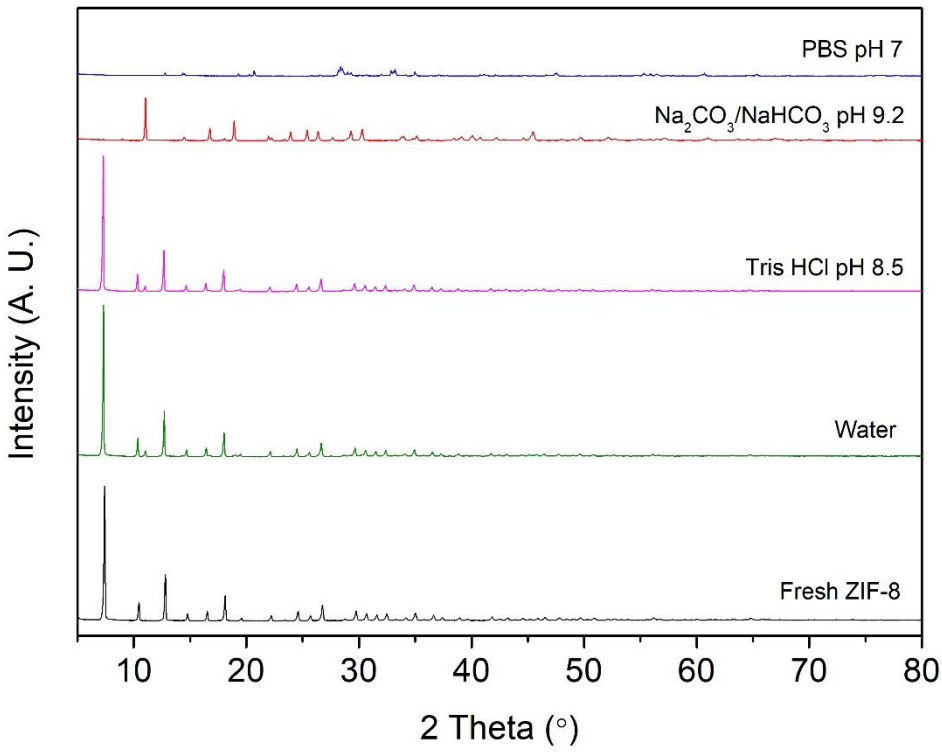

Figure 5.12. PXRD patterns of fresh ZIF-8 and ZIF-8 immersed in water and buffers for 24 hours

In conclusion, the stability of ZIF-8 is crucial considering that it will serve as a support for heterogeneous catalysts and ω-TAs. Therefore, neither phosphate nor carbonate are suitable as

buffers for chemoenzymatic cascade reactions. Instead, Tris HCl buffer at pH 8.5 is selected as a solvent for the chemoenzymatic cascade reaction because of its relatively acceptable ZIF-8 compatibility and its compatibility with the conversion of aerobic 1-PE oxidation reaction.

5.3.2.2 Attempt of "one-pot/one-step" cascade system

A one-pot/one-step cascade reaction combining PdAu@ZIF-8 and the 3HMU ω-TA was hence attempted in Tris HCl buffer (pH 8.5) to produce (S)-α-methylbenzylamine from 1-phenylethanol with L-alanine as amine donor and LDH/GDH system. Disappointingly, no conversion of 1-PE was observed after 24 hours. The results displayed in the previous section have highlighted the negative impact of the presence of the amine compounds 2-Amino-2-(hydroxymethyl)-1,3-propanediol) (2-AHP) and its corresponding ammonium salt on the performances of the PdAu NPs. However, as discussed in Section 5.3.6, the inhibitory effect of 100 mM Tris HCl buffer is only partial since a 38% conversion of 1-PE is still achieved in this buffer. This suggests that Tris-HCl buffer is not the only inhibition source and that other components also contribute to the inhibition of PdAu@ZIF-8, so that the cumulative effect of multiple inhibitors leads to the total inhibition of 1-PE oxidation. To investigate the inhibitory effect of other components on the oxidation of 1-PE catalyzed by PdAu@ZIF-8, we conducted a series of control experiments using PdAu@ZIF-8-catalyzed oxidation of 1-PE in water and in the presence of the most concentrated compounds involved in the transamination reaction which were tested separately (See Figure 5.13). LDH and GDH enzymes, as well as PLP and NADH co-catalysts, were ignored because they were assumed to be too large to diffuse within the micropores of ZIF-8 and reach the Pd_9Au_1 NPs mostly located within the bulk of the MOF crystals (see chapter 4). Oxidation of 1-PE in water is used in a positive control experiment. The concentrations of the various components in each experimental group are consistent with those allowing a significant acetophenone amination.

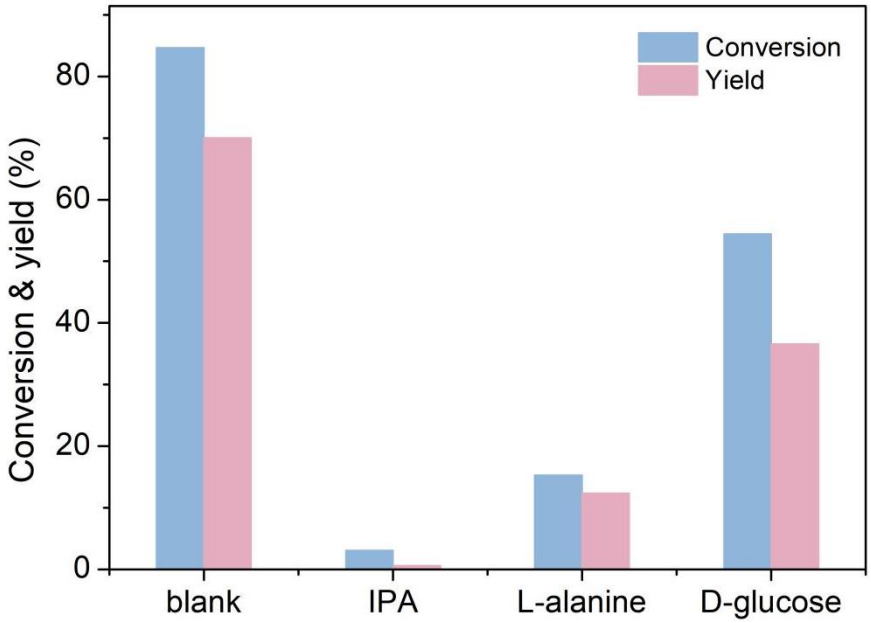

Figure 5.13. 1-PE aerobic oxidation over Pd_9Au_1@ZIF-8 in water with different components
Test conditions: water 2 mL, 1-PE 100 mM, 50 °C, O_2

In the presence of 250 mM L-alanine, the conversion rate of 1-PE and the yield of AP were found to be 15% and 12%, respectively. It is hypothesized that this inhibitory effect arises from the reversible adsorption of amino groups onto PdAu NPs.[46,47,49] The inhibitory role of amine on PdAu@ZIF-8 activity was further supported by achieving the same tests with IPA as another amine donor. In the presence of 1 M IPA, the conversion rate of 1-PE and the yield of AP are only 3% and 1%, respectively. It is noteworthy that, under the presence of 150 mM D-glucose, the conversion rate of 1-PE and the yield of AP are 54% and 37%, respectively, which are also lower than the data obtained in pure aqueous solution. The inhibitory mechanism of D-glucose on the activity of PdAu NPs remains unknown but it could be hypothesized that the 1-PE oxidation compete with the glucose one.[51] We speculate that this may also be related to the adsorption of D-glucose onto PdAu NPs.[52] In summary, within the context of the "one-pot" cascade chemical enzyme catalysis carried out in a one-step fashion, several components of the enzyme-catalyzed reactions induce a cumulative inhibitory effect on the activity of PdAu@ZIF-8, thus limiting the alcohol oxidation extent.

However, "One-pot/one-step" cascade catalysis is not the only method to perform multiple steps in a "one pot" fashion. The sequential mode of "one-pot/two-step" step also offers significant

advantages, such as avoiding the separation of reaction intermediates.[53,54] Therefore, we subsequently explored the feasibility of a stepwise cascade catalyzed amination reaction of 1-PE by the "one-pot/two-step" method.

5.3.2.3. "One-pot/ two-step" cascade system oxidation and amination of alcohols

In this system, the first step consists in the aerobic oxidation of 1-PE in water, catalyzed by PdAu@ZIF-8, with 75% yield within 24 hours (See Scheme 5.5). Tris HCl buffer then was added and the pH was adjusted to 8.5. Subsequently, 3HMU, L-alanine, PLP and the LDH/GDH system components were added. This second step yields up to 65% conversion of acetophenone to S-MBA after 20 h. The combined yield of the two-step reaction reaches 49% in terms of S-MBA. Therefore, the "one-pot/two-step" chemoenzymatic cascade catalyzed by PdAu@ZIF-8 and 3HMU is feasible.

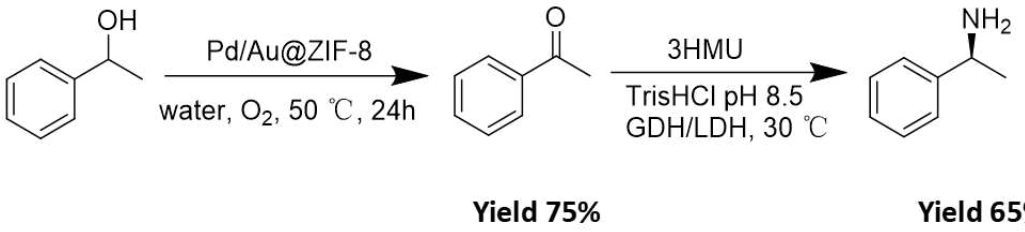

Scheme 5.6. One-pot/two-step system combining oxidation and transamination reactions of 1-PE in a one-pot fashion, catalyzed by Pd_9Au_1@ZIF-8 and 3HMU

5.4. Conclusion

In this chapter, we systematically investigated the feasibility of a "one-pot" chemoenzymatic cascade coupling 1-phenylethanol oxidation followed by acetophenone amination reactions. Firstly, we investigated the optimal working pH for two ω-transaminases, 3HMU and *Cv*-ω-TA which was found to be 8.5-9.5 and pH 8.0, respectively. Subsequently, two model substrates, benzaldehyde and acetophenone, were tested for the transamination model reaction with ω-transaminases 3HMU and *Cv*-ω-TA. It was experimentally ascertained through ^{1}H-NMR and

ESI-HRMS analyses that benzaldehyde, the benzyl alcohol oxidation product, spontaneously underwent a side reaction with isopropylamine, a foreseen amine donor of the transamination reaction. Indeed, benzylamine forms a Schiff base with benzylamine in aqueous solution at room temperature. Moreover, due to the low solubility of the formed Schiff base, its formation led to precipitation, driving the equilibrium of the chemical reaction toward the direction favoring Schiff base formation. Consequently, benzaldehyde was unsuitable and discarded as a substrate for the transamination reaction due to this side reaction. On the other hand, 1-phenylethanol, a secondary alcohol, was also considered as a model oxidation substrate. Acetophenone, its corresponding oxidation product is not prone to react with amine to form a Schiff base and is thus a more suitable. It is moreover prochiral and is therefore a suitable substrate to evidence the advantage of using ω-transaminases as enantioselective amination catalyst.

Subsequently, we explored different strategies to overcome the unfavorable thermodynamic equilibrium of the transamination reaction. The first strategy involved an excess of isopropylamine and 1,2-propanediamine as the amine donors. Under a 20:1 isopropylamine to acetophenone ratio, the transamination of acetophenone catalyzed by 3HMU reaches 29% yield of S-α-methylbenzylamine. The second strategy involved using L-alanine as the amine donor and coupled with a LDH/GDH multi-enzyme system to drive the conversion of pyruvate, a co-product, and shift the thermodynamic equilibrium. In such conditions and with a 5:1 L-alanine to acetophenone molar ratio, the amination of acetophenone catalyzed by 3HMU achieves a maximum yield of 77% of S-α-methylbenzylamine.

In the second part of this chapter, we investigated the PdAu@ZIF-8-catalyzed oxidation of 1-phenylethanol at different pHs using different buffers in view of establishing the optimal reaction conditions for the cascade chemoenzymatic catalysis systems. The catalyst exhibits the best activity in water/pH 7 and $NaHCO_3/Na_2CO_3$ buffer/pH 12 solutions. In contrast, the catalytic activity is lower in Tris HCl/pH 8.5 and NaH_2PO_4/Na_2HPO_4/pH 9.2 buffers. Furthermore, the structure of ZIF-8 is damaged in NaH_2PO_4/Na_2HPO_4 and $NaHCO_3/Na_2CO_3$ buffers, which is a clear limitation in view of the use of this MOF as support of both PdAu NPs

and ω-transaminases.

The oxidation step in the presence of Tris/HCl highlighted the detrimental effect of this buffer. It is hypothesized that the main cause is a partial poisoning of metal nanoparticles through the amine groups of the main component of the buffer, ca 2-amino-2-hydroxyméthylpropane-1,3-diol. However, as the oxidation inhibition is only partial, an acetophenone yield of approximately 30% is indeed still obtained in this solvent. Considering the high activity of the enzyme 3HMU in this buffer with alanine as amine donor (Table 5.6), we decided to use Tris HCl buffer to assess the combination of the oxidation and amination steps starting from 1-phenylethanol in a one-pot experiment in the presence of PdAu@ZIF-8 and 3HMU together with the auxiliary multienzymes system LDH/GDH using L-alanine as an amine donor. Unfortunately, no oxidation of 1-phenylethanol was observed. As it has been checked that isopropylamine, L-alanine and glucose tested separately all partially inhibit the oxidation reaction, it can be assumed that the presence of all these components, including 2-amino-2-hydroxyméthylpropane-1,3-diol are responsible for this total oxidation inhibition.

These results indeed preclude any “one-pot/one-step” setup of the oxidation/amination reaction. Alternatively, a "one-pot/two-steps-" approach was investigated, the oxidation step being performed first in water and in the presence of the alcohol and the oxidation step catalyst, PdAu@ZIF-8. The idea in thesis approach is to avoid any contact between the PdAu NPs of PdAu@ZIF-8 and any amines during the first step of alcohol oxidation. Indeed after 24 hours, PdAu@ZIF-8 was removed, the transamination catalytic system was added and pH adjusted to 8.5. In such conditions, oxidation yield of 1-phenylethanol and the transamination of acetophenone reaches 75% and 65% in the first and the second step, respectively, leading to an overall yield of 49% toward S-α-methylbenzylamine. The feasibility of the one-step and stepwise reactions catalyzed by PdAu@ZIF-8 and 3HMU in the "one-pot" approach was thus successfully ascertained.

References

(1) Liu, Y.; Liu, P.; Gao, S.; Wang, Z.; Luan, P.; González-Sabín, J.; Jiang, Y. Construction of Chemoenzymatic Cascade Reactions for Bridging Chemocatalysis and Biocatalysis: Principles, Strategies and Prospective. *Chem. Eng. J.* **2021**, *420*, 127659. https://doi.org/10.1016/j.cej.2020.127659.

(2) Li, Q.; Ma, C.-L.; He, Y.-C. Effective One-Pot Chemoenzymatic Cascade Catalysis of Biobased Feedstock for Synthesizing 2,5-Diformylfuran in a Sustainable Reaction System. *Bioresour. Technol.* **2023**, *378*, 128965. https://doi.org/10.1016/j.biortech.2023.128965.

(3) Tan, Z.; Zhang, X.; Xu, M.; Fu, Y.; Zhuang, W.; Li, M.; Wu, X.; Ying, H.; Ouyang, P.; Zhu, C. Cooperative Chemoenzymatic Synthesis of N-Heterocycles via Synergizing Bio- with Organocatalysis. *Sci. Adv.* **2022**, *8* (36), eadd1912. https://doi.org/10.1126/sciadv.add1912.

(4) Debecker, D. P.; Smeets, V.; Van der Verren, M.; Meersseman Arango, H.; Kinnaer, M.; Devred, F. Hybrid Chemoenzymatic Heterogeneous Catalysts. *Curr. Opin. Green Sustain. Chem.* **2021**, *28*, 100437. https://doi.org/10.1016/j.cogsc.2020.100437.

(5) Zhou, Y.; Wu, S.; Bornscheuer, U. T. Recent Advances in (Chemo)Enzymatic Cascades for Upgrading Bio-Based Resources. *Chem. Commun.* **2021**, *57* (82), 10661–10674. https://doi.org/10.1039/D1CC04243B.

(6) Calvelage, S.; Dörr, M.; Höhne, M.; Bornscheuer, U. T. A Systematic Analysis of the Substrate Scope of (S)- and (R)-Selective Amine Transaminases. *Adv. Synth. Catal.* **2017**, *359* (23), 4235–4243. https://doi.org/10.1002/adsc.201701079.

(7) Pavlidis, I. V.; Weiß, M. S.; Genz, M.; Spurr, P.; Hanlon, S. P.; Wirz, B.; Iding, H.; Bornscheuer, U. T. Identification of (S)-Selective Transaminases for the Asymmetric Synthesis of Bulky Chiral Amines. *Nat. Chem.* **2016**, *8* (11), 1076–1082. https://doi.org/10.1038/nchem.2578.

(8) Weiß, M. S.; Pavlidis, I. V.; Spurr, P.; Hanlon, S. P.; Wirz, B.; Iding, H.; Bornscheuer, U. T. Amine Transaminase Engineering for Spatially Bulky Substrate Acceptance. *ChemBioChem* **2017**, *18* (11), 1022–1026. https://doi.org/10.1002/cbic.201700033.

(9) Schätzle, S.; Höhne, M.; Redestad, E.; Robins, K.; Bornscheuer, U. T. Rapid and Sensitive Kinetic Assay for Characterization of ω-Transaminases. *Anal. Chem.* **2009**, *81* (19), 8244–8248. https://doi.org/10.1021/ac901640q.

(10) Steffen-Munsberg, F.; Vickers, C.; Thontowi, A.; Schätzle, S.; Tumlirsch, T.; Svedendahl Humble, M.; Land, H.; Berglund, P.; Bornscheuer, U. T.; Höhne, M. Connecting Unexplored Protein Crystal Structures to Enzymatic Function. *ChemCatChem* **2013**, *5* (1), 150–153. https://doi.org/10.1002/cctc.201200544.

(11) Toro, R.; Bonanno, J. B.; Ramagopal, U.; Freeman, J.; Bain, K. T.; Miller, S.; Sauder, J. M.; Burley, S. K.; Almo, S. C. Crystal Structure of a Class III Aminotransferase from Silicibacter Pomeroyi, 2009. https://doi.org/10.2210/pdb3hmu/pdb.

(12) Humble, M. S.; Cassimjee, K. E.; Håkansson, M.; Kimbung, Y. R.; Walse, B.; Abedi, V.; Federsel, H.-J.; Berglund, P.; Logan, D. T. Crystal Structures of the Chromobacterium Violaceumω-Transaminase Reveal Major Structural Rearrangements upon Binding of

Coenzyme PLP. *FEBS J.* **2012**, *279* (5), 779–792. https://doi.org/10.1111/j.1742-4658.2012.08468.x.

(13) Merz, L. M.; van Langen, L. M.; Berglund, P. The Role of Buffer, Pyridoxal 5'-Phosphate and Light on the Stability of the Silicibacter Pomeroyi Transaminase. *ChemCatChem* **2023**, *15* (2), e202201174. https://doi.org/10.1002/cctc.202201174.

(14) Gairola, P. Association of Metal-Organic Framework and Transaminase for Chemoenzymatic Production of Amines. These de doctorat, Sorbonne université, 2019. https://www.theses.fr/2019SORUS107 (accessed 2023-09-03).

(15) Kaulmann, U.; Smithies, K.; Smith, M. E. B.; Hailes, H. C.; Ward, J. M. Substrate Spectrum of ω-Transaminase from Chromobacterium Violaceum DSM30191 and Its Potential for Biocatalysis. *Enzyme Microb. Technol.* **2007**, *41* (5), 628–637. https://doi.org/10.1016/j.enzmictec.2007.05.011.

(16) Land, H.; Ruggieri, F.; Szekrenyi, A.; Fessner, W.-D.; Berglund, P. Engineering the Active Site of an (S)-Selective Amine Transaminase for Acceptance of Doubly Bulky Primary Amines. *Adv. Synth. Catal.* **2020**, *362* (4), 812–821. https://doi.org/10.1002/adsc.201901252.

(17) Chen, S.; Land, H.; Berglund, P.; Humble, M. S. Stabilization of an Amine Transaminase for Biocatalysis. *J. Mol. Catal. B Enzym.* **2016**, *124*, 20–28. https://doi.org/10.1016/j.molcatb.2015.11.022.

(18) Sayer, C.; Isupov, M. N.; Westlake, A.; Littlechild, J. A. Structural Studies of Pseudomonas and Chromobacterium ω-Aminotransferases Provide Insights into Their Differing Substrate Specificity. *Acta Crystallogr. D Biol. Crystallogr.* **2013**, *69* (4), 564–576. https://doi.org/10.1107/S0907444912051670.

(19) Cassimjee, K. E.; Humble, M. S.; Miceli, V.; Colomina, C. G.; Berglund, P. Active Site Quantification of an ω-Transaminase by Performing a Half Transamination Reaction. *ACS Catal.* **2011**, *1* (9), 1051–1055. https://doi.org/10.1021/cs200315h.

(20) Chen, S.; Berglund, P.; Humble, M. S. The Effect of Phosphate Group Binding Cup Coordination on the Stability of the Amine Transaminase from Chromobacterium Violaceum. *Mol. Catal.* **2018**, *446*, 115–123. https://doi.org/10.1016/j.mcat.2017.12.033.

(21) Ruggieri, F.; Campillo-Brocal, J. C.; Chen, S.; Humble, M. S.; Walse, B.; Logan, D. T.; Berglund, P. Insight into the Dimer Dissociation Process of the Chromobacterium Violaceum (S)-Selective Amine Transaminase. *Sci. Rep.* **2019**, *9* (1), 16946. https://doi.org/10.1038/s41598-019-53177-3.

(22) Koszelewski, D.; Lavandera, I.; Clay, D.; Rozzell, D.; Kroutil, W. Asymmetric Synthesis of Optically Pure Pharmacologically Relevant Amines Employing ω-Transaminases. *Adv. Synth. Catal.* **2008**, *350* (17), 2761–2766. https://doi.org/10.1002/adsc.200800496.

(23) Schätzle, S.; Steffen-Munsberg, F.; Thontowi, A.; Höhne, M.; Robins, K.; Bornscheuer, U. T. Enzymatic Asymmetric Synthesis of Enantiomerically Pure Aliphatic, Aromatic and Arylaliphatic Amines with (R)-Selective Amine Transaminases. *Adv. Synth. Catal.* **2011**, *353* (13), 2439–2445. https://doi.org/10.1002/adsc.201100435.

(24) Xiang, C.; Ao, Y.-F.; Höhne, M.; Bornscheuer, U. T. Shifting the PH Optima of (R)-Selective Transaminases by Protein Engineering. *Int. J. Mol. Sci.* **2022**, *23* (23), 15347.

https://doi.org/10.3390/ijms232315347.

(25) Banerjee, R.; Furukawa, H.; Britt, D.; Knobler, C.; O'Keeffe, M.; Yaghi, O. M. Control of Pore Size and Functionality in Isoreticular Zeolitic Imidazolate Frameworks and Their Carbon Dioxide Selective Capture Properties. *J. Am. Chem. Soc.* **2009**, *131* (11), 3875–3877. https://doi.org/10.1021/ja809459e.

(26) Park, K. S.; Ni, Z.; Côté, A. P.; Choi, J. Y.; Huang, R.; Uribe-Romo, F. J.; Chae, H. K.; O'Keeffe, M.; Yaghi, O. M. Exceptional Chemical and Thermal Stability of Zeolitic Imidazolate Frameworks. *Proc. Natl. Acad. Sci.* **2006**, *103* (27), 10186–10191. https://doi.org/10.1073/pnas.0602439103.

(27) Dawood, A. W. H.; Weiß, M. S.; Schulz, C.; Pavlidis, I. V.; Iding, H.; de Souza, R. O. M. A.; Bornscheuer, U. T. Isopropylamine as Amine Donor in Transaminase-Catalyzed Reactions: Better Acceptance through Reaction and Enzyme Engineering. *ChemCatChem* **2018**, *10* (18), 3943–3949. https://doi.org/10.1002/cctc.201800936.

(28) Carey, F. A.; Sundberg, R. J. *Advanced Organic Chemistry: Part A: Structure and Mechanisms*; Springer Science & Business Media, 2007.

(29) Saggiomo, V.; Lüning, U. On the Formation of Imines in Water—a Comparison. *Tetrahedron Lett.* **2009**, *50* (32), 4663–4665. https://doi.org/10.1016/j.tetlet.2009.05.117.

(30) Saggiomo, V.; Lüning, U. Remarkable Stability of Imino Macrocycles in Water. *Eur. J. Org. Chem.* **2008**, *2008* (25), 4329–4333. https://doi.org/10.1002/ejoc.200800462.

(31) Simion, A.; Simion, C.; Kanda, T.; Nagashima, S.; Mitoma, Y.; Yamada, T.; Mimura, K.; Tashiro, M. Synthesis of Imines, Diimines and Macrocyclic Diimines as Possible Ligands, in Aqueous Solution. *J. Chem. Soc. Perkin 1* **2001**, No. 17, 2071–2078. https://doi.org/10.1039/B102749M.

(32) Westheimer, F. H.; Taguchi, K. Catalysis by Molecular Sieves in the Preparation of Ketimines and Enamines. *J. Org. Chem.* **1971**, *36* (11), 1570–1572. https://doi.org/10.1021/jo00810a033.

(33) Bunnelle, W. H.; Singam, P. R.; Narayanan, B. A.; Bradshaw, C. W.; Liou, J. S. An Efficient, Scaleable Procedure for the Conversion of Esters to Isoxazoles. *Synthesis* **1997**, *1997* (04), 439–442. https://doi.org/10.1055/s-1997-1211.

(34) Oliphant, S. J.; Morris, R. H. Density Functional Theory Study on the Selective Reductive Amination of Aldehydes and Ketones over Their Reductions to Alcohols Using Sodium Triacetoxyborohydride. *ACS Omega* **2022**, *7* (34), 30554–30564. https://doi.org/10.1021/acsomega.2c04056.

(35) Payer, S. E.; Schrittwieser, J. H.; Kroutil, W. Vicinal Diamines as Smart Cosubstrates in the Transaminase-Catalyzed Asymmetric Amination of Ketones. *Eur. J. Org. Chem.* **2017**, *2017* (17), 2553–2559. https://doi.org/10.1002/ejoc.201700253.

(36) Dawood, A. W. H.; Weiß, M. S.; Schulz, C.; Pavlidis, I. V.; Iding, H.; de Souza, R. O. M. A.; Bornscheuer, U. T. Isopropylamine as Amine Donor in Transaminase-Catalyzed Reactions: Better Acceptance through Reaction and Enzyme Engineering. *ChemCatChem* **2018**, *10* (18), 3943–3949. https://doi.org/10.1002/cctc.201800936.

(37) Weiß, M. S.; Pavlidis, I. V.; Spurr, P.; Hanlon, S. P.; Wirz, B.; Iding, H.; Bornscheuer, U. T. Protein-Engineering of an Amine Transaminase for the Stereoselective Synthesis of a

Pharmaceutically Relevant Bicyclic Amine. *Org. Biomol. Chem.* **2016**, *14* (43), 10249–10254. https://doi.org/10.1039/C6OB02139E.

(38) Truppo, M. D.; Rozzell, J. D.; Moore, J. C.; Turner, N. J. Rapid Screening and Scale-up of Transaminase Catalysed Reactions. *Org. Biomol. Chem.* **2008**, *7* (2), 395–398. https://doi.org/10.1039/B817730A.

(39) Dimitratos, N.; Villa, A.; Wang, D.; Porta, F.; Su, D.; Prati, L. Pd and Pt Catalysts Modified by Alloying with Au in the Selective Oxidation of Alcohols. *J. Catal.* **2006**, *244* (1), 113–121. https://doi.org/10.1016/j.jcat.2006.08.019.

(40) Nishimura, S.; Yakita, Y.; Katayama, M.; Higashimine, K.; Ebitani, K. The Role of Negatively Charged Au States in Aerobic Oxidation of Alcohols over Hydrotalcite Supported AuPd Nanoclusters. *Catal. Sci. Technol.* **2013**, *3* (2), 351–359. https://doi.org/10.1039/C2CY20244A.

(41) Wang, A.; Wang, J.; Sheti, S.; Dahlin, S.; Han, J.; Woo, J.; Xie, K.; J. Pettersson, L.; Olsson, L. A Deactivation Mechanism Study of Phosphorus-Poisoned Diesel Oxidation Catalysts: Model and Supplier Catalysts. *Catal. Sci. Technol.* **2020**, *10* (16), 5602–5617. https://doi.org/10.1039/D0CY00589D.

(42) Rokosz, M. J.; Chen, A. E.; Lowe-Ma, C. K.; Kucherov, A. V.; Benson, D.; Paputa Peck, M. C.; McCabe, R. W. Characterization of Phosphorus-Poisoned Automotive Exhaust Catalysts. *Appl. Catal. B Environ.* **2001**, *33* (3), 205–215. https://doi.org/10.1016/S0926-3373(01)00165-5.

(43) Ilmasani, R. F.; Yao, D.; Ho, P. H.; Bernin, D.; Creaser, D.; Olsson, L. Deactivation of Phosphorus-Poisoned Pd/SSZ-13 for the Passive Adsorption of NOx. *J. Environ. Chem. Eng.* **2022**, *10* (3), 107608. https://doi.org/10.1016/j.jece.2022.107608.

(44) J. Velásquez-Hernández, M. de; Ricco, R.; Carraro, F.; Ted Limpoco, F.; Linares-Moreau, M.; Leitner, E.; Wiltsche, H.; Rattenberger, J.; Schröttner, H.; Frühwirt, P.; M. Stadler, E.; Gescheidt, G.; Amenitsch, H.; J. Doonan, C.; Falcaro, P. Degradation of ZIF-8 in Phosphate Buffered Saline Media. *CrystEngComm* **2019**, *21* (31), 4538–4544. https://doi.org/10.1039/C9CE00757A.

(45) Luzuriaga, M. A.; Benjamin, C. E.; Gaertner, M. W.; Lee, H.; Herbert, F. C.; Mallick, S.; Gassensmith, J. J. ZIF-8 Degrades in Cell Media, Serum, and Some—but Not All—Common Laboratory Buffers. *Supramol. Chem.* **2019**, *31* (8), 485–490. https://doi.org/10.1080/10610278.2019.1616089.

(46) Neukum, D.; Baumgarten, L.; Wüst, D.; Sarma, B. B.; Saraçi, E.; Kruse, A.; Grunwaldt, J.-D. Challenges of Green Production of 2,5-Furandicarboxylic Acid from Bio-Derived 5-Hydroxymethylfurfural: Overcoming Deactivation by Concomitant Amino Acids. *ChemSusChem* **2022**, *15* (13), e202200418. https://doi.org/10.1002/cssc.202200418.

(47) Altmann, L.; Kunz, S.; Bäumer, M. Influence of Organic Amino and Thiol Ligands on the Geometric and Electronic Surface Properties of Colloidally Prepared Platinum Nanoparticles. *J. Phys. Chem. C* **2014**, *118* (17), 8925–8932. https://doi.org/10.1021/jp4116707.

(48) Guan, Q.; Wang, B.; Chai, X.; Liu, J.; Gu, J.; Ning, P. Comparison of Pd-UiO-66 and Pd-UiO-66-NH_2 Catalysts Performance for Phenol Hydrogenation in Aqueous Medium. *Fuel*

2017, *205*, 130–141. https://doi.org/10.1016/j.fuel.2017.05.029.

(49) Cui, W.; Xiao, Q.; Sarina, S.; Ao, W.; Xie, M.; Zhu, H.; Bao, Z. Au–Pd Alloy Nanoparticle Catalyzed Selective Oxidation of Benzyl Alcohol and Tandem Synthesis of Imines at Ambient Conditions. *Catal. Today* **2014**, *235*, 152–159. https://doi.org/10.1016/j.cattod.2014.04.015.

(50) Liu, H.; Guo, P.; Regueira, T.; Wang, Z.; Du, J.; Chen, G. Irreversible Change of the Pore Structure of ZIF-8 in Carbon Dioxide Capture with Water Coexistence. *J. Phys. Chem. C* **2016**, *120* (24), 13287–13294. https://doi.org/10.1021/acs.jpcc.6b03772.

(51) Zhang, H.; Watanabe, T.; Okumura, M.; Haruta, M.; Toshima, N. Catalytically Highly Active Top Gold Atom on Palladium Nanocluster. *Nat. Mater.* **2012**, *11* (1), 49–52. https://doi.org/10.1038/nmat3143.

(52) Wu, C.-W.; Chiang, M.-H.; Lee, C.-L. Pd@Au Core-Shell Octahedral, Truncated Octahedral, and Cubic Nanocrystals as Nonenzymatic Glucose Sensors for Drinks. *Microchem. J.* **2023**, *190*, 108697. https://doi.org/10.1016/j.microc.2023.108697.

(53) Heuson, E.; Froidevaux, R.; Itabaiana, I.; Wojcieszak, R.; Capron, M.; Dumeignil, F. Optimisation of Catalysts Coupling in Multi-Catalytic Hybrid Materials: Perspectives for the next Revolution in Catalysis. *Green Chem.* **2021**, *23* (5), 1942–1954. https://doi.org/10.1039/D0GC04172F.

(54) Muschiol, J.; Peters, C.; Oberleitner, N.; Mihovilovic, M. D.; Bornscheuer, U. T.; Rudroff, F. Cascade Catalysis – Strategies and Challenges En Route to Preparative Synthetic Biology. *Chem. Commun.* **2015**, *51* (27), 5798–5811. https://doi.org/10.1039/C4CC08752F.

Chapter 6.

Immobilization of ω-TA onto PdAu@ZIF-8 and sequential oxidation-amination cascade reaction

6.1. Introduction

In Chapters 3 to 5, a comprehensive exploration was undertaken concerning two reactions, the oxidation of alcohols, the amination of aldehydes or ketones and their association in a chemoenzymatic cascade reaction. PdAu@ZIF-8 was developed as a catalyst for the aerobic oxidation of 1-phenylethanol (1-PE), and the ω-transaminases (ω-TAs) 3HMU was selected as biocatalyst for the amination of acetophenone, the product of 1-PE oxidation. The feasibility and optimization of the one-pot sequential reactions were investigated. This chapter now focuses on the immobilization of 3HMU onto PdAu@ZIF-8 and its application in the one-pot sequential oxidation-amination cascade reaction. In the literature, several articles focus on the immobilization of ω-TAs, because similar to many valuable enzymes, their utilization as soluble free enzymes in practical applications faces several challenges, including their poor stability, the difficulties in enzyme-product separation and issues related to continuous flow operation. The non-recyclability of free enzymes indeed inadvertently escalates the operational costs associated with the application of ω-TAs.[1–3] Therefore, there is a strong anticipation to address the aforementioned issues through enzyme immobilization processes. Despite the continuous development of widely applicable and user-friendly immobilization techniques, the loss of enzyme activity remains one of the most prevalent challenges during the immobilization process. Consequently, the immobilization of enzymes onto specific carriers typically necessitates iterative experimentation. Presently, numerous successful cases of ω-TAs immobilization have been reported.[4–9] However, there are relatively limited reports regarding the use of Metal-Organic Frameworks (MOFs) as supports for ω-TAs. Q. Jiao's group employed several MOFs including ZIF-8, HKUST-1, Zr-*fum* ($Zr_6O_4OH_4$(fumarate)$_6$), and UiO-66-NH_2 ([$Zr_6O_4(OH)_4$(OOC-(NH_2)C_6H_4-COO)$_6$]) for the immobilization of ω-TA from *Bacillus megaterium* (*Bm*-STA)).[10] The *Bm*-STA immobilized on UiO-66-NH_2 and Zr-*fum* exhibit good relative activity (95.8 % and 90.8 %). In the previous work of our group,[11] UiO-66 was tentatively used as ω-TA support but its pronounced surface Lewis acidity catalyzed the protein degradation reaction, making this MOF unsuitable for this application. The superactivity of

MOF-808, a Zr based MOF as UiO-66, toward the hydrolysis of the peptidic bond has also been reported by N. Parac-Vogt's group in 2018.[12]

In this thesis, UiO-66 was replaced by ZIF-8, a MOF that was shown to be compatible with the enzyme working conditions (aqueous basic environment) and harmless (See Chapter 1, Section 1.1.4.3). However, this MOF, whose synthesis conditions are compatible with the conditions of enzyme activity, was mainly used to encapsulate the enzymes in an "in-situ" manner, leading to their entrapment within the hybrid framework (See Chapter 1, Section 1.1.4.2 iii). This strategy of enzyme immobilization is however not compatible with the approach developed in this thesis since here the PdAu NPs expected to catalyze the alcohol oxidation must also be embedded inside ZIF-8. As the synthesis method of the nanoparticles include a thermal step at temperature higher than 300 °C, this process is thus not compatible with the enzyme activity preservation. Thus, in this thesis the ω-TA 3HMU was immobilized onto the external surface of the PdAu@ZIF-8 crystals, in order to form a final multi-functional chemoenzymatic catalyst where the two active sites are compartmentalized: the metal PdAu NPs within the micropores of the bulk ZIF-8 and the ω-TA on the surface of the crystals (See Scheme 1.8 in Chapter 1).

In this chapter, to immobilize 3HMU onto the PdAu@ZIF-8, different strategies are used. The first one is to directly use the exposed Zn^{2+} of the ZIF-8 crystal as an anchor to coordinately bind to the His_6-tag of 3HMU (See Chapter 1, Section 1.1.4.2 i). In addition, there are other clusters of histidine on the surface of 3HMU which could coordinate to Zn^{2+}, namely His 20-21 and 23 and His 173,183-184 (Scheme 6.1). The second strategy is to immobilize the enzyme through electrostatic interactions between ZIF-8 crystal and 3HMU. In order to improve the electrostatic interaction, different metal cations including Ni^{2+}, Cu^{2+}, Ca^{2+}, Fe^{2+} were used for surface charge modification of ZIF-8 crystals. The third strategy is to build possible covalent bonds. ZIF-8 crystals were functionalized with amine and aldehyde groups via ligand engineering. The amino or aldehyde groups on the ZIF-8 crystal surface may form covalent bonds with the carboxyl or amino groups of 3HMU. We loaded 3HMU on PdAu@ZIF-8 through the above different strategies and compared the activity of so-immobilized 3HMU.

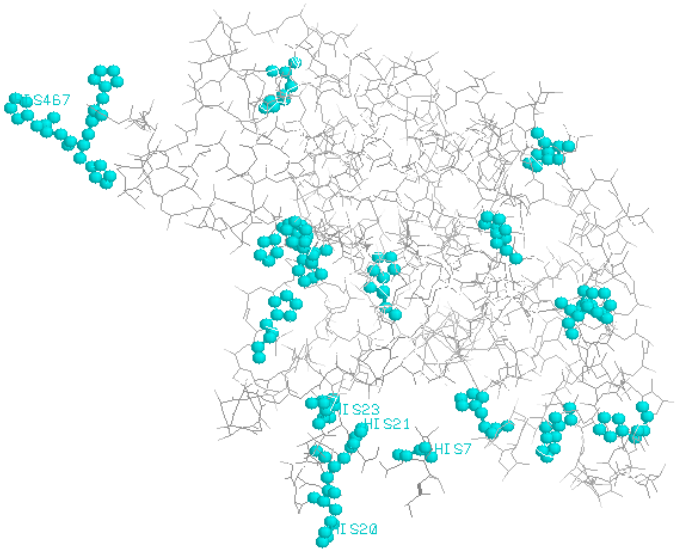

Scheme 6.1. 3HMU 3D structure. Histidine residues are shown as cyan balls. Only 3 histidines residues of the His_6-tag at the C-terminal part are visible from crystallographic data

6.2. Methods

6.2.1. Metal cation surface modification of PdAu@ZIF-8

The modification of PdAu@ZIF-8 (In this chapter, PdAu@ZIF-8 represents Pd_9Au_1@ZIF-8 unless further explained) with metal cations (Ni^{2+}, Fe^{3+}, Ca^{2+}, Cu^{2+}) was based on the method reported by X. Yang et al. with minor modification.[13] 0.0125 mmol of $Ni(NO_3)_2$ (or $CuCl_2$, $Ca(NO_3)_2$, $Fe(NO_3)_3$) was dissolved in 500 µL of ethanol. 2.5 mg of ZIF-8 or PdAu@ZIF-8 dispersed in 500 µL of ethanol was then added. The suspension was vigorously stirred from 30 minutes to 48 hours (depending on the experiments) at room temperature. The modified sample named PdAu@ZIF-8-M (M= Ni, Fe, Ca, and Cu) was collected by centrifugation and washed with 1 mL of water for 3 times.

6.2.2. Preparation of amine-functionalized PdAu@ZIF-8 by post-synthetic ligand-exchange method

Amine-functionalized PdAu@ZIF-8 were prepared following the post-synthetic ligand exchange method reported by Cho, K. Y., et. al with minor modification.[14] 100 mg of as-activated PdAu@ZIF-8 were dispersed in 50 mL of ethanol. The suspension was sonicated for 30 min at T = 25 °C. Then, 293 mg of 3-amino-1,2,4-triazole (3-ATZ) were dissolved in the suspension. The reaction suspension was stirred under 600 rpm at 50 °C. Reactions were kept for different times to obtain different ligand exchange rates. After the reaction, the materials were washed by 30 mL of ethanol for 3 times and dried under vacuum at 100 °C.

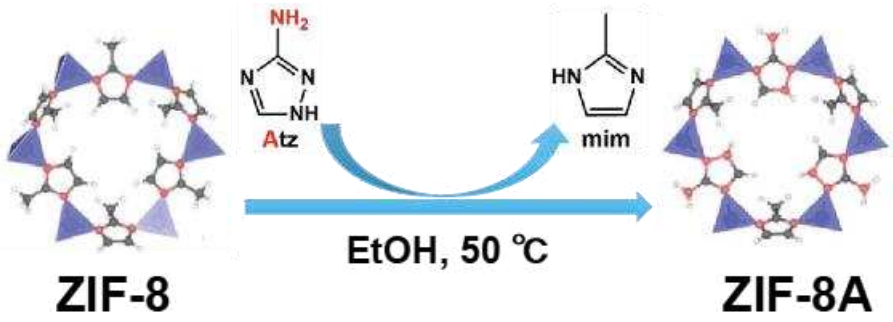

Scheme 6.2. Schematic representation of amine-functionalized PdAu@ZIF-8 synthesis by a post-synthetic ligand exchange method with 3-ATZ

Ligand exchange rates of amine-functionalized PdAu@ZIF-8 were assessed by ^{1}H-NMR. (As described in Chapter 2).

6.2.3. Preparation of ZIF-8-90

Carbonyl-doped ZIF-8 was prepared using an *ab initio* synthesis method. The exact method was referenced and slightly modified from the work of K. Eum et al.[15] 480 mg of Imidazole-2-carboxaldehyde, 410 mg of 2-methylimidazole, 680 mg of $NaHCO_2$ (sodium formate) were dissolved in methanol in a round flask of 100 mL. To this solution was added 25 mL of an aqueous solution of 740 mg of $Zn(NO_3)_2 \cdot 6H_2O$. A brownish precipitate quickly forms. The

reaction mixture was then placed under magnetic stirring in an oil bath at T = 50 °C during 1 h. A brown powder was recovered after filtration and drying at 70 °C for 24 h. The activation (freeing of the porosity) was achieved at 80 °C for 24 h under vacuum.

6.2.4. Adsorption of 3HMU on ZIF-8 and its derivatives

1.5 mg of 3HMU was dissolved in 250 µL of Tris HCl buffer (100 mM, pH 8.5) containing pyridoxal 5'-phosphate hydrate (PLP, 1 mM). Then, 3 mg of support (ZIF-8, ZIF-8-90, PdAu@ZIF-8, PdAu@ZIF-8-M, or PdAu@ZIF-8A) was added and vortexed in order to obtain a homogeneous suspension. The suspension was then rotated under 40 rpm in an incubator at 4 °C. The duration of this step (between 1 hour and 24 h) is as described in the text. After the immobilization, 3HMU@supporter was separated from the supernatant by centrifugation at 13000 rpm for 15 minutes. The supernatant was collected to monitor the protein concentration and enzyme activity. Besides, 3HMU@support was rinsed twice with 250 µL of Tris HCl buffer (100 mM at pH 8.5) containing PLP (1 mM), then re-dispersed a third time in 250 µL of Tris HCl buffer (100 mM at pH 8.5) containing PLP (1 mM) and used to test the activity of the immobilized enzyme.

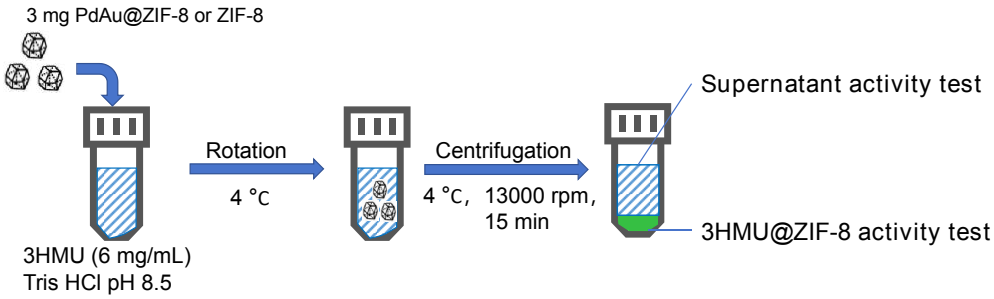

Scheme 6.2 Immobilization of 3HMU on PdAu@ZIF-8-based supports

6.2.5. Enzyme activity assay

The activity assay for free 3HMU follows the same procedure as described in Section 5.2.1. For the activity assay of the immobilized 3HMU, the totality of the tested solid (3 mg) was redispersed in 250 µL of Tris HCl buffer (100 mM at pH 8.5) containing PLP (1 mM). 10 µL of

this suspension were added to 2 mL of a solution whose composition is the same as one used to test the soluble ω-TA activity (2.5 mM sodium pyruvate, 2.5 mM benzylamine, 0.1 mM PLP, Tris-HCl buffer 50 mM pH 8.5, at 37 °C). The suspension was continuously stirred into the cuvette during the measurement course (1 to 5 minutes).

In order to conveniently monitor and compare the extent of enzyme immobilization, the activities of the immobilized enzymes as well as the one of the enzymes in the supernatant were expressed as relative activities as referred to the total activity of the solution at t=0 of the immobilization experiment (the relative activity of free enzyme before immobilization is thus 100%). The calculation of relative activity follows the formula:

$$\text{Relative activity (\%)} = \frac{\text{Slope of the immobilized 3HMU or supernatant}}{\text{Slope of the initial free 3HMU}} * 100$$

6.2.6. Protein concentration assay

Protein concentration assay was performed using a Pierce BCA Protein Assay Kit from Thermo Fisher. Bovine Serum Albumin (BSA) was chosen as a protein standard in a concentration range from 0-2 mg/mL. ω-TAs solutions to be tested were at most 1mg/mL. Three replications of each tested BSA or ω-TAs sample were performed.

6.3. Results and discussion

6.3.1. Adsorption of 3HMU on ZIF-8 and PdAu@ZIF-8

We first immobilized 3HMU directly onto ZIF-8 and PdAu@ZIF-8 without any further treatment using physical adsorption method. The activity of each tested 3HMU solution was measured before adding the solid and was used as a reference to calculate the relative activity of the supernatant and the one on the support at the end of the immobilization step. In order to exclude the effect of the possible enzyme inactivation under the immobilization conditions (but

without the solid), a control experiment without any support was performed in parallel. The control experiments showed that no loss of activity was observed when 3HMU was solubilized in Tris HCl buffer (100 mM) at pH 8.5, containing PLP 1 mM and rotating at 40 rpm for 24 hours at 4°C. The relative activities of the enzymes immobilized by the physical adsorption method and the enzyme activities and protein concentrations in the supernatant after 24 h of immobilization are shown in Table 6.1. It is noteworthy that ZIF-8 could not be properly dispersed in the aqueous enzyme immobilization solution due to the excessive hydrophobicity of its framework. Consequently, the 3HMU immobilized on ZIF-8 could not be separated by centrifugation, even though high-speed centrifugation at 13000 rpm was used in the process to separate the ZIF-8-immobilized enzymes from the supernatant. After the centrifugation, it could be observed that the 3HMU@ZIF-8 solid floated on the surface layer of the liquid. As a result, we were unable to accurately collect 3HMU@ZIF-8, making it difficult to accurately measure its activity.

In contrast to ZIF-8, PdAu@ZIF-8 could be properly dispersed in the enzyme solution and the resulting 3HMU@PdAu@ZIF-8 could be collected at the bottom of the centrifuge tube after high-speed centrifugation. This increase in hydrophilicity of PdAu@ZIF-8 compared to ZIF-8 most likely originates from ZIF-8 framework modification during the synthesis of PdAu@ZIF-8, such as the formation of structural defects that favor its interaction with water molecules. This aspect was not further investigated in the context of this thesis.

Table 6.1 Physical adsorption of 3HMU on ZIF-8 and PdAu@ZIF-8. Initial concentration of 3HMU: 6 mg/mL

Support	Activity on the solid (%)	Activity in supernatant (%)	Protein concentration in supernatant (mg/mL)
ZIF-8	-	15%	0.8
PdAu@ZIF-8	6 ± 2%	10 ± 3%	1.1

After immobilization, the relative activity of the immobilized enzymes could not be measured when ZIF-8 was used as a support, while the relative activity of the enzyme in the supernatant was around 15%. Therefore, the percentage of deactivated 3HMU could not be calculated. On 3HMU@PdAu@ZIF-8, only 6% of the initial activity is detected, while the relative activity of the enzyme in the supernatant is 10%. An "activity balance" thus shows that the enzyme is partly deactivated by the immobilization process since only around 16% of the initial activity is overall recovered. As far as material balance is concerned, 3HMU concentration of the supernatant is found to be 0.8 mg/mL and 1.1 mg/mL when ZIF-8 and PdAu@ZIF-8 are used as supports, respectively, whereas on the basis of the activity measurement in the supernatant and assuming that the specific activity of the enzyme remains unchanged, 0.9 and 0.6 mg/mL are expected, since the initial concentration of 3HMU is 6 mg/mL. These results indicate that in case of PdAu@ZIF-8, about half of the enzyme remaining in the supernatant is deactivated while in the presence of ZIF-8, both activity and concentration measurements are consistent with a preservation of the specific activity of 3HMU. In case of ZIF-8 however, since no activity is detected on the support, it can be assumed that about 85 % of 3HMU is immobilized but fully deactivated.

The reasons for the deactivation of immobilized 3HMU may result either from the immobilization conditions or the support itself, or unfavorable interactions between the support and the protein as a consequence of the hydrophobicity of ZIF-8.[16,17]

A solution to stabilize the enzyme is to pre-coat it with a polymer or a surfactant, etc.[18,19] Therefore, we also attempted to pre-coat 3HMU using the polymer polyvinylpyrrolidone (PVP) before immobilizing the enzyme by physical adsorption. First, the influence of the presence of these additives (2% w/v each) on free 3HMU (6 mg/mL, 1 mM PLP) in Tris HCl (100 mM at pH 8.5) solution was checked.). The mixture was then incubated at 4 °C for 24 h. Almost no loss of activity is observed for 3HMU in PVP solution, with 87% relative activity recovered. Subsequently, an attempt to immobilize 3HMU in the presence of 2% w:v of PVP was performed

The activity recovered on the solid was only 8% of the initial one, thus there is no significant improvement in the immobilization efficiency of 3HMU in the presence of PVP.

The modest immobilization yield of active 3HMU observed with PdAu@ZIF-8 and worse, the absence of any active 3HMU on ZIF-8 could result from the hydrophobicity of this MOF,[20,21] although hydrophobic interactions are reported to drive the immobilization of some enzymes by physical adsorption.[8] Indeed, the adsorption of the enzyme may have a deleterious effect on the structure of the enzyme, leading to its unfolding to form favorable hydrophobic interaction between the support and hydrophobic residues of the protein mostly buried inside the protein under its native form.[22–24] A strategy to circumvent this drawback could therefore be to modify ZIF-8 surface in order to enhance its hydrophilicity and thus inducing favorable interactions between the hydrophilic residues on the active protein surface and the solid, which would keep the protein folding, and consequently its activity unchanged.[25–27]

6.3.2. Immobilization of 3HMU on modified ZIF-8

6.3.2.1. Incorporation of metal cations on PdAu@ZIF-8

One way to optimize the hydrophilicity and charge of the ZIF-8 surface is to adsorb transition metal cations on it through interactions with pending semi-liganded 2-methylimidazoles present on the ZIF-8 surface, as recently shown by X. G. Yang et al. in 2023. According to the authors, the amine groups on these half-coordinated 2-methylimidazoles can be coordinated with guest metal cations, thus forming anchors for enzyme immobilization (See Scheme 6.3). Also, the introduction of metal cations is likely to reduce the hydrophobicity of ZIF-8 by changing its surface polarity and thus its hydrophobicity.[13]

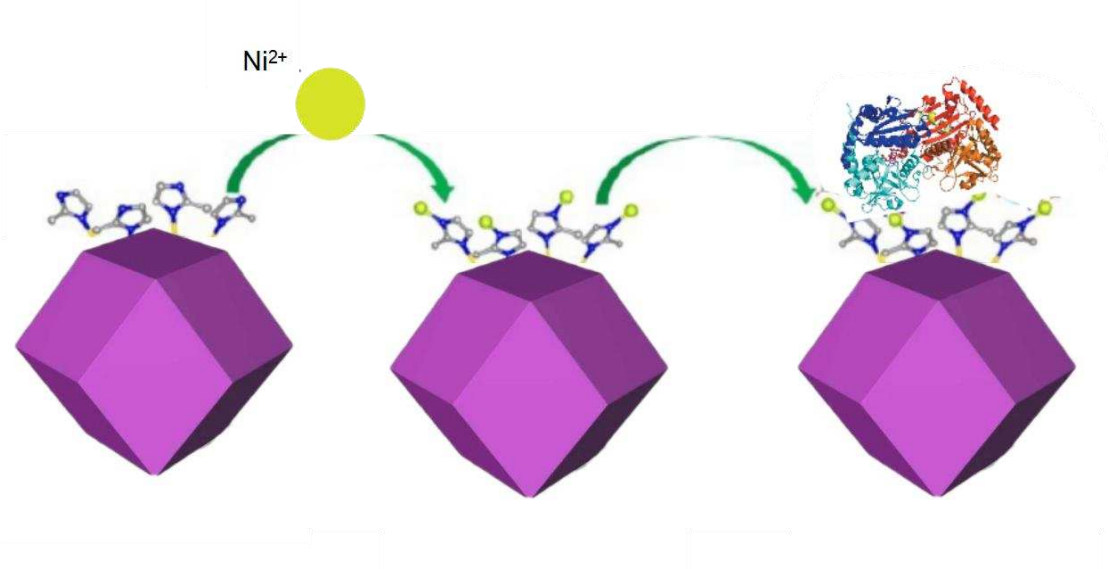

Scheme 6.3. Immobilization of 3HMU on Ni^{2+}-modified PdAu@ZIF-8. Adapted from[13]

Inspired by this work, we modified the surface of PdAu@ZIF-8 using different metal salts including $CuCl_2$, $Ca(NO_3)_2$, $Fe(NO_3)_3$ and $Ni(NO_3)_2$ with minor modifications.[13] PdAu@ZIF-8 was immersed in an ethanol solution of metal salts and stirred at 40°C for two hours. Since PdAu@ZIF-8 itself is a dark brown powder, the $CuCl_2$, $Ca(NO_3)_2$, and $Ni(NO_3)_2$ modifications had no effect on its appearance or color. However, only a yellow-brown colloidal solution was recovered from the samples treated in $Fe(NO_3)_3$ suggesting the partial degradation of PdAu@ZIF-8. ZIF-8 is likely unstable under the acidic conditions imposed by the $Fe(NO_3)_3$ solution and therefore decomposes.[28]

As the presence of additional metal cations on ZIF-8 surface are likely to modify the surface charges of the solid, zeta potential measurements were performed in Tris HCl buffer at pH 8.5 in order to check the efficiency of the modification procedure. Although 2-methylimidazole is uncharged at this pH (pKa of 7.86 at 25°C), zeta potential of ZIF-8 is positive 22.6 ± 0.8mV) at pH 8.5, due to the presence of partly uncoordinated zinc ions on its surface. In the presence of PdAu NPs, the zeta potential of PdAu@ZIF-8 slightly increases to 32.1 mV, maybe as a result of the presence of some unreduced Pd^{2+} ions (See Figure 6.2).

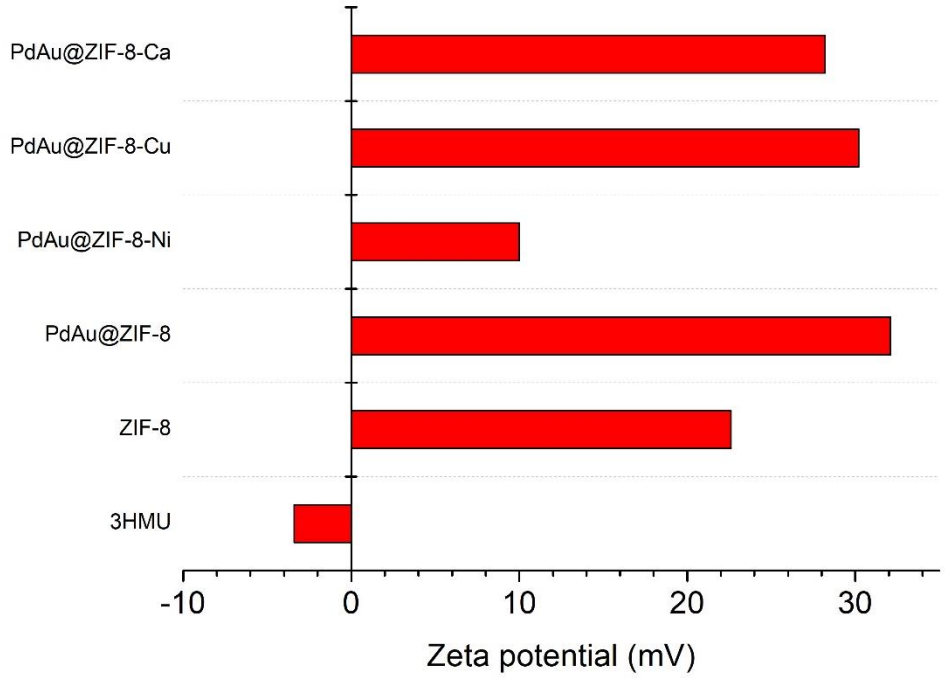

Figure 6.2. Zeta potential of 3HMU and supports in Tris HCl buffer 100 mM at pH 8.5

PdAu@ZIF-8 modified with Ca^{2+}, Cu^{2+}, and Ni^{2+} also all shows positive Zeta potential of 28.2 ± 0.9 mV, 30.2 ± 1.7 mV, and 10 ± 0.3 mV, respectively. However, the Zeta potential of ZIF-8 modified with Ni^{2+} decreases compared to ZIF-8. The evolution of the surface positive charge of PdAu@ZIF-8 after its modification with the additional metal cations is difficult to explain. Several factors, such as the charge (2+ or 3+) and polarizability of the cation as well as the nature of its counter ion (Cl^- or NO_3^-), may influence the affinity of the metal cations with the imidazolate linkers and the capacity of the cation to exchange with Zn^{2+} in the ZIF-8 framework or affect the double layer around the material. We could not explain, for instance why Ni^{2+} results in a significant charge decrease.

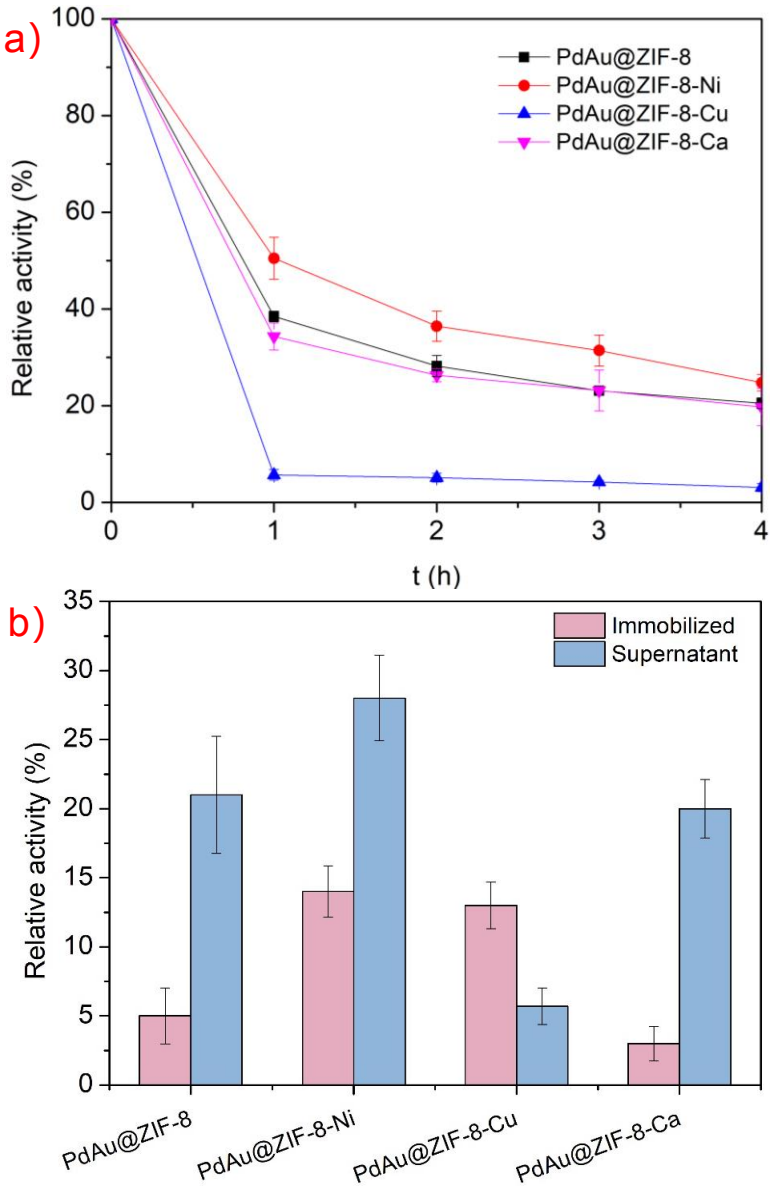

Figure 6.3. Relative enzymatic activities of 3HMUs a) in the supernatant as a function of time b) at the end of the immobilization experiment (4h), with PdAu@ZIF-8, PdAu@ZIF-8-Ni PdAu@ZIF-8-Cu, and PdAu@ZIF-8-Ca. Exchange experiment duration: 2 hours

However, all materials show positive Zeta potential, which is likely to induce favorable electrostatic interactions with 3HMU, and thus facilitate its adsorption. Indeed, 3HMU shows a negative surface charge, -3.4 ± 1.2 mV, at pH 8.5. The enzyme is thus negatively charged at pH 8.5, as expected from its isoelectric point (pI 5.57).

The immobilization of 3HMU on Ca^{2+}, Cu^{2+}, and Ni^{2+} modified PdAu@ZIF-8 was investigated because some positive results have been reported by X.G. Yang's group about pepsin

immobilization on these modified materials (although the lack of experimental evidence of any higher hydrophilicity compared to ZIF-8). The relative enzyme activities of the supernatants of PdAu@ZIF-8, PdAu@ZIF-8-Ni, PdAu@ZIF-8-Cu, and PdAu@ZIF-8-Ca decreases by 61%, 49%, 94%, and 66%, respectively, one hour after the beginning of the immobilization experiment and slows down dramatically over the next three hours, regardless of the support (Figure 6.3b). Hypothesizing that the enzyme activity measured is directly related to the amount of enzyme in solution, this decrease of enzyme activity in the supernatant suggests that most of the 3HMU of the solution are adsorbed on the surface of the MOF during the first hour. The slowdown in the rate of immobilization after the first hour may be attributed to the change in the surface charge of ZIF-8 by 3HMU. The adsorption of 3HMU could result in the decrease of the ZIF-8 surface charge that could become negatively charged, as suggested by the Zeta potential measurement of PdAu@ZIF-8-Ni after 3HMU immobilization (Figure 6.5). The electrostatic repulsion between the negatively charged 3HMU and the 3HMU@PdAu@ZIF-8 surface may hinder further adsorption. Especially, PdAu@ZIF-8-Cu allows the highest immobilization during the first hour whereas PdAu@ZIF-8-Ni is the less efficient. Such a result is consistent with the hypothesis that favorable electrostatic interaction could be the driven force of 3HMU adsorption since this material with the highest Zeta potential allow a better adsorption. However, if it can explain a tendency among the materials with the higher Zeta potential, such an interpretation fails in explaining why among materials with quite similar Zeta potentials (25-30 mV), PdAu@ZIF-8-Cu shows the better adsorption results. A deeper insight into the relative activities at the end of the adsorption process (after 4 hours) shows that (Figure 6.3 b) both PdAu@ZIF-8-Cu and PdAu@ZIF-8-Ni solids allow to recover the highest activity of immobilized 3HMU, showing the poor correlation between the activity remaining in the supernatant and the immobilization of active enzyme efficiency. However, the metal cation exchange on ZIF-8 strategy is successful since about 13 % of the initial 3HMU activity is recovered on both PdAu@ZIF-8-Cu and PdAu@ZIF-8-Ni, ca more than twice more than on PdAu@ZIF-8.

The fact that there is no obvious relation between the zeta potential of PdAu@ZIF-8,

PdAu@ZIF-8-Cu and PdAu@ZIF-8-Ni and the relative activity of immobilized 3HMU suggests that the reason of the immobilization improvement is not due to a simple modification of electrostatic interactions between the enzymes and the surface of the supports. The amount of metal cations adsorbed and accessible on the ZIF-8 surface as well as the creation of Lewis acid sites (through the creation of structural defects on the ZIF-8 surface) may also be important parameters that may have an effect on the interactions between the enzymes and the support. We did not investigate in this study because of lack of time. This will be the topic of forthcoming investigations.

In this thesis, PdAu@ZIF-8-Ni was regarded as the most promising support and further studied in the following.

6.3.2.2. Optimization of PdAu@ZIF-8-Ni

As an attempt to further enhance the immobilization efficiency, PdAu@ZIF-8-Ni was selected as the most promising material. An optimization of the nickel exchange was achieved by varying the duration of the exchange experiment from 30 minutes (conditions used for the results shown in Figure 6.3) to 48 hours. PXRD of the modified samples is shown in Figure 6.4.

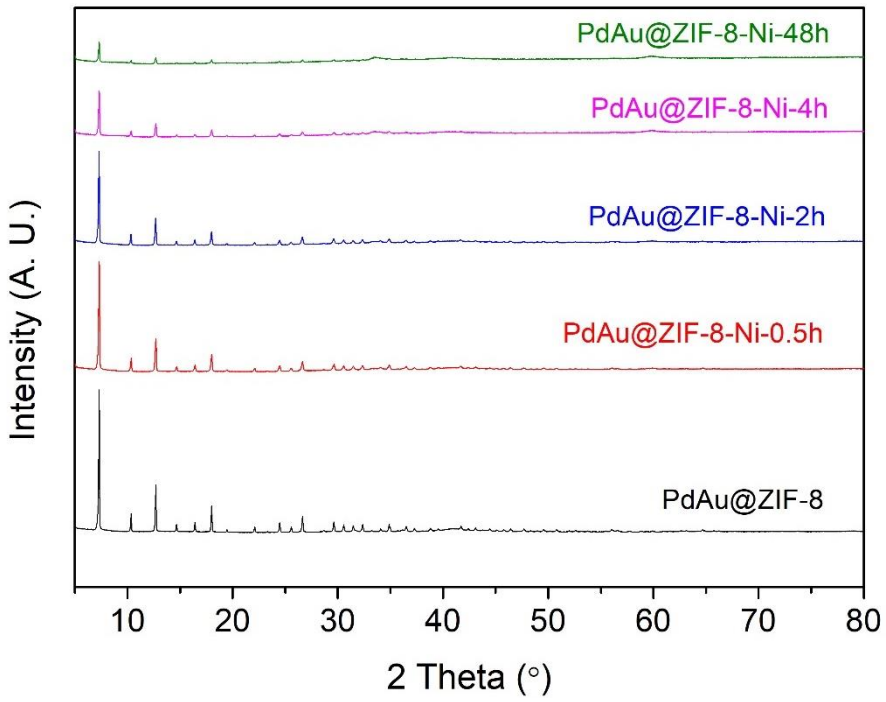

Figure 6.4 PXRD of the modified PdAu@ZIF-8-Ni during 0.5h, 2h, 4h and 48h.

It can be seen that the XRD patterns of modified PdAu@ZIF-8-Ni all show typical ZIF-8 characteristics. Ni^{2+} modification therefore does not modify the crystal structure of the MOF or generates any crystalline impurities. However, the intensity of the XRD peaks decreases gradually with the increase of the modification time, implying that this parameter affects the quality of ZIF-8 crystals. This may be attributed to the weak acidity of the $Ni(NO_3)_2$ solution, acidic conditions under which ZIF-8 is known to be unstable. It is noteworthy that the crystallinity of ZIF-8 is not significantly affected if the exchange lasts less than 2 hours. We also performed ICP-OES elemental analysis of samples with different Ni^{2+} modification times. (See Table 6.2) The Ni elemental content of the samples gradually increases with the increase of the modification time. As it is also observed that the amount of Zn in the solid decreases if the modification process takes more than 2 hours, it could be assumed that the nickel cation replaces Zn^{2+} in the ZIF-8 structure, then significantly modifying it, which is consistent with the PXRD measurements showing that the crystallinity losses become significant in the same experimental conditions.

Table 6.2. ICP-OES elemental analysis of Ni and Zn

Samples	Elemental analysis	
	Ni (wt.%)	Zn (wt.%)
PdAu@ZIF-8	0	29.7
PdAu@ZIF-8-Ni-0.5h	5.3	25.3
PdAu@ZIF-8-Ni-2h	9.4	28
PdAu@ZIF-8-Ni-4h	14.1	22.8
PdAu@ZIF-8-Ni-48h	18.9	21.2

The Zeta potentials of the samples with different Ni^{2+} modification times are shown in Figure 6.5. As already shown in Figure 6.2, the surface charge of PdAu@ZIF-8 decreases after Ni^{2+} modification, whatever is the duration of the modification process. The PdAu@ZIF-8-Ni with modification times of 0.5h, 2h, 4h, and 48h have zeta potentials of the same order, which are

13.9 ± 1.1mV, 10 ± 0.3mV, 8 ± 0.2mV, and 11.4 ± 1.1 mV.

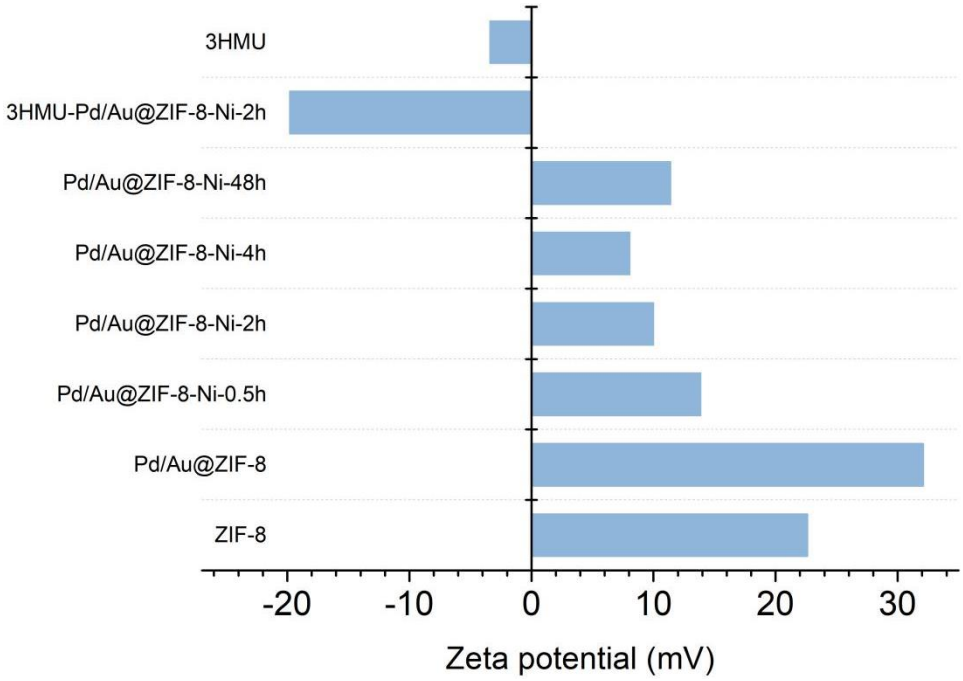

Figure 6.5. Zeta potential of 3HMU and supports in Tri HCl buffer 100 mM at pH 8.5

This decrease of surface charge of PdAu@ZIF-8 may be related to the loss of crystallinity experienced by the material during the modification process. Indeed, the exposition of the material to the solution of $Ni(NO_3)_2$ may lead to a partial exchange of Zn^{2+} cations with Ni^{2+} sites that resulting in the amorphization of the surface of ZIF-8 that eliminating (or screen) a part of the positive charges.

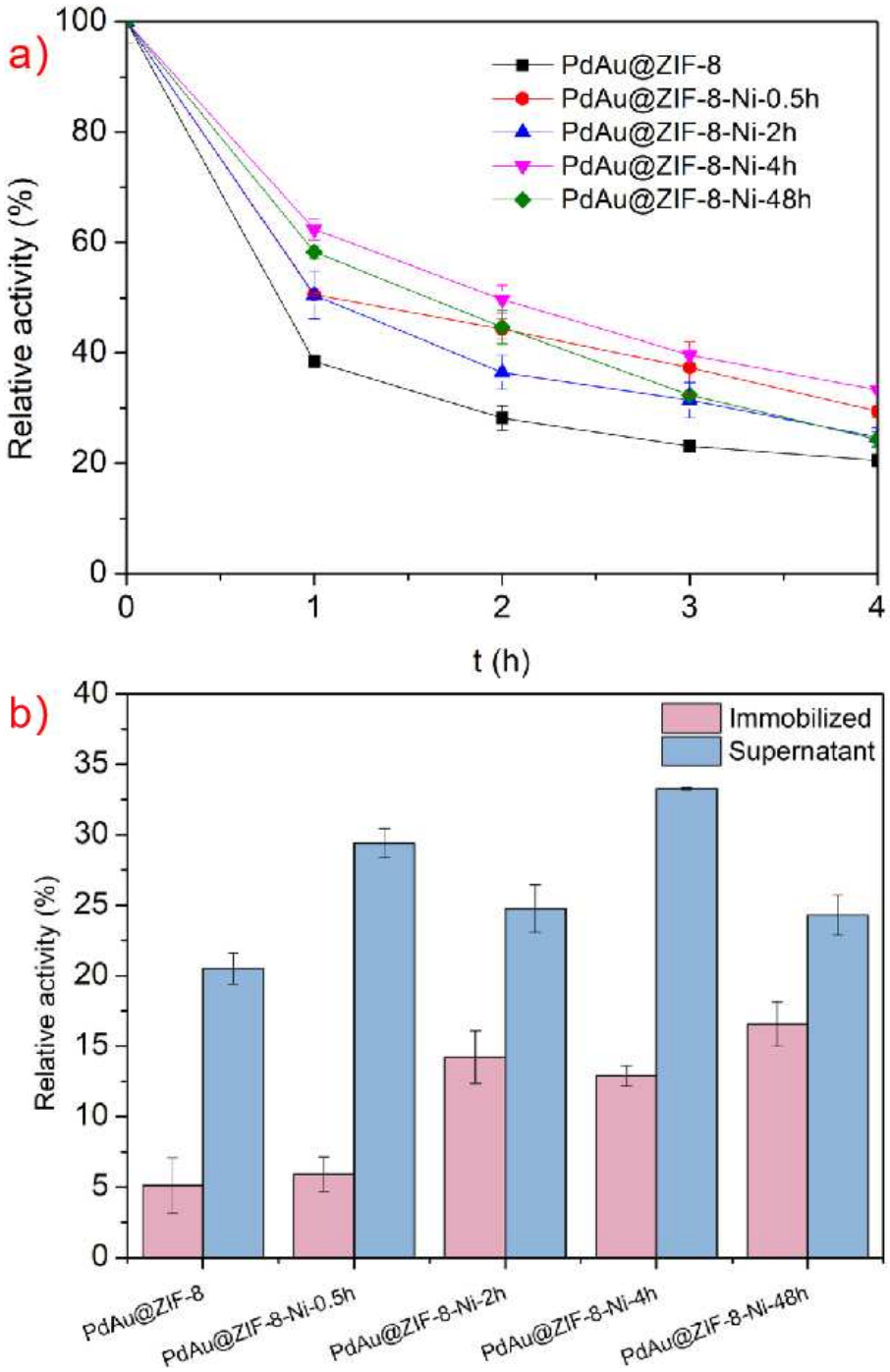

Figure 6.6. a) Relative enzymatic activity 3HMU on PdAu@ZIF-8, PdAu@ZIF-8-Ni-0.5 h, PdAu@ZIF-8-Ni-2h, PdAu@ZIF-8-Ni-4h, and PdAu@ZIF-8-N-48h in the supernatant and b) in the supernatant and on the solid after a 4 hours immobilization process.

We subsequently investigated the immobilization of 3HMU on PdAu@ZIF-8 with different Ni^{2+} modification times. The relative activities of immobilized 3HMU on PdAu@ZIF-8-Ni and remaining in the supernatant for different Ni^{2+} modification times are shown in Figure 6.6 b. For PdAu@ZIF-8 and PdAu@ZIF-8-Ni modified with Ni^{2+} for 0.5 to 48 hours, the recovered

immobilized enzyme activities are 5 ± 2%, 6 ± 1%, 14 ± 2%, 13 ± 1%, and 17 ± 2%, respectively. Specifically, the immobilized enzyme activity with a Ni^{2+} modification time of 0.5 hours is very close to that of the unmodified PdAu@ZIF-8. This suggests that too short modification time is insufficient to modify the ZIF-8 crystal surface with Ni^{2+}. On the other hand, after a 2 hours modification process, the obtained PdAu@ZIF-8-Ni significantly enhances the affinity for 3HMU. However, when immobilizing 3HMU on PdAu@ZIF-8-Ni modified during 2, 4, and 48 hours, similar activities were recovered on the support. Prolonged modification time not only has no further enhancement of the Ni^{2+} adsorption on the ZIF-8 surface but also leads to the decomposition of ZIF-8 crystals. Therefore, a 2-hour Ni^{2+} modification represents a compromise between ZIF-8 crystallinity preservation and active 3HMU immobilization extent. Compared to some literature results about ω-TAs immobilization on different supports (Table 6.3), the relative activity of immobilized 3HMU on PdAu@ZIF-8-Ni (ca 14%) of course remains modest. However, this is maybe enough to catalyze the amination of the targeted amount of acetophenone. Indeed, assuming that the specific activity of 3HMU is 0.5 U/mg (although measured in different experimental conditions), about 0.2 U can be immobilized of 5 mg of PdAu@ZIF-8-Ni, thus allowing to perform the amination of 0.2 mmol of acetophenone (standard conditions for the oxidation step) within 17 hours.

Table 6.3. Reported 3HMU immobilization and ω-TA immobilization on MOFs

Enzyme	support	Immobilization methods	Relative activity (%)	reference
3HMU	chitosan beads	glutaraldehyde	13.4	[29]
3HMU	chitosan beads	divinylsulfone	50	[29]
bm-STA	ZIF-8	physical adsorption	13.3	[10]
bm-STA	HKUST-1	physical adsorption	3.4	[10]
bm-STA	UiO-66-NH_2	physical adsorption	95.8	[10]
3HMU	PdAu@ZIF-8-Ni	physical adsorption	14	This work

6.3.3. Immobilization of 3HMU on functionalized ZIF-8 and PdAu@ZIF-8

The advantage of MOFs as enzyme supports is that the functional groups eventually existing on their organic ligands can be utilized as anchors for enzyme immobilization. In this section, we prepared carbonyl- and amine-functionalized PdAu@ZIF-8 by ab initio synthesis and post-synthesis ligand exchange, respectively, and tested their performances as supports for 3HMU immobilization.

6.3.3.1. Synthesis of carbonyl-functionalized ZIF-8-90

Similar to ZIF-8, ZIF-90 is a MOF built from the assembly of zinc-imidazolate complexes, but with imidazole-2-carboxaldehyde (ImC) instead of 2-methylimidazole (2-MeIM) as organic ligand. It possesses the same structure as ZIF-8.[30] The aldehyde function on its ligand was used by others as reactive sites to chemically modify the surface of its pores and as anchorage points on which biological molecules were efficiently immobilized.[31,32]

In this study, we prepared mixed ligand ZIF-8-90 crystals with surfaces covered with aldehyde functions expected to be able to interact with the amine functions intrinsically existing of the surface of the ω-TA to form imine covalent bonds.

ZIF-8-90 was synthesized under hydrothermal conditions from a mixture of zinc cations precursor, 2-MeIM and ImC, leading to a powder whose brownish color reminding that of the ImC ligand. The PXRD pattern of this material shows that it is well-crystallized and pure (Figure 6.7). As expected, this XRD profile is similar to that of ZIF-8. The ImC ligand content in the sample was however not assessed yet. But the brownish color of the material strongly suggests the existence of this ligand in the sample composition.

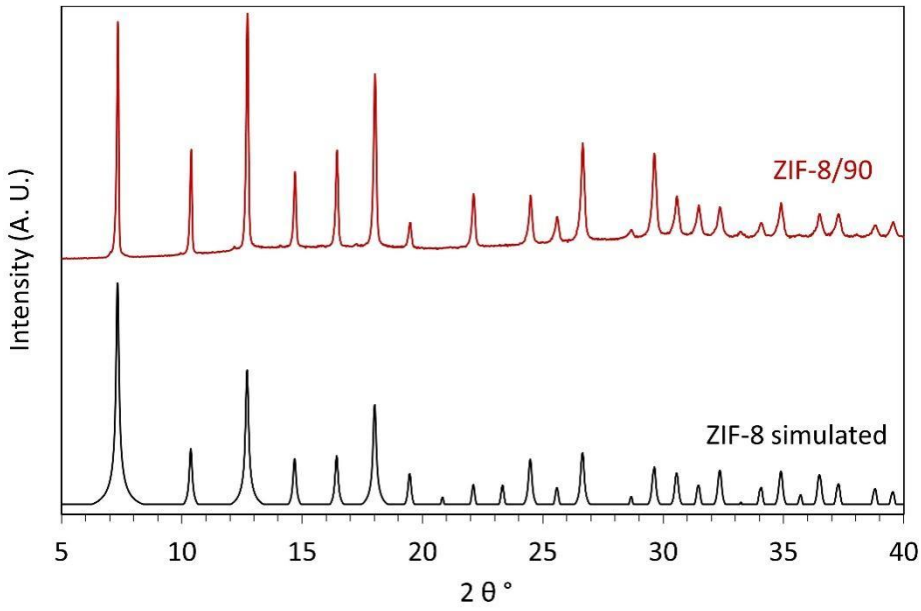

Figure 6.7. Experimental PXRD pattern of ZIF-8-90 and simulated pattern of ZIF-8.

In the following (Section 6.3.3.3.), this material is employed as model support to immobilized ω-TA. Because of lack of time, only these preliminary immobilization tests are presented in this manuscript. The synthesis of PdAu@ZIF-8-90 and the tests of its alcohol oxidation activity are currently undergoing.

6.3.3.2. Amine-functionalization of PdAu@ZIF-8 by 3-amino-1，2，4-triazole by post-synthesis ligand-exchange

A partial exchange of some of the 2-methylimidazole ligands of ZIF-8 with amino substituted 1,2,4-triazole are expected to modify the hydrophilicity of ZIF-8 crystals. Amino groups are also commonly used as anchor points for covalent enzyme immobilization. We employed a post-synthesis ligand exchange approach consisting in partially replacing the 2-MeIM) within the ZIF-8 framework with 3-amino-1,2,4-triazole (3-ATZ), to prepare a series of supports labelled PdAu@ZIF-8A. The effect of the exchange time was first studied. The efficiency of the process was assessed by monitoring the ligand exchange ratios using liquid state ^{1}H-NMR. To do so, PdAu@ZIF-8A samples prepared with different ligand exchange times and

PdAu@ZIF-8 were dissolved (digested) in D_2O containing 2%, w/v nitric acid prior to ^{1}H-NMR analysis. The ^{1}H-NMR spectra are presented in Figure 6.8.

The calculation of ligand exchange ratios is based on the comparison of integrated peak areas of characteristic protons a and c of 2-methylimidazole and 3-ATZ. After ligand exchange for 1 h, 5 h, and 24 h, the proportions of 3-ATZ are 6.5%, 7.4%, and 19% of the total ZIF-8 ligands, respectively. Whatever the ligand exchange duration, the proportion of 3-ATZ remains lower than that reported in the literature.[14] We attribute this discrepancy to the size of ZIF-8 crystals. In cases reported in the literature, ZIF-8 crystals display a nanoscale size (mean size 100 nm), whereas in this study, sub-micrometer-sized ZIF-8 with an average size of 500 nm was employed. It is assumed that the reduced external surface area and longer diffusion path due to the larger crystal size limit the diffusion of 3-ATZ through the crystal bulk and thereby the extent of the ligand exchange

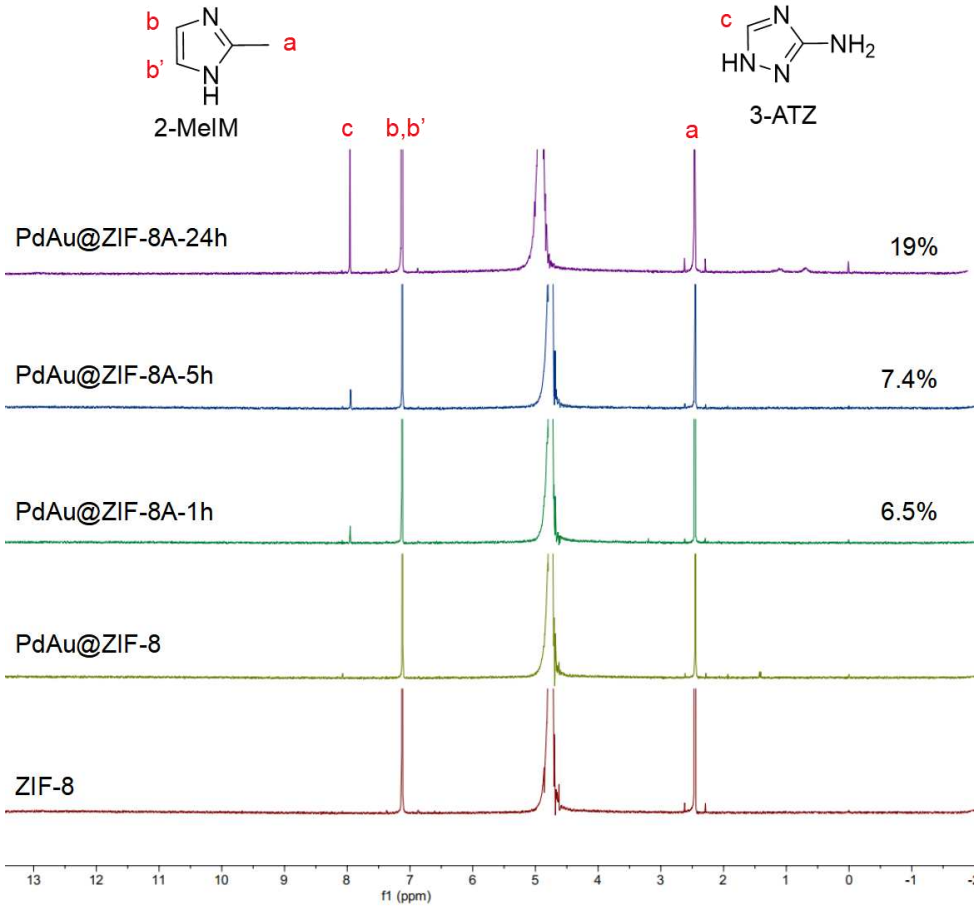

Figure 6.8. ^{1}H NMR spectra of ZIF-8, PdAu@ZIF-8, and PdAu@ZIF-8A prepared with different 2-MeIM to 3-ATZ exchange times.

The PXRD patterns of PdAu@ZIF-8A at different ligand exchange times are shown in Figure 6.9. It can be observed that with ligand exchange times ranging from 1 to 24 hours, PdAu@ZIF-8A keeps its characteristic ZIF-8 pattern, with no significant loss in crystallinity. The N_2 adsorption-desorption isotherms of PdAu@ZIF-8A with varying ligand exchange times are depicted in Figure 6.10. The ligand exchange not only does not diminish the specific surface area of PdAu@ZIF-8, but actually increases it. It is in agreement with literatures that ligand exchange can influence the specific surface area of MOFs.[33,34] In conclusion, the ligand exchange of PdAu@ZIF-8 with 3-ATZ does not exhibit a noticeable impact on the crystalline structure of ZIF-8.

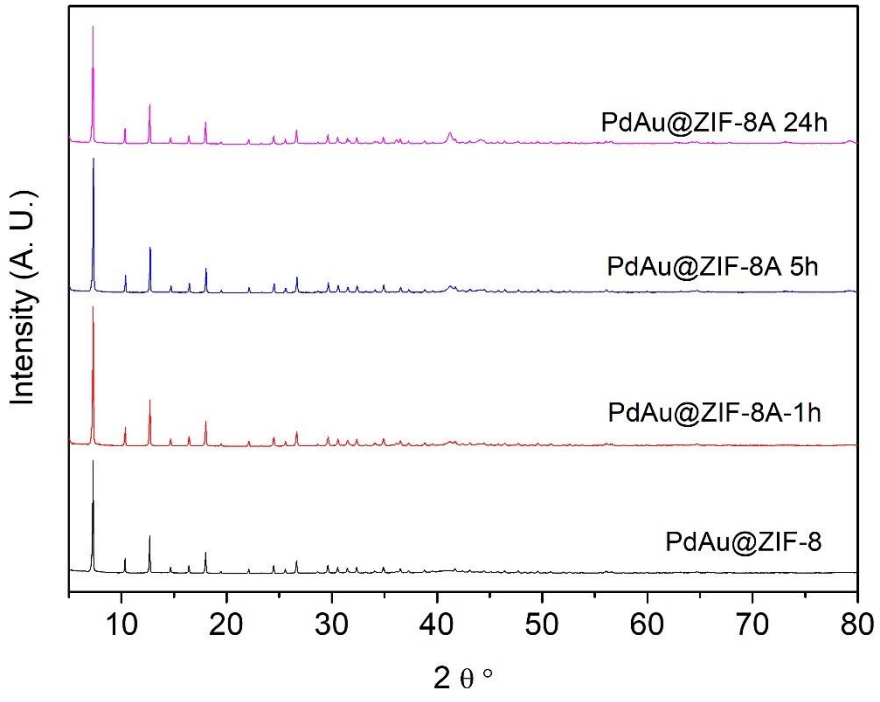

Figure 6.9. PXRD of PdAu@ZIF-8A with different time of 3-ATZ ligand-exchange

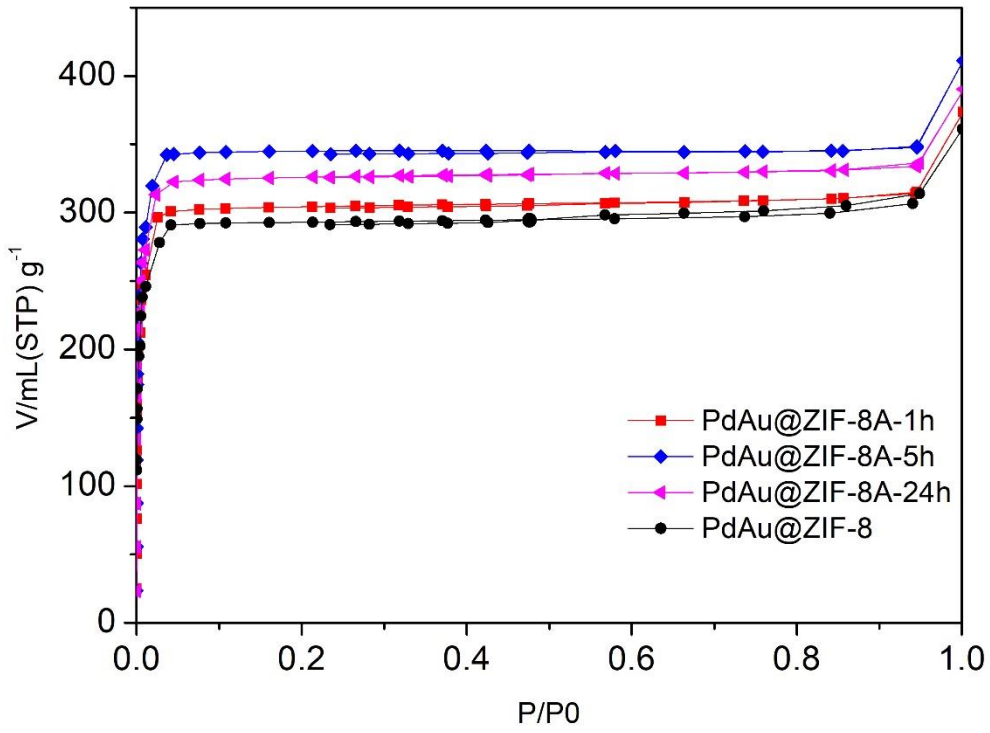

Figure 6.10. N_2-isothermals of PdAu@ZIF-8A with different time of 3-ATZ ligand-exchange

6.3.3.3. Immobilization of 3HMU on PdAu@ZIF-8A and ZIF-8-90

The synthesized PdAu@ZIF-8A and ZIF-8-90 were used for the immobilization of 3HMU according to a protocol similar to that described in Section 6.3.1. although some slight modifications of the initial enzyme concentration (Table 6.4). No 3HMU activity was detected on the solid after the enzyme immobilization process with PdAu@ZIF-8A. While 39 % of the initial activity was recovered in the supernatant, showing that compared to what is observed with ZIF-8, the deactivation of 3HMU is limited. However, as no activity is recovered on the solid, the result is overall deceiving.

On the other hand, a relative activity of 82 ± 6% is detected in the supernatant of ZIF-8-90, which is much more than what is observed with PdAu@ZIF-8-Ni-2h and could be interpreted as a lower immobilization efficiency. However, in case of PdAu@ZIF-8-Ni-2h)- the "activity balance" was not achieved, so that it is not relevant to deduce immobilization yield from activity

measurements. Encouragingly, 56 ± 3% of the initial 3HMU activity is recovered on the solid. Assuming that the activity measurements of both the supernatant and on the solid are representative of the amount of 3HMU, ca that 3HMU is not denaturated during the immobilization process, it could be expected from the activity of the supernatant that at most 18 % of the initial activity could be recovered on the solid. Whereas 56 % of the initial activity was measured on 3HMU@ZIF-8-90, it can be concluded than the 3HMU immobilized activity is 4-fold enhance compared to the solubilized enzyme. This suggests that carbonyl-functionalized ZIF-8 enhances the activity of the immobilized enzyme, although of the 3HMU immobilization yield remains limited.

Table 6.4. Immobilization of 3HMU on PdAu@ZIF-8A and ZIF-8-90.

Support	Activity on the solid (%)	Activity in supernatant (%)
PdAu@ZIF-8A[a]	-	39 ± 4%
ZIF-8-90[b]	56 ± 3%	82 ± 6%

a: immobilization time = 4 h
b: immobilization time = 2 h

6.4. Conclusion

In this chapter we investigate different strategies to immobilize 3HMU on PdAu@ZIF-8. Attempts toward 3HMU immobilization on ZIF-8 and PdAu@ZIF-8 by physical adsorption led to low loading of active enzyme since only 6 ± 2% of the initial activity was recovered on 3HMU@PdAu@ZIF-8. This poor result was interpreted as an effect of the hydrophobicity of ZIF-8 which induces a significant denaturation of 3HMU. Carbonyl-functionalized ZIF-8-90, on the other hand, greatly reduced the 3HMU immobilization rate, with 82 ± 6% relative activity in the supernatant after 2 h of immobilization. However, the relative activity of 3HMU immobilized on ZIF-8-90 significantly increased to 56 ± 3%. This suggests that the immobilized 3HMU is 4-fold more active than in solution.

In conclusion, comparing the above immobilization strategies, the carbonyl-functionalized ZIF-

8-90 has the highest immobilized activity, followed by Ni^{2+} surface modification. Both methods of immobilization of 3HMU can be used to test the catalytic one-pot/two-step cascade amination of 1-phenylethanol.

References

(1) Guo, F.; Berglund, P. Transaminase Biocatalysis: Optimization and Application. *Green Chem.* **2017**, *19* (2), 333–360. https://doi.org/10.1039/C6GC02328B.

(2) Singh, R. K.; Tiwari, M. K.; Singh, R.; Lee, J.-K. From Protein Engineering to Immobilization: Promising Strategies for the Upgrade of Industrial Enzymes. *International Journal of Molecular Sciences* **2013**, *14* (1), 1232–1277. https://doi.org/10.3390/ijms14011232.

(3) Chen, S.; Land, H.; Berglund, P.; Humble, M. S. Stabilization of an Amine Transaminase for Biocatalysis. *Journal of Molecular Catalysis B: Enzymatic* **2016**, *124*, 20–28. https://doi.org/10.1016/j.molcatb.2015.11.022.

(4) Mallin, H.; Menyes, U.; Vorhaben, T.; Höhne, M.; Bornscheuer, U. T. Immobilization of Two (R)-Amine Transaminases on an Optimized Chitosan Support for the Enzymatic Synthesis of Optically Pure Amines. *ChemCatChem* **2013**, *5* (2), 588–593. https://doi.org/10.1002/cctc.201200420.

(5) Cárdenas-Fernández, M.; Neto, W.; López, C.; Álvaro, G.; Tufvesson, P.; Woodley, J. M. Immobilization of Escherichia Coli Containing ω-Transaminase Activity in LentiKats®. *Biotechnology Progress* **2012**, *28* (3), 693–698. https://doi.org/10.1002/btpr.1538.

(6) Truppo, M. D.; Strotman, H.; Hughes, G. Development of an Immobilized Transaminase Capable of Operating in Organic Solvent. *ChemCatChem* **2012**, *4* (8), 1071–1074. https://doi.org/10.1002/cctc.201200228.

(7) Yi, S.-S.; Lee, C.; Kim, J.; Kyung, D.; Kim, B.-G.; Lee, Y.-S. Covalent Immobilization of ω-Transaminase from Vibrio Fluvialis JS17 on Chitosan Beads. *Process Biochemistry* **2007**, *42* (5), 895–898. https://doi.org/10.1016/j.procbio.2007.01.008.

(8) Neto, W.; Schürmann, M.; Panella, L.; Vogel, A.; Woodley, J. M. Immobilisation of ω-Transaminase for Industrial Application: Screening and Characterisation of Commercial Ready to Use Enzyme Carriers. *Journal of Molecular Catalysis B: Enzymatic* **2015**, *117*, 54–61. https://doi.org/10.1016/j.molcatb.2015.04.005.

(9) Van den Biggelaar, L.; Soumillion, P.; Debecker, D. P. Enantioselective Transamination in Continuous Flow Mode with Transaminase Immobilized in a Macrocellular Silica Monolith. *Catalysts* **2017**, *7* (2), 54. https://doi.org/10.3390/catal7020054.

(10) Yu, J.; Zong, W.; Ding, Y.; Liu, J.; Chen, L.; Zhang, H.; Jiao, Q. Fabrication of ω-Transaminase@Metal-Organic Framework Biocomposites for Efficiently Synthesizing Benzylamines and Pyridylmethylamines. *Advanced Synthesis & Catalysis* **2022**, *364* (2),

380–390. https://doi.org/10.1002/adsc.202100997.

(11) Gairola, P.; Millot, Y.; Krafft, J.-M.; Averseng, F.; Launay, F.; Massiani, P.; Jolivalt, C.; Reboul, J. On the Importance of Combining Bulk- and Surface-Active Sites to Maximize the Catalytic Activity of Metal–Organic Frameworks for the Oxidative Dehydrogenation of Alcohols Using Alkyl Hydroperoxides as Hydride Acceptors. *Catal. Sci. Technol.* **2020**, *10* (20), 6935–6947. https://doi.org/10.1039/D0CY00901F.

(12) Ly, H. G. T.; Fu, G.; Kondinski, A.; Bueken, B.; De Vos, D.; Parac-Vogt, T. N. Superactivity of MOF-808 toward Peptide Bond Hydrolysis. *J. Am. Chem. Soc.* **2018**, *140* (20), 6325–6335. https://doi.org/10.1021/jacs.8b01902.

(13) Yang, X.-G.; Zhang, J.-R.; Tian, X.-K.; Qin, J.-H.; Zhang, X.-Y.; Ma, L.-F. Enhanced Activity of Enzyme Immobilized on Hydrophobic ZIF-8 Modified by Ni2+ Ions. *Angewandte Chemie International Edition* **2023**, *62* (7), e202216699. https://doi.org/10.1002/anie.202216699.

(14) Cho, K. Y.; An, H.; Do, X. H.; Choi, K.; Yoon, H. G.; Jeong, H.-K.; Lee, J. S.; Baek, K.-Y. Synthesis of Amine-Functionalized ZIF-8 with 3-Amino-1,2,4-Triazole by Postsynthetic Modification for Efficient CO2-Selective Adsorbents and Beyond. *J. Mater. Chem. A* **2018**, *6* (39), 18912–18919. https://doi.org/10.1039/C8TA02797H.

(15) Eum, K.; Jayachandrababu, K. C.; Rashidi, F.; Zhang, K.; Leisen, J.; Graham, S.; Lively, R. P.; Chance, R. R.; Sholl, D. S.; Jones, C. W.; Nair, S. Highly Tunable Molecular Sieving and Adsorption Properties of Mixed-Linker Zeolitic Imidazolate Frameworks. *J. Am. Chem. Soc.* **2015**, *137* (12), 4191–4197. https://doi.org/10.1021/jacs.5b00803.

(16) Zoungrana, T.; Findenegg, G. H.; Norde, W. Structure, Stability, and Activity of Adsorbed Enzymes. *Journal of Colloid and Interface Science* **1997**, *190* (2), 437–448. https://doi.org/10.1006/jcis.1997.4895.

(17) Rabe, M.; Verdes, D.; Seeger, S. Understanding Protein Adsorption Phenomena at Solid Surfaces. *Advances in Colloid and Interface Science* **2011**, *162* (1), 87–106. https://doi.org/10.1016/j.cis.2010.12.007.

(18) Vaidya, L. B.; Nadar, S. S.; Rathod, V. K. Entrapment of Surfactant Modified Lipase within Zeolitic Imidazolate Framework (ZIF)-8. *International Journal of Biological Macromolecules* **2020**, *146*, 678–686. https://doi.org/10.1016/j.ijbiomac.2019.12.164.

(19) Lyu, F.; Zhang, Y.; Zare, R. N.; Ge, J.; Liu, Z. One-Pot Synthesis of Protein-Embedded Metal–Organic Frameworks with Enhanced Biological Activities. *Nano Lett.* **2014**, *14* (10), 5761–5765. https://doi.org/10.1021/nl5026419.

(20) Zhang, K.; Lively, R. P.; Dose, M. E.; Brown, A. J.; Zhang, C.; Chung, J.; Nair, S.; Koros, W. J.; Chance, R. R. Alcohol and Water Adsorption in Zeolitic Imidazolate Frameworks. *Chem. Commun.* **2013**, *49* (31), 3245–3247. https://doi.org/10.1039/C3CC39116G.

(21) Zhang, K.; Lively, R. P.; Zhang, C.; Koros, W. J.; Chance, R. R. Investigating the Intrinsic Ethanol/Water Separation Capability of ZIF-8: An Adsorption and Diffusion Study. *J. Phys. Chem. C* **2013**, *117* (14), 7214–7225. https://doi.org/10.1021/jp401548b.

(22) Mungikar, A. A.; Forciniti, D. Conformational Changes of Peptides at Solid/Liquid Interfaces: A Monte Carlo Study. *Biomacromolecules* **2004**, *5* (6), 2147–2159. https://doi.org/10.1021/bm049808s.

(23) Talbert, J. N.; Goddard, J. M. Enzymes on Material Surfaces. *Colloids and Surfaces B: Biointerfaces* **2012**, *93*, 8–19. https://doi.org/10.1016/j.colsurfb.2012.01.003.
(24) Kondo, A.; Murakami, F.; Higashitani, K. Circular Dichroism Studies on Conformational Changes in Protein Molecules upon Adsorption on Ultrafine Polystyrene Particles. *Biotechnology and Bioengineering* **1992**, *40* (8), 889–894. https://doi.org/10.1002/bit.260400804.
(25) Norde, W.; Zoungrana, T. Surface-Induced Changes in the Structure and Activity of Enzymes Physically Immobilized at Solid/Liquid Interfaces. *Biotechnology and Applied Biochemistry* **1998**, *28* (2), 133–143. https://doi.org/10.1111/j.1470-8744.1998.tb00523.x.
(26) Sörensen, M. H.; Ng, J. B. S.; Bergström, L.; Alberius, P. C. A. Improved Enzymatic Activity of Thermomyces Lanuginosus Lipase Immobilized in a Hydrophobic Particulate Mesoporous Carrier. *Journal of Colloid and Interface Science* **2010**, *343* (1), 359–365. https://doi.org/10.1016/j.jcis.2009.11.014.
(27) Koutsopoulos, S.; Patzsch, K.; Bosker, W. T. E.; Norde, W. Adsorption of Trypsin on Hydrophilic and Hydrophobic Surfaces. *Langmuir* **2007**, *23* (4), 2000–2006. https://doi.org/10.1021/la062238s.
(28) Liu, H.; Guo, P.; Regueira, T.; Wang, Z.; Du, J.; Chen, G. Irreversible Change of the Pore Structure of ZIF-8 in Carbon Dioxide Capture with Water Coexistence. *J. Phys. Chem. C* **2016**, *120* (24), 13287–13294. https://doi.org/10.1021/acs.jpcc.6b03772.
(29) Mallin, H.; Höhne, M.; Bornscheuer, U. T. Immobilization of (R)- and (S)-Amine Transaminases on Chitosan Support and Their Application for Amine Synthesis Using Isopropylamine as Donor. *Journal of Biotechnology* **2014**, *191*, 32–37. https://doi.org/10.1016/j.jbiotec.2014.05.015.
(30) Morris, W.; Doonan, C. J.; Furukawa, H.; Banerjee, R.; Yaghi, O. M. Crystals as Molecules: Postsynthesis Covalent Functionalization of Zeolitic Imidazolate Frameworks. *J. Am. Chem. Soc.* **2008**, *130* (38), 12626–12627. https://doi.org/10.1021/ja805222x.
(31) Abubakar, A.; Abdulmalek, E.; Norhamidah Wan Ibrahim, W.; Cordova, K. E.; Abdul Rahman, M. B. ZIF-90 Nanoparticles Modified with a Homing Peptide for Targeted Delivery of Cisplatin. *Frontiers in Chemistry* **2022**, *10*.
(32) Chen, C.; Vázquez-González, M.; O'Hagan, M. P.; Ouyang, Y.; Wang, Z.; Willner, I. Enzyme-Loaded Hemin/G-Quadruplex-Modified ZIF-90 Metal–Organic Framework Nanoparticles: Bioreactor Nanozymes for the Cascaded Oxidation of N-Hydroxy-l-Arginine and Sensing Applications. *Small* **2022**, *18* (11), 2104420. https://doi.org/10.1002/smll.202104420.
(33) Hu, Z.; Faucher, S.; Zhuo, Y.; Sun, Y.; Wang, S.; Zhao, D. Combination of Optimization and Metalated-Ligand Exchange: An Effective Approach to Functionalize UiO-66(Zr) MOFs for CO2 Separation. *Chemistry – A European Journal* **2015**, *21* (48), 17246–17255. https://doi.org/10.1002/chem.201503078.
(34) Kim, S.; Lee, J.; Jeoung, S.; Moon, H. R.; Kim, M. Surface-Deactivated Core–Shell Metal–Organic Framework by Simple Ligand Exchange for Enhanced Size Discrimination in Aerobic Oxidation of Alcohols. *Chemistry – A European Journal* **2020**, *26* (34), 7568–7572. https://doi.org/10.1002/chem.202000933.

Conclusion and perspectives

Chiral amines are one of the key chemicals for medicinal chemistry. Asymmetric synthesis of chiral amines directly from sustainable alcohols via chemo-bio-catalytic asymmetric synthesis is in line with the requirements of green chemistry. The ultimate aim of this study was to create a fully heterogeneous chemoenzymatic catalyst based on a metal-organic framework (MOF), on which both the chemical and the bio-catalysts are immobilized. Such a multifunctional catalyst was expected to be, capable of catalyzing this eco-friendly amination of alcohols in a cascade "one-pot" fashion. The MOF selected in this work was ZIF-8 ($Zn(2\text{-}MeIM)_2$), a zeolite-like MOF consisting of Zn^{2+} node and 2-methyimidazole (2-MeIM). Its excellent stability in water and thermal stability give it advantage as a support for enzymes. In this work, this cascade process was first disassembled into the two steps, the oxidation of alcohols catalyzed by the chemocatalyst, leading to intermediate ketones or aldehydes and the amination of these intermediates catalyzed by the ω-transaminases (ω-TAs) in order to study them separately. One of the main challenges of this project was to select a chemical catalyst able to catalyze the oxidation of alcohols under the mild and aqueous conditions required for the efficient functioning of the transaminase enzymes. Another challenging issue was to heterogenized these catalysts within ZIF-8 framework without affecting their catalytic performances.

Based on ZIF-8, we developed two different types of supported nanoparticle catalysts and successfully used them for the aerobic oxidation of alcohols under mild conditions.

The first catalytic system deals with the heterogenization of Cu^{2+} on ZIF-8 as heterogeneous catalyst for the aerobic oxidation of benzyl alcohol in the presence of TEMPO (2,2,6,6-Tetramethylpiperidine 1-oxyl) as a co-catalyst (Chapter 3). After the attempt of direct wet impregnation of Cu^{2+} on ZIF-8, significant leaching during the catalytic cycle was observed. We subsequently found that reducing Cu^{2+} impregnated on ZIF-8 into Cu nanoparticles (NPs) can effectively inhibit the leaching of Cu^{2+}. Two different reduction methods were applied to prepare Cu NPs@ZIF-8 (dry reduction by H_2 flow and wet reduction by $NaBH_4$). We conducted

detailed characterization of Cu/ZIF-8 reduced by two different methods through XRD, N_2 adsorption, TEM, and XPS. We found that although different reduction methods prepared Cu NPs with similar sizes (18 nm), they resulted in completely different NP dispersion. Only the dry reduction route under H_2 atmosphere allowed the synthesis of well-dispersed Cu NPs located within the bulk of ZIF-8 crystals. The entrapment of Cu NPs in the microporous hybrid network endows the catalyst (Cu/ZIF-8(H_2)) with high stability and selective catalytic potential based on the substrate molecular size. In contrast, the use of $NaBH_4$ resulted in the formation of Cu NPs loosely deposited only on the external surface of ZIF-8 crystals. In addition to this, the formation of ZnO species was also observed in the wet-reduced catalyst (Cu/ZIF-8($NaBH_4$)). We also observed the impact of this distribution difference on the catalytic properties. With similar catalytic activity, the stability of the catalyst Cu/ZIF-8($NaBH_4$) is lower than that of Cu/ZIF-8(H_2). Therefore, the innovative significance of this study is to reveal the impact of different reduction methods on the distribution of NPs on MOFs, and to explore the impact of this NP distribution difference on the stability of supported metal NPs catalysis. Finally, this study also realized the one-pot cascade catalytic aerobic oxidation of alcohol/Knoevenagel condensation to prepare benzylidene mononitrile. Unfortunately, Cu/ZIF-8(H_2) was confirmed to have no catalytic activity in water and therefore could not be used in the heterogeneous chemoenzymatic catalysts.

Outlooks: Since the mechanism of this reaction is still controversial, in the future, the proposed mechanism should be further confirmed by performing computational modeling experiments.

Therefore, we studied the ZIF-8 supported PdAu bimetallic alloy NPs catalyst for the base-free catalytic aerobic oxidation of alcohol in water (Chapter 4). Pd and Au precursors were introduced using the impregnation method and reduced under H_2 atmosphere to prepare PdAu bimetallic NPs@ZIF-8 with different Pd/Au atomic ratios. The prepared PdAu bimetallic nanoparticles have uniform size (4-6 nm) and are evenly distributed inside the ZIF-8 crystal. The formation of a PdAu alloy was confirmed by both XRD and HRTEM. According to XPS analysis, the Au in PdAu is all Au^0 species, while Pd is a mixture of Pd^0 and Pd^{2+}. The

synthesized bimetallic NPs have excellent activity for catalyzing the aerobic oxidation of both primary and secondary alcohols in water. And no additional base is needed. Among them, the catalyst activity is the strongest when the Pd/Au atomic ratio is 9:1 (Conversion 62% and 83% for benzyl alcohol and 1-PE). The aqueous phase compatibility and mild reaction temperature and pH of PdAu@ZIF-8 make it an ideal candidate for constructing heterogeneous chemoenzymatic catalysts.

Subsequently, we focused on the second step of the chemoenzymatic process, that is the biocatalytic amination of ketones (Chapter 5). Two different S-selective ω-TAs, 3HMU and *Cv*-ω-TA, were tested in the optimal working pH range, which are pH 8.5-9.5 and pH 8.0 respectively. Subsequently, they were investigated to catalyze the asymmetric amination reaction of acetophenone (AP) to prepare S-α-methylbenzylamine (S-MBA). Due to the need to overcome the unfavorable thermodynamic equilibrium of the reversible reaction, excess isopropylamine (IPA), 1,2-propylenediamine, and L-alanine associated to the LDH/GDH multi-enzyme cascade system were used as amine donors to shift the reaction equilibrium, respectively. When L-alanine was used as the amine donor for pyruvate conversion, the amination of AP catalyzed by 3HMU achieved a maximum yield of 77% of MBA, which is the best performance obtained in this study. Therefore, 3HMU associated to the L-alanine amine donor and its LDH/GDH axillaries (used to shift the transamination equilibrium) was selected as an enzyme system because of its excellent biocatalytic amination activity.

Outlooks: In the future, other methods of shifting the equilibrium of chemical reactions could be explored, such as searching for new smart amine donors, or alternative low-cost multi-enzyme cascade catalysis for converting by-products.

Also, the estimation of the enantioselectivity for the substrate methylbenzylamine will be achieved by using a HPLC column that is packed with a chiral stationary phase.

Then, the possibility to combine the alcohol catalysis with the enzymatic catalysis in a one-pot process, namely where all the components composing the chemical and enzymatic processes are mixed within a same reaction mixture, was monitored., To this end, the catalysis of the

aerobic oxidation reaction of 1-phenylethanol (1-PE) by Pd_9Au_1@ZIF-8 was studied under 3HMU working conditions (Chapter 5). The effects of substances composing the amination catalysis system, including buffers (Tris HCl, phosphate, carbonate), amine donor (L-alanine, IPA), and part of the LDH/GDH system components (i.e D-glucose) on Pd_9Au_1@ZIF-8 activity were tested. Unfortunately, phosphates and carbonates damaged the ZIF-8 structure, while Tris HCl, L-alanine, IPA, and D-glucose were shown to partially inhibit the Pd_9Au_1 NP activity. Hence, the targeted one-pot/one-step cascade alcohol amination process was demonstrated not to be feasible. With the aim to avoid any interferences, we tested a one-pot/two-step cascade reaction where the oxidation and amination reactions are achieved into two steps: in this process, the transamination catalytic system is added to the reaction mixture (and the pH adjusted to 8.5) once the oxidation step is complete. Under these conditions, 1-PE oxidation yield and acetophenone amination yield in the first and second steps reached 75% and 65%, respectively, resulting in a total yield of S-MBA of 49%. Therefore, a cascade catalytic system based on one-pot/two-step reaction of PdAu@ZIF-8 and 3HMU was successfully realized.

Outlooks: In the future, in order to understand the reasons for the inhibition of Pd_9Au_1@ZIF-8 under different conditions, Pd_9Au_1@ZIF-8 before and after the reaction can be characterized by XPS, XRD, FTIR, etc.

Finally, attempts to develop a heterogeneous the one-pot/two-step cascade catalytic system were carried out by immobilizing 3HMU on Pd_9Au_1@ZIF-8 (Chapter 6). Different strategies were applied to immobilize 3HMU. First, 3HMU was directly fixed on Pd_9Au_1@ZIF-8 through physical adsorption. The immobilized 3HMU only harvested 6% relative activity. PVP was employed to improve the structure stability of 3HMU, but with little success. As revealed by Zeta potential, Pd_9Au_1@ZIF-8 and 3HMU respectively have opposite surface charges at pH 8.5. Therefore, attractive electrostatic interaction is likely to be one of the driving forces for the immobilization of 3HMU via adsorption. In addition, due to the strong hydrophobicity of Pd_9Au_1@ZIF-8 crystals, hydrophobic interactions may also be one of the reasons for the adsorption and deactivation of 3HMU.

Outlooks: In the future, FTIR, Raman spectroscopy and/or circular dichroism can be applied as useful technique to study the secondary structure (amide band) of free and immobilized 3HMU, to understand the correlation between 3HMU activity and its structure.

We then modified the surface of Pd_9Au_1@ZIF-8 with metal cations to change its surface charge and hydrophobicity. Among the four metal cations tested (Ni^{2+}, Cu^{2+}, Ca^{2+}, Fe^{2+}), Ni^{2+} was the most promising one and hence selected for detailed study. We demonstrated that Ni^{2+} modification can reduce the Zeta potential intensity of the Pd_9Au_1@ZIF-8 surface. 3HMU immobilized on Ni^{2+}-modified Pd_9Au_1@ZIF-8 for 2 hours retained 14% of the total initial activity of the enzyme in solution, which was slightly improved compared to unmodified Pd_9Au_1@ZIF-8.

Finally, we tested the immobilization of 3HMU on ligand-exchanged Pd_9Au_1@ZIF-8 and ZIF-8. The exchange of a part of ZIF-8 methyl-imidazole ligands with triazolate and imidazolate derivatives bearing amine and aldehyde moieties was expected to modify the chemistry of ZIF-8 crystal surface and hence improve the interactions between 3HMU and ZIF-8. In case of the amino-functionalized Pd_9Au_1@ZIF-8A, although a significant ligand exchange proportion could obtain (19%), 3HMU immobilized on Pd_9Au_1@ZIF-8A did not gain any activity. As another strategy of ZIF-8 modification, it was hoped that when using aldehyde substituted ligands, a covalent bond is likely to take place between the aldehyde group of the MOF ligand and the lysine amino groups of the enzyme, leading to the formation of an imine. Indeed, we discovered that 4-fold more active 3HMU can be immobilized on ZIF-8-90 (ZIF-8 modified with the imidazolate derivative bearing the aldehyde moiety) compared to PdAu@ZIF-8-Ni. Therefore, carbonyl functionalization is a promising ZIF-8 modification method for the immobilization of 3HMU. This aldehyde functionalization of the Pd_9Au_1@ZIF-8, as well as the effect of this modification on its catalysis activity for the oxidation of 1-PE are currently undergoing.

The synthesis of the chemoenzymatic catalyst composed of ZIF-8 supporting both the alcohol oxidation catalyst (PdAu NPs) and the amination enzymatic catalyst (3HMU) is hence still

under process. The time frame of this PhD course did not allow us to fulfill the ultimate final goal, that is, the implementation of the chemoenzymatic one-pot/two-step cascade process allowing to synthesize amines from alcohol catalyzed by a fully recyclable heterogenous chemoenzymatic catalyst.

Nevertheless, this PhD work resulted in significant advances:

- The creation of a new catalyst for the aerobic alcohol oxidation made of copper nanoparticles supported on ZIF-8. This catalyst was shown to be active, selective and stable under mild temperature. Moreover, the critical effect of the method of copper cation reduction to form the copper metal nanoparticles within the structure of the MOF was demonstrated for the first time. This study was published in the peer-reviewed journal ACS Applied Materials & Interfaces:

Copper Nanoparticles Supported on ZIF-8: Comparison of Cu(II) Reduction Processes and Application as Benzyl Alcohol Oxidation Catalysts

Yifan Zan, Ferdaous Ben Romdhane, Antoine Miche, Christophe Méthivier, Jean-Marc Krafft, Claude Jolivalt, Julien Reboul ACS Appl. Mater. Interfaces 2023, 15, 32, 38716–38728. DOI: 10.1021/acsami.3c08906

This study was also presented in several French national and international congress by means of posters and oral presentations.

- The creation of another heterogeneous catalyst for the aerobic oxidation of alcohols in water, based on the deposition of PdAu nanoparticles with the proper Pd/Au ratio in the framework of ZIF-8 (Pd_9Au_1@ZIF-8). Noteworthy, PdAu nanoparticles supported on ZIF-8 was successfully applied for the first time as catalyst for the aerobic oxidation of alcohols.

- The creation of an original chemoenzymatic system made by the combination of PdAu@ZIF with the transaminase 3HMU. Although not fully heterogeneous (the enzyme 3HMU is not attached on the ZIF-8 yet), this chemoenzymatic system already allowed the one-pot/two-step amination of 1-phenylethanol into methylbenzylamine.

- The discovery of the positive effect of MOF ZIF-8-90 used as a support of transaminase. This mixed-ligand ZIF was indeed demonstrated to significantly enhance (4-fold increase) the activity of supported 3HMU compared to the best results obtained with PdAu@ZIF-8Ni, but also, from the preliminary results obtained, allow to enhance the specific activity of the immobilized 3HMU. This unexpected finding will be confirmed and further studied in a forthcoming study.

Further perspectives.

In the future, it is recommended to continue to explore the following pathways to realize one-pot/two-step cascade catalytic amination of 1-PE to synthesize chiral amines:

- Change the 3HMU/ZIF-8-90 mass ratio in the immobilization operation to optimize the immobilization rate.
- The carbonyl functionalization will be achieved on the Pd_9Au_1@ZIF-8 (leading to Pd_9Au_1@ZIF-8/90) and tested for its activity in catalyzing the aerobic oxidation of 1-PE. If Pd_9Au_1@ZIF-8-90 still retains satisfactory aerobic oxidation catalytic activity, the same immobilization method as 3HMU on ZIF-8-90 will be achieved and the one-pot/two-step cascade catalytic amination of 1-PE will be tested with the fully heterogenized 3HMU@Pd_9Au_1@ZIF-8-90 catalyst.